Electric control of magnetic behavior in artificial multiferroic composites

Thi Thanh Huyen Nong

To cite this version:

Thi Thanh Huyen Nong. Electric control of magnetic behavior in artificial multiferroic composites. Mechanics of materials [physics.class-ph]. Université Sorbonne Paris Cité, 2018. English. NNT : 2018USPCD070 . tel-02619825

HAL Id: tel-02619825
https://theses.hal.science/tel-02619825v1

UNIVERSITÉ PARIS 13
École doctorale de l'Institute Galilée

THÈSE

Pour obtenir le grade de
DOCTEUR de l'UNIVERSITÉ PARIS 13
Sorbonne Paris Cité (USPC)

Spécialité

Sciences des Matériaux

Présentée et soutenue publiquement par

Thi-Thanh-Huyen NONG

le 20 décembre 2018

Sujet de la thèse :

Electric control of magnetic behavior in artificial multiferroic composites

Directrice de thèse : **Mme. Silvana MERCONE**

JURY :

M. Noureddine Jouini	Professeur de l'université Paris 13, LSPM	Président
M. Philippe Lecoeur	Professeur de l'université Paris Sud, C2N	Rapporteur
M. Thomas Hauet	Maitre de conférences (HDR), Université de Lorraine, IJM	Rapporteur
Mme. Brigitte Leridon	CR1, ESPCI ParisTech, LPEM	Examinatrice
Mme. Laure Arbenz	Docteur-Ingénieur, Valeo Powertrain Electrical Systems, Creteil	Examinatrice
Mme. Silvana Mercone	Maitre de conférences (HDR), Université Paris 13, LSPM	Examinatrice

Thèse préparée au sein de Laboratoire des Sciences des Procédés et des Matériaux
LSPM, CNRS-UPR 3407, Villetaneuse

UNIVERSITÉ PARIS 13
École doctorale de l'Institute Galilée

THÈSE

Pour obtenir le grade de
DOCTEUR de l'UNIVERSITÉ PARIS 13
Sorbonne Paris Cité (USPC)

Spécialité

Sciences des Matériaux

Présentée et soutenue publiquement par

Thi-Thanh-Huyen NONG
le 20 décembre 2018

Sujet de la thèse :

Electric control of magnetic behavior in artificial multiferroic composites

Directrice de thèse : **Mme. Silvana MERCONE**

JURY :

M. Noureddine JOUINI	Professeur de l'université Paris 13, LSPM	Président
M. Philippe LECOEUR	Professeur de l'université Paris Sud, C2N	Rapporteur
M. Thomas HAUET	Maitre de conférences (HDR), Université de Lorraine, IJM	Rapporteur
Mme. Brigitte LERIDON	CR1, ESPCI ParisTech, LPEM	Examinatrice
Mme. Laure ARBENZ	Docteur-Ingénieur, Valeo Powertrain Electrical Systems, Creteil	Examinatrice
Mme. Silvana MERCONE	Maitre de conférences (HDR), Université Paris 13, LSPM	Examinatrice

Thèse préparée au sein de Laboratoire des Sciences des Procédés et des Matériaux
LSPM, CNRS-UPR 3407, Villetaneuse

Acknowledgment

I would like to express my sincere gratitude to my supervisor Dr. Silvana MERCONE. Thank you for your enthusiasm guidance and your support over three years. You always have different points of view on science and positive sight on the results, which helps to conduct the research stay on the correct line and solve the problems. Beside, I like your big smile on your face everyday when I come to see you for asking questions and proposing discussion. Thank you also for the cake that you prepared and brought to me sometimes which let me feel like I stay close to my mom in Vietnam.

I am very grateful to the jury members M. Noureddine JOUINI, M. Philippe LECOEUR, M. Thomas HAUET, Mme. Brigitte LERIDON and Mme. Laure ARBENZ for the careful review my thesis and the valuable comments to improve the manuscript as well as the interesting questions during the defense.

I would like to express my sincere thanks to all the colleagues who worked in collaboration with me and help me during my PhD:

Thank to Johan MOULIN, Khouloud MRAD, Chirine Ben OSMAN for elaborating and fabricating the samples.

Thank to Mme. Brigitte LERIDON for your collaboration in MPMS VSM SQUID measurements.

Thank to Alexis GARCIA-SANCHEZ for training me in MFM measurement.

Thank to Andres GOMEZ for training me in PFM measurement at ICMAB (Barcelona, Spain) and work in collaboration with me in PVDF hybrid film.

Thank to Ngoc Anh NGUYEN for fabricating the samples and work in collaboration in PVDF hyrid film.

Thank to Kha Tuan MAI for your help when I learned to use NMAG package for micromagnetic simulation part.

Thank you very much also to all my colleagues and friends at LSPM: Katya PASHOVA, Roland MAHAYRI, Mine ER, Kader CHIMISTE, Easeng SIV, Annika PILLE, Salima KASRI, Ahmed ANDALOUCI, Amal ALLOUCH, Rania DADI, Lahcene MEHMEL, Moustafa EL KASS FHAYLY and many others.

I would like to acknowledge the financial grant from USPC IDEX PHD GRANT - project "ArchiMEdes" (New Architected Magneto-Electric devices) for my PhD, the NFFA Eurpean project for accessing to PFM, XRD, FTIR techniques in ICMAB-CSIC, Barcelona, Spain and the $Eramus^{++}$ fellowship for my traveling to Vietnam for training in micromagnetic simulation.

Last but not least, I would like to send my thanks to my family for alway being beside

and support me all the time even they stay very far from France. I wish to thank my husband Tuong for staying beside me during the hard time and gives me the useful advices and discussion in science during the last year of my PhD.

The science today is
the technology of tomorrow.

EDWARD TELLER

Contents

List of symbols

A	Exchange stiffness
BH_{max}	Magnetic energy product
B_r	Remanent magnetic flux density
d	Piezoelectric coefficient
E	Electric field
E_C	Electric coercive field
E_{mc}	Magnetocrystalline anisotropy energy
E_Z	Zeeman energy
E_A	Anisotropy energy
E_D	Demagnetizing energy
f	Frequency
g	Electromechanical constant
H	Magnetic field
H_C	Magnetic coercive field
H_S	Saturate field
H_d	Demagnetizing field
H_{mc}	Magnetocrystalline anisotropy field
K	Anisotropy constant
K_u	Uniaxial anisotropy constant
M	Magnetization
M_S	Saturation magnetization
M_r	Remanent magnetization
N_d	Demagnetizaing factor
P	Polarization
P	Packing density
P_S	Saturation polarization
P_r	Remanent polarization
SQ	Squareness
T_C	Curie temperature
T_N	Neel temperature
T_G	Glass temperature
α_E	Direct magnetoelectric coupling constant
α_H	Converse magnetoelectric coupling constant

λ	Magnetostrictive coefficient
ϵ	Dielectric constant
μ	Magnetic permeability
μ_0	Magnetic permeability in vacuum
l_{ex}	Magnetic exchange length
ε	strain
σ	stress

Acronyms

AC	Alternating current
BFO	$BiFeO_3$
BTO	$BaTiO_3$
CFO	$CoFe_2O_4$
DC	Direct current
DIC	Digital Image Correlation
EA	Easy axis
FC	Field cooling
FE	Ferroelectric
Finemet	FeCuNbSiB
FM	Ferromagnetic
F-PVDF	PVDF/NPs composite with Functionalized NPs
FTIR	Fourier Transform Infrared Spectroscopy
LSMO	$La_{1-x}Sr_xMnO_3$
M-AR	Macroscopic- Aspect ratio
MERAM	Magnetoelectric Random Access Memory
ME	Magnetoelectric
MFM	Magnetic Force Microscopy
MRAM	Magnetic Random Access Memory
MPMS	Magnetic property measurement system
NFO	$NiFe_2O_4$
NF-PVDF	PVDF/NPs composite with Non-functionalized NPs
NPs	Nanoparticles
NWs	Nanowires
NZFO	$Ni_{0.5}Zn_{0.5}Fe_2O_4$
PFM	Piezoelectric Force Microscopy
PLZT	Lead Lanthanum Zirconate Titanate
PMN-PT	$Pb(Mg_{1/3}Nb_{2/3})_{0.72}Ti_{0.28}O_3$
PMN-PZT	$Pb(Mg_{1/3}Nb_{2/3})_y(Zr_xTi_{1-x})O_3$
PVDF	Polyvinylidene Fluoride
PZN-PT	$Pb(Zn_{1/3}Nb_{2/3})O_3$ - $PbTiO_3$
PZT	Lead Zirconate Titanate
SEM	Scanning Electron Microscopy

SPM	Scanning Probe Microscopy
SPS	Spark Plasma Sintering
STM	Scanning Tunneling Microscopy
SQUID	Superconducting Quantum Interference Device
TEM	Transmission Electron Microscopy
VSM	Vibrating Sample Magnetometer
XRD	X-Ray diffraction
ZFC	Zero Field Cooling
ZFO	$Zn_{0.1}Fe_{2.9}O_4$
1D	One dimensional
2D	Two dimensional
3D	Three dimensional

The references are ordered by the alphabet of the first author's family name.

List of Figures

Introduction

Materials that possessing at least two ferroic orders, among ferroelectricity, ferromagnetism and ferroelasticity, are called multiferroic materials. They are attractive systems due to the possible giant cross coupling between these three orders. Indeed, a ferromagnetic material show a spontaneous magnetization **M** that can be controlled by applying a magnetic field **H** (blue part in Figure 1). Similarly, the electric spontaneous polarization **P** of a ferroelectric material can be controlled by applying an electric field **E** (pink part in Figure 1). In the case of multiferroic magnetoelectric (ME) materials, the cross coupling occurs between two ferroics orders (magnetic and electric one) and it can give rise to a large direct and/or converse ME effect. Indeed, thanks to an efficient direct ME effect, it becomes possible to control the electric polarization **P** by a magnetic field **H** and respectively thanks to an efficient converse ME effect, it becomes possible to control the magnetization **M** by an electric field **E** (grey part in Figure 1). This coupling effect opens fascinating possibilities for a new generation of devices targeting new smart multi-states memories, magnetic sensors, actuators, transformers and also spintronic systems.

It is important to underline that the interplay between magnetism and electricity was well-known already in 1888 when Rontgen observed the appearance of a magnetic moment in a dielectric material moving in an electric field [163] [1]. The reverse effect was then reported by Wilson in 1905 [213], who observed an electric polarization appearing in a dielectric material moving in a magnetic field. In 1926, the term "magnetoelectric" was introduced by Debye [36]. However, the effect was successfully observed only in 1960 after the prediction of Dzyaloshinskii [39] of a magnetoelectric effect in the chromium oxide (Cr_2O_3) compound which was confirmed by Astrov experiments. [11].

In 1966 the group of Ascher and Schmidt in Geneva [10] discovered multiferroicity also in nickel-iodine boracite materials. Since then, the number of researches upon intrinsic multiferroics compounds have increased significantly (section 1.3.1). However, the research on this topic is saturated because the magnetoelectric coupling has been often found to be weak and to happen at low temperature (*i.e.* below room temperature).

In the 1990s, with the occurring of the spintronics industry, the possibility offered by the multiferroic materials of the electric control of the magnetization triggered again the attention upon the multiferroics systems. This renewing interest shifted the researches of the scientific community from the single phase (or intrinsic) multiferroic materials to the artificial multiferroics compounds. Thanks to their high ME coupling at high temperature, these artificial multiferroics become a hot topic in the last decades. This success

---

[1] Please note that the bibliography is ordered by the first author's family name.

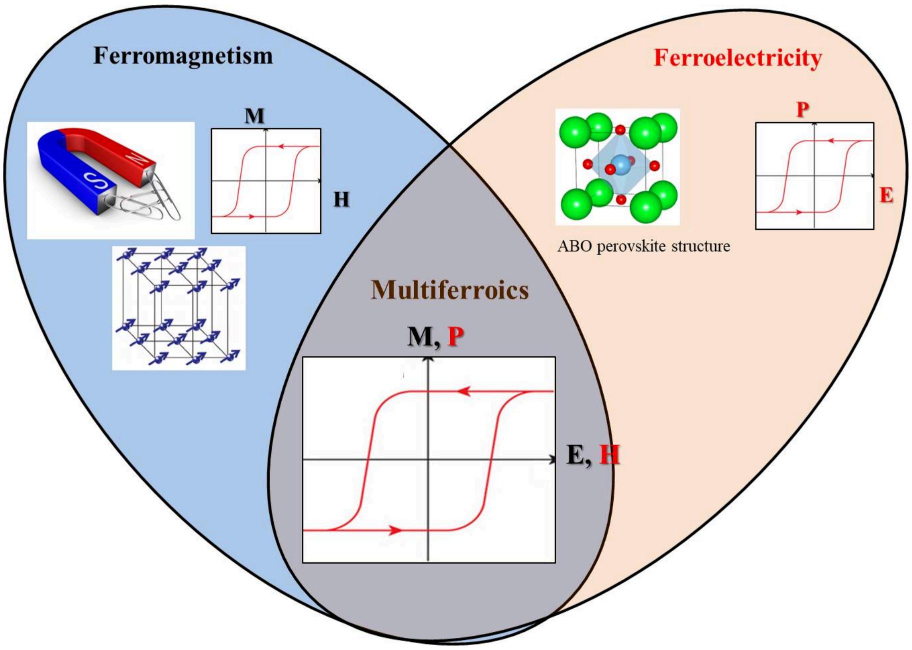

Figure 1: Multiferroic materials display a coexistence of magnetic and electric ferroic orders. The coupling between these different orders provides an opportunity to control the magnetic properties by an external electric field and vice versa.

is witnessed by a large number of published works. In these composite structures, two (or three) phases are artificially coupled together (e.g. the piezoelectric phase/material can be coupled to a magnetostrictive one). In these artificial ME composites, showing physically separated phases, both direct ME and converse ME coupling can be mediated through different physical mechanism: (a) the strain, (b) the charge carrier and (c) the spin exchange [204]. Among them, the strain-mediated ME coupling attracting a lot of attention since it opens novel potential applications in new generation of devices willing to be more efficient and lower power consumption.

This train-mediated effect is based on the elastic coupling between the two phases allowing the control of magnetic behaviors in ME composites by an electric field. In this frame, a steady growth of new ideas for novel nanostructures have been developed in order to improve the strain-mediated ME effect. For practice applications, these composites have to satisfy several requirements: they have to display large ME coupling at room temperature, should be easy to fabricate and consist of cheap chemical elements and compounds. Moreover, the composite nanostructures must be suitable for fabrication at micro- and nano-scale sizes without loss of functionality, in order to be easily integrated at chip/wafer level. Some of these requirements have been already fulfilled, many other still remain to be solve.

Following the developing of these strain-mediated ME composites, flexible PVDF-polymer-based multiferroic composite have attracted a lot of interest during the past ten years [103] [105] [108] [155] [159]. Several research groups have been developing these systems as they open the hope for a new flexible technology, able to cover any kind of surface and being eco-friendly. Many different artificial structures can be studied: bidimensional heterostructures, nano-particulate composites including nanoparticles inside the PVDF matrix, ect. These new artificial materials open new challenges, among others: (i) Optimizing ferroelectric phase of the PVDF as function of the nano-inclusions and the fabrication method; (ii) Understanding the effect of the nano-inclusions on the local physical properties of the composites; (iii) Studying the effect of the quality of the interface between the organic PVDF phase and the inorganic nano-inclusion on the ME coupling; (iv) Characterizing the mechanical properties of the ME nanostructures.

In this frame, the main goal of this work is to investigate the magnetic behavior of ME composites system presenting different type of nanostructure and to control it by the elastic properties of the materials via an electric field application.

This manuscript is divided into five Chapters:

- **Chapter 1. State of the art:** This chapter will briefly describe the theoretical background of materials used in ME multiferroic composites (including magnetic and ferroelectric/piezoelectric systems) and the principle of the ME effect. A state of the art in single-phase and composite multiferroics is reviewed shortly. In particular, an overview on electric control of magnetic properties by strain-mediated effect is presented in three main types of composites structure depending on the dimensionality of the interface between the two phases (so-called 2-2, 0-3 and 1-3 types). Finally, several factors that may affect the ME coupling in multiferroic composites are discussed. Two main potential applications of electric control of magnetic behavior in multiferroic composites are also reported.

- **Chapter 2. Experimental technique and micromagnetic simulation:** Experimental techniques use to characterize the samples and micromagnetic simulation method used in this thesis are discussed here.

- **Chapter 3. Electric control of magnetic domain in 2-2 type ME composites:** The ME 2-2 type based on a magnetostrictive film/flexible substrate/actuator heterostructure is studied by a standard Magnetic Force Microscopy (MFM). The magnetic domain and local magnetic moments orientation is controlled by using an *in situ* external electric field. The results are then compared to the magnetic domain behavior observed under the *in situ* external magnetic field.

- **Chapter 4. 0-3 type ME particulate nanocomposites based on PVDF:**

  In this part, the ME nanocomposite 0-3 type structure with magnetic nanoparticles embedded in an electro-active polymer (PVDF) substrate is studied. The effects of nano-inclusions on the electro-active phase and the piezoelectric response of PVDF are studied by using the Piezoelectric Force Microscopy (PFM). Moreover, we studied the stain-mediated effect on the magnetic behavior of nanoparticles by studying the ME structure under different temperatures/elastic conditions. We performed the magnetic measurement vs. temperature by using a Quantum Design MPMS SQUID-VSM.

- **Chapter 5. Optimizing ferromagnetic properties of anisotropic nanoparticles toward 1-3 type ME nanocomposite:**

  The magnetic properties of cobalt nanowires are investigated by both experiment and simulation techniques. Firstly, we studied the magnetic properties of cobalt nanowires by using the experimental characterization in order to analysis the effect of the morphology and the growing faults in their crystal structure. Moreover, the magnetic behavior of this cobalt anisotropic nanoparticles have been investigated as function of their organizations and interactions inside a non-magnetic media. By using micromagnetic simulation based on finite element method, this cobalt nanoparticles assembly have been studied for different arrangement. Their misalignment effect is discussed as well as the macroscopic magnetic properties of the nanoparticles assembly.

- Finally, a general **conclusion and perspective** will be presented.

- You will find at the end of the manuscript four **Appendices** (From A to D).

Chapter 1

State of the art

1.1 Generalities on Ferroic Materials: theoretical background on ferromagnetism and ferroelectricity

1.1.1 Magnetic materials

The origin of magnetism was firstly understood by using a model of free atoms. Each atom presents a magnetic dipole moment. This magnetic dipole moment is created by the revolution of unpaired electron around the nucleus (orbital angular momentum) and the spinning around their own axis (spin angular momentum) [123]. The atomic magnetic moments interact with their neighbors producing a network of ordered magnetic moments. Different interactions between those moments are possible and can give place to several magnetic ordered materials. Indeed, in some materials there are no collective interaction among the atomic magnetic moments, whereas in other materials very strong interactions can happen. Base on these latter and on the response of the materials to an external magnetic stimulus, we can classified them into five groups: diamagnetics, paramagnetics, ferromagnetics, antiferromagnetics and ferrimagnetics (see Figure 1.1).

Diamagnetic materials cannot be represented by a network of magnetic moments since in their atomic structure there are no unpaired electron. When these materials are exposed to a magnetic field, a negative magnetization is produced (see the Figure 1.2). Unlike diamagnetic materials, paramagnetic materials have a network of random disordered magnetic moment. The interactions between them are very weak and lead to a random order (Figure 1.1). Paramagnetic materials respond to the external field by a linear increasing magnetization (see Figure 1.2). Nevertheless, when removing field, the magnetization returns back to zero like in the case of the diamagnetic materials.

Ferromagnetic materials present strong interactions between the atomic magnetic moments. This interaction, so called exchange interaction, leads to a parallel alignment of the magnetic moments giving rise to a large net magnetization (which is called spontaneous magnetization) even in the absence of an applied magnetic field [123]. Two distinct peculiarities of ferromagnetic materials are: (i) the spontaneous magnetization and (ii) the presence of a critical temperature called Curie temperature. The spontaneous magnetiza-

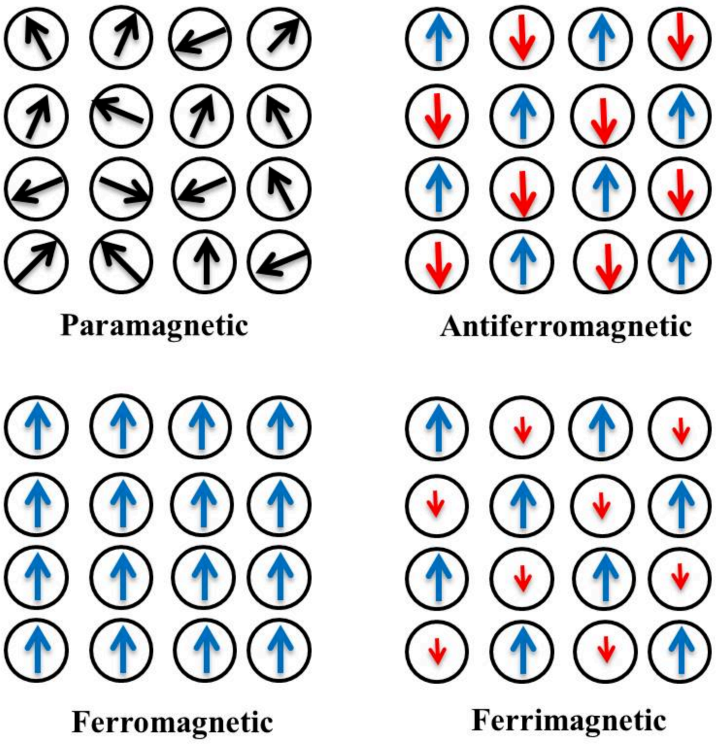

Figure 1.1: Network of ordered magnetic moments in different magnetic materials.

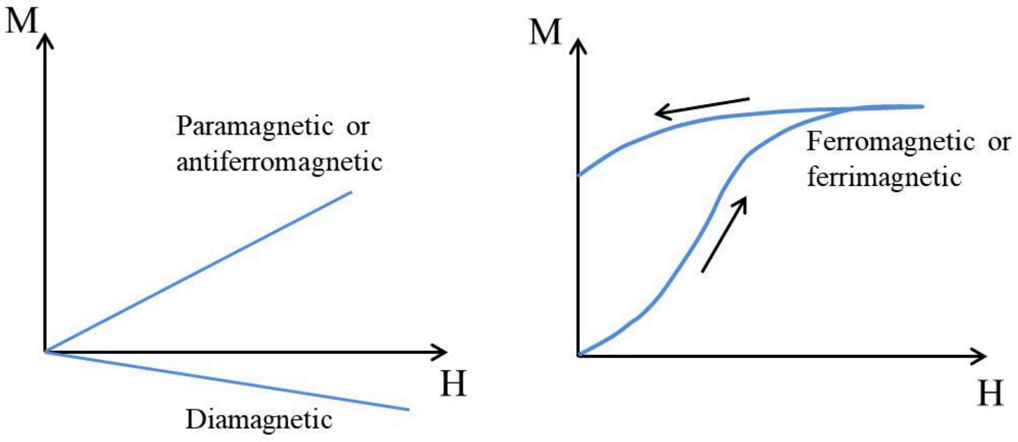

Figure 1.2: Magnetic response of different kind of magnetic materials.

tion tends to align to a preferred direction, which is associated with the magnetocrystalline anisotropy (see section 1.1.3). Although the exchange interaction in ferromagnetics is very large, thermal energy can eventually overcomes the exchange one and thus destroying the ferromagnetic order. This occurs at the critical temperature called the Curie temperature (T_C). Below the Curie temperature, the magnetic moments are ordered (ferromagnetic phase) and above it, disordered state occurs (paramagnetic phase). In ferromagnetic materials, in order to minimize the total magnetic energy, the magnetic moments tend to form small regions (called magnetic domains) where the magnetic moments are aligned parallel to each other [183]. The region between domains oriented differently is called domain wall. When a ferromagnetic materials is bring into a magnetic field, magnetic domains inside the materials tend to align toward the direction of the external stimulus. Removing the magnetic field, a remanent magnetization is observed that can be very close to the one observed in the full oriented network. This behavior is described by the hysteresis characterization of the materials and will be discussed deeply in the Section 1.1.2. Ferromagnetic materials have a larger range of application, in information recording, permanent magnet and magnetic sensors.

Both of antiferromagnetic materials and ferrimagnetic one present a spontaneous magnetization, which is similar to the ferromagnetic systems. However, the strong interactions between the magnetic moments arrange them in this case in an anti-parallel configuration (see Figure 1.1). Thus in the case of antiferromagnetic materials, the total net spontaneous magnetization is zero and can be increased by the applied external field as for paramagnetic materials. In ferrimagnetic materials, the magnetic moments oriented in opposite directions are not equal. This bring to the fact that, although the spontaneous magnetization is also zero, the magnetic moments aligned in one direction are not balanced by the ones aligned in the opposite direction. Thus they present a total magnetization that behaves like the ferromagnetic network (see Figure 1.3).

1.1.2 Magnetic hysteresis loop

The magnetic properties of a ferromagnetic materials are studied by measuring their magnetization under the application of an external magnetic field (M-H curve). The typical M-H hysteresis loop is shown in Figure 1.3 and it is characterized by:

- The saturation magnetization (M_S) representing the maximum magnetization that can be obtained under the application of a magnetic field.
- The remanent magnetization (M_r) being the magnetization presented by the material after removing the applied magnetic stimulus.
- The coercive field (H_C) being the intensity of the applied magnetic field required to reduce the magnetization of the material from the saturation value to the zero one.

The magnetization process of the ferromagnetic materials is based on the growing of the magnetic domains and on the magnetic domain wall motion (see Figure 1.3) [123]. Initially, in the non-magnetized state, all domains are randomly arranged and the total magnetization is zero. When the magnetic field is applied, domains grow leading to the motion of the domain walls. Domains with the spontaneous magnetization aligned along the applied magnetic field will grow as function of this latter. Increasing the magnetic field up to the so called saturation field, brings the material to be characterized to one single magnetic domain. Further increases of the external force pushes the macroscopic magnetization to rotate from the magnetic easy axis to the direction of the field applied.

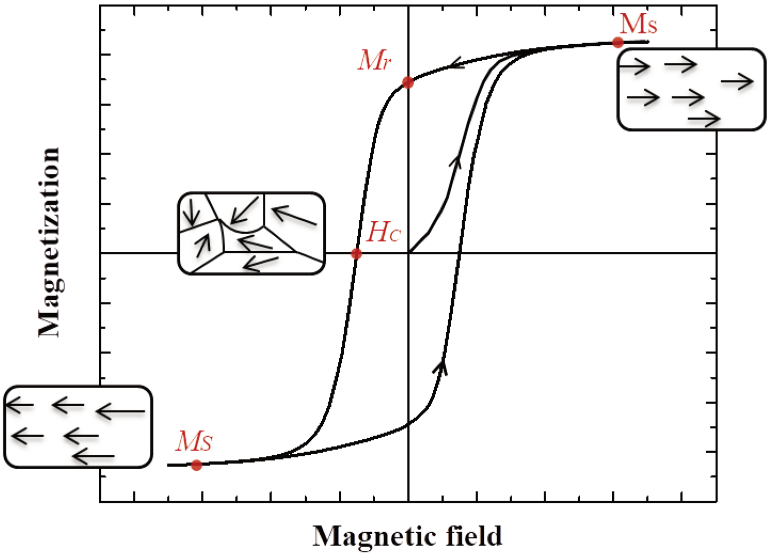

Figure 1.3: A typical hysteresis loop of ferromagnetic materials.

At this point the magnetization has reached its saturation value (M_S). The magnetic easy axis will be discussed into details in section 1.1.3. Removing the magnetic field does not bring the magnetization back to the random state of the domains and a remanent magnetization (M_r) is measured. In the case of strong ferromagnetic material, the remanent state is similar to the saturated one. When the magnetic field is reversed (see Figure 1.3 in the negative values), the material is fully demagnetized to zero at a critical field (i.e. coercive field (H_C)). This is described by the demagnetized curve of the second quadrant in Figure 1.3

1.1.3 Magnetic anisotropy

Magnetic anisotropy is a characteristic of the ferromagnetic material that identifies the magnetization dependence upon the direction along which it is measured. For ordered magnetic materials, the magnetic properties are affected by the magnetic anisotropy. Thus, the nature and the type of the magnetic anisotropy is an important factor to determine the use of the materials for specific applications. Two types of magnetic anisotropy are discussed in the following: the magnetocrystalline anisotropy and the shape anisotropy.

Magnetocystalline anisotropy

In ferromagnetic crystals, the magnetization tends to align along certain preferred crystallographic directions. The preferred directions are called the easy axis. When an external magnetic field is applied along this direction, it is easy to saturate the magnetization. In contrast, it is difficult to saturate the magnetization of the system along a crystallographic direction called hard axis. The other directions are intermediate axis. Depending on the crystallographic symmetry, the easy axis can be different from one crystal structure to another. For instance, in body-centered cubic (bcc) iron system, the easy directions are the six cube edge axis (i.e.[100], [010], [001], [100], [010] and [001] [78]) while the hard directions are four body diagonal orientations. By contrast, the easy axis of face-centered cubic (fcc) Ni is the [111] body diagonal and in the hexagonal close-packed (*hcp*) Co the easy axis is along the [0001] direction, see Figure 1.4.

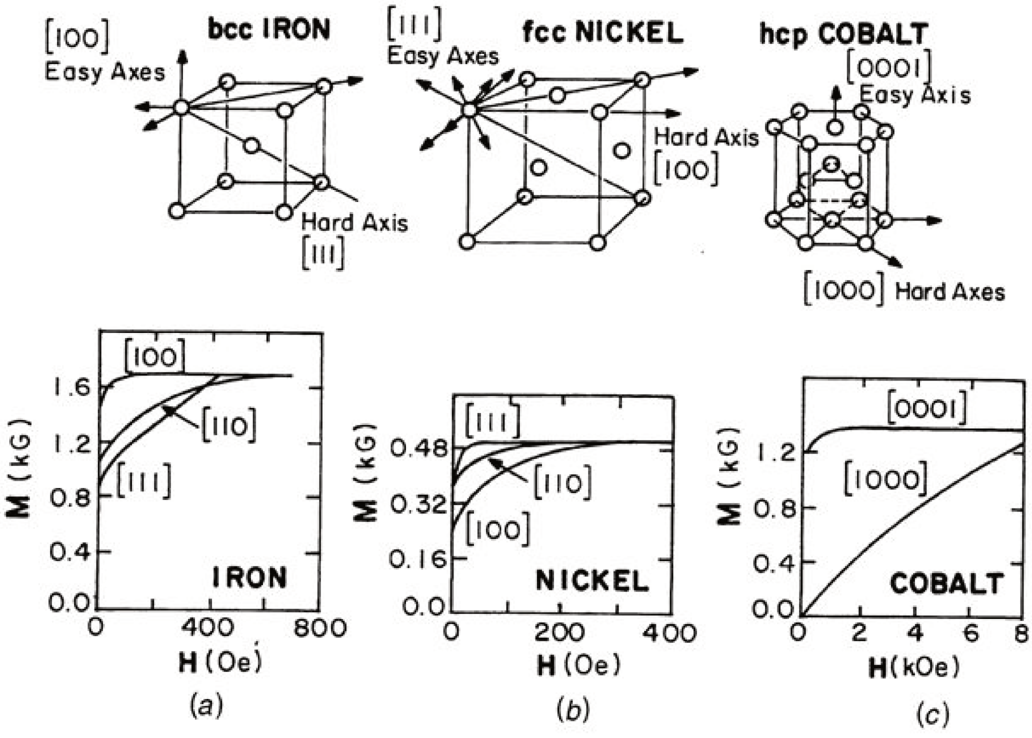

Figure 1.4: Crystal structures showing the easy and hard axes for Fe (a), Ni (b) and Co (c) bulk material. The corresponding magnetization curve along different crystallographic axes are presented below along different crystallographic axes [78].

The magnetocrystalline anisotropy energy (E_{mc}) is the energy needed to moves the magnetization away from the easy direction. We do not know a priori the dependence of the energy of the crystal on the orientation of the magnetic moment. It can be shown [78] that the energy can be expanded into power series of direction cosines related to the crystal axes. For example, in cubic crystal such as iron, the E_{mc} can be written as:

$$E_{mc} = K_0 + K_1(\alpha_1^2\alpha_2^2 + \alpha_2^2\alpha_3^2 + \alpha_3^2\alpha_1^2) + K_2\alpha_1^2\alpha_2^2\alpha_3^2 + ... \tag{1.1}$$

Where K_0, K_1, K_2,... are the anisotropy constants for a given material at a given temperature. The experience shows that it is enough to use very limited number of expansion terms to describes the magnetic moment.

As already seen, for hexagonal crystals such as Co, the easy direction of the magnetization at room temperature is along the c-axis while all the others are hard axises. Due to this unique easy direction, the magnetocrystalline anisotropy is called uniaxial anisotropy. The magnetic energy of this uniaxial anisotropy case can be written as [78]:

$$E_{mc} = K_0 + K_{u1} sin^2\theta + K_{u2} sin^4\theta + ... \tag{1.2}$$

Where K_0, K_{u1} and K_{u2} are the anisotropy constants and θ is the angle between the magnetization vector and the magnetocrystalline easy axis. The subscript ‘u’ is used to identify the uniaxial anisotropy. Whereas the subscript ‘1’ (or ‘2’) defines the first (or second) order term of the magnetic energy.

Shape anisotropy

As indicated by the name, the shape anisotropy identifies the magnetic properties dependence on the shape of the material. In the case of a spherical material it is easy to imagine that all the directions in the space will be equivalent for the application of a magnetic stimulus and thus the response of the material is also isotropic. However, if the material is not isotropic in the space, for example like in Figure 1.5, then it will be easier to magnetize the material along a specific direction (i.e. the long axis in Figure 1.5).

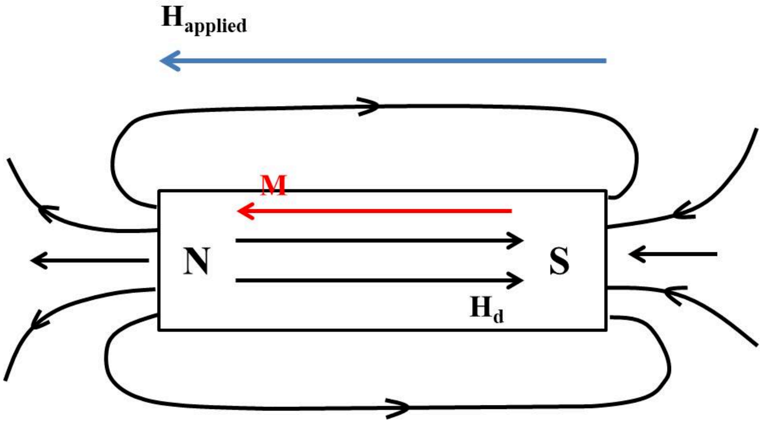

Figure 1.5: **H** field is applied along a magnetic bar.

The origin of the shape anisotropy comes from the demagnetizing field inside the materials. If we consider a magnetic bar which is magnetized a north pole at one end and a south pole at the opposite side appear. By definition, the lines of the magnetic field **H** radiates from the north pole and ends at the south pole (see Figure 1.5). Inside the magnetic bar, the field lines are also oriented in the same direction and hence they are opposed to the magnetization and thus tends to reduce it. The magnetic field inside the magnetic bar creates the so-called demagnetizing field, H_d, which is defined as:

$$H_d = -N_d.\mathbf{M} \tag{1.3}$$

Sample geometry	Shape Factor,N_d (dimensionless)
Flat sheet, $\vec{M}$ normal to surface	1
Flat sheet, $\vec{M}$ in-plane	0
Long cylinder, $\vec{M}$ along length	0
Long cylinder, $\vec{M}$ along width	1/2
Sphere, $\vec{M}$ along orthogonal axes	1/3

Table 1.1: Demagnetizing factor of some simple geometries.

where N_d is the demagnetizing factor, and is determined by the shape of the sample, **M** is the magnetization of the sample. The demagnetizing factor of some simple geometries are shown in table 1.1 [139]:

The magnetostatic energy of this demagnetizing field can be written as:

$$E_D = \frac{1}{2}\mu_0 H_d M = \frac{1}{2}\mu_0 N_d M^2 \tag{1.4}$$

where M is the magnetization and H_d is the demagnetizing field.

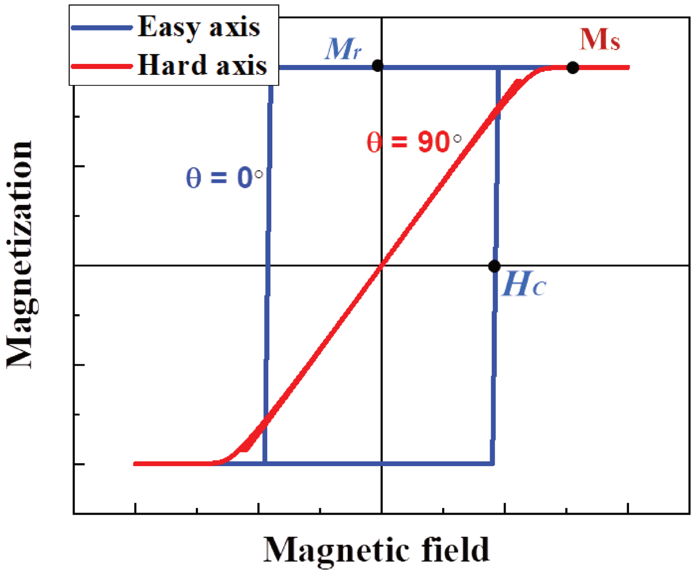

Figure 1.6: Expected hysteresis loop of a ferromagnetic material for the perfect case of magnetic field applying along the easy axis (blue) and the hard axis (red).

Considering an anisotropic ferromagnetic object that owns a magnetocrystalline anisotropy along the length of the object (i.e. the uniaxial anisotropy and the shape one have the same direction), if an external magnetic field is applied parallel to the easy axis, the hysteresis of the object will be presented by a rectangle shape ($\theta = 0°$) (see Figure 1.6, blue line). In contrast, when the magnetic field is applied along the hard axis (perpendicular to the easy one), the hysteresis loop is shown by a straight line ($\theta = 90°$) (see the red line in Figure 1.6). The M_r/M_S ratio is equal 1 for perfect alignment between the **H** field and the magnetization while equal 0 in the contrary case. In general, the hysteresis loop shape of the magnetic materials is represented by a M-H curve which is intermediate in between these two behaviors described before. Thus, the M_r/M_S value is an indication of the mutual align between the external **H** field and the anisotropy axis. depends strongly on the direction of the external applied magnetic field. In which, if the magnetic field is applied along the easy axis, the hysteresis loop will be an open cycle with a M_r/M_S ratio close to 1. On the contrary, the hysteresis loop will be a narrow cycle with a M_r/M_S ratio close to 0, when the magnetic field is apply along the hard axis.

1.1.4 Magnetostriction

Magnetostriction (or Joule magnetostriction) is the effect that describes the deformation of materials when a magnetic field is applied (Figure 1.7). This phenomenon is observed in all ferromagnetic materials. The magnetostrictive effect is defined by the magnetostriction coefficient, $\lambda(H) = \frac{\Delta l(\mu_0 H)}{l} = \frac{l(\mu_0 H) - l_0}{l_0}$. It represents the change in length arising from application of the magnetic field on the ferromagnetic material during the process of magnetization. The magnetostriction coefficient can be positive (expansion), negative (contraction), or zero as in the case of some alloys ($Ni_{82}Fe_{18}$) [78].

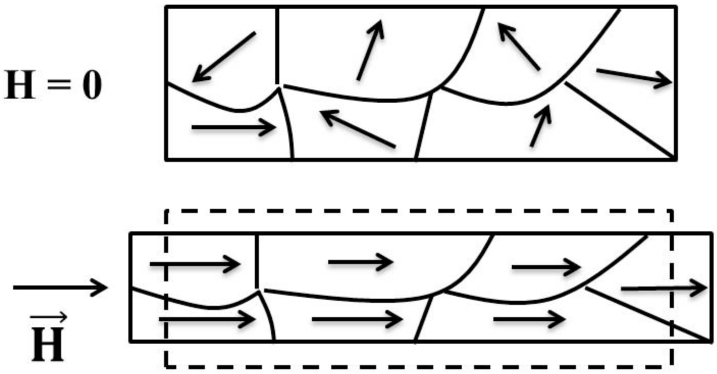

Figure 1.7: Example of magnetostriction effect. The rotation of the spontaneous magnetization in each domain is also accompanied by a deformation of sample while applying a magnetic field, **H**.

The origin of magnetostriction is the coupling between the magnetic and the elastic properites of the materials (so called the magnetoelastic coupling). In a crystal structure, this arises from the tendency of neighboring ions to shift their positions in response to the rotation of the magnetic moment under the application of **H** [114]. Other explanations are linked to the domain walls motion and the domain rotations during the magnetization process, followed by a spontaneously deformation of the crystal lattice inside each domain along the direction of their domain magnetic moment. Finally, at the saturation magnetization, this results in a macroscopic deformation of the sample, $\Delta l(\mu_0 H)$ [78].

The inverse effect of magnetostriction is called the Villari effect, and concerns the change in magnetization due to an applied stress. This effect is explained by the change of the domain structure when a mechanical force is applied. The Villari effect is commonly used in the magnetic sensors and in the multifunctional devices [53], [208], [226].

1.1.5 Ferroelectric materials and piezoelectricity

Ferroelectric materials

Materials that display a spontaneous polarization, P, that can be reversed using an external electrical field, are called ferroelectrics [216]. A pair of electrical charges (+ and -) constitutes an electric dipole which is defined by an electric dipole moment (p) (the moment is directed from the negative charge (-) to the positive one (+)). The polarization (P) is the amount of electric dipoles (p) per unit volume (V): P = p/V.

Similarly as ferromagnetic materials, ferroelectric materials have ferroelectric domains with the electric dipole moments parallel to each other inside each domain. The main characteristic of ferroelectric materials is their hysteresis loop (P-E), see Figure 1.8.

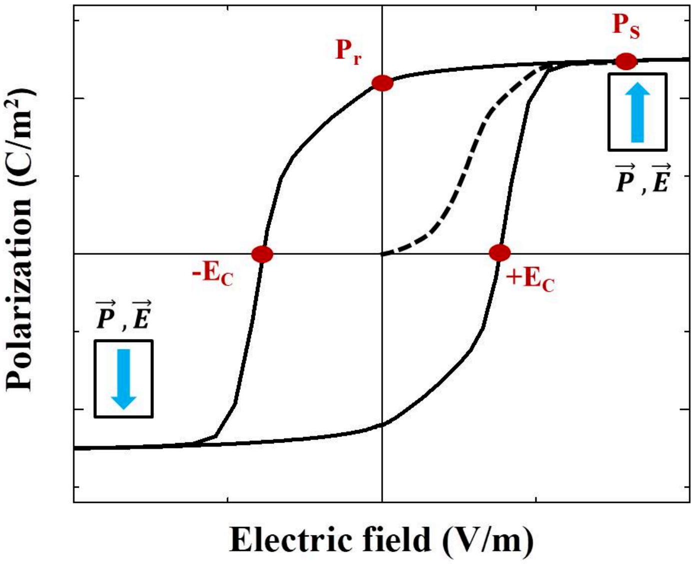

Figure 1.8: A typical hysteresis loop of a ferroelectric material representing the polarization as function of the external stimulus.

This P-E hysteresis loop represents (similarly to the ferromagnetic case) the reversal mechanism of the spontaneous polarization in the ferroelectric materials when an electric field is applied. From a depolarized state, the ferroelectric domains start to align in the positive direction following the increasing of the electric field (E-field), giving rise to a rapidly increasing of the polarization. At very high E-field, the polarization reaches a saturation value (P_S). The polarization does not go to zero when the external field is removed. At zero E-field, some of the domains remain aligned in the positive direction, hence the materials reaches a remanent polarization (P_r). The materials cannot be completely depolarized (P = 0) until a field (coercive field, E_C) is applied in the negative direction. If the field is increased to a higher negative value, the direction of polarization flips and hence the hysteresis loop is obtained (see Figure 1.8).

Similarly as in the ferromagnetic materials, ferroelectric systems have a transition temperature, which is called Curie temperature (T_C). Above T_C, ferroelectric materials do not exhibit the ferroelectricity behavior, while below T_C they are ferroelectric.

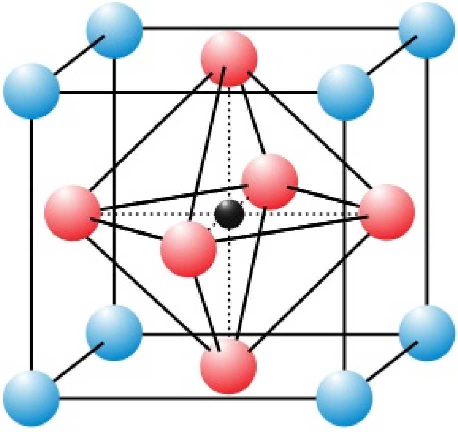

.

Figure 1.9: Schematic illustration of the ABO_3 perovskite crystal structure. **A** sites are occupied by cations (blue) and are at the corners of the unit cell. **B** cations (black) are at the center of an octahedron of oxygen anions (pink/red)

A typical ferroelectric crystal structure is the perovskite type structure ABO_3 [69] [216] (see Figure 1.9), where A and B are cations and the oxygen form a characteristic octahedron. Several well-known ferroelectric materials possess a perovskite structure like the Barium Titanate ($BaTiO_3$), Lead Titanate ($PbTiO_3$), Lead Zirconate Titanate (PZT), Lead Lanthanum Zirconate Titanate (PLZT). These latters based on the lead element are commonly used in the daily technology of piezoelectric sensors.

Piezoelectric materials

Piezoelectric materials are the materials that can generate an electric polarization when they are subjected to a mechanical stress (direct piezoelectric effect). Conversely, when an electric field is applied to these materials, a macroscopic deformation appears (inverse piezoelectric effect). The piezoelectric properties exist in certain compounds which show a non centered symmetry of the crystal structure (e.g. quartz, ceramics and polymer). Only some of them are ferroelectric [62]. Thus, all ferroelectric materials exhibit piezoelectric properties while not all the well-known piezoelectric systems show ferroelectric behavior.

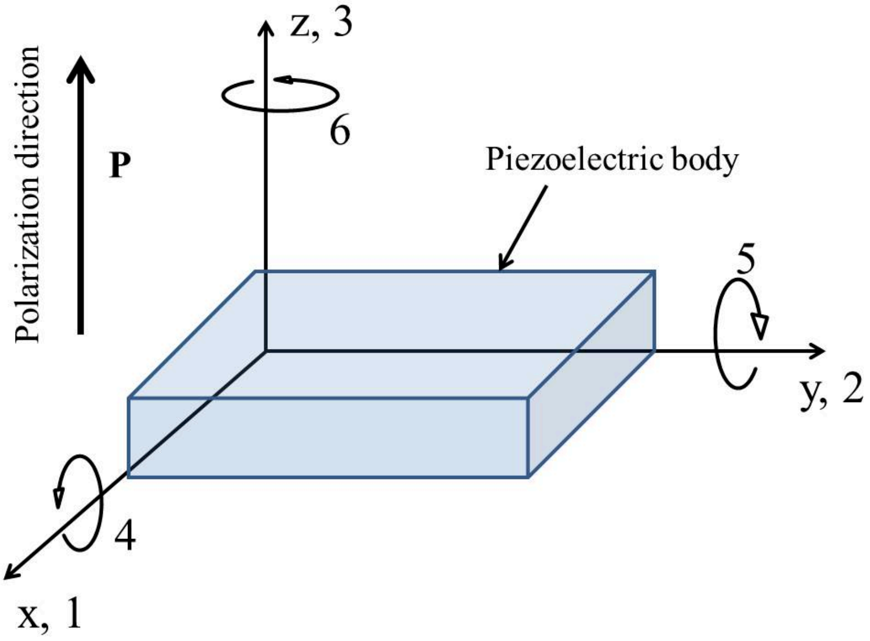

Figure 1.10: Axis nomenclature

Piezoelectric properties are characterized by piezoelectric coefficient d and g which are determined by electromechanical equations. Considering the electromechanical equations for a piezoelectric material [8], [37], [62], [122]:

$$\begin{aligned} \varepsilon_i &= S_{ij}^{E}\sigma_j + d_{mi}E_m \\ D_m &= d_{mi}\sigma_i + \xi_{ik}^{\sigma}E_k \end{aligned} \tag{1.5}$$

or they can be re-written as:

$$\begin{aligned} \varepsilon_i &= S_{ij}^{D}\sigma_j + g_{mi}D_m \\ E_i &= g_{mi}\sigma_i + \beta_{ik}^{\sigma}D_k \end{aligned} \tag{1.6}$$

where the indexes i, j = 1, 2, . . . ,6 and m, k = 1, 2, 3 refer to different directions within the material coordinates system, as shown in Figure 1.10. The superscripts D, E, and σ represent respectively the electric displacements, the electric fields and the stresses.

- ε is the strain vector (without unities)
- σ is the stress vector (N/m^2)
- ξ is the permitivity (F/m)
- d is the matrix of the piezoelectric strain coefficients (m/V or pC/N)
- S is the matrix of the compliance coefficients (m^2/N)

- E is the vector of the applied electric field (V/m)
- D is the vector of the electric displacement (C/m^2)
- g is the matrix of the piezoelectric constants (m^2/C)

Several common piezoelectric materials are lead-based ceramics ($Pb(ZrTi)O_3$ (PZT), $PbTiO_3$ (PTO)), single crystals (Quartz, $LiTaO_3$, $LiNbO_3$, PZN-PT) and polymers (PVDF and its copolymers).

1.2 Multiferroic materials and magnetoelectric effect

As introduced at the beginning of this manuscript, multiferroic materials are special materials, in which at least two ferroic orders such as magnetic, electric, or elastic phases coexist. These materials are very attractive for technological applications since the coupling between the ferroic-phases facilitates a direct control between them. Indeed, in multiferroics possessing ferromagnetic and ferroelectric orders, the coupling between these two phases (so called magnetoelectric (ME) coupling) give an ability to control the electric polarization, P, by a magnetic field (direct ME effect) and the magnetization, M, by an electric field (converse ME effect).

The ME effect is described through the expansion of the free energy of the ME material [47]:

$$\begin{aligned} F(E,H) =& F_0 - P_i^S E_i - M_i^S H_i - \frac{1}{2}\varepsilon_0\varepsilon_{ij}E_iE_j - \frac{1}{2}\mu_0\mu_{ij}H_iH_j \\ & - \alpha_{ij}E_iH_j + \frac{\beta_{ijk}}{2}E_iH_jH_k + \frac{\gamma_{ijk}}{2}H_iE_jE_k + ... \end{aligned} \tag{1.7}$$

where E and H are the external electric and magnetic field respectively. ε and μ are the dielectric permittivity and magnetic permeability respectively. The second and the third term are the temperature dependence of the electrical polarization, P_i^S, and the magnetization, M_i^S. Fourth and fifth terms describe the effect of the electric and magnetic field on the electric and magnetic behavior respectively, while the sixth term consist of α_{ij} coefficient describing the linear magnetoelectric coupling (or crossing terms). The next two terms consisting of β_{ijk} and γ_{ijk} are third rank tensors and represent higher order of the coupling coefficients. In the purpose of our work, we will neglect these latters.

Minimizing the Equation 1.7 with respect to the electric and the magnetic fields leads to the calculation of the polarization and the magnetization as follows:

$$\begin{aligned} P_i &= -\frac{\partial F(E,H)}{E_i} = P_i^S + \varepsilon_0\varepsilon_{ij}E_j + \alpha_{ij}H_j + \frac{\beta_{ijk}}{2}H_jH_k + ... \\ M_i &= -\frac{\partial F(E,H)}{H_i} = M_i^S + \mu_0\mu_{ij}H_j + \alpha_{ij}E_i + \beta_{ijk}E_iH_j + ... \end{aligned} \tag{1.8}$$

The linear ME effect is presented by the linear ME coefficient, α_{ij}. This coefficient basically quantifies the dependence of the polarization upon the magnetic field or the magnetization upon the electric field. The Equation 1.8 allows calculating the variation of the polarization (or magnetization) over the changing of the magnetic field (or electric field):

$$\begin{aligned} \Delta\mathbf{P} &= \alpha_E \Delta\mathbf{H} \\ \Delta\mathbf{M} &= \alpha_H \Delta\mathbf{E} \end{aligned} \tag{1.9}$$

Where α_E and α_H are respectively the direct ME coefficient and converse ones.

ME multiferroics compounds include single-phase and artificial composites materials that we will discuss into details in the following sections. Briefly, single-phase of intrinsic multiferroics are materials in which the magnetic and electric orders coexist in the same chemical compound while artificial ME present these two ferroic states by two chemical compounds artificially combined together. In general, single-phase ME multiferroic materials exhibit a weak coupling at low temperature and thus they are not suitable for applications. Artificial (or extrinsic) ME multiferroic composites can overcome this problem.

In artificial ME multiferroic composites, the ME coefficients can derives from three different mechanism: exchange coupling, charge carrier effect and the strain mediated one [147], [205] . The most efficient and studied effect is the one deriving directly from the elastic interaction between the magnetic and ferroelectric/piezoelectric phase (i.e. strain mediated ME coupling). Indeed, for the direct ME coefficient, the magnetic phase goes under a mechanical deformation due to the application of a magnetic field thanks to the magnetostrictive effect. If the deformation is efficiently transmitted to the ferroelectric/piezoelectric phase, this can be conversed into the appearance of an electric polarization in the ferroelectric/piezoelectric phase due to the piezoelectric effect. In the same way, applying an electric field to the ferroelectric/piezoelectric phase can give rise to a transmission of the deformation to the magnetostrictive phase and lead to the change of the magnetic moment. These couplings are called strain-mediated ME couplings are described by the following Equation 1.10:

$$\begin{aligned} \text{Direct ME effect :} & \frac{magnetic}{mechanical} \times \frac{mechanical}{electric} \\ \text{Converse ME effect :} & \frac{electric}{mechanical} \times \frac{mechanical}{magnetic} \end{aligned} \tag{1.10}$$

These equations show the tensor nature of the strain-mediated ME effect linked to the mechanical tensor. Since in this case the ME effect is an extrinsic effect, the ME coefficient may depend on many factors like: the interface interaction between the two coupled phases, the microstructure of the material and the intrinsic properties of each phase. Thus the goal of the researches on these kind of artificial multiferroics is optimizing the material structures, their interfaces and their single phase properties in order to reach the highest ME coefficient at room temperature. We will discuss in the following section the state of the art of the optimization of the magnetoelectric coefficient in these multiferroic composite systems.

1.3 A short review on multiferroic materials

1.3.1 Intrinsic ME materials

Single-phase (or intrinsic) multiferroic materials exhibit both magnetization and electric polarization in a single phase compound, as stated in previous paragraph. The number of single-phase multiferroics in nature as well as the one synthesized in the laboratory is very small. The first discovered single-phase multiferroic is the nickel iodine boracite ($N_3B_2O_{13}I$) [10], followed by several synthesized multiferroic boracite compounds. However, these materials present the problem of a low Curie and a low Neel temperatures excluding a ME coupling at room temperature.

The single-phase multiferroics studied have then focused on the perovskites oxides compounds such as rare earth manganates $TbMn_2O_5$, $YMnO_3$ and $BiMnO_3$, as they present higher critical temperatures (the perovskite crystal structure is presented in Figure 1.9, section 1.1.5). For example, $BiMnO_3$ displays a ferromagnetic transition (T_C) around 105 K and a ferroelectric transition at 750 K [38]. This allows the coexistence of the two ferroic states for $T < T_C$. Besides, Lorentz *et al.* [96] reported a magnetoelectric coupling in $HoMnO_3$ compound which shows a decrease of 8 % of the dielectric constant (ϵ) by the application of an external magnetic field (7 T). In addition, an impressive switching of the electric polarization induced by the application of a magnetic fields (see Figure 1.11) was reported by Kimura *et al.* [75] in $TbMnO_3$ bulk compound. All these behaviors are presented in Figure 1.11.

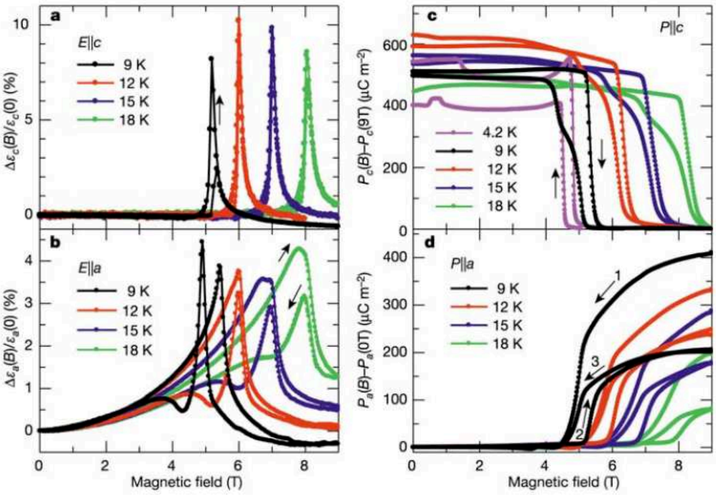

Figure 1.11: Magnetocapacitance and magnetoelectric effects in $TbMnO_3$ [75].

Beside the bulk structures, several single-phase multiferroic nanostructures have been studied. For instance, $BiMnO_3$ thin films grown on (100) Si substrates with film thickness of 400 nm, shows a ferromagnetic transition at 105 K and a ferroelectric one around 450K [38]. By using the pulsed laser depositions technique, $BiFeO_3$ thin films were also elaborated and presented a better spontaneous polarization compare to their bulk relative structure [85] [146], [210].

All these examples (and more) brought the scientific community working on these single-phase multiferroic materials, to understand that although these intrinsic multiferroics are of great interest from a fundamental point of view, their critical temperatures always exhibited below the room temperature, exclude them for applications. Therefore, artificial multiferroic compounds attracted the scientific community due to the possibility of observing a ME coupling at room temperature opening a novel way for multifunctional devices such as sensors, magnetic-electric transducers, actuators [99] [131] [162].

1.3.2 Extrinsic ME multiferroic composites

Artificial (or extrinsic) ME multiferroic compound are obtained by artificially combining ferroelectric/piezoelectric materials with magnetic ones. These bi-phased systems can present several different connectivities between the two phases. The variety of the phase connectivities was introduced by Newham *et al.* [135]. The artificial bi-phased structure can be described using the connectivity notations like: 0-3, 2-2, 1-3, *etc.*, where each number denotes the self-connected dimension of each phase (Figure 1.12), see section 1.5.1 for more detail. Indeed, in particulate composites (0-3), the ferroelectric or magnetic oxide particles are included respectively in a magnetic/ferroelectric phase matrix. Whereas, the laminate composites (2-2) consist of a combination of ferroelectric and magnetic layers, also fiber/rod composites (1-3) include ferroelectric/magnetic fibers or rods embedded respectively in a magnetic/ferroelectric phase matrix. When one of the two phases is nanometric in size, we use the nanocomposite definition.

Various multiferroic nanocomposites (also called in this manuscript as bi-phased materials) from bulk to thin film nanostructures have been investigated, such as ceramic based composites, magnetic alloy based ones and polymer-based nanocomposites.

The bulk multiferroic ceramic composites were first made via co-sintering ferroelectric oxides and ferrites [18] [59] [95] [98], which created interfacial inter-diffusion and reaction problems, that deteriorated the magnetoelectric response. To reduce these problems, chemical solution processing and spark plasma sintering (SPS) [67] techniques have been used. In such composite structures, when an electric field (E-field) is applied to the ferroelectric/piezoelectric matrix, a deformation of the ferroelectric/piezoelectric phase is observed due to the piezoelectric effect. If the elastic coupling between the two phases is efficient, a strain is exerted to the ferromagnetic phase included into the matrix, which alters the magnetic anisotropy or domain structure of the ferromagnetic phase due to the converse magnetostrictive effect. This ME effect produces a large ME coupling in ceramic composites. For example, in $BaTiO_3$ (BTO) - $CoFe_2O_4$ (CFO) ceramic systems [200], [201], [202], a large ME coefficients of 0.13 $Vcm^{-1}Oe^{-1}$ is obtained at room temperature which is hundred times higher than the one observed in single-phase systems. An other

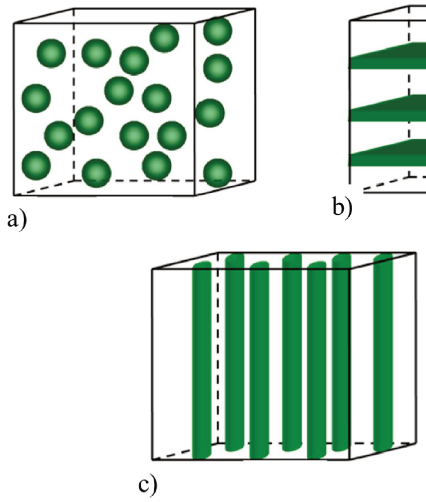

Figure 1.12: Schematic illustration of three bulk artificial structures showing three common connectivity schemes: (a) 0–3 type (particulate composite), (b) 2–2 type (laminate composite), and (c) 1–3 type (fiber/rod composite) [131].

example is the $NiFe_2O_4$ (NFO)/ $Pb(Zr_xTi_{1-x})O_3$ (PZT) ceramic [184] [185] [186] [187], in which a high ME coefficients up to 0.4 $Vcm^{-1}Oe^{-1}$ has been observed. More work on ceramic composites still remain to be done in order to overcome the chemical problems linked to the need of high temperature for the sintering process of these materials that can bring to chemical reactions between the two phases and thermal expansion mismatch between them. Also the brittle character of most of these ceramics compounds is still an ongoing issue.

Compared to the ceramic composites discussed above, magnetic alloy-based composites consisting of a magnetostrictive alloy as $SmFe_2$, $TbFe_2$, Terfenol-D or Metglas and piezoelectric layer as PMN-PT or PZT, exhibited higher ME response. For instance, a giant magnetoelectric (GME) effect is reported in Terfenol-D/PZT laminates by Ryu *et al.* [166]. Also a large ME coefficients $\alpha_E = 4.8$ $Vcm^{-1}Oe^{-1}$ is reported in disk-shape structures of these laminates (i.e. 2-2 composite). In general, these laminate composites are fabricated by bonding magnetostrictive and piezoelectric layers using an epoxy resin, annealed afterwards at 80-100°C. However, the fragility of the interfacial binders can significantly affect the magnetoelectric effect of the composites as already stressed [130]. Therefore, sputtering [172] [189] and electro-deposition [148] have been used to deposite magnetic alloy layer directly on the ferroelectric layer. Much larger magnetoelectric coupling value of 33 $Vcm^{-1}Oe^{-1}$ was demonstrated in 0.4 mm Ni/0.25 mm PZT/0.4 mm Ni heterostructure obtained by the electrodeposition method.

It is important to underline that, in comparison to bulk multiferroic ME composites, the nanostructured ME one offers a way to investigate the physical mechanism of the ME effect at a nanoscale level. For instance, a good ME coupling have been reported in a 1-3 type columnar nanostructures consisting of a magnetic spinel phase (CFO) epitaxially embedded into the ferroelectric matrix (BTO, $BiFeO_3$ (BFO) and $PbTiO_3$) (see Figure

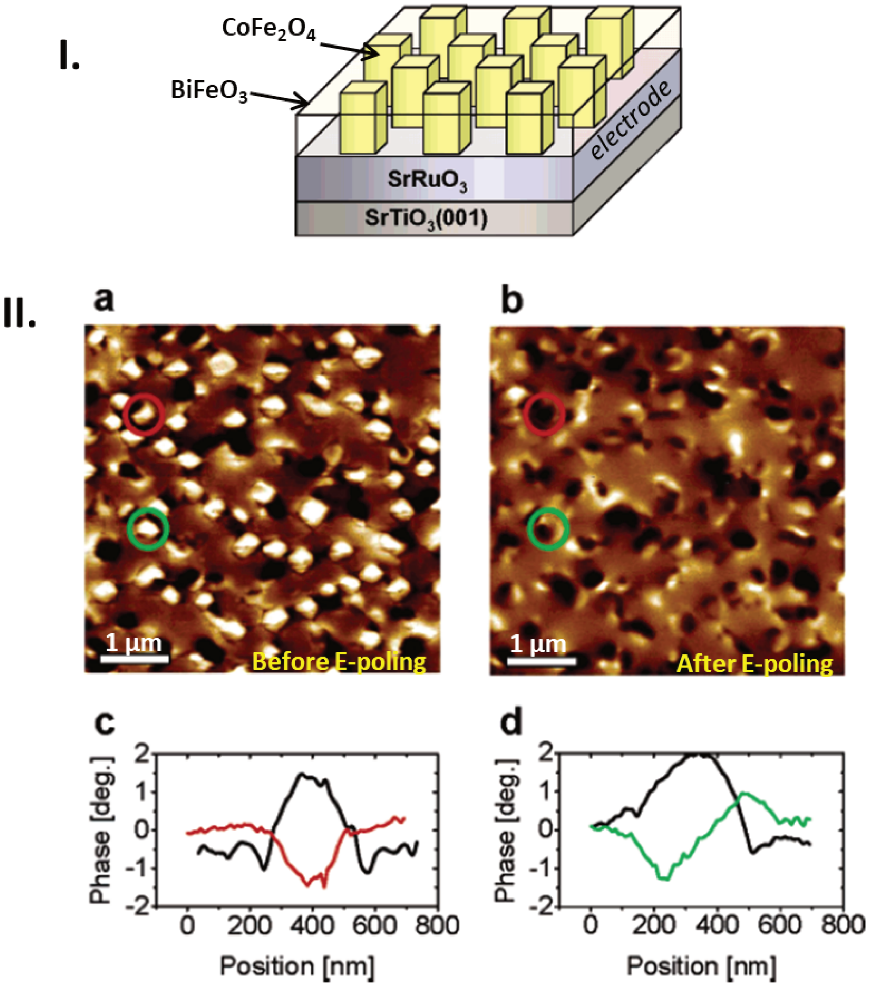

Figure 1.13: (I) - Sketch of the $CoFe_2O_4$ - $BiFeO_3$ 1-3 structure; (II) - Changes in the magnetic configuration of $CoFe_2O_4$ - $BiFeO_3$ observed by magnetic force microscopy (MFM). (a) Before electrical poling and after magnetization in an upward oriented 20 kOe perpendicular field; (b) After electrical poling at +12 V; (c and d) Line profiles measured over two $CoFe_2O_4$ pillars emphasized in the MFM images with red and green, respectively. The black curves stand for the MFM signal before electrical poling [220].

1.13) [86] [220] [222] [228] [229] [230] . The ME coupling in these cases are emphasized by the peculiar design of the columnar structure which reduces the clamping effect coming from the substrate. Thanks to the vertical architecture an efficient strain-mediated coupling is promoted at the interfacial surface area. However, the design and control of these kind of structures still remain a technical challenge for elaborators [203]. As 2-2 type of ME nanostructures are easier to fabricate, various of them have been reported like PZT/CFO ($\alpha_E = 15\ mVcm^{-1}Oe^{-1}$) [60] [176], BTO/NFO ($\alpha_E \approx 32\ mVcm^{-1}Oe^{-1}$) [89], PZT/$Ni_{0.8}Zn_{0.2}Fe_2O_4$ (α_E = 15 - 30 $mVcm^{-1}Oe^{-1}$) [167].

In all bulk and nanostructured composites discussed above, ceramic-based magnetoelectric and magnetic alloy-based composites exhibit a better ME cross coupling compared

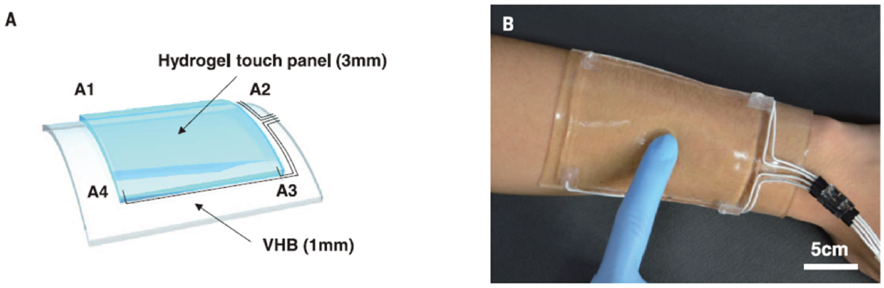

Figure 1.14: A flexible technology in biology applications [71].

to all the others ME composites. However, they still present some disadvantages. In fact as already stated, they are often brittle, costly and frequently present high leakage current density due to the grain structure. Thus good candidates to overcome these problems may be the polymer-based composites which are easy to process and less expensive elaboration costs, good mechanical properties [103] [155] [160]. These polymer-based composites opens the way to potential applications in flexible multifunctional devices which can be very interesting for a new technology covering non-flat surfaces (see Figure 1.14).

Polymer-based ME composite film:

The research on polymer-based composite focuses, up to now, mainly on particulate nanocomposites. They are made by a polymer piezoelectric matrix obtained by various methods which are low cost and very easy to process (the solution casting, sol-gel spin-coating methods). These artificial composites are based on the most common organic piezoelectric materials which is the polyvinylidene fluoride (PVDF) and also on its copolymers. The magnetic nanofillers used to elaborate these composites are selected on the base of their large magnetostrictive coefficient (λ) and high magnetic order at room temperature. Thus, the most common nanoparticles used as nanofillers are iron-based oxides such as: CFO, NFO, Fe_3O_4, $Ni_{0.5}Zn_{0.5}Fe_2O_4$, Fe_2O_4 and $Zn_{0.2}Mn_{0.8}Fe_2O_4$ [54] [102] [105] [108] [155] [156] [157] [158] [159].

In the particulate nanocomposite type structure, the main research issue is to optimize the nanofillers content as it can affect the electric polarization (or electro-active phase) of PVDF and thus the magnetoelectric response of the composites. Indeed, it has been observed that the polarization of PVDF increases by adding a critical concentration [1] of nanofillers such as 5%wt for PVDF/CFO, 10%wt for PVDF/NFO and 15%wt for PVDF/ZFO [157], [159]. This behavior can be explained by the increasing of free charges in the composites when nanofillers are added. These free charges need to compensate and stabilize the polarization domain. The nanofillers act as heterogeneous nucleation centers for ferroelectric domains during the polarization (see Figure 1.15) [79], [109] [110]. Moreover, large interfacial areas in the composites including nanofillers promote the exchange coupling effect through a dipolar interface layer and results in higher polarization [107], [155]. The ME coupling in such PVDF particulate nanocomposite is discussed into literature by studying the P_{max} behavior as function of the external magnetic field for example

---

[1] the concentration is the percentage of nanofiller's weight to the weight of polymer

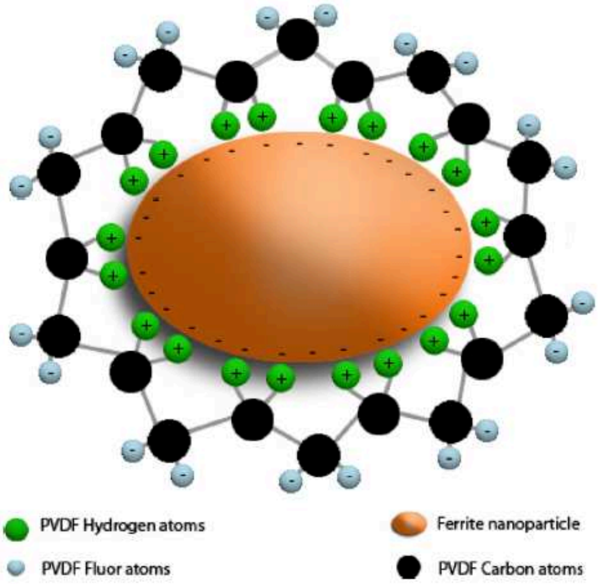

Figure 1.15: Schematic representation of the proposed mechanism of the polarization formation in PVDF-nanofillers composites [110].

in PVDF/NFO system, (see Figure 1.16) [156].

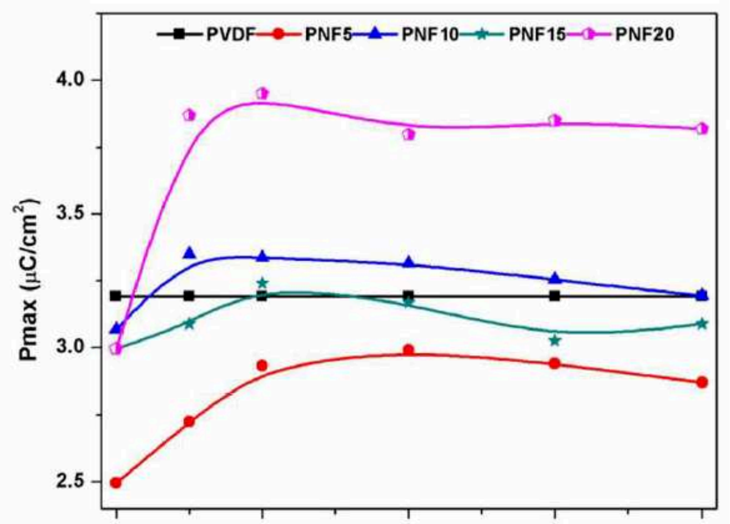

Figure 1.16: ME response in PVDF/NFO composite [156] with different concentration of nanofillers. Symbols including: pure PVDF, PNF5 (PVDF/NFO (5% wt)), PNF10 (PVDF/NFO (10% wt)), PNF15 (PVDF/NFO (15% wt)), PNF20 (PVDF/NFO (20% wt)).

Note that in all the above results the films have been poled before the measurements. These results let to conclude that the ME coupling in polymer-based composite depends strongly on the magnetostriction coefficient of the magnetic fillers as well as of the fillers concentration. In fact, the P_{max} of the composite is strictly depended from the magnetic field applied (see Figure 1.16).

In addition to particulate nanocomposites, laminate type ME polymer-based ones have also been studied. In this case, the magnetic and the polymer phase are stacked layer-by-layer. Several laminate type polymer-based composites have been already reported, i.e. Metglas/P(VDF-TrFE) [68] and Metglas/PVDF [103], [221]. These laminate composites have shown a good direct ME coefficient at the piezoelectric resonance frequency by applying a small external magnetic field. Indeed, on Metglas/PVDF composites, the ME coefficient, α_{31}, has been found to be 238 Vcm^{-1} Oe^{-1} at the resonance frequency (50 kHz) and 7.2 Vcm^{-1} Oe^{-1} at lower frequencies [221]. On Metglas/P(VDF-TrFE) composites, a α_{31} = 383 Vcm^{-1} Oe^{-1} have been reported at resonance frequency (65 kHz) and 17.7 Vcm^{-1} Oe^{-1} at low one (20 Hz) [68].

1.4 Electric control of magnetic behaviors in ME multiferroic composites through strain-mediated effect

As discussed in section 1.2, the strain-mediated ME coupling is an effective and interesting route to control the magnetic behavior by applying an electric field. Many experiments on strain-mediated ME coupling have been reported in different types of composite structures. The most studied one is the 2-2 laminate type as it shows the highest efficiency in the magneto-elasto-electric coupling. This is probably linked to the fact that the 2-2 structure offers a better control of the surface connectivity quality between the two phases compared to the 0-3 particulate and the 1-3 fiber/rod type structures. In the following paragraphs we will present and discuss a variety of magnetic properties control in these systems.

1.4.1 2-2 laminate structures

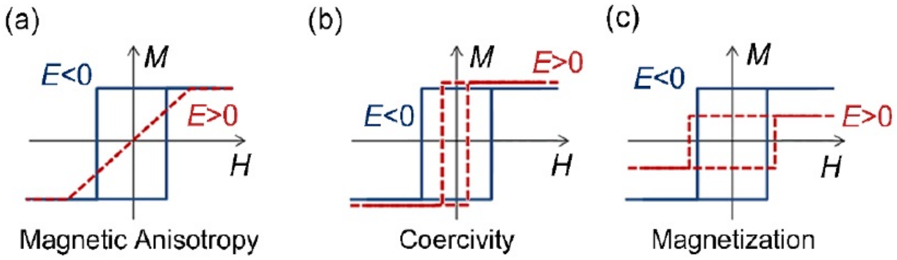

Figure 1.17: Sketches of several different magnetic performances expected under the application of an electric field [179].

As explained earlier, the 2-2 laminate nanostructure is constituted by a magnetic thin films grown on a ferroelectric substrate/layer. The magnetic thin films can be either based on transition metal (e.g., Fe, Ni and Ni-Fe alloy) or on oxide-based compounds (e.g.,Fe_3O_4, CFO, NFO and $La_{1-x}Sr_xMnO_3$ (LSMO)). The most reported ferroelectric substrates are BTO, PZT, PMN-PT or PZN-PT materials. The strain-induced effect in this composite opens the possibility of controlling the static magnetization, the coercive field as well as the magnetic anisotropy and (depending on the composition) the magnetic domain local configuration (see Figure 1.17). All these possibilities are discussed below.

Controlling the magnetization and the coercive field values

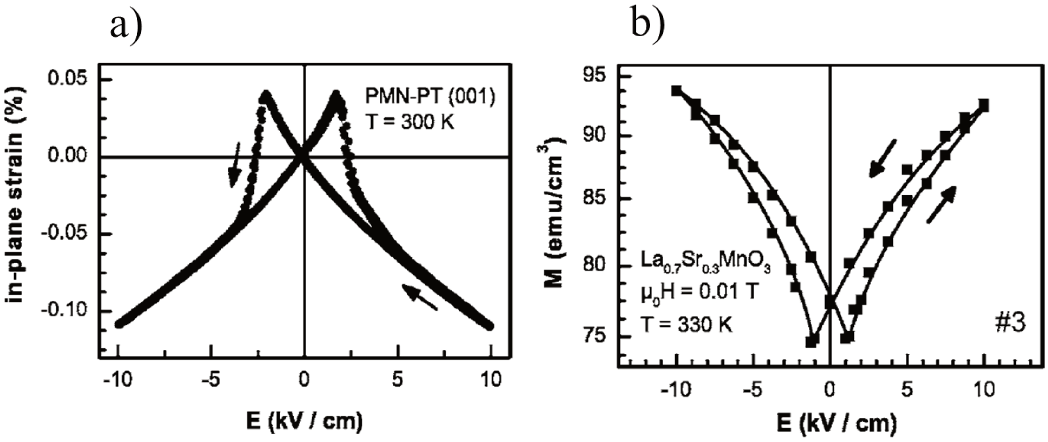

Figure 1.18: a) In-plane piezoelectric strain versus applied electric field of a $Pb(Mg_{1/3}Nb_{2/3})_{0.72}\ Ti_{0.28}O_3$ (PMN-PT); b) In-plane magnetization of LSMO film grown on single PMN-PT (001) substrate vs. an applied electric field on the substrate. The arrows show the direction of the electric field sequence [194].

The strain-mediated control of the static magnetization was first observed in ferromagnetic perovskite manganite thin films ($La_{0.67}Sr_{0.33}MnO_3$) grown on ferroelectric single crystal substrate of BTO [40] and PMN-PT [194]. In LSMO/PMN-PT heterostructure, Thiele *et al.* [194] reported the in-plane magnetization of LSMO (001) film changing as function of the applied electric field in [001] direction of the substrate (see Figure 1.18). In fact, the piezoelectric PMN-PT substrate show a reversible compression of the isotropic in-plane lattice parameter under the application of an electric field (see Figure 1.18(a)). The in-plane strain-induced on the substrate alters the magnetization of the LSMO thin film thanks to an effective elastic coupling at the film-substrate interface. The M-E loop is presented as a butterfly-shaped curve corresponding to the butterfly-shaped piezo-strain one (Figure 1.18). This clearly demonstrates the direct connection between these two ferroic properties allowed by the elastic strain. In LSMO/BTO heterostructure, the switching of ferroeletric domain in the BTO substrate by the application of an external electric field alters the local strain in the LSMO film plane and thus lead to modify the LSMO macroscopic magnetization [40] due to the magnetostrictive effect.

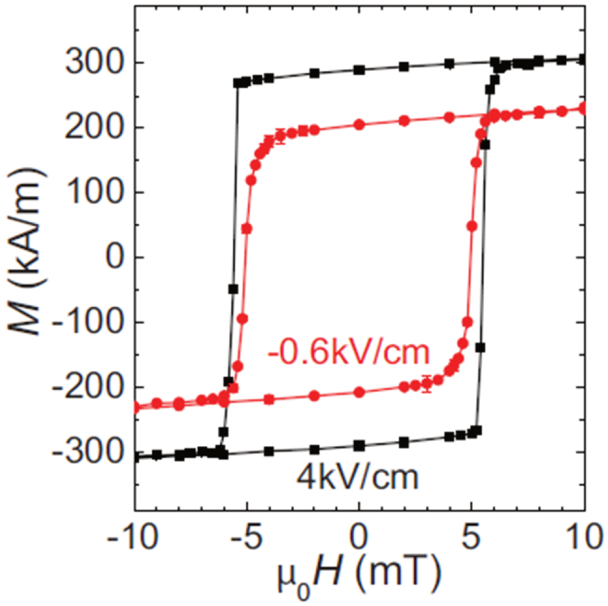

Figure 1.19: In-plane magnetic hysteresis loops M(H) of Ni/BTO heterostructure for two different electric fields applied across the BTO substrate [52].

Geprägs *et al.*[52] have presented the manipulation of the ferromagnetic magnetization via electric fields in Ni/BTO structures (see Figure 1.19). The rectangular shape of the hysteresis loops observed at E = +4 kV/cm indicates that **H** is aligned in the plane of the film along the easy magnetic direction of the Ni (see section 1.1.3). The magnetization **M** is reduced of 20 % from its saturation value when electric field of -0.6kV/cm is applied in the BTO substrate. This process is reversible and driven, as in the previous heterostructure by the mechanical strain transferred from the BTO substrate into the Ni thin film. Similarly, the electric-induced modification of magnetization has been observed also in many others heterostructures like Fe/BTO [168], $Fe_{0.5}Rh_{0.5}$/BTO [26], CoPd/PZT [74] [82], FeCo and CoFeB/PZT [23], Fe_3O_4/PMN-PT [91], $Zn_{0.1}Fe_{2.9}O_4$/ PMN-PT [92], Co-Fe-B/ PMN-PT [83] [224]. All these examples are based on the same mechanism previously explained and they show how universal and efficient can be this strain-mediated magnetization control at room temperature.

Similarly to the electric control of magnetization, the coercive field, H_C, of the magnetic/ferroelectric 2-2 heterostructures can also be controlled. The $H_C - E$ butterfly-shaped curve has been reported in $Co_{50}Fe_{50}$ thin films deposited on PZT substrate [126] (see Figure 1.20a). The changing of H_C has been also observed in Fe/BiScO$_3$-PbTiO$_3$ heterostructures. This $H_C - E$ curve shows an hysteresis loop similar to a ferroelectric P-E one (see Figure 1.20b). As can be seen in Figure 1.20(b), during the first positive bias application (denoted by arrow 1), once the positive electric field is switched off, the magnetic hysteresis loop immediately returns to its original state at $E = 0$. In contrast, when the negative electric field is applied, the change cannot be completely recovered after the negative electric field is switched off. In particular, after the negative electric field reaches the

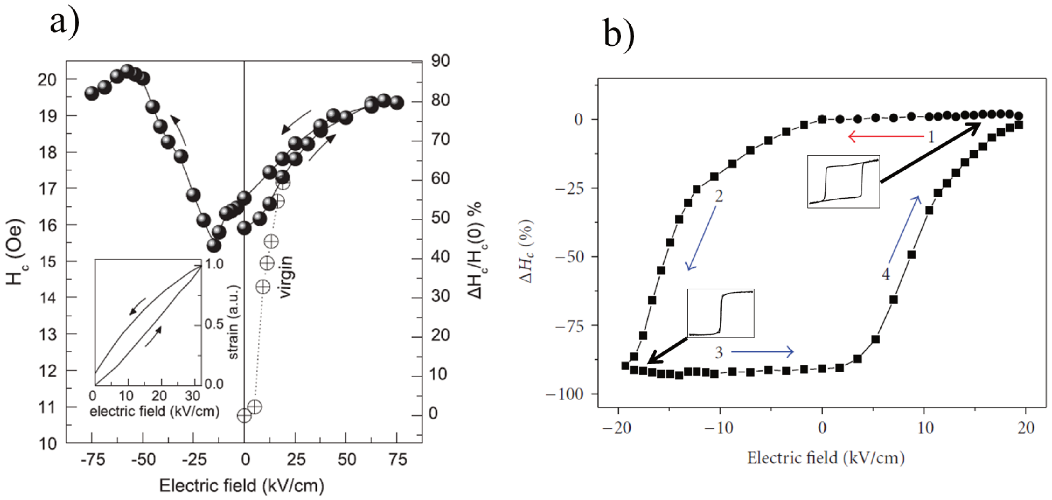

Figure 1.20: (a) The variation of the magnetic coercivity fields of the $Co_{50}Fe_{50}$ hybrid 2-2 structure as a function of an external electric field applied to the PZT. Inset of (a): Strain versus electric field curve for the commercial PZT piezoelectric ceramic [126]; (b) The change in the magnetic coercivity field (ΔH_C) Fe/$BiScO_3$-$PbTiO_3$ composite vs. the applied electric field. The ΔH_C is measured after the switch-off of each bias voltage [211].

minimum value (i.e., $-19kV/cm$), ΔH_C measured remains constant (see arrow 3). The change in the H_C recover when a positive field of about $+16kV/cm$ is applied (see arrow 4). Such switching "on" and "off" of the magnetic-coercive-field variation, is achieved by the application of a small electric fields, offering a clear potential way to new magnetic memories.

Controlling the magnetic anisotropy value

Not only magnetization and coercive field but also the magnetic anisotropy constant can be well controlled via the strain by using an electric field as it is shown in Figure 1.21. The electric field induced change in the magnetic anisotropy has been reported in CFO thin film deposited on PMN-PT substrate [218] (Figure 1.21). When an electric field is applied, the in-plane magnetization of the heterostructures increases and the out-of-plane magnetization decreases. The relative change in the magnetization ΔM/M(0) - E hysteresis loops are reported in Figure 1.21, where Δ M = M(E) - M(0) and M(E) is the magnetization under an electric field E, and M(0) is the magnetization under zero electric field. It can be seen that the loop has again a butterfly shape both for the in-plane and the out-of-plane magnetization, which again agrees with the strain-electric field loop of the PMN-PT [43]. This observation confirms the role of the strain induced mechanism in the piezoelectric substrate by E-field application and its connection with the observed variation of the magnetic anisotropy. Similar observations are reported in CFO/BTO [28], Ni/PZT [21], Fe_3O_4/BTO [190] [196] [203], Ni/Kapton/actuator [237].

The E-control of the magnetic anisotropy via this strain-mediated effect, has potential

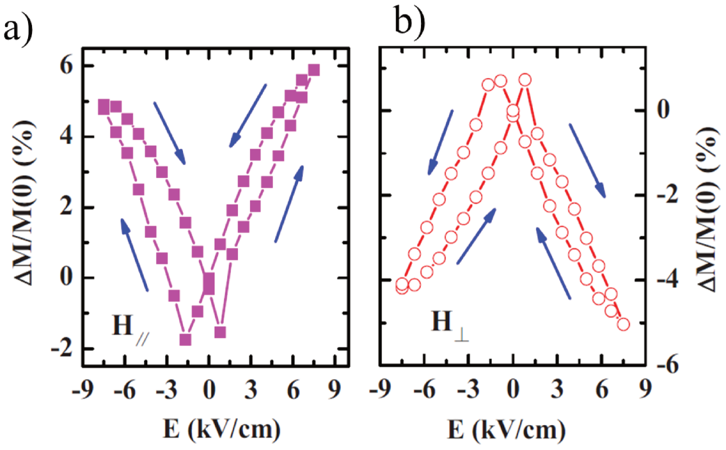

Figure 1.21: Electric field induced change in magnetic anisotropy via the strain on CFO/PMN-PT heterostructure. (a) In-plane Δ M /M (0) - E loop, the magnetic field is 0.05 T; (b) Out-of-plane Δ M /M (0) - E loop, the magnetic field is 0.2 T [218].

applications in magnetic sensors and spintronic devices [207].

Controlling magnetic domain configuration

The strain-mediated control of the magnetic domain configuration have been measured by using local microscopy techniques. Chung *et al.* [30] observed a reversible magnetic domain-wall motion in (100 nm) Ni/ (1.28) μm PZT bilayer thin films by using a standard Magnetic Force Microscopy (MFM). In fact, some ferromagnetic thin films present an out-of-plane magnetization alignment which gives rise to a maze/stripe domain pattern (see Figure 1.22). The dependence of the domain stripes upon the thickness of the Ni thin film is well understood [57]. In this heterostructure of Ni/PZT, the PZT layer is polarized out-of-plane so that the electric field induces an in-plane strains and subsequently changes the magnetic stripe-domain pattern of the Ni layer (see Figure 1.22(a) for a schematic view of the configuration; here the substrate is PZT and not PMN-PT like in the figure). The magnetic domain patterns is controlled reversible. In fact it is possible to return it to its initial configuration after removing the electric field [30].

Similar observations are reported in (60 nm) Ni thin film grown on (001) PMN-PT substrate [63] (see Figure 1.22). The external electric field was applied to the PMN-PT substrate through the Pt electrode deposited on both sides of the PMN-PT. The in-plane strain-induced in PMN-PT layer as function of applied electric field is shown in Figure 1.22 (a)). As a result, the strain-induced of the PMN-PT substrate altered the domain-patterns configuration of the Ni thin film. The stripe domain-patterns are pretty much destroyed by the electric field induced compression strain at 0.8 MV/m (see Figure 1.22(b), picture III). After removing the external electric field, the domain patterns returned to its original configuration (see Figure 1.22(b), picture IV). Some domain walls were pinned due to the surface roughness of the ferroelectric substrate (see the white arrow in picture

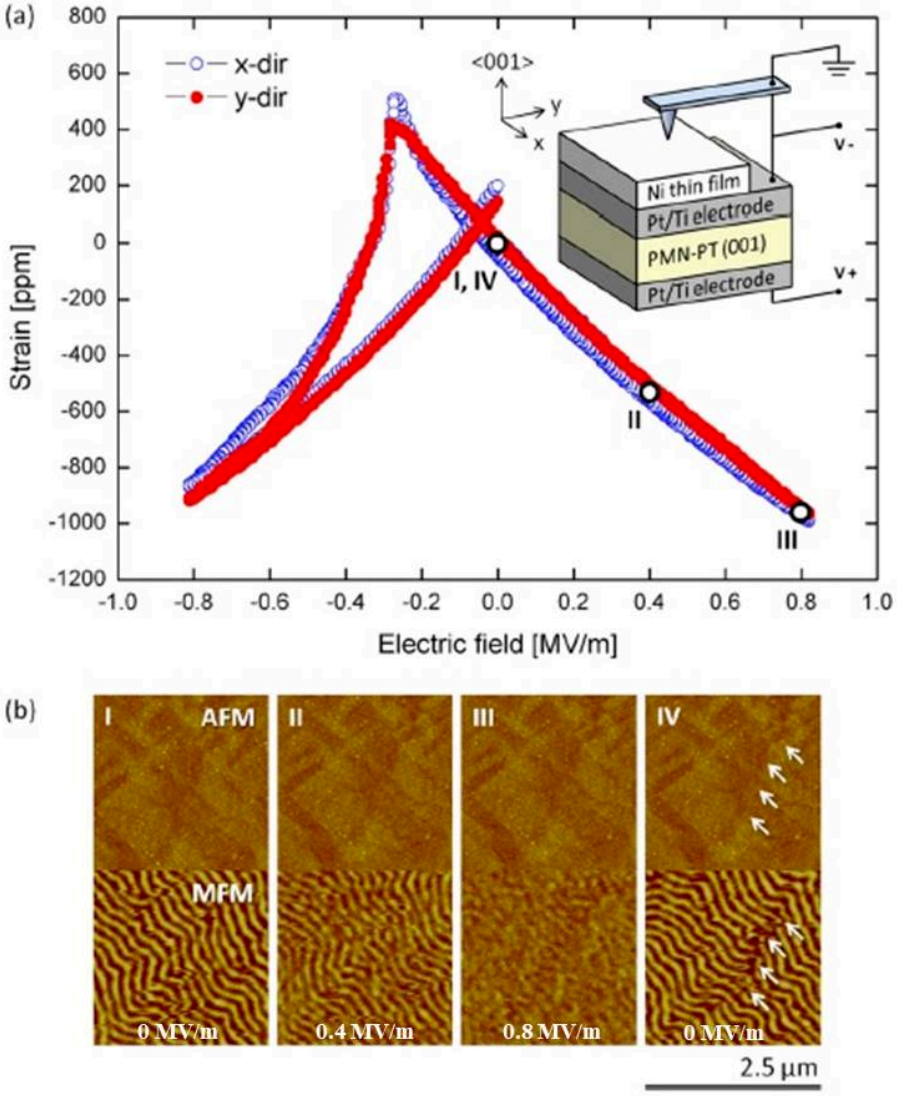

Figure 1.22: (a) In-plane piezoelectric response of PMN-PT (001) sample, (b) AFM and MFM images of 60 nm thick Ni thin film on PMN-PT (001) substrate under different E-Field: 0 MV/m, 0.4 MV/m, 0.8 MV/m, and 0 MV/m [63].

IV).

The electric control of the magnetic domain structure provides a possibility to control the domain walls motion and to turn the magnetic domains from the out-of-plane alignment to an in-plane one at a local level without significantly influencing the macroscopic properties of the material. These results open novel potential applications in the electric writing/magnetic reading for low energy cost.

1.4.2 1-3 fiber/rod and 0-3 particulate type structures

Very few publication can be found in literature concerning the in E-field control of the magnetic properties in 1-3 fiber/rod and 0-3 particulate type nanostructures since these kind of nanostructures exhibit several difficulties. Indeed, the ME coupling depend strongly on the exact composition of the magnetic phase, the crystallite size, and the nano-grain arrangement, giving rise to a large variability of relevant parameters playing a fundamental role on the ME properties of the nanocomposites [120] [151]. Other difficulties relate to the low electrical resistivity of the magnetic component which limit the electric field strength used for poling the materials [185]. Moreover, the presence of voids and spurious phases and defects in the crystalline structure of each phase can reduce the mechanical coupling. In addition, the intrinsic properties of each phases may reduces due to the fabrication process. Thus the magnetization and the electric polarization, the magnetostrictive and the piezoelectric coefficients as well as the magnetic anisotropies and dielectric response of each phase can be affected (i.e. reduced) by the elaboration process [120], [188].

In 1-3 type structure, the electric control of the magnetic properties through the strain-mediated have been reported in BFO/CFO columnar heterostructured film based on ferrimagnetic CFO nanopillars embedded in a BFO matrix. The results show that electric field could change the magnetic configuration of the CFO pillar (see Figure 1.13) [220] [227]. The strength of the ME coupling between the ferroelectric matrix and the ferrimagnetic nanopillars has been estimated to be $\alpha_H = 10^2$ Oe.cm.V^{-1}.

K. Ban et al [13] reported the electric control of the magnetization also in a 0-3 ceramic composite based on an antiferromagnetic $LaMnO_3$ particulate phase embedded in a ferroelectric BTO matrix. This composite has been prepared by conventional sintering process in the range temperature of 1100-1200 °C. A large change in the magnetization of the composite is observed as a function of the applied electric field. The spontaneous magnetization reduces of the 70 % when an electric field of 2.3 kV/mm is applied at room temperature to the ceramic.

Recently, H. Kim et al. demonstrated an electric-field induced change of the magnetic properties in a composite containing a superparamagnetic nickel nanoparticles array on a PMN-PT piezoelectric substrate [72] (see Figure 1.23(A-a)). The strain-induced in PMN-PT substrate as function of the applied electric field is shown in Figure 1.23(A-b). Before poling (Figure 1.23(B-a,b)), a small coercive fields is observed in both x- and y-direction indicating that the sample is magnetically isotropic and dominantly superparamagnetic (i.e., they show near zero net magnetization). After poling, a hard magnetic axis appears parallel to the x-direction with a magnetic anisotropy of 600 Oe. In contrast, a magnetic easy axis is created along the y-direction. This result demonstrates that a net magnetization equivalent to the saturation magnetization of Ni is "turn on" by the application of an electric field in the y-direction. In other words, this system can be switched between a superparamagnetic state and a single-domain ferromagnetic one at room temperature. In addition to the change in magnetic anisotropy, the blocking temperature of the 16 nm Ni nanoparticles is shifted approximately of 40 K after applying the electric field. Such control in a nanoscale magnetic material may provide exciting opportunities to explore

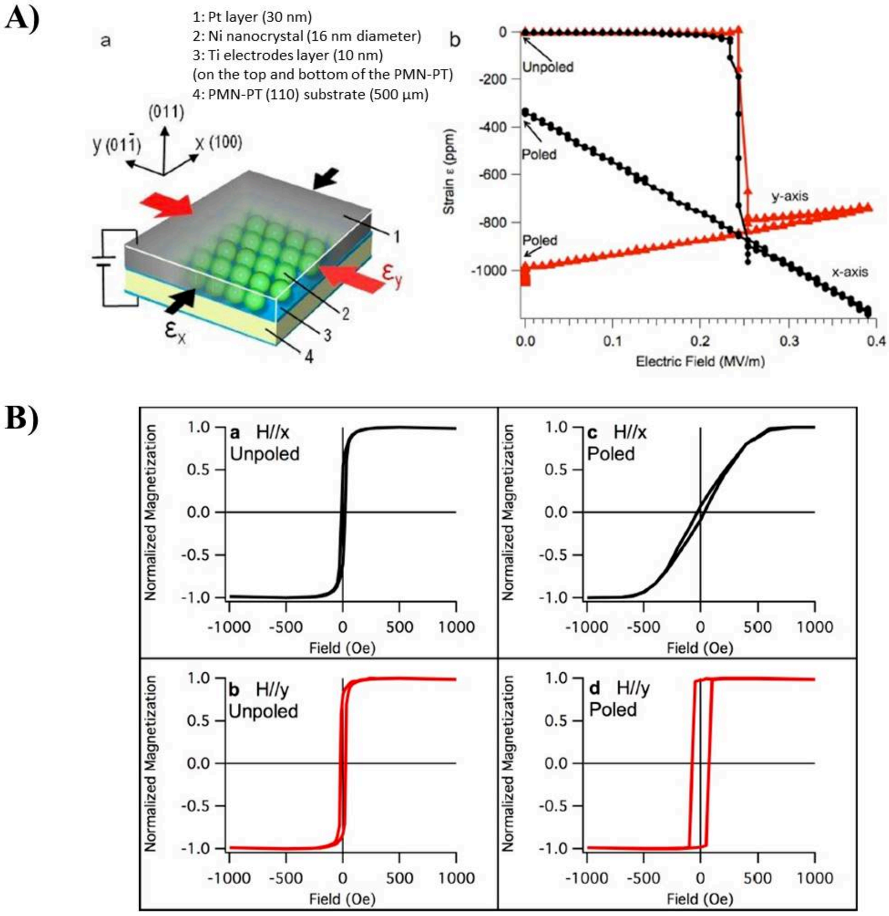

Figure 1.23: (A) - (a) A schematic representation of the full device; (b) The strain induced in PMN-PT via an electric field applied along the (011) direction. Red triangles indicate strain along the y-axis, black circles along the x-axis. (B) - Magnetic hysteresis curves obtained on nickel nanocrystals embedded in Pt thin film on top of (011) PMN-PT at 298 K. (a) and (b) show the data measured with the magnetic field applied parallel to the x- and y-axes, respectively, on the unpoled sample. (c) and (d) show the data measured with the magnetic field applied parallel to the x- and y-axes, respectively, on the poled sample [72].

new types of electromagnetic devices.

1.4.3 Conclusion

The electric control of the magnetic properties on various ME composites through the strain-mediated effect has been discussed in three main type structures, i.e. 2-2, 0-3 and 1-3. Most of the reports presented into literature are in 2-2 type structure and are controlled in both macroscopic magnetic properties (M, H_C, magnetic anisotropy) and local ones at nanoscale level, like in the case of the configuration of the magnetic domain pattern and magnetic domain walls motion. As explained before, the E-control of the static magnetic behaviors in 0-3 and 1-3 type structures still remains an open challenge since they exhibit critical elaboration parameters playing an important role on the ME coefficient value. As these nanocomposite configurations are of great interest in our work, in the following section we will discuss into detail several factor influencing the ME coefficient value in 2-2, 0-3 and 1-3 ME nanostructures.

1.5 Factors affecting the ME coupling in multiferroic composites

1.5.1 Connectivity and interface bonding

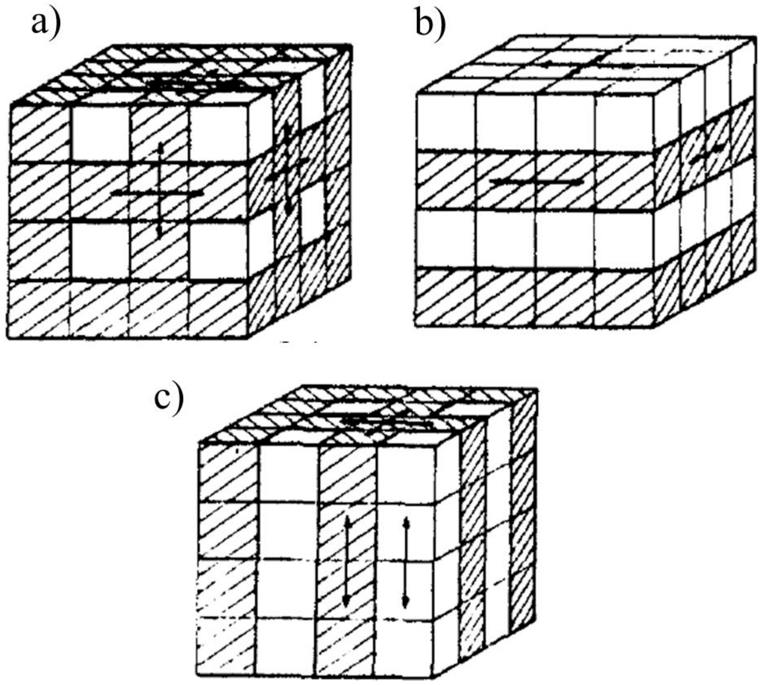

Figure 1.24: Connectivity sketches in the bi-phased composites described by Newham et al. [135]: (a) 0-3 type, (b) 2-2 type and (c) 1-3 type. White cubes represent one ferroic phase and filled pattern the other one.

The phase connectivity and interface bonding of the ME composite materials have an important role on the elastic coupling between the ferroic phases and their ME response. A good mechanical bonding at the interface between phases provides an efficient strain transferring and improves the ME response. As mentioned in section 1.3.2, the most common multiferroic composites have been designed and fabricated in three connectivities: 0-3, 2-2 and 1-3 (see Figure 1.24). The number ”0”, ”1”, ”2”, ”3” denotes the self-connected dimension of the phases. For instance, in the 0-3 type connectivity, magnetic particles are fully dispersed and embedded in a piezoelectric matrix. Thus, the number "0" denotes the zero-dimension of the connectivity between the magnetic particles (the nanoparticles are not connected between them, see white cube in Figure 1.24). The number "3" denotes the self-connection of the piezoelectric phase along the three-directions in the space (see arrows in the filled pattern in Figure 1.24). Similarly, in 2-2 type structure, the magnetic and piezoelectric phases are macroscopically assembly in a multilayer structure. The number "2" is in this case the dimension of both the self-connection for both the ferromagnetic and the ferroelectric layers. The 1-3 type structures are obtained by embedded magnetic fibers/rods/wires in the piezoelectric matrix. In this case, the fibers are connected along 1-direction (see arrow in Figure 1.24(c)) as well as the piezoelectric matrix. In all type of structures mentioned above, the 2-2 laminate structure currently displays the larger ME response compare to the 0-3 and 1-3 structures as already discussed in section 1.3.2 and 1.4. This results can be explained by their larger magnetic anisotropy compare to the 0-3 and the 1-3 nanostructures. Moreover, the 2-2 laminate composites preserve the physical properties of the individual phases while this can be easily modified during the fabrication process in the case of the 0-3 and 1-3 nanostructures. It is also important to note that the interface interactions between magnetic and piezoelectric phases are very sensitive to the quality of the interface that may induce a magnetic pinning. Thus, the interface roughness is also important and should be taken into account.

1.5.2 Materials and their properties

The material selection is a fundamental step to the fabrication of a good ME composites with large ME response. Thus, choosing the materials with suitable properties is mandatory. In the magnetic phase, some magnetic characteristic parameters are essential to be taken into account as the magnetic permeability (μ), the remanence magnetization (M_r), the coercive magnetic field (H_C), the magnetostriction (λ_{ij}), and the Curie and Neel temperatures (T_C and T_N). The same has to be done for the piezoelectric/ferroelectric phase. Thus, several parameters are important to be selected like: the dielectric constant (ϵ_r), the remanence polarization (P_r), the coercive electric field (E_C), the piezoelectric strain constant (d_{ij}), the piezoelectric voltage constant (g_{ij}), and the Curie temperature (T_C). Thanks to their good ferroic properties, various common piezoelectric and magnetic materials that are used for fabricating the ME composites, are listed in table 1.2.

1.5.3 Fabrication process

Magnetoelectric coupling of ME composites maybe reduced through the fabrication process. Some factors as temperature, interface bonding materials and clamping effect could deteriorate the intrinsic properties of the component and/or strain transfer between phases, as well as the ME response of the composite materials.

Using high temperature during the fabrication process has been reported to dampen the ME response. Indeed, 0-3 particulate bulk composites synthesized by ceramic sintering

Piezoelectric phase	**Magnetic phase**
$Pb(Zr,Ti)O_3$ (PZT)	**Metals**: Fe, Co, Ni
$Pb(Mg_{1/3}Nb_{2/3})O_3$ - $PbTiO_3$	**Alloys**: FeNi-based,
(PMN-PT)	FeCo-based, CoNi-based
$Pb(Zn_{1/3}Nb_{2/3})O_3$ - $PbTiO_3$	Terfenol-D
(PZN-PT)	**Fe-based metallic glasses**:
$Pb(Mg_{1/3}Nb_{2/3})_y(Zr_xTi_{1-x})O_3$	FeBSi, FeBSiC,
(PMN-PZT)	FeCuNbSiB, FeCoB,
	FeCoSiB, FeCoSi
$BaTiO_3$ (BTO) - based	**Ceramics**: Fe_3O_4,
Polyvinylidene difluoride (PVDF)	$Zn_{0.1}Fe_{2.9}O_4$ (ZFO),
and copolymers	$La_xSr_yMnO_3$ (LSMO)
	Ferrites: $NiFe_2O_4$ (NFO),
	$CoFe_2O_4$ (CFO)

Table 1.2: List of common materials used to fabricate ME composites.

process at high temperature show several problems such as: (i) the thermal expansion mismatch between the piezoelectric and ferromagnetic phases lead to the misfit strain at the interface of phases; (ii) interdiffusion and chemical reactions during high temperature sintering weaken the strain transfer between the two phases and the intrinsic properties of the piezoelectric or magnetostrictive phase; (iii) the current leakage due to the low resistivity of the randomly distributed magnetic phase inside the piezoelectric matrix makes the electric poling more difficult [131] [161]. Some other fabrication methods have been developed in order to solve these issues. Hot pressing and spark plasma sintering (SPS) at low pressure and temperature conditions, have been used recently in this purpose.

2-2 laminate bulk ME composites have been widely prepared by epoxy bonding between the two phases. Silver epoxy have been also used as a conductive bond and improves the interface interaction between piezoelectric and magnetostrictive phase. However, the epoxy layer must be kept as thin as possible to optimize the ME coupling. Although epoxy bonding method shows advantages since the process is performed at lower temperature (80-100°C), the mechanical viscoelastic properties of the epoxy may dampen the generated strain and lead to a huge loss of the ME coupling at the interface. Various deposition methods have been used to optimize this issue: pulsed laser deposition, chemical vapor deposition, sputtering, molecular beam epitaxy and spin coating. However, most ME film-based composites reported in literature present a ME response strongly affected by the substrate clamping. Several 0-3 type ME nanocomposites have been synthesized by dispersing magnetic nanoparticles inside the piezoelectric matrix using the spin coating method. The agglomeration and/or dispersion of the magnetic nanoparticles also can reduce/increase the ME coupling. Thus, a good balance between the concentration and dispersion of nanoparticles is mandatory in order to optimize the ME response in this kind of systems [115]. 1-3 type ME nanocomposites are mostly prepared by using self-assembly process [228]. This fabrication process shows less substrate clamping effect and better strain coupling due to the large interfacial surface area between the two phases [147]. However, the design and control of this kind of composite structure remain to be developed, and the ME coefficients should be measured since up to now the low resistance of the magnetic nano-pillars prevents to do it.

1.6 Application

ME materials are promising for a widely range of applications such a multifunctional devices, as recording media, memories, sensors, actuator, energy harvesters, spintronic devices and biology devices. Depending on ME coupling (including direct and converse ones), the ME materials are used in different applications as detailed in [99] [131] [147] [162] [207]. In this section, I will present two promising applications of ME materials showing converse ME coupling: magnetic memories and Magnetoelectric Random Access Memory (MERAM).

1.6.1 Magnetic memories

Current magnetic storage devices used in daily technology base their writing process on material presenting two possible states of the magnetization ($\pm M$) and they write the recorded data by using a magnetic field. In order to get security and stability for the data, a hard magnetic materials with high coercivity and high anisotropy is required. In fact, a high coercivity needs a high magnetic field for the magnetization reversal process in order to to go from a + M "recorded domain" to a - M one. Therefore, the magnetic memories have high power consumption since the magnetic field is driven by current. Also these memories have low writing speed due to the limits of movement of the writing-head.

Magnetoelectric materials opens a novel way to record the data by using an electric field, that can overcome the drawbacks of the magnetic-write memories reported above. In principle, the ME coupling gives a possibility to 'write' the data by applying an electric field and then reading them by a magnetic field sensor. In the electric writing process, the magnetization is inverted electrically thank to the converse ME coupling. If the electric field can switch completely the magnetization via the ME coupling effect, the ME nanostructures can be used as an electric-written magnetic-read storage device with a high density of magnetic data and high writing speed. Such novel storage devices still remain to be demonstrated experimentally.

Another way to design a new storage device using ME materials is by using the control of the coercivity (H_C). As discussed in the previous paragraph (see section 1.4), the H_C of the magnetic thin films grown on ferroelectric substrate can be reduced significantly by applying the external electric field. Thus the writing data process needs much smaller magnetic field applied and they are lower power consumption. Moreover, manipulation of H_C also opens a new way to record data where the data would be written in two H_C-states ($high - H_C$ and $low - H_C$) rather than two states of M ($\pm M$). These two different states of H_C are induced by an external electric field via the ME coupling (see section 1.4). Thus the external magnetic field would not affect the H_C. In other words, the recorded data is stable and secure. This principle is demonstrated by Li et al. [88]. Such memories with high security, stability and low power consumption are compatible with the currently recording technology, and suggests the revival of a new generation of storage devices pretty soon.

1.6.2 Magnetoelectric Random Access Memory

Binary information is also at the base of the storage process characterizing the Random Access Memory (RAM) device which is an important component in computer memories and daily life electronics. There are a few types of RAM devices including ferroelectric random access memory (FeRAM) and magnetic random access (MRAM). FeRAMs use ferroelectric polarization states to store data bits, while MRAMs use magnetization states and the magneto-resistance properties in multilayers (i.e. the variation of resistivity as function of the magnetic field). However, FeRAM and MRAM devices show some disadvantages like the need for destructive read and reset operations in FeRAM and high power consumption in MRAM. These limits can be solved by using multiferroic materials to design a new type of RAM called MERAM. The magnetoelectric coupling in multiferroic materials offers the opportunity to combine the best features of FeRAM and MRAM, and thus to create a novel type of non-volatile MERAM with four-states storage possibilities of data bits [50]. This new MERAM generation would present some great advantages as better memory density, lower power consumption and could improve thermal stability.

The practical challenge in such MERAM devices is to switch completely the magnetization by applying an E-field. Several groups proposed a hybrid MERAM device by fabricating AFM/FM/FE heterostructures that combine the ME coupling of multiferroics layers with the interfacial exchange bias of AFM/FM layers [17] [61] [90] [217]. The magnetization in these heterostructures is switched by nearly 180°by applying the electric voltage. This achievement opens a possibility in experimental fabrication of MERAM technology in the near future.

Chapter 2

Experimental technique and micromagnetic simulation

2.1 Experimental technique

2.1.1 Vibrating sample magnetometer

The vibrating sample magnetometer (VSM) that measures the macroscopic magnetic properties of materials was first developed by S. Foner in 1956 (B. D. Cullity 2002). It has been accepted as a standard approach worldwide due to its simplicity and high sensitivity. The working principle of VSM is based on Faraday's law of electromagnetic induction. The magnetic sample is placed at the end of a vibrating non-magnetic rod dived in a uniform magnetic field produced by electromagnets. In the MPMS VSM SQUID (Superconducting Quantum Interference Device) system, the magnetic field is induced by superconducting coils which are cooled by helium liquid. The MPMS 3 system that we used for our measurements allows changing the temperature from 4K to 400K and putting an external field (generally applied vertically to the ground - see Figure 2.1) going from -7 Tesla to +7 Tesla. In addition, the MPMS 3 system allows a high sensitivity up to 10^{-8} emu thanks to the use of a Josephson junctions for the detection of the sample magnetization.

The MPMS 3 provides three possible measurement modes: DC, VSM and AC modes. In DC mode, MPMS measures the magnetic moment of the sample by reading the output of the SQUID detector. This output is recorded as a voltage signal when the sample moves upward, from the initialization position, through the SQUID pickup coils. This upward movement through the SQUID pickup coils is obtained by a vertical scan of the sample. The SQUID detected data are taken as a function of the sample's position in the coils and correspond to the so-called raw measurement data. After collecting the raw voltages data, MPMS MultiVu computes the magnetic moment of the sample by performing a fit. In VSM mode, the sample vibrates vertically through the coils with a frequency of f = 14 Hz. The vibration of the sample induces a changing of magnetic flux though the coils which consequently induces a change in the voltage of the pickup coil. The magnitude of this voltage is related to the frequency and amplitude of the oscillations as well as the total

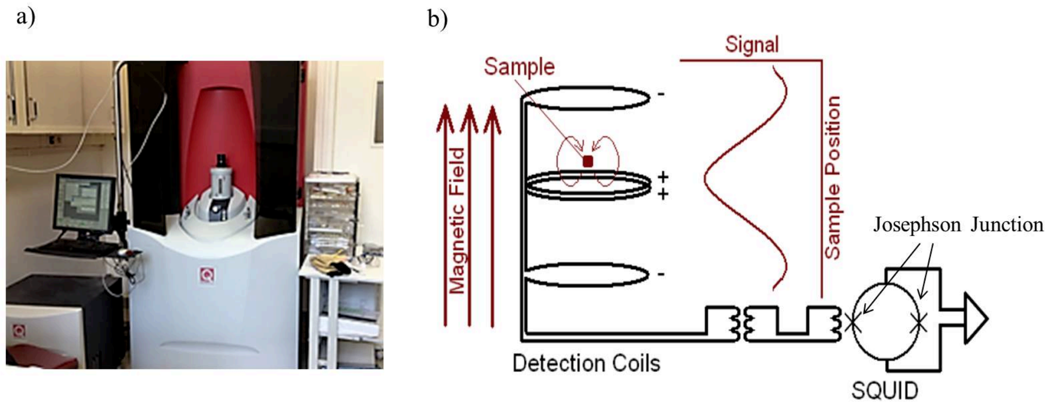

Figure 2.1: (a) Photo of the VSM-SQUID used at LPEM (ESPCI) laboratory in order to measure the magnetization of our samples as function of H, T and frequency; (b) Scheme of VSM-SQUID principle showing the Josephson junction for the SQUID detection.

magnetization of the sample. The MPMS then computes the magnetization of the sample from this recorded voltage. In DC and VSM modes, the magnetic field is a DC field which is vertical to the ground (see Figure 2.1(b)). In the AC mode, an oscillating AC magnetic field is applied to the sample. The change in magnetic flux seen by the detection circuit is caused by the changing of the magnetic moment of the sample due to its response to the applied AC field. In our study, we performed SQUID VSM measurements in collaboration with Mme. B. Leridon (Chargée de Recherche) at LPEM laboratory at ESPCI–ParisTech on a Quantum Design MPMS 3 magnetometer by Quantum Design factory.

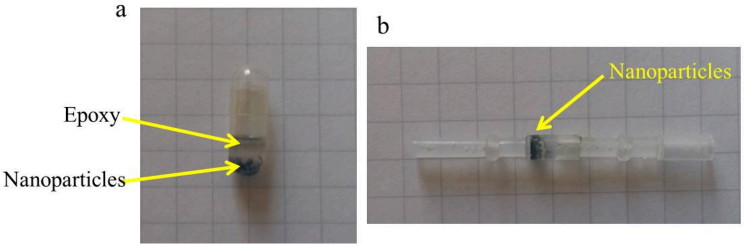

Figure 2.2: Nano-powders blocked within: (a) an epoxy resin in a plastic pill; (b) in a Quantum Design factory's clips.

Different magnetic materials have been measured during our study by VSM SQUID including bulk, nano-objects inside their solution (liquid polyol) and nano-powders. The nano-powders (i.e. nanowires or nanoparticles), have been blocked in an epoxy resin at room temperature in a plastic pill before doing the measurement. Also, we could measure these nanopowders by blocking them in specific clips engineered by the QD factory (see Figure 2.2). Whereas in the case of nano-objects measured in their polyol solution (i.e. nanowires dispersed in their solution), the magnetic objects are blocked by cooling down the temperature below the glass temperature (T_G) of their solution (i.e. T_G of the polyol solution is 220K). We measured standard zero field cooled (ZFC) and field cooled (FC) hysteresis cycles at different temperatures for each sample by cooling down the solution containing the nano-object without (ZFC) and with (FC) the application of the vertical magnetic field inside the MPMS system. In the DC measurement, the magnetic moment is obtained after each scan of sample. A scan of sample takes one seconds for a length of one scan equal to 30 mm. Typical DC measurements time are of the order of 1 to 100 s. For the AC mode, the measurements were performed within a temperature range among 2K and 300K and frequency has been varied from 9Hz to 999Hz (i.e. 10^-1 s up to 10^-3 s).

2.1.2 Near field microscope

The near-field microscope is based on the Scanning Probe Microscopy (SPM) principle whose was firstly invented by Binning and Rohrer in 1982 with the name of Scanning Tunneling Microscope (STM) . Based on the principle of SPM, many different techniques have been developed as: atomic force microscope (AFM), the magnetic force microscopy (MFM) and the piezoelectric force microscopy (PFM). Their principles are based on the control of short range interactions between the surface of the sample and the nanometric tip used as a probe. We used MFM and PFM to probe local magnetic and piezoeletric properties of our artificial multiferroic systems.

Magnetic Force Microscope (MFM)

We measured magnetic properties by MFM using a standard Veeco DI-3100 microscope. This is a tapping mode of the near field microscopy technique which general concept is the measurements of the magnetic force interactions between the ferromagnetic-coated tip and the sample's magnetic stray field (see Figure 2.3).

At the edge of a micrometric cantilever there is a nanometric tip which is coated with a ferromagnetic thin film. In our work, we used a standard hard magnetic tip (PPP-MFMR tips) with a coercivity of 300 Oe and a remanent magnetization around 300 emu/cm^3. These kind of tips allow high magnetic contrast and avoid the reversal magnetic mechanism of the magnetic moment of the tip. This is mandatory for the detection of weak magnetic stray field and allows high lateral resolution domain imaging ($\approx$ 50 nm). The stray field perpendicular to the film surface is detected by the height variation of the tip (see Figure 2.3(a)). The cantilever holding the nanometric ferromagnetic tip, scans the sample surface while excited at its resonance frequency (typically of 70-100 kHz). A laser beam, heating the edge of the cantilever, indicates the vertical position of the tip on a photodiode. Magnetic forces exist between the tip and the sample and they change with the distance between the tip and the surface of the system. In order to extrapolate them from the surface topography, a so-called lifting mode is used (working distances typically used are around 80 to 150nm). The magnetic force acting on the tip causes the bending of the cantilever which needs to be decorrelated from the topography induced bending. Knowing this latter by a first tip scan in a contact mode with the surface, all vertical deviations from this first scan are detected by the light beam deflection on the photodiode and allows the extrapolation of the magnetic interaction effects (see Figure 2.3(b)). In

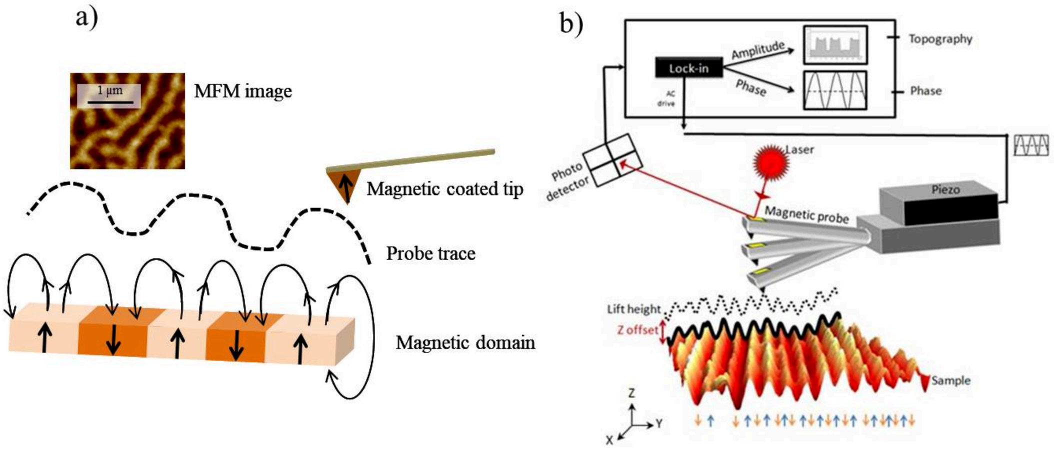

Figure 2.3: MFM working principle. (a) Magnetic moments of the magnetic domains are represented by the arrows inside the film (colored plate), stray field lines are also schematically represented by the straight line and a magnetic phase shift images recorded by the MFM scan is reported as example. The dashed line represent the height movement of the nanometric tip under the magnetic interaction with the stray field coming from the sample; (b) The MFM signals are detected by a laser beam heating the edge of the MFM cantilever then deflecting on the photodiode [119].

our study (see chapter 3), the MFM has been used as an *in situ* probe of the static magnetic domain configuration under the influence of an applied in-plane elastic strain by a piezoelectric device and/or an *in situ* magnetic field obtained by a home-atomic force microscopy (AFM)-costumed electromagnet (see Figure 2.4).

In a simple model, when a magnetic coated tip is brought into the stray field of a magnetic sample, it will have the following magnetic potential energy E:

$$E = -\mu_0 \int \vec{M}_{tip}.\vec{H}_{sample} dV_{tip} \tag{2.1}$$

where μ_0 is the vacuum permeability. The force acting on an MFM tip can thus be calculated by:

$$\vec{F} = -\vec{\nabla}E = \mu_0 \int \vec{\nabla}(\vec{M}_{tip}.\vec{H}_{sample}) dV_{tip} \tag{2.2}$$

The stray field from the sample is strongly dependent from the magnetic local moment (i.e. the magnetization of the magnetic domains) and the distance between this moment and the magnetic tip. This stray field can be easily calculated by using a single magnetic moment model oriented randomly in the space:

$$\vec{H}_r = \frac{3\vec{n}(\vec{n}\vec{m}_{sample}) - \vec{m}_{sample}}{\vec{r}^3} \tag{2.3}$$

where $\vec{n}$ is the unit vector in $\vec{r}$ direction, $\vec{m}_{sample}$ is the magnetic moment of the sample.

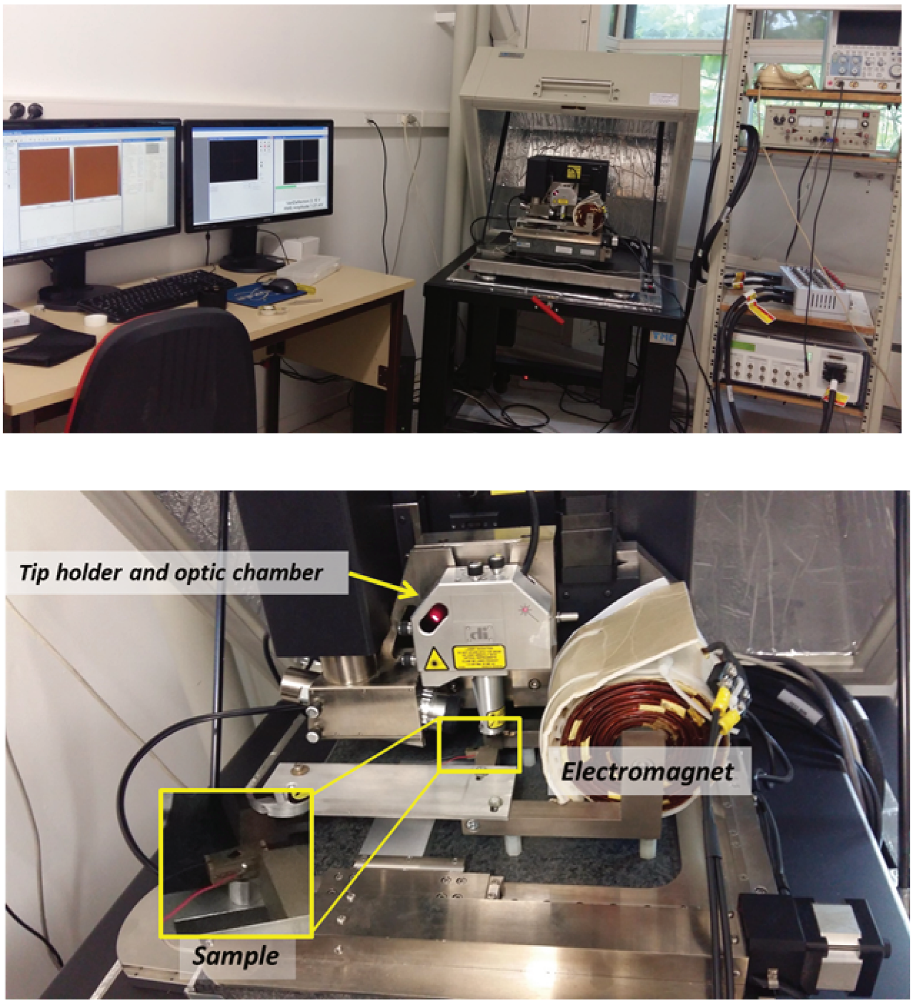

Figure 2.4: The MFM system at LSPM (top); Experimental setup with *in situ* E and H field applied (bottom).

In this frame, it is easy to understand that any deviation of the tip from the resonance frequency and from the topography height (pre-recorded) profile, are sensing the magnetic changes due to the sample stray field interacting with the magnetic moment of the tip. Thus the recorded changes of the phase, amplitude and frequency of the tip can be expressed as [65]:

$$\Delta\varphi \approx \frac{Q}{k}.M_{tip}.\frac{\partial F}{\partial z} \tag{2.4}$$

$$\Delta A \approx \frac{2A_0.Q}{3\sqrt{3k}}\frac{\partial F}{\partial z} \tag{2.5}$$

$$\Delta\omega_0 \approx -\frac{1}{2k}\frac{\partial F}{\partial z}\omega_0 \tag{2.6}$$

Where k is the cantilever spring constant, Q is the vibrating system quality factor, A_0 is the amplitude of the cantilever oscillation at the resonant frequency in absence of any external force gradient.

From equations 2.4 to 2.6, it is clear that the phase shift recorded is proportional to the magnetic contrast between the opposite force applied to the tip by the opposite oriented magnetic domains (see Figure 2.3). In our measurements, we worked at lift distances of 100nm and at a scan frequency of 0,5Hz (very low scan speed) in order to have an optimized image resolution and to be able to compare phase shifts resulting from experiments done in different days. Also, the experimental conditions for the magnetization procedure of the tip have been kept constant (same magnitude and direction of the field) in order to have a well-controlled constant value of the magnetic moment of the tip. The quality factor and the spring constant have also been kept constant and calibrated before each experimental working procedure (i.e. tips from the same batch were carefully characterized for the whole set of results presented in this manuscript).

MFM image analysis:

This analysis has been done on a 530 nm thin FeCuNbSiB film deposited on a compliant substrate. FeCuNbSiB, also called Finement, has excellent magnetic softness and stripe magnetic domain structures. The MFM images of our sample (see chapter 3) presents the magnetic domain stripes pattern. Thanks to the Nanoscope Analysis software and the OriginPro program we had the possibility to analyze the stripe-domain width and the magnetic moment orientation. This has been done on a large number of images and thus represent a large range of statistical studies.

The magnetic domains width were deduced from MFM images by doing hundreds of sections per image using the Nanoscope Analysis software. The typical screen snapshot of Nanoscope Analysis is shown in Figure 2.5.

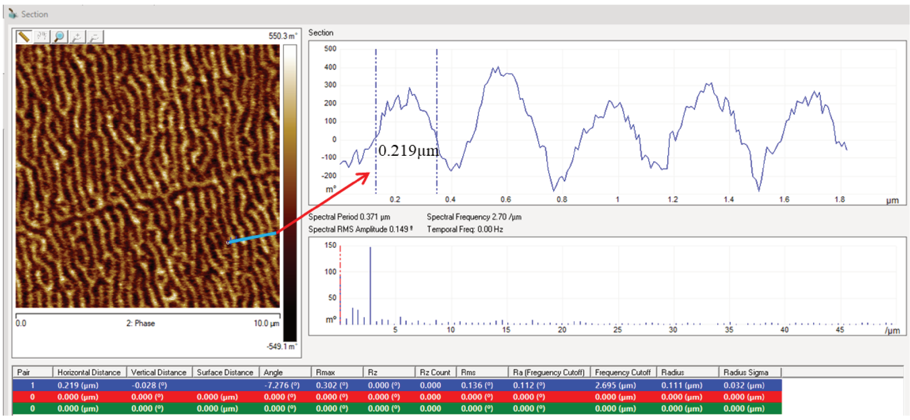

Spectral Period 0.371 µm
Spectral Frequency 2.70 /µm
Spectral RMS Amplitude 0.149 °
Temporal Freq: 0.00 Hz

Pair	Horizontal Distance	Vertical Distance	Surface Distance	Angle	Rmax	Rz	Rz Count	Rms	Ra (Frequency Cutoff)	Frequency Cutoff	Radius	Radius Sigma
1	0.219 (µm)	-0.028 (°)		-7.276 (°)	0.302 (°)	0.000 (°)	0.000	0.136 (°)	0.112 (°)	2.695 (µm)	0.111 (µm)	0.032 (µm)
0	0.000 (µm)	0.000 (°)	0.000 (µm)	0.000 (°)	0.000 (°)	0.000 (°)	0.000	0.000 (°)	0.000 (°)	0.000 (µm)	0.000 (µm)	0.000 (µm)
0	0.000 (µm)	0.000 (°)	0.000 (µm)	0.000 (°)	0.000 (°)	0.000 (°)	0.000	0.000 (°)	0.000 (°)	0.000 (µm)	0.000 (µm)	0.000 (µm)

Figure 2.5: Screen snapshot obtained by the Nanoscope Analysis. The width of the stripe-domain is easily deduced by the blue section performed by the program. This section gives the variation of the phase along the blue segment. The mean width is calculated on the bases of hundreds sections performed in different zone of the MFM images. The final value is a statistical average.

The magnetic moment orientation has been also studied starting from the MFM images. In order to do this, we used the simple model presented by Gyanendra et al. [177]. If we consider a distribution of moment schematically represented in Figure 2.6, then the angle θ between the local magnetic moment **M** and the film plane can be obtained using the following equation 2.7:

$$\theta(x,y) = sin^{-1}\left(\frac{MFM(x,y)}{\|MFM_{max}\|}\right) \tag{2.7}$$

Where $MFM(x,y)$ is the magnitude of the MFM signal in the (x,y) position of the squared image, $\|MFM_{max}\|$ is its maximum value corresponding to the perpendicular alignment of the domain moment. The perpendicular direction is defined as the direction perpendicular to the sample surface. The (x,y) plane is the plane of the studied magnetic film scanned by the tip. A schematic view of the angle θ is presented in Figure 2.6(a).

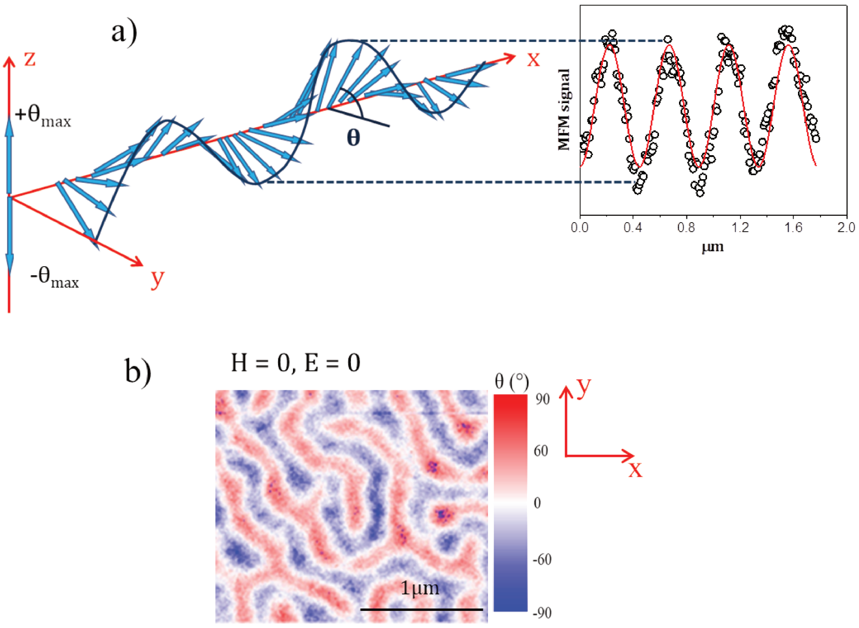

Figure 2.6: (a) Angle θ between the magnetic moments (blue arrows) and the magnetic film plane (x,y). The right panel shows the MFM signals of the cross section across the domain stripe (i.e. section of the x0z plane), which fits well with a sinusoidal function (red line); (b) The angle distribution of the magnetic moments extracted from the MFM image analysis at zero external force applied (i.e. H = 0 and E = 0).

In order to do this calculation, the MFM signals have been extracted. A matrix of data of 512 × 512 values corresponding to the resolution used to acquire the images (ie. 512 × 512 pixels) is obtained. Each pixel in the MFM image corresponds to a value of the signal, so an angle value. Thus, the images of the angle distribution can be deduced from the MFM phase images by calculating the Equation 2.7 for each point in the matrix. This extraction and analysis has been performed by OriginPro software. See an example of the angle distribution image in Figure 2.6 (b). As can be seen in this latter, the magnetic moments **M** are oriented along different angles varying from -90°(blue) to +90°(red) respect to the (x, y) plane of the sample. The red patterns are called domain "up" while the blue patterns are called domain "down". The white lines between domains "up" and "down" correspond to the domain wall where the angle θ is rotating around the zero angle (i.e. the (x,y) plane). It is important to underline here that to be sure of the sign of the angle and thus the up and down direction of the domains, we had to magnetized the tip always in the same direction. The magnetization of the tip is thus always kept as in Figure 2.3.

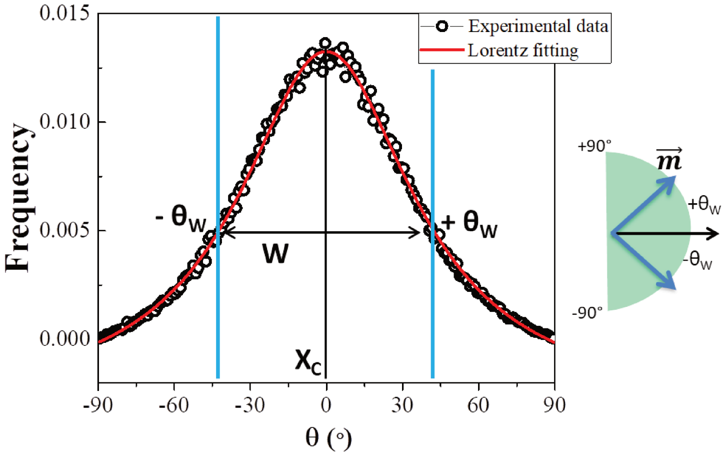

Figure 2.7: An example of statistic analysis of the angle θ varying from -90 °to +90 °. The existence of each angle value is presented by its frequency reported in the vertical axis. Inset on the right: the orientation of the majority of the magnetic moment (blue arrow) compared to the plane of the film (black arrow) is schematized here and -θ_W and +θ_W angle are reported.

The statistic analysis of the magnetic moment orientation in each angle-image is presented in Figure 2.7. Thanks to OriginPro software, each angle value is counted from the matrix of angle data. The range of counted angle is from -90°to +90°. After extracting the number N(θ_i) which is the number of occurrences of θ_i in the studied angle image/-matrix, we converted it to frequency f(θ_i) = N (θ_i)/N_{total} with N_{total} being the total number of angles in the image (N_{total} =512 × 512). This frequency of θ is presented as function of θ in Figure 2.7 and is well-fitted by a nonlinear curve with the peak around 0°for the considered example. It means that the majority of θ is in the range $[-\theta_W, +\theta_W]$. The orientation of the magnetic moment depends on the external force applied during the measurement.

Thus, in order to find the parameters that can represent the orientation of the magnetic moment, we fitted the nonlinear curve by a Lorentz distribution function which shows **W** as a the width of the distribution and X_C as the central position of it (see red line in Figure 2.7). **W** represents the range of θ $[-\theta_W, +\theta_W]$, which have the highest probability in the studied angle image. Therefore, from the **W** value, we can estimate the orientation of the local magnetic moment which are mostly in-plane (i.e. small **W** value) or out-of-plane (ie. lager **W** value), see the sketch inset in the right side of the in Figure 2.7. In our experiment, we will investigate the local magnetic moment orientation by considering the **W** and X_C values, obtained as a function of the external stimulus field applied *in situ* during the MFM measurements.

Piezoresponse Force Microscopy (PFM)

Piezoresponse force microscopy (PFM) is a SPM technique allowing to image and to manipulate the piezoelectric/ferroelectric domains. By applying an alternating current (AC) to the probe tip which is in this case a sharp conductive tip. The deformation of the piezoelectric/ferroelectric sample is detected through standard photo-diode detector methods. The basic working principle of PFM is shown in Figure 2.8.

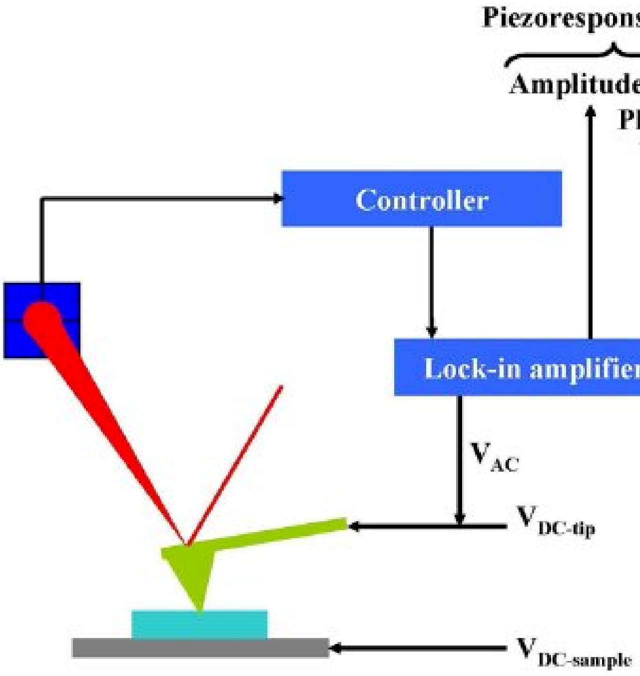

Figure 2.8: PFM working principle [66].

In PFM measurement, the piezoelectric/ferroelectric sample is placed between a bottom electrode and a conductive PFM tip serving as a movable top electrode. Measurements are performed in the contact mode in this case (i.e. the conductive tip is in contact with the surface of the sample) and allows to get informations on the out-of-plane component of the electromechanical surface response (vertical PFM) as well as on the in-plane component via the frictional forces (lateral PFM). By applying an AC electric bias to the probing tip, this results in a sample surface oscillation due to the converse piezoelectric effect (see section 1.1.5 in Chapter I). The surface oscillation of the sample results in the displacement of the cantilever. Therefore, the piezoelectric (electromechanical) response of the sample as a function of the applied electric field through the tip, can be deduced. This relationship is described by a rank-3 tensor, $Z_i = d_{ik}E_k$. The most important component of this tensor for typical vertical PFM is the d_{33} component which is directly coupled with the vertical motion of the cantilever. The voltage applied to the tip is:

$$V_{tip} = V_{DC} + V_{AC}\cos(\omega t) \tag{2.8}$$

Where V_{DC} is the DC bias (switching bias for the ferroelectric domains), V_{AC} is the AC bias (probing bias) and ω is the AC bias frequency (driving frequency).

Due to the piezoelectric strain in the material that causes the cantilever displacement, this latter can be roughly obtained as:

$$Z = z_{ac} + A(\omega, V_{ac}, V_{dc})\cos(\omega t + \varphi) \tag{2.9}$$

Where the first term is the static surface displacement and the second term is the cantilever displacement induced by the surface deformation when the voltage is applied. The φ is the phase shift between the driving voltage V_{AC} and the voltage induced deformation.

When the voltage is driven at a frequency well below the resonance one of the cantilever in contact with the surface of the sample, this expression becomes:

$$Z = d_{33}V_{dc} + d_{33}V_{ac}\cos(\omega t + \varphi) \tag{2.10}$$

Where we have implicitly assumed that d_{33} depends on the polarization state of the ferroelectric material. In conclusion, as the V_{dc} and V_{ac} are fully known, the magnitude of the oscillating response is a measure of the magnitude of d_{33} and the phase is sensitive to the polarization direction of the sample.

It is worth mentioning that, there are three typical PFM imaging modes: vertical PFM, lateral PFM and vector PFM. The most popular using mode is the vertical PFM which measures the out-of-plane polarization configuration of the sample by recording the tip-deflection signal at the frequency of the applied AC modulation. In the lateral PFM mode, the in-plane component of polarization is detected as a lateral torsion of the cantilever due to bias-induced surface shearing. An example of vertical PFM mode is showed in Figure 2.9 on a standard piezoelectric lithium niobate material presenting a periodic poled stripe domain.

We performed PFM measurements in the frame of a NFFA European project in collaboration with A. Gomez responsible of the Scanning Probe Microscopy Laboratory at ICMAB, Barcelona Autonoma University UAB (Spain). In our PFM measurements, we used the vertical PFM mode to detect the out-of-plane piezoelectric response by using an Agilent 5500 SPM with the AC Mode III accessory. The AC frequency is 20 kHz for all our PFM measurements, out of the main resonance of the tip, in order to avoid possible artifacts related to resonant frequency [19]. The sample that we studied by PFM is an electro-active (or ferroelectric) polymer (PVDF, see chapter 4). Therefore, this sample is very sensitive to be scratched by the PFM tip. Thus, we used a soft PFM tip (RMN 12PT 300B) with a soft spring constant of 0.8N/m. All the images and the electromechanical

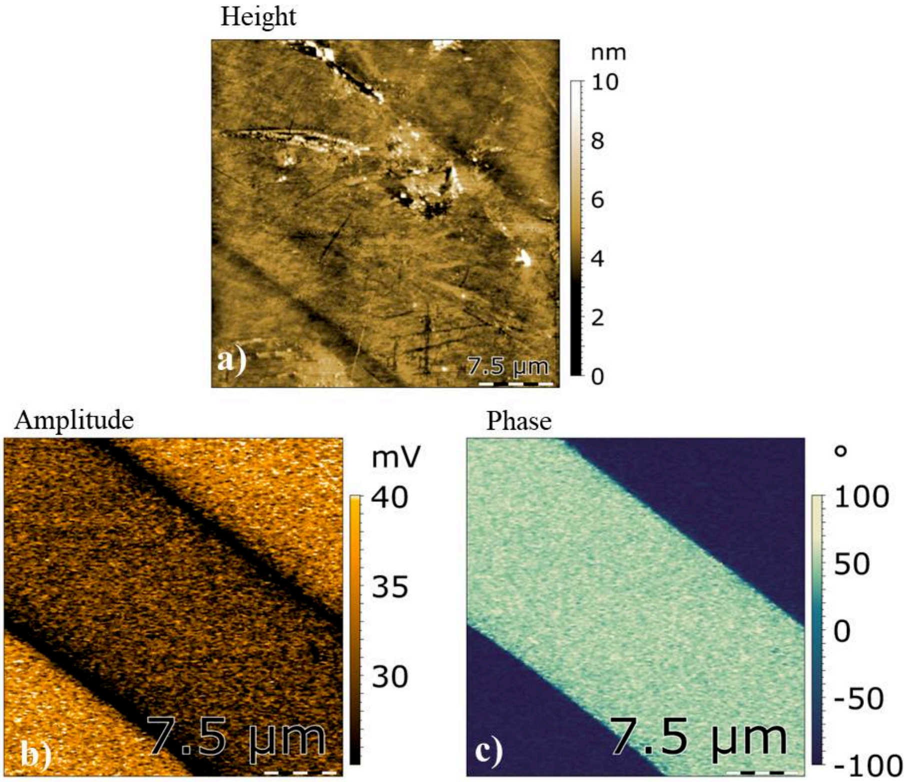

Figure 2.9: A PFM measurement in the periodically poled lithium niobate (PPLN) was taken at ICMAB (UAB) Barcelona (Spain). (a) Surface topography (height), (b) PFM amplitude, (c) PFM phase. The width of domain stripe is 20μm.

measurements were acquired in controlled humidity conditions (less than 10%). It is worth saying here that, in the frame of the NFFA project, we also measured the piezoelectric properties of the standard inorganic films (PPLN and PZT). For more detail, see the Annexes D.

2.2 Micromagnetic simulation

In order to simulate the static magnetic properties of unidimensional cobalt-based nano-magnet, we use the NMAG package [48]. NMAG is a finite element micromagnetic simulation package based on Python programming language. This software allows solving the free energy equation of complex shape nano-objects. The magnetization configuration of nano-objects is obtained at each step of the applied external field. On each node of the finite element in the mesh, the Landau-Lifshitz-Gilbert equation is solved [171]. All the parameters that we used in this simulation are obtained by the room temperature characteristics of the cobalt bulk material.

The finite element of the mesh is formed using the automatic mesh generation program named NETGEN. This open source tool allows generating triangular or quadrilateral meshes in two dimensions, and tetrahedral meshes in three dimensions. The input parameters define the geometry of the object and the general script is like the following:

```
algebraic3d
solid cyl = cylinder (−50,0,0; 50,0,0;5)
and plane (−50,0,0;−1,0,0)
and plane (50,0,0;1,0,0);
tlo cyl;
```

Where `algebraic3d` is the constant keyword for defining the mesh, `cylinder` is the object geometry which can be `cylinder`, `sphere`, `ellipsoid` or `cube`, etc. (cylinder in the example). The `(x1,y2,z1;x2,y2,z2;R)` are the coordinates of the cylinder vertex and R is the radius of cylinder. The unity is in nanometer. By this way, an infinity of cylinder can be defined. In order to limit the length of cylinder, the planes `(-x3,y3,z3;-1,0,0)` and `(x4,y4,z4;1,0,0)` are used. See an example of cylinder's mesh in Figure 2.10(a).

Once we have created the wished geometry for the nano-obejct, NETGEN reads the geometry file describing the three-dimensional structure and creates the mesh. The number of nodes constituting the mesh depends on the morphology and the size of the object. The distance between two nodes should be of the order of the exchange length $l_{ex} = \sqrt{2A/\mu_0 M_S^2}$, where A is the exchange stiffness of the material constituting the nano-object, μ_0 is the vacuum permeability and M_S is the saturation of magnetization of the material. In order to use the mesh in NMAG, we convert the neutral type to ".nmesh.h5" type of mesh to which the NMAG script will attribute the magnetic parameters.

These latters are defined by a typical NMAG script reported below:

```
import nmag
from nmag import SI, at
sim = nmag.Simulation()
Co = nmag.MagMaterial(name=”Co”,
Ms=SI(1400e3, ”A/m”),
exchange_coupling=SI(12e−12, ”J/m”),
anisotropy=nmag.uniaxial_anisotropy(axis=[1, 0, 0],
K1=SI(520e3, ”J/mˆ3”)))
sim.load_mesh(”Co.nmesh.h5”, [(”nano”, Co)],
unit_length=S(1e−9,”m”))
sim.set_m([0,0,1.])
Hs = nmag.vector_set(direction=[1.,0.001,0],
norm_list=[2, 1.995, [], −2, −1.995, [], 2]
units=1e6∗SI(’A/m’))
sim.hysteresis(Hs, save=[(’averages’,’fields’,
at(’convergence’))])
```

A description line-by-line of this script is given in the NMAG tutorial [48]. We just emphasized here the important parameters of Co that we used: the saturation of magnetization $M_S = 1400 kA/m$ and the exchange coupling $A = 12.10^{-12} J/m$ [193]. The magnetocrystalline anisotropy used for the micromagnetic simulation corresponds to the one of the cobalt hexagonal phase at room temperature, $K_1 = 520 \times 10^3 J/m^3$ with the anisotropy axis along the length of the nanowire. The magnetocrystalline anisotropy and the shape one are parallel (see example in chapter 1, section 1.1.3). The external field, H_s, can be applied in different directions. In the script reported, H_S is in the direction along the length of cylinder. The H_S value has been changed from $2.10^6 A/m$ ($\sim$ 2.5 T) to $-2.10^6 A/m$ ($\sim$ - 2.5 T) with the step of 0.005 A/m ($\sim$ 6.18 mT). The unity is in SI unity system for all the parameters.

The hysteresis command of NMAG software, takes this list of applied fields as the input parameter, and computes the hysteresis loop. The Stoner – Wolfarth model was performed for one cylinder as a test. The simulation results are shown in Figure 2.10(c).

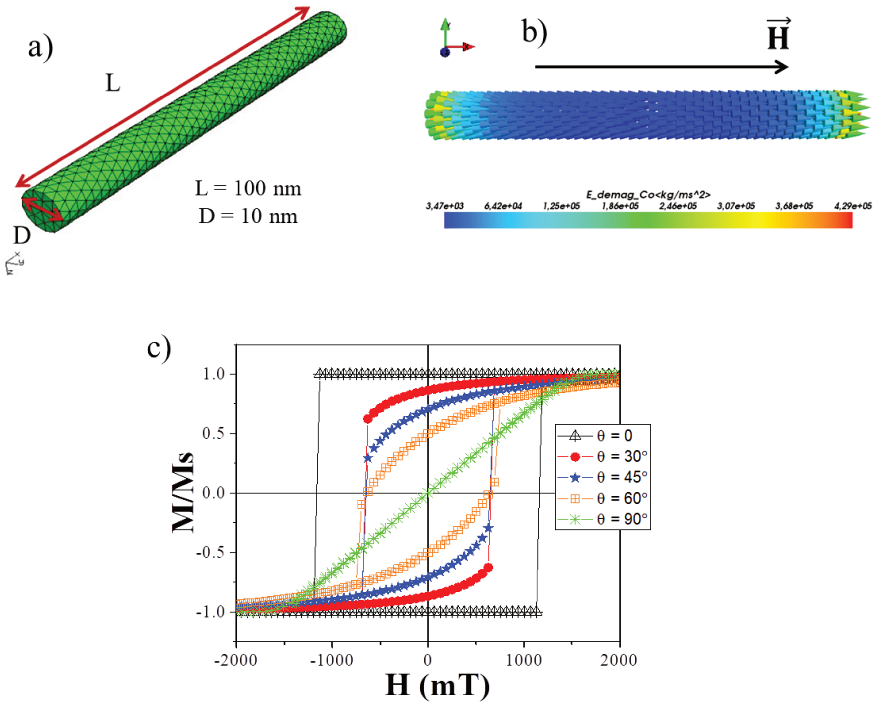

Figure 2.10: (a) A nano-cylinder mesh, with the length L = 100nm, the Diameter D = 10 nm. (b) Magnetization configuration at saturation state of the nano-cylinder; (c) Hysteresis loop of the nano-cylinder when the angle θ between the external field and the length (i.e. easy axis) of the nano-cylinder variates from 0° to 90°.

In our work, we also performed the simulation for a finite number of cylinders which can be arrange in 2D or 3D nanostructures (see Chapter 5). We considered Co nanowires with a cylinder-shaped morphology with a length L = 100 nm and a radius r = 5 nm (see Figure 2.10(a)). These dimensions are typically observed into literature for Co nanowires presenting the best magnetic performances needed for applications requiring high magnetic energy [42] [113] [128] [149] [150]. The magnetic parameters used for the performed calculations correspond to the one measured for the *hcp* (hexagonal-close-packed) cobalt thin film and bulk which are presented in the NMAG script above. In this case, the exchange length can be easily calculated and found to be $l_{ex} = \sqrt{2A/(\mu_0 M_s^2)} \approx 3.2nm$ which is the critical distance to take into account for the mesh nodes distances in order to keep the exchange interaction between the magnetic moments of the elements inside the mesh. These chosen magnetic characteristics are important in order to simulate an assembly of nano-objects, each of which presents (when isolated from the others) the best magnetic performances at room temperature. We fixed the length axis of the perfectly aligned nanowires along the Ox axis. Thus, various directions of H_s have been applied from 0 °to 90 °from the Ox direction in order to study the effect of the various configurations over the magnetic properties of the nanowires assembly.

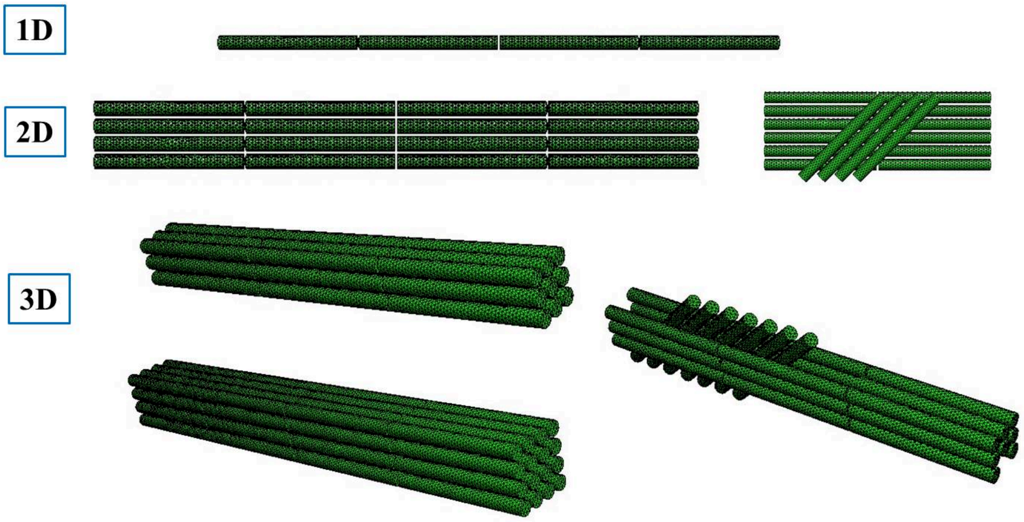

Figure 2.11: Nanowires assembly organized in different configurations presenting 1-dimension, 2-dimension and 3-dimension. The meshes are obtained by NETGEN.

Each nanowire as well as the assembly was meshed using automatic mesh generation of NETGEN (see Figure 2.11) [170] with the distance between two consecutive nodes inside each mesh of 3.5 nm. This distance is of the same order of the calculated exchange length as reported before and it allows a good discretization of the mesh nodes by maintaining acceptable calculation time. We did verify in advance that this decision was not affecting our results. We observed that using mesh length of $l_{ex} = 1.9nm$ brings a change of the switching field values of 5 % ((i.e. an increase of 5% of H_C) compared to the one obtained in the same condition for a node length of 3.5 nm). According to our verifications, the overall behavior of the magnetization under the application of the magnetic field and for different configuration it is not affected by the chosen distance used (3.5 nm). This confirms also the results by I. Panagiotopoulos et al. [150] that used distances of 7 nm between nodes in their simulations. All the magnetization configuration of the nanowires assembly at each reversal/critical step shown in this work has been obtained by using the Mayavi2 software.

Chapter 3

Electric control of magnetic domain in 2-2 type ME composites

3.1 Introduction

As discussed in section 1.4, the E-field control of magnetic properties in ME composites through the strain-mediated effect, have been studied in different structures, especially the 2-2 type one. The converse ME effect in these composites is usually studied by manipulating the macroscopic properties as their magnetic hysteresis loops and their magnetic anisotropy. There are few studies on the local interaction between the piezoelectric/-ferroelectric phase and strain induced changes of the magnetic domain presented by the magnetic phase. For instance, the local coupling of ferroelectric and magnetic domains has been reported in t-Py/$BaTiO_3$ heterostructure [41]. This local coupling comes from the uniaxial strain-induced in the ferroelectric ($BaTiO_3$) phase by the thermal expansion when the $BaTiO_3$ substrate is heated up at high temperature (150°C) then cooled down to room temperature. However, this changing of the magnetic domain by using thermal treatment method has a lack of control due to the non-reversible modification of the magnetic domain. Another ME heterostructures showing the local ME coupling has been reported for Ni/PZT [30] and Ni/PMN-PT bi-layered system [63]. The strain-induced changes of the magnetic domain configuration in these ME heterostructures has been observed under the application of an electric field. In Ni/PZT heterostructure, the E-field-induced curving, bending, branching, and elongation of the magnetic stripe-domain patterns has been reported by [30] (see Figure 3.1). Whereas, in Ni/PMN-PT structure, the magnetic domain patterns are switched from out-of-plane to the in-plane configuration in the Ni film (see Figure 1.22 in chapter 1). However, these switching need a large voltage (800kV/m) in order to pole the ferroelectric PMN-PT [63]. This large electric voltage is not sufficient for fully destabilized the magnetic domain pattern and to bring to a homogeneous magnetic state.

In this frame, we focused on controlling the local magnetic stripe-domain patterns and the magnetic moment orientation of a 530nm FeCuNbSiB (Finemet) magnetostrictive film by using a low electric field/energy. This magnetostrictive film has been deposited

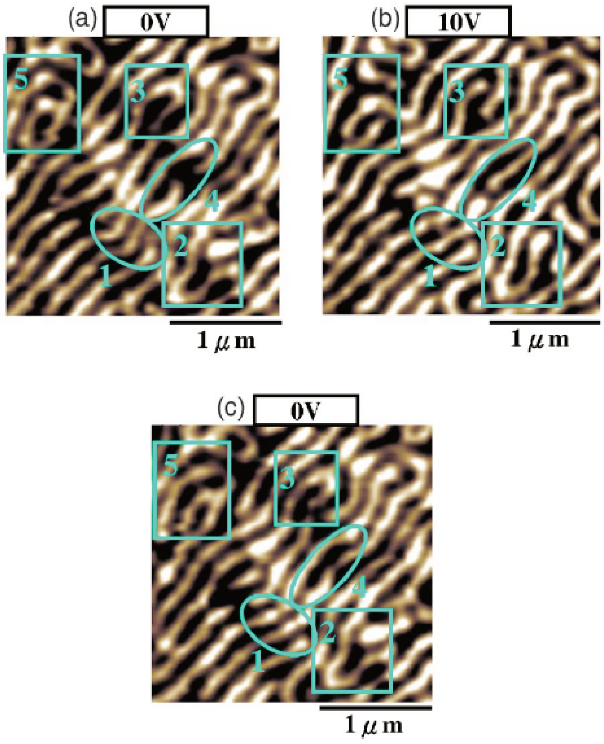

Figure 3.1: Electrical control of magnetic stripe-domain patterns in thin film of Ni/PZT. MFM images were taken at (a) 0 V, (b) 10 V, and (c) back to 0 V [30].

onto a compliant polyimide substrate (Kapton) and glued afterwards on a piezoelectric (PE) actuator (see Figure 3.2). By using this commercial PE device which shows a strong piezoelectric properties, the electric control of the magnetic domain stripes pattern should be easy and efficient. The amorphous soft magnetic compound (Finemet) is widely investigated in the literature because of its easy and low cost elaboration and thus its potential application in magnetic devices.

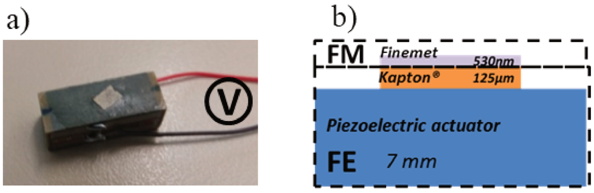

Figure 3.2: (a) Photo of the sample; (b) Sketch of the studied heterostructure showing the 530 nm thick Finemet film deposited onto a 125 μm thick Kapton substrate and glued on to the piezoelectric actuator (thick 7 mm).

FeCuNbSiB has excellent magnetic softness and stripe magnetic domain structures that are well known to be very sensitive to the internal stress generated during the deposition on a polymer substrate as well as by surface irregularities [125] [134] [173]. Internal stresses coupled with a good magnetostriction of the amorphous finemet film may result in a high magnetic anisotropy. Both internal stresses and pinning centers in the film can significantly vary with the film thickness [174]. All these reasons promote the finemet to be a good candidate for an easy and efficient electric-/strain-mediated control of the magnetic properties.

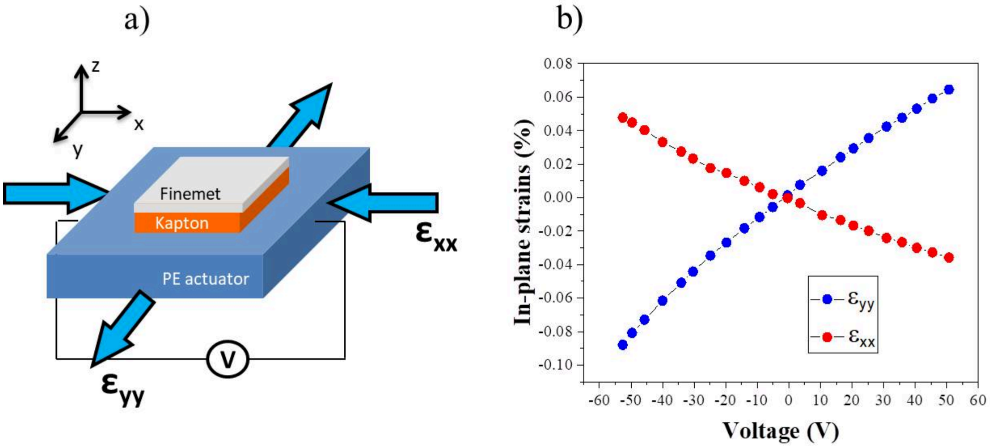

Figure 3.3: (a) Sketch of the studied heterostructure with the arrows qualitatively representing the in plane strains of the finemet film, (b) In-plane strain-induced in x and y direction by applying voltage from 0V to ±50V [80] [236]].

The detail of the fabrication process of our sample are reported in [236]. In this structure, the magnetic properties of finemet film can be controlled by applying a voltage to the PE actuator which induces a uniaxial strain/stress by converse piezoelectric effect. The PE actuator is a PZT commercially available with typical dimensions 1.8x0.7x0.7 cm^3. A voltage applied across the PZT actuator results in the deformation of the actuator which is then transfered to the thin film. The polyimide Kapton substrate allows to avoid the clamping effects of the magnetic film that can lead to low transmission of the strains from the actuator to the finemet film/substrate system. In fact, previous results from our group have already shown that a compliant polyimide substrate allows having a nearly 100% strain transmission in between the PE actuator and the finemet film [56] [236] [234]. Owing to the converse piezoelectric effect inherent in piezoelectric materials, a mechanical expansion (resp. contraction) is observable along the dominant elongation direction (along x-axis) when a positive (resp. negative) voltage is applied across it. In particular, a positive voltage results in an elongation with a related uniaxial strain ϵ_{xx}¿0 along x. Due to elasticity, this tensile strain is accompanied by compressive strains ϵ_{yy}, ϵ_{zz}¡0 along the orthogonal in-plane direction y and the orthogonal out-of-plane direction z. A quantitative characterization of the voltage dependence of the induced strain along the xx and yy directions at the surface of the finemet film, was performed using Digital Image Correlation (DIC) technique [80] [236] [234]. The voltage applied to PE actuator was varied from +50V to -50V. In this measurement, the reference image was taken at 0V after applying a voltage of +50V in order to avoid hysteresis effects due to the piezoelectric material. Homogeneous biaxial strains (ε_{xx} and ε_{yy}) were measured as a function of the applied voltage allowing a fully equivalence between the voltage and the strain values (see Figure 3.3). Note that the maximum (resp. minimum) value of 0.065 % (resp. -0.035%) for ε_{yy} (resp. ε_{xx}) are slightly lower that the value of -0.085% for ε_{yy} and 0.045% for ε_{xx} obtained at -50V. This behavior is due to the non-linear and hysteresis behavior of the piezoelectric actuator. However, it has been verified that no variations of these values are observed after several sweeps voltage of +50V to -50V. The sketch depicts in Figure 3.3(a) indicates a tensile stress in the film when a positive voltage is applied (when a negative voltage is applied, the film is compressively stressed). This ME heterostructure of finemet/Kapton/PE device has been reported to present a good ME coupling. Indeed, the in-plane magnetic anisotropy has been controlled by the strain-induced/voltage application (applied voltage from 0V to 100V), see Figure 3.4 [236].

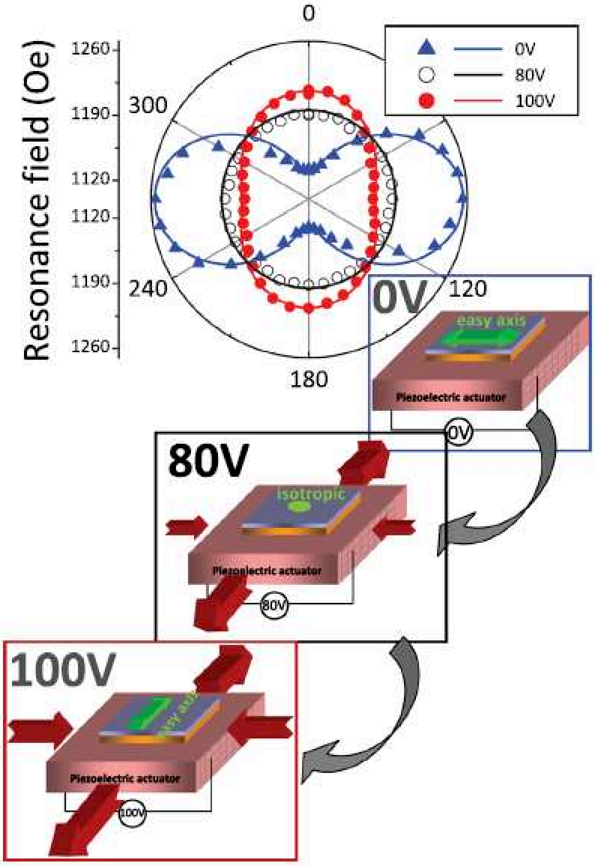

Figure 3.4: In-plane angular (i.e. angle between the magnetic field to the x-axis (easy axis)) dependence of the resonance field measured at 12 GHz for three different applied voltages: 0, 80, and 100 V. The sketches correspond to 3D view of the heterostructure showing the voltage-switch of the easy axis from x to y direction [236].

This easy axis manipulation together with all the results reported in [236] and also others, push us to get interested in the experimental observation of the local changing of the magnetic domain pattern typical of the finemet film. The orientation of the local magnetic domain moment by an applied electric field have been done by Magnetic Force Microscope (MFM) measurements. The results have been compared with the standard behavior of the magnetic pattern under the application of a magnetic field in order to demonstrate the efficiency of the ME coupling. Experimental details are reported in Chapter 2, section 2.1.2.

3.2 Magnetic background of the sample

In order to study the effect of the *in situ* strain/electric field (E-field) on the magnetic domain of finemet film, the magnetic background state of the sample was firstly investigated. Before doing the local MFM analysis of the magnetic domain pattern, a macroscopic measurement has been done via the VSM. The magnetic hysteresis loops of the finemet with the magnetic field applied parallel and perpendicular to the plane of the film are shown in Figure 3.5. An in-plane magnetic anisotropy is observed (see black curve). Moreover, the typical loop of a weak stripe domain pattern is observed and reported in the top inset [31] [214]. This loop shape suggests different stages in the reversal process of the magnetic domains: a quick nucleation followed by the domain propagation and a slow domain expansion and saturation. The behavior observed in the out-of-plane loop (see the red curve) is coherent with a behavior of the magnetization along the hard axis.

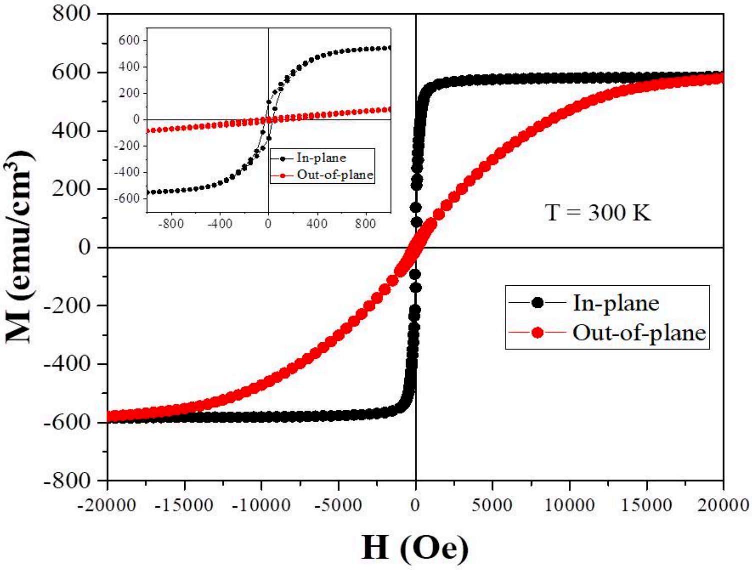

Figure 3.5: The magnetic hysteresis loop of the finemet with the field applied parallel and perpendicular to the plane of the film. The inset show the zoom-in of the in-plane and out-of-plane hysteresis loop.

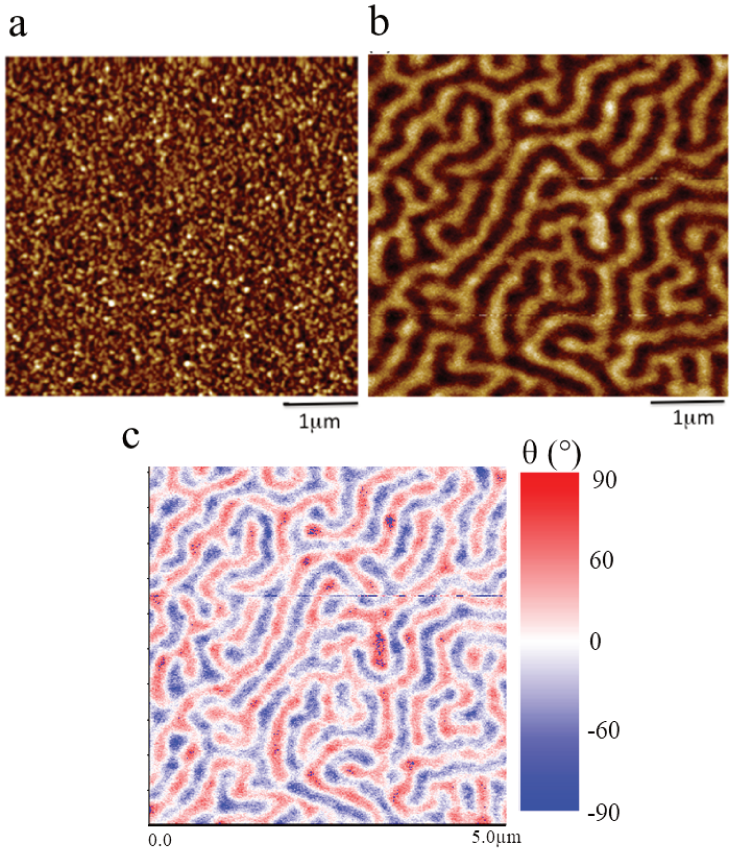

Figure 3.6: The magnetic state of finemet film at H = 0 Oe and E = 0 V; (a) Topography of the sample showing nanometric grains; (b) Magnetic background: typical magnetic stripe domain structures observed by MFM showing the contrast between opposite orientated moments; (c) The corresponding angle image showing the orientation of the magnetic domain ranged from -90°to +90°. Domain wall is clearly shown by the white line corresponding to the transition ($\theta \approx 0$) region between the domain "up" ($\theta = +90°$) and "down" ($\theta = -90°$).

The MFM images at the magnetic remanence (i.e. after the application of an in plane 1.8 Tesla magnetic field) of the Finemet film (H = 0 Oe and E = 0V) are shown in Figure 3.6(b) and clearly reveal the presence of the stripes domain pattern. This magnetic configuration is energetically favored if the following criteria are fulfilled: (1) the out-of-plane uniaxial anisotropy energy has to be lower than the demagnetizing one and (2) the thickness of the film has to be higher than a critical thickness $t_c = 2\pi\sqrt{A/K_{out}}$, where A is the exchange stiffness and K_{out} is the out-of-plane anisotropy constant of the finemet alloy (similar stripe configuration are stabilized also in other compounds, for details see the following references [41], [52], [80], [132], [225]). This is the case of our sample as it can be seen from the MFM results shown in Figure 3.6(b). Magnetic domain stripes form a very well-constructed pattern with the mean domain width of $0.2\mu m$. The opposite color of observed domain stripes represents two opposite orientations of the local magnetic domain. One is parallel to the magnetic moment of the probe (i.e., the MFM tip), and the other is anti-parallel to it [45]. This has been explained into details in section 2.1.2 of chapter 2.

The local orientation of the domain stripe is confirmed by the corresponding angle image in Figure 3.6(c). The angle θ range from +90 °(red, so called domain "up") to -90°(blue, so called domain "down") which are parallel and anti-parallel to the magnetic moment of the MFM tip, respectively. Comparing the domain stripes in Figure 3.6(b) and the domain orientations in Figure 3.6(c), we can verify that the white patterns in MFM image (see Figure 3.6(b)) correspond to the domain "up" and brown patterns correspond to the domain "down". In addition, the domain wall is also clearly presented by the white line between red and blue pattern in Figure 3.6(c).

3.3 Electric control of the magnetic domain stripes and local magnetic moment orientation

From the magnetic domain state at zero-field applied, we decided to study the effect of the E-field/strain-induced on the magnetic domain stripes and local magnetic moment orientation in this multiferroic heterostructure. The measurement of the in-plane strain value induced in the finemet film by varying the electric field applied to the PE actuator from +50 V to -50 V has been reported previously [80] [236] (see Figure 3.3b). Thanks to a quantitative characterization of the voltage dependence of the induced strain at the surface of the finemet film, we could translate the applied voltage/electric field directly into the strain value along the traction axis (yy) and perpendicular to it (xx). We report here the most representative MFM images obtained for several strain values of ε_{yy} and ε_{xx}, as shown in the inset of Figure 3.7(a)–(d).

For each voltage, we recorded both the AFM and the MFM images, in order to verify that any topographic artifact would take place and affect the MFM phase image analysis (see Figure 3.6(a) and (b)). We present the statistical analysis of the domain stripe width as function of the biaxial applied strain in Figure 3.7(a)-(d). In order to be representative of the sample, we analyzed different areas of $5 \times 5 \mu m^2$ on the surface of the sample for each voltage/strain condition. For each MFM images in Figure 3.7 and also for those reported in [80], we could measure the magnetic domain "up" and "down" widths as a function of the local biaxial strain transmitted from the PE material to the magnetostrictive finemet layer.

We measured this behavior for both the increasing value of the strain (positive and negative directions) and the decreasing one. [Arrows in Figure 3.7(a)–(d) indicate the direction.] Black/red full circles in Figure 3.7(a)–(d) represent the magnetic domain behavior as a function of the increasing voltage (positive (from 0V to +50V) and negative directions (from 0V to -50V)) and open circles represent the decreasing ones (from ±50V back to 0V). This analysis clearly shows that for a small strain value ($\varepsilon_{yy} = 0.04\%$ and $\varepsilon_{xx} = 0.023$ %), the magnetic stripe pattern is fully destroyed (domain width = 0 nm)

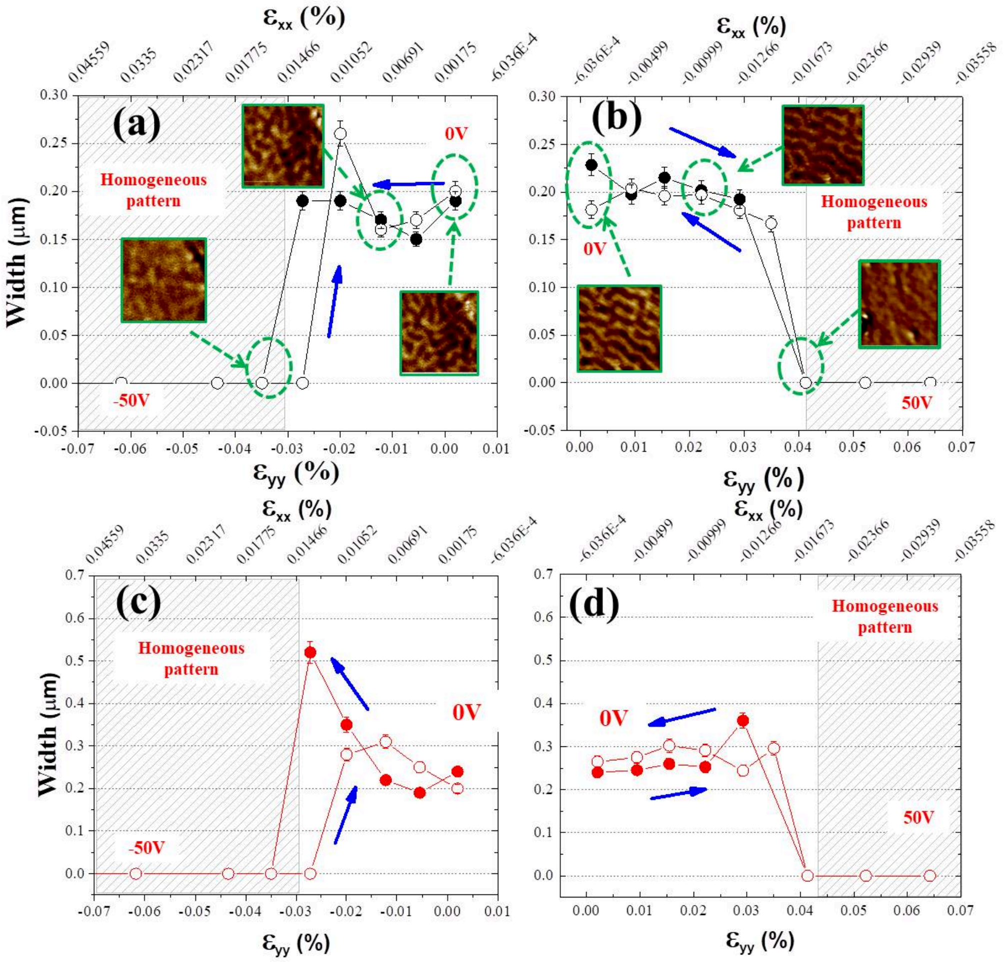

Figure 3.7: (a) and (b) Magnetic domain width of the up-oriented domains (white patterns) as a function of the biaxial applied strain of the PE actuator (ε_{xx} and ε_{yy}). Black full circles represent the magnetic domain behavior as a function of the increasing strain (positive and negative directions) and open circles the decreasing ones. (c) and (d) Magnetic domain width of the down-oriented domains (brown patterns) as a function of the biaxial applied strain of the PE sensor (ε_{xx} and ε_{yy}). The red full circles represent the magnetic domain behavior as a function of the increasing strain (positive and negative directions) and open circles the decreasing ones.

and gives place to a magnetic homogeneous MFM phase image [see inset of Figure 3.7(a) and (b)]. In the absence of the magnetic contrast, the MFM images suggest a mono-domain structure having the magnetization component aligned in the plane of the film [45]. Figure 3.7(a)–(d) shows that the mechanism of switching the magnetization of the magnetic stripe domains toward the in-plane direction is a completely reversible process when considering the mean width of the domain (follow the arrows for the direction of the strain variation) and also symmetric respect to zero. Indeed, increasing the *in situ* elongation/compression applied to the finemet film during the MFM measurements gives place to a similar magnetic pattern behavior. Similar critical electric field/strain value are obtained for both elongation/compression deformation (i.e., black/red full circles superpose with black/red open circles in Figure 3.7(a)–(d)).

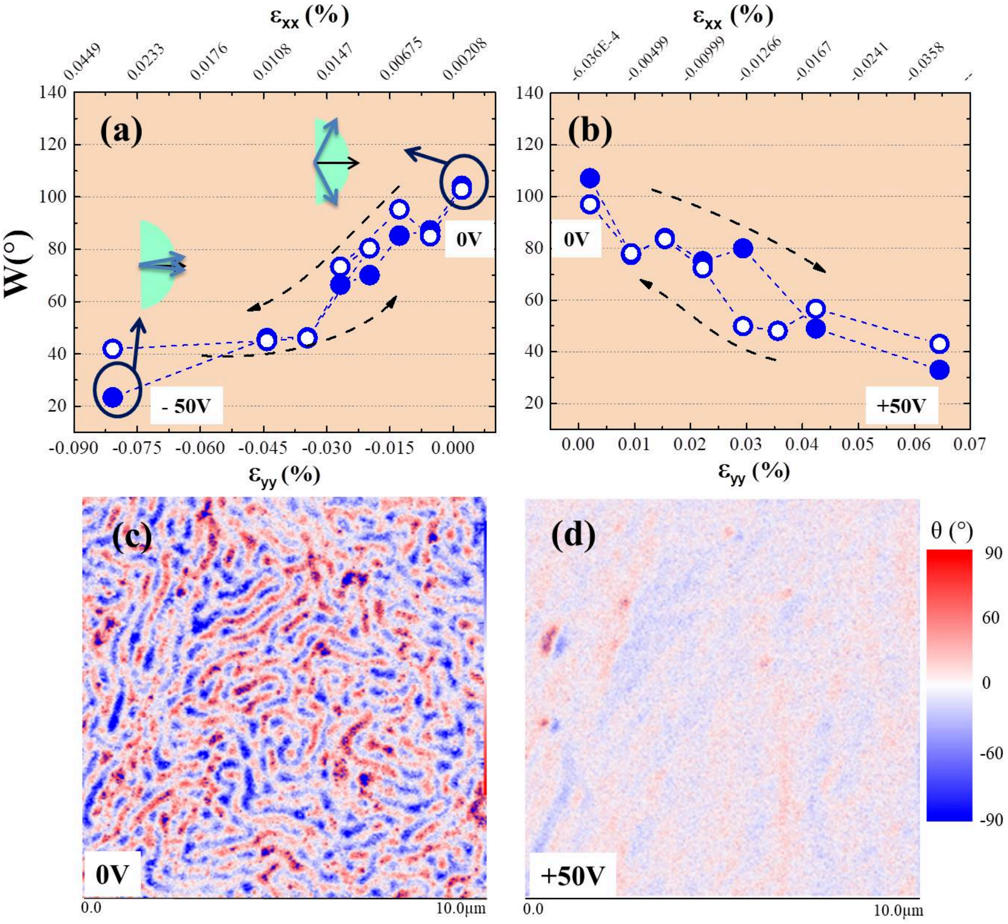

Figure 3.8: Width of distribution, **W**, as a function of the biaxial applied strain by the PE actuator (ε_{xx} and ε_{yy}): (a) from 0V to -50V and (b) from 0V to +50V. Blue full circles represent the increasing voltage (positive and negative directions) and open circles the decreasing ones; (c) The angle image at U = 0V; (d) The angle image at U = +50V.

In order to confirm the switching of the magnetic domains (”up” and ”down”) from the out-of plane to the in-plane direction of the film, we investigated the orientation of the magnetic moments by using the angle model reported in chapter II, section 2.1.2 [177]. The results are shown in Figure 3.8 and Figure 3.9 (more angle images are reported in Appendix A). As can be seen from the Figure 3.8(a) and (b), the **W** of the angle distribution (as well as the angle θ) decreases gradually toward to the increase of the induced strain ε_{yy} and ε_{xx} (i.e. as function of the applied voltages) in both positive and negative direction, see the blue full circle in Figure 3.8. This behavior clearly indicates that the majority of the magnetic moment rotates from the out-of plane direction (**W** around 110°) to the in-plane one (**W** is around 20°to 40°) of the film (see the angle image

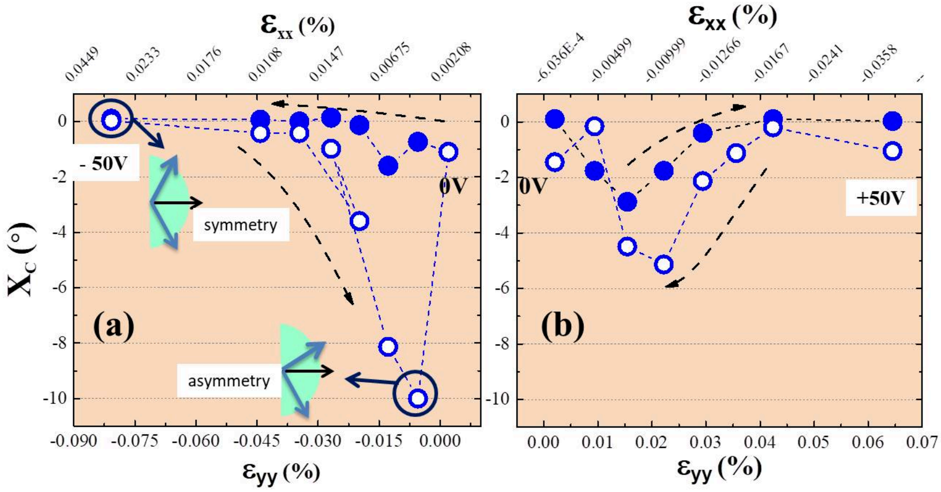

Figure 3.9: Center **Xc** of the angle distribution as a function of the biaxial applied strain by the PE actuator (ε_{xx} and ε_{yy}): (a) from 0V to -50V and (b) from 0V to +50V. Blue full circles represent the increasing voltage (positive and negative directions) and open circles the decreasing ones.

in Figure 3.8(c), (d) and inset sketches in Figure 3.8a). Moreover, the rotation of the magnetic moments is a reversible process as indicated by the backward curves obtained by decreasing the strain values (see the blue open circle). Indeed, when the induced strain/voltage decreases after the domain stripes destabilization, the **W** increases back to the out-of plane orientation. These results agree with the switching of the magnetic domain stripe width discussed in the previous paragraph. In addition, looking on the critical strain/voltage value inducing the domain stripes disappearance, the **W** value at the critical strain is around 50°(corresponding to a common $\theta \approx 25°$). It means that, although the domain patterns are destroyed, they still have a small components out-of-the plane that our MFM sensitivity is not able to detect.

Considering the symmetry of the angle distribution, X_C, presented in Figure 3.9, we can notice that a small asymmetry of distribution appears as the X_C shift to a negative value when a critical strain/voltage is applied, especially during the backward processes (from ±50V back to 0V). This result can be explained by the elongation and the compression of the film which is not expected to be homogeneous at the nanoscale level.

These results discussed above shade light on the electric field local control of the magnetic domain magnetization. They show that, thanks to a good ME coupling [80] [236] [237] between the PE actuator and the magnetostrictive finemet thin film, we are able to control not only the in-plane magnetic anisotropy of the film [236], but also to reverse the local magnetization of the nanometric domain from the out-of-plane direction to the in-plane one. The electric field control of this switching mechanism is highly reversible and opens the way for a local control of the magnetic information in magnetoelectric devices.

3.4 Magnetic control of the magnetic domain stripes and the local magnetic moment orientation

In order to compare the strain-induced/voltage control of the local magnetic domain orientation to the standard reversal mechanism induced by applying an external magnetic field, we performed MFM measurements under an *in situ* magnetic field application. In this case, the electric field is kept at zero (i.e., zero voltage applied to the PE actuator) while the magnetic field is applied in the plane of the film. The *in situ* magnetic field is applied thanks to the use of a costumed-AFM electromagnet (BOUHNIK SAS, Villacoublay, France). Technical details are reported in section 2.1.2 of Chapter 2.

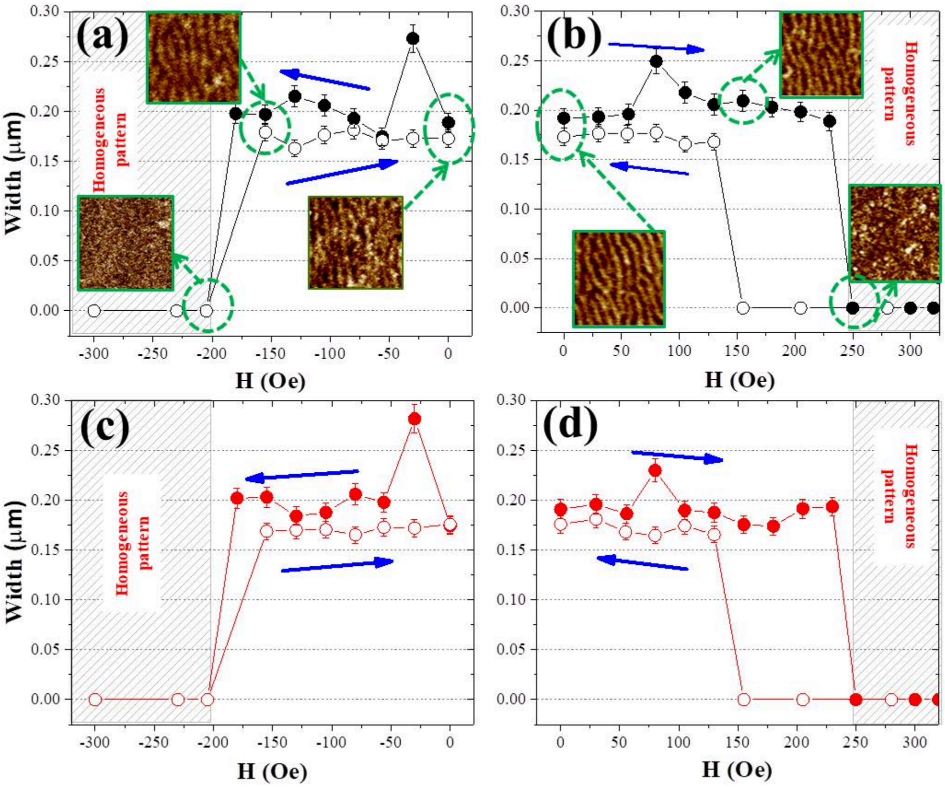

Figure 3.10: Magnetic domain width of two opposite oriented domains: (a), (b) up-oriented domains; and (c), (d) down-oriented domains as a function of the applied magnetic field in the in-plane direction of the film. The black/red full circles represent the width dependence for the increasing magnetic field values (positive and negative) and the black/red open circles represent the width tendency as a function of the decreasing magnetic field applied (see the sense of the blue arrows).

Figure 3.10(a)–(d) shows the magnetic domain width analysis of the MFM images (see inset of Figure 3.10) performed as described in the previous paragraph. Increasing the in-plane magnetic field value destroys the magnetic stripe domain pattern. The critical magnetic field values necessary for obtaining the homogeneous MFM images are of the same order of the critical fields observed in the magnetostatic measurements ($H_{saturation} = 400Oe$) and able to reverse the magnetization (see Figure 3.5). This suggests that once we destroyed the magnetic contrast of the stripe domains, the finemet film has a macroscopic magnetic moment mainly oriented in the plane of the film and parallel to the magnetic field applied. Thus, the process observed here is, without any doubt, connected to the switch of the magnetic local moment from the initially out-of-plane orientation toward the in-plane field direction. The result of this mechanism allows the observation of MFM images very similar to the one observed in the previous paragraph (see inset in Figures 3.7 and 3.10). This corroborate our hypothesis on the strain-mediated switching of the magnetic domain orientation developed above. Nevertheless, it is important to notice that the magnetic field dependence of the width does not present the same characteristics observed for the electric field width dependence. In Figure 3.10(a)-(d), the width behavior of the magnetic stripe domains is clearly not reversible and also non-symmetrical around the remanence state (H = 0 Oe). The difference between the widths of the domain between the increasing magnetic field dependence (positive and negative) and the decreasing one varies between 30 nm and 130 nm depending on the absolute value of the magnetic field applied. When the film is thus brought back to the remanence state by decreasing the magnetic field from the saturation state, the magnetic pattern is not necessary the same. Statistically, the stripes have not the same width before and after the application of the magnetic field [see Figure 3.10(a)-(d)]. Also the magnetic pattern is completely destabilized at different critical field values in the case of the positive quadrant (230 Oe) compared to the negative one (-175 Oe). The observed non-reversibility is a major problem for the application of this system in standard magnetic sensor and/or magnetic recording devices using the magnetic field to detect and record the informations.

A peculiar feature observed in Figure 3.10(a)-(d) at a magnetic field of 80 Oe [positive field, Figure 3.10(b) and (d)] and -25 Oe [negative field, Figure 3.10(a) and (c)] is the stabilization of a larger width of the magnetic domain compared to the remanent configuration. This behavior can be explain by the evolution and stabilization of the stripe-domain patterns under the in-plane applied magnetic field. Indeed, the magnetic domain patterns start to rotate toward the direction of the magnetic field when the field is applied. As the magnetic field increases, all the magnetic domains tend to align along the direction of the field, thereafter the stabilized state is reached for larger domain size. If the applied field continues increasing, the magnetic moment starts to turn from the out-of-plane toward the in-plane direction of the film. These processes were already described in literatures [35] [70]. The way back to the remanence from the saturation magnetization state does not present this effect. Besides, this has not been observed under the application of the electric field and put in evidence a different mechanism of the local control of the magnetic moment at low magnetic and/or low electric field (strain).

Similarly to the previous section (section 3.3), we analyzed the orientation of the local magnetic moment by obtaining the relative angle images. The results are presented in Figure 3.11 and 3.12 (more angle images are reported in Appendix A).

The Figure 3.11(a) shows the **W** characteristic of the angle distribution as a function of

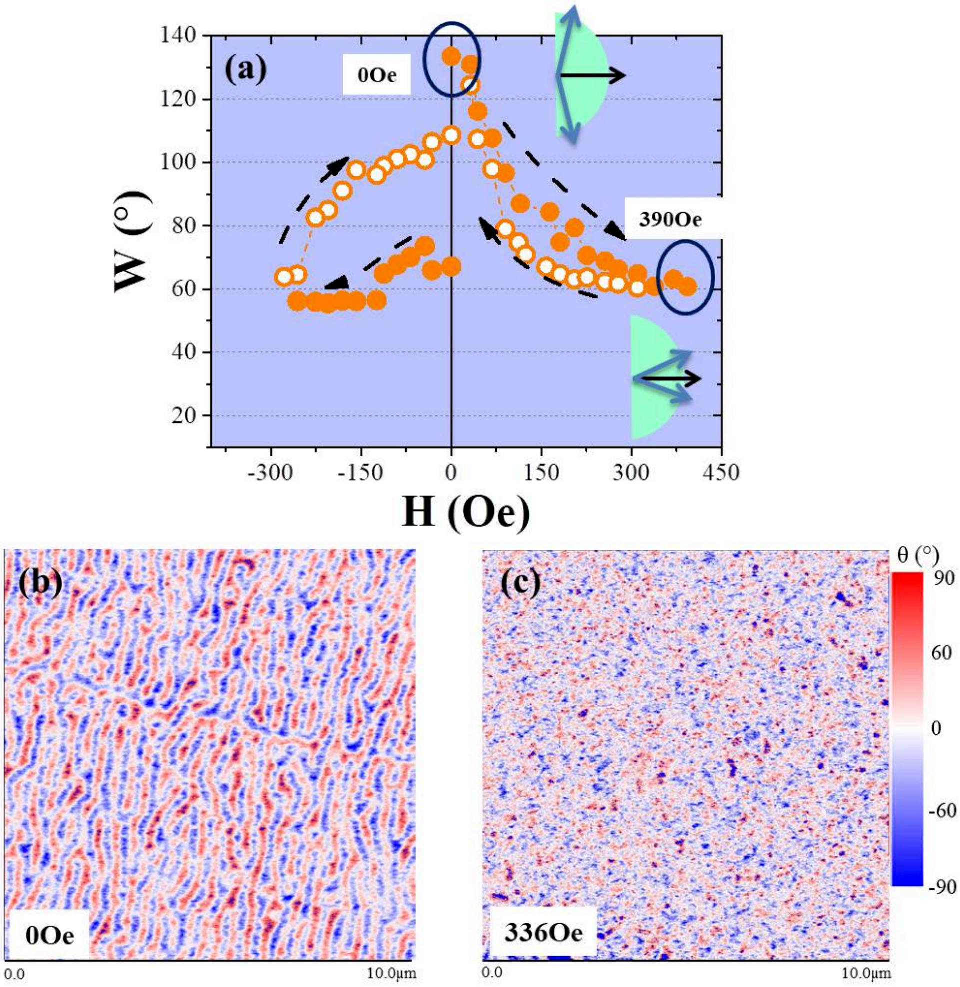

Figure 3.11: (a) Local magnetic moment orientation under the variation of the in-plane magnetic field. The orange full circle represent the behavior under an increasing external magnetic field (positive and negative direction) and the orange open circle represent the decreasing ones (see the sense of the black arrows). Insets: sketches of the orientation of magnetic moments (blue arrows) compared to the plane of the film (black arrow); (b) The angle image at H = 0 Oe; (c) The angle image at H = 336 Oe. The contribution of the granular topography is visible due to the very small magnetic contribution of the phase image.

the applied magnetic field. Considering the positive direction of the applied magnetic field, as expected, **W** decreases rapidly toward to the increase of the in-plane applied magnetic field. In other words, the magnetic moments rotate from the out-of-plane orientation toward the direction of the external magnetic field (in-plane), see Figure 3.11(b) and (c). After the critical applied magnetic field which destroys the domain stripe, the **W** value is in the range of 60°-70°(so the θ is in the range of [30°to 35°]). This is much higher than the value obtained during the E-control of the magnetic moment orientation. This

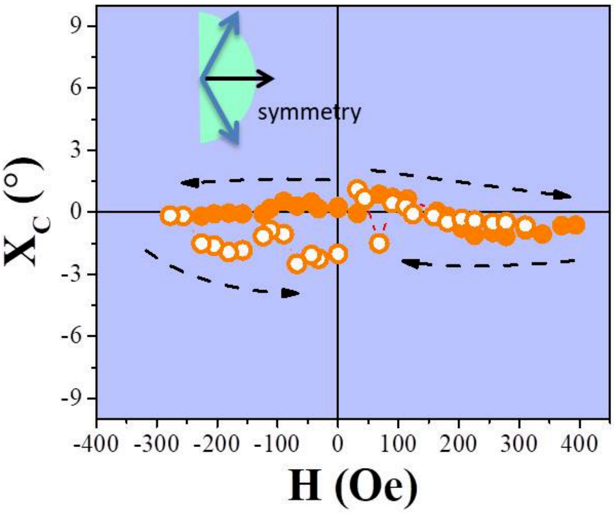

Figure 3.12: The center of the angle distribution, X_C, between the domain ”up” and the domain ”down” as function of the applied magnetic field.

result shows that the E-control of the magnetic moment orientations is more efficient than the H-control. In addition, again, although the domain stripes are destroyed, the local magnetic moments are not completely oriented to the in-plane of the film. In the case of positive applied magnetic field, the H-control of the magnetic moment orientation is reversible. However, it is not the case of the negative field applied. Indeed, the **W**(H) curves as function of the increasing (full circle) and decreasing (open circle) magnetic field application are different (see Figure 3.11). From this results we can conclude that, the H-control of the magnetic domain orientations is not reversible and strongly depends on the magnetic hysteresis of the sample as well as of the magnetic initial configuration.

The symmetry of the angle distribution between the domain ”up” and ”down” (X_C) is presented in Figure 3.12. The X_C in both positive and negative applied magnetic field is located around zero. This means that the orientation of the magnetic moments ”up” and ”down” are symmetrical to the plane of the film all along the magnetic field application.

3.5 Conclusion

To conclude, we reported here the detailed analysis of the characteristic stripe magnetic domain pattern and the local magnetic moment orientation of a soft magnetic finemet alloy thin film under the application of an in-plane electric field/strain applied. We compared the results of this analysis with the magnetic domain pattern behavior and moment orientation under an in-plane magnetic field. In both cases, the external field is applied *in situ* during the MFM measurements (see details in section 2.1.2 of chapter 2). The analysis of the magnetic MFM images is reported in details and mainly presented by the magnetic domain width behavior and the angle θ one under the application of an external force. θ is the angle between the local magnetic moment and the plane of the film. Our results show that both the E and H external fields allow the destabilization of the magnetic domain pattern in favor of an homogeneous magnetic configuration. When the critical field applied is higher than a critical value (ε_C, E_C, and H_C), the MFM image is contrast less and presents an homogeneous phase image. The comparison between the effects observed under the application of a magnetic field with the ones observed under the electric field, let us deducing that both the external stimulus allow the twisting of the domain magnetizations. Relatively low fields are able to turn the magnetic domain moments from the out-of-plane direction to the in-plane one. In order to confirm these results, we deduced the angle images from the MFM images and did the statistic analysis of the angle θ in both strain-induced/E-control and H-control cases. The results confirm that the angle θ (presented through $\mathbf{W}$ width distribution) decreases gradually toward to the external field orientation. Our results also clearly state that the strain-induced/E-control is more efficient and reversible compare to H-control method. A small in-plane strain can destroy the magnetic pattern and can bring it up in a reversible way. The same conclusions are possible for the angle distribution. This is not the case when an in-plane magnetic field is applied to the magnetic pattern. Our results reinforce the idea that ME heterostructure can open the way for new devices allowing the electric control of the magnetic information at the nanoscale level.

Chapter 4

0-3 type ME particulate nanocomposites based on PVDF

4.1 Introduction

In this chapter, I will present our studies on the ME particulate nanocomposite with 0-3 type interface. In this nanocomposite, the magnetic nanoparticles are included in a polymer matrix. The number "0" and "3" denotes respectively the connectivity of the nanoparticles phase (also called nano-fillers - NFs) and the one of the polymer matrix. As discussed in the section 1.3.2, the polymer-based ME composite show several advantages: flexible, lightweight, low cost and not brittle, overcoming the typical drawbacks of ceramic ME composite. In addition, polymer based ME composites can provide colossal ME response due to a large piezoelectric stress coefficient and a great displacement transfer capability linked to the polymer mechanical properties [103] [109] [215].

Among organic piezoelectric materials, polyvinylidene fluoride (PVDF) polymer has been largely studied as it presents a good piezoelectric coefficient than that observed in any other polymer, and also excellent mechanical flexibility. It shows large piezoelectric coefficient with the d_{33} in the best case found to be around -30 pC/N and in the worst cases around $-6/-7$ pC/N [58]. Thus it is a good candidate for developing flexible multifunctional composites for the electric control of the magnetic properties. As a common agreement in literature (see section 1.3.2), nano-fillers (NFs) favor the crystallization of the polar phase of the PVDF [102], which in principle may increase the piezoelectric macroscopic response. The efficiency of this latter as well as the mechanical properties of the (PVDF/NFs) particulate nanocomposite should also be related to the uniform dispersion of the nano-fillers [29] [140] [223].

As a matter of fact, there are several studies in literature focusing on the influence of the mechanical properties upon the dielectric and piezoelectric macroscopic behavior of the PVDF and hybrid PVDF films, while only few reports are available on their local piezoelectric properties [195] . Besides, the effect of the magnetic inclusions and their dispersion (i.e. functionalization) on the electro-active local response of the polymer based ME composite, has not received attention so far, even more in the case of very thin films (less than 100 nm). In addition, the influence of elastic properties of PVDF matrix on the magnetic properties of magnetostrictive nano-fillers have not been studied.

In order to fulfill these lack, we have therefore investigated in this chapter two factors that influence the piezoelectric/magnetic response of PVDF/NFs hybrid films: (i) The effect of NFs on the electro-active phase and the local piezoelectric intrinsic response of non-poled PVDF/NFs hybrid thin film; (ii) The influence of the elastic properties of the PVDF matrix on the magnetic properties of the NFs. These effects have been studied in two types of structure: PVDF/NFs hybrid thin film (< 100 nm) deposited on Si substrate and PVDF/NFs hybrid self-standing films. Pure PVDF samples in both cases (thin films and self-standing ones) are studied for comparison.

4.2 Samples

4.2.1 Samples

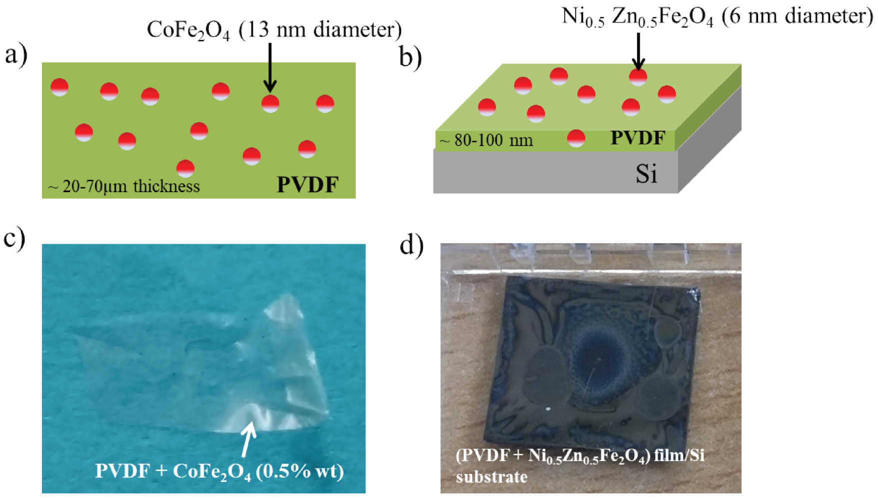

Figure 4.1: Sketches and photos of studied samples: (a) and (c) Hybrid self-standing sample; (b) and (d) Hybrid thin film on Si substrate.

As shown in Figure 4.1, we studied in this chapter the following samples:

- Hybrid thin film of PVDF/ $Ni_{0.5}Zn_{0.5}Fe_2O_4$ (NZFO) nanoparticles deposited on a silicon substrate [1]
- Hybrid self-standing film of PVDF/ $CoFe_2O_4$ nanoparticles [2]

The detail of fabrication processes are reported elsewhere [87], [140], [144].

---

[1] Fabricated by Ngoc Anh Nguyen (USTH Master 2 student, internship at LSPM)

[2] Synthesized by Dr.Chirine Ben Osman (Post Doctorate researcher at ITODYS, Universite Paris Diderot).

The neat-PVDF and hybrid thin film of PVDF/ NZFO nanoparticles were deposited by spin coating on conductive substrates in order to perform the electromechanical characterization. Very flat neat-PVDF films with mean roughness between 3 to 11 nm and homogeneous microstructures were obtained after an optimization of the spin coating process and the elaboration parameters. In order to control the dispersion of the nanoparticles inside the PVDF matrix, we used 2 categories of nanoparticles: the functionalized and non-functionalized one. The NZFO nanoparticles used to elaborate our hybrid thin film were synthesized by using a soft chemistry polyol route [5] [64]. In order to avoid as much as possible their agglomeration and to promote their dispersion in the PVDF matrix, we functionalized them with specific molecules. The procedure for the functionalization of the nanoparticles has been done on the basis of the process reported previously [94] [110]. Very flat films have been obtained also in this case, with mean roughness between 5 and 10 nm and homogeneous microstructures. All the studied films present a mean thickness between 80 and 100 nm and they were not poled in order to study the intrinsic electro-active properties of the as-grown polymer. In the case of the hybrid films, the nanoparticles content was kept of 0.5% in weight (wt) both for the functionalized and non-functionalized cases.

The hybrid self-standing films of PVDF/CFO were fabricated by depositing the PVDF/CFO solution on a glass substrate using doctor blade technique [140]. The films's thickness are controlled in between 20 and 70 μm by a casting knife from Elcometer. The CFO nanoparticles used to elaborate these hybrid films were synthesized again by a polyol process [4] [140]. Similarly to the hybrid thin films described above, we studied the functionalized and non-functionalized nanoparticles inside the PVDF matrix in order to analyze the effect of the dispersion/agglomeration. The nanoparticles content has been variated from 0.5% wt to 1% wt and 5% wt for both the functionalized and non-functionalized cases. The hybrid self-standing films with higher nanoparticles content in weight then the one used here have been investigated and reported elsewhere [144]. In this thesis, I will study the magnetic response of nanoparticles under the influence of the elastic properties of the PVDF matrix.

First of all, the properties of the single phases (PVDF and nanoparticles) are presented in the section below. They will be of great importance to detect the influence of one phase on the other.

4.2.2 Single ferroic phase: Piezoelectric and ferromagnetic one

The PVDF polymer

PVDF shows a complex structure and exhibits five crystalline phases related to different chain conformations: β, α, γ, δ and ε phases [97] [169]. The most investigated and common one are α, β and γ (see Figure 4.2).

The α phase is non-polar and non piezoelectric and is the most commonly obtained during elaboration [16], whereas the remaining phases are polar. Especially, the β phase possesses the largest spontaneous polarization among all the others and is responsible for the best ferroelectric and thus piezoelectric properties [55]. This is due to its orthorhombic

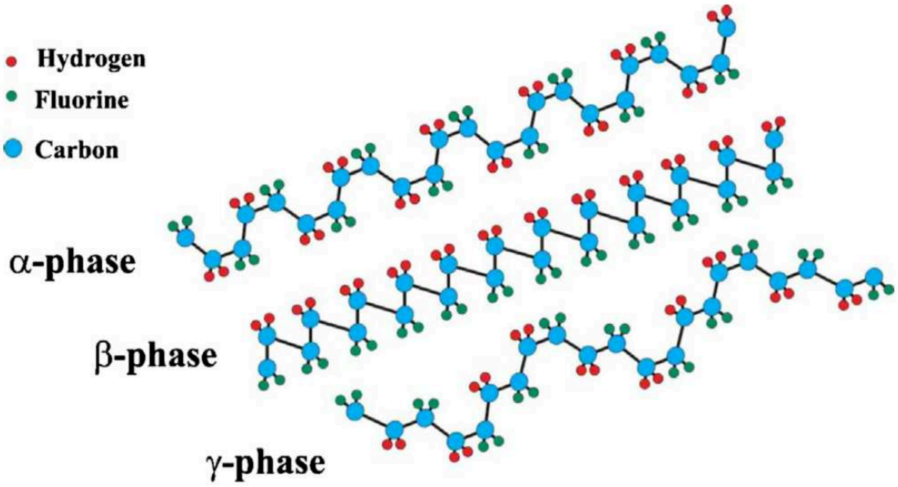

Figure 4.2: Schematic representation of the chain conformation for the α, β and γ phases of PVDF [104].

structure in which all fluoride atoms (F) are in the same plane according to the carbon (C) backbone as shown in Figure 4.2. This configuration allows a high polarity. In addition, when these dipolar moments are parallel, they can contribute together to form a macroscopic dipolar moment, enhancing the spontaneous polarization. Therefore, the improvement of β phase content in a PVDF-based structure is highly recommended for ferroelectric applications.

The ferrite nanoparticles (NPs)

Two types of magnetostrictive nanoparticles (NPs) have been chosen: $CoFe_2O_4$ and $Ni_{0.5}Zn_{0.5}Fe_2O_4$.

NPs can present superparamagnetic (SP) behavior when they have a diameter lower that a critical size (going from few nanometers to a couple of tenth of nanometer), see Figure 4.3. In this cases, the single domain particle, can randomly flip direction due to the thermal energy. The typical time between two flips is called the relaxation time. In the absence of an external magnetic field, when the time used to measure the magnetization of the SP-NPs is much longer than their relaxation time, magnetization appears to be (on average) zero. When the measurement time equals the relaxation time the NPs appeared to be in their ferro-/ferrimagnetic state. If the measurement time is not change, and the magnetization is measured as a function of temperature, the temperature of the transition from the superparamagnetic state to ferro-/ferrimagnetic one is called the blocking temperature, T_B. Thus, above T_B, the NPs are superparamagnetics while under T_B, they are ferro-/ferrimagnetics. Note that, a superparamagnetic NPs can also be magnetized by a magnetic field as a paramagnetic particles (i.e. their hysteresis loop shows a $H_C = 0$ and $M_r = 0$). However, the magnetic magnetization of these NPs is much larger than that of the paramagnetic material when a magnetic field is applied.

$CoFe_2O_4$ (CFO) nanoparticles are well-known to be ferrimagnetic and magnetostrictive

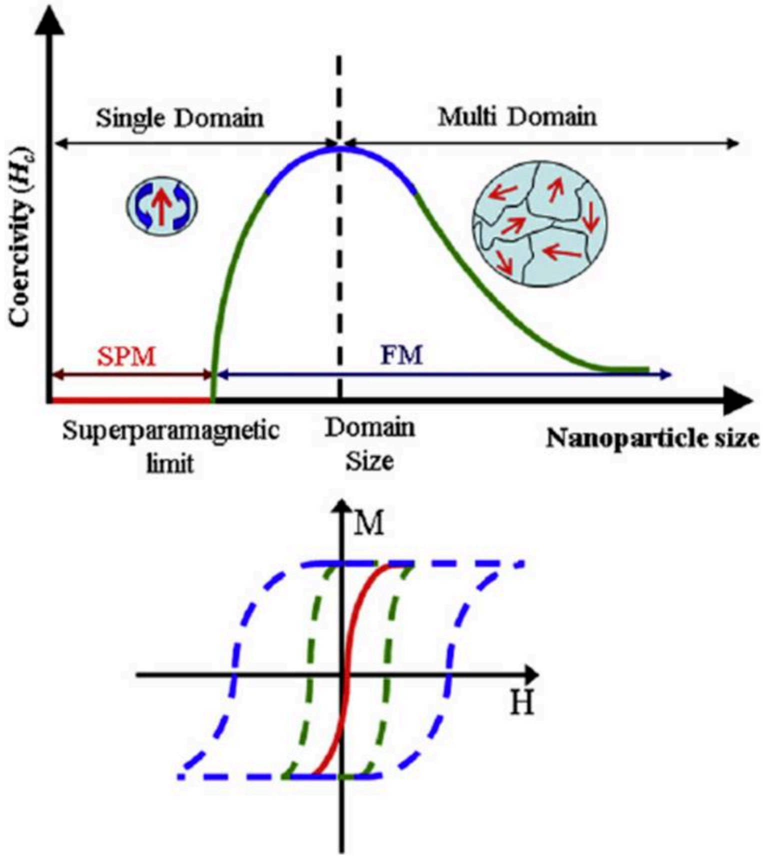

Figure 4.3: (Dependence of magnetic coercive field on the size of nanoparticles (top) and their corresponding hysteresis loops (bottom) [116].

NPs. The magnetostrictive coefficient (λ) has been reported from -1.11×10^{-4} to -2×10^{-4} at room temperature [33] [138] [219]. They exhibit high Curie temperature range from 300K to 870K [49]. Blocking temperature has been observed from 250 K to 315 K [9] [100]. The magnetic properties of CFO nanoparticles (diameter 13 nm) used to elaborate our hybrid films are shown in Figure 4.4 and Table 4.1.

Temperature (K)	H_C (Oe)	M_r (emu/g)	M_S (emu/g)
300	287	19	157
200	1976	57	172
100	8138	122	181
5	14581	149	184

Table 4.1: Magnetic properties of CFO nanoparticles powder at different temperature.

$Ni_{0.5}Zn_{0.5}Fe_2O_4$ (NZFO) nanoparticles are also ferrimagnetic with a good magnetostriction properties. The magnetostrictive coefficient have been reported of -2.1×10^{-5} [129]. NZFO NPs show a high Curie temperature around 523K and the blocking temperature has been reported to be 50 K [32] [124]. In this case the NPs have a diameter of

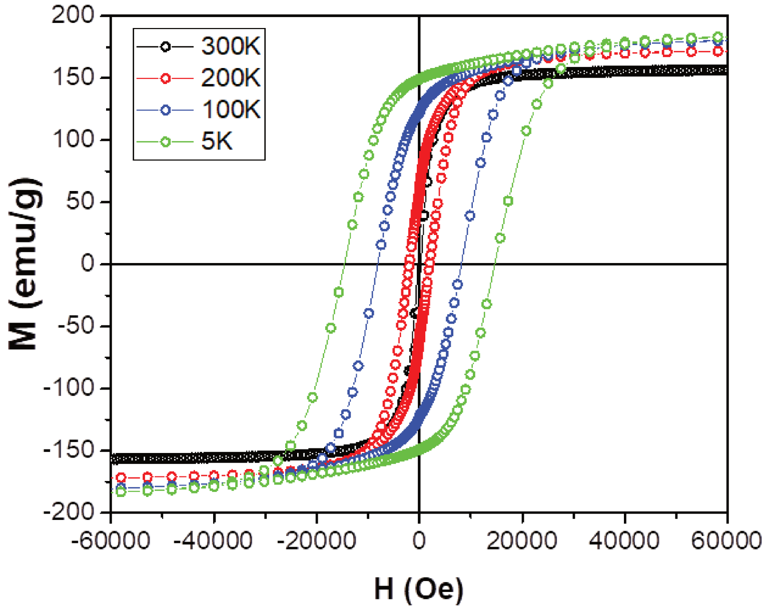

Figure 4.4: Magnetization curve of CFO nanoparticles at different temperatures.

5-6 nm.

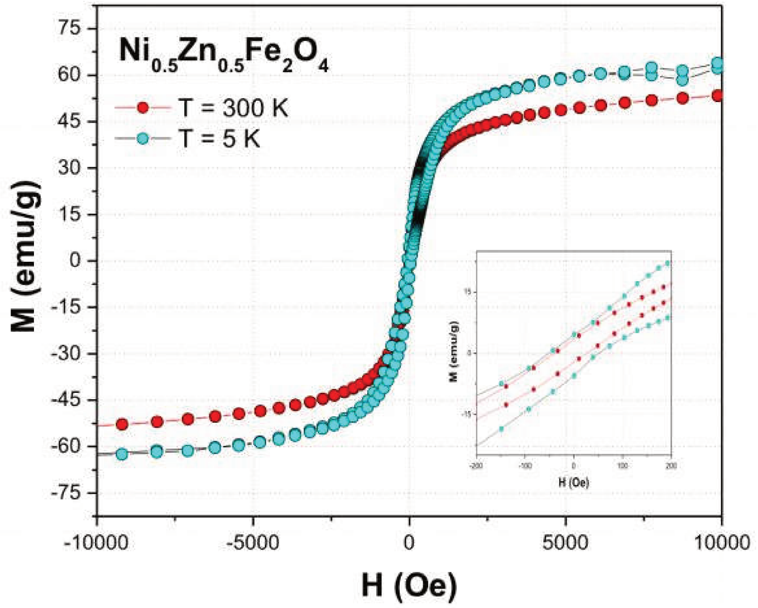

Figure 4.5: Magnetization curve of $Ni_{0.5}Zn_{0.5}Fe_2O_4$ NPs at different temperatures.

Figure 4.4 and Figure 4.5 show that the saturation magnetization as well as the critical fields and temperature for both CFO and NZFO NPs, confirm the literature results for high quality ferrite NPs.

4.3 Influence of the hybrid interface on the electro-active phase and electromechanical response of PVDF/NZFO hybrid thin film

The idea of mixing piezoelectric polymers with magnetostrictive dopants can open pathways for engineering flexible composites that exhibit combination of electrical, magnetic and mechanical characteristics. The main aim is relaying on the electro-active properties of the polymer emphasizing the local deformation by applying an electric field. This will allow to efficiently stress the magnetostrictive phase and thus to control the ferromagnetic orientation of the nano-fillers for new magnetic sensor applications (see section 1.3.2 in chapter 1). Unfortunately, several parameters can influence the artificial coupling between the ferroelectric/matrix and the magnetostrictive/nano-fillers in these hybrid systems: the good crystalline phase, the shape and the size of the nano-fillers, the weight content of these latter, the quality and distribution of the interfacial interactions between the two coupled materials. It is important thus to underline that if on one hand several studies in literature have already demonstrated that the embedded matrix rarely destroys the quality of the magnetic properties of the nano-fillers mostly dominated by the dipolar interactions; on the contrary the presence of the nano-fillers can induce some drawbacks on the elastic and piezoelectric properties of the matrix. In this frame we address the problem of the hybrid interface effect on the electro-mechanical local response of the β-PVDF-based composite thin films in order to insure the efficiency of the local deformation on the magnetic nano-fillers. In this aim, we compared the electromechanical response of the hybrid film with functionalized and not functionalized nanoparticles to the one of the neat PVDF films presenting similar characteristics. Keeping in mind the needs in microelectronic applications, we focus our studies on very thin (mean thickness about 100 nm), smooth PVDF and hybrid PVDF films (mean roughness about 10 nm), containing the smallest possible percentage of inorganic nanoparticles in order not to destroy the elastic properties of the polymer and to optimize at the same time the electro-active phase content. All the necessary characterization (RX, IR, AFM, PFM and profilometer) has been performed in order to shade light on the connection between the elaboration process variables and the structural and physical properties of the films. The technical informations of these measurements are presented in chapter 2.

4.3.1 Influence of hybrid interface on the microstructure and β-phase content of PVDF/NZFO hybrid thin films

Adding nano-fillers into the PVDF matrix comes basically from the idea that the nano-objects can promote the nucleation of the electro-active β phase. The enhancement of the β phase by using nano-fillers depends on two factors: the types of nano-fillers and their surface charges [25] [106]. The interaction between the electric charged surface of the nano-fillers and the bonds of PVDF chains has already been proposed as a key factor for increasing the nucleation of the β phase of the polymer [231]. Indeed, the presence of nano-fillers in a PVDF polymer matrix directly affects the charge distribution in the PVDF (i.e. its ferroelectric polarization) and strongly depends on the size, shape and weight content of the nano-fillers via the interaction between the local electric field around the nano-fillers and the PVDF dipoles at the hybrid interface [197]. Remarkably, when hydrophilic molecules functionalize the surface of the nano-fillers, a uniform dispersion of the nano-fillers is obtained. These hydrophilic parts interact with the carbon-fluorine polar bonds in PVDF matrix through the hydrogen bonding and all dipoles along the molecular chains of the polymer can align. Consequently, the β-phase content is enhanced [7], [102] as well as the polymer structure.

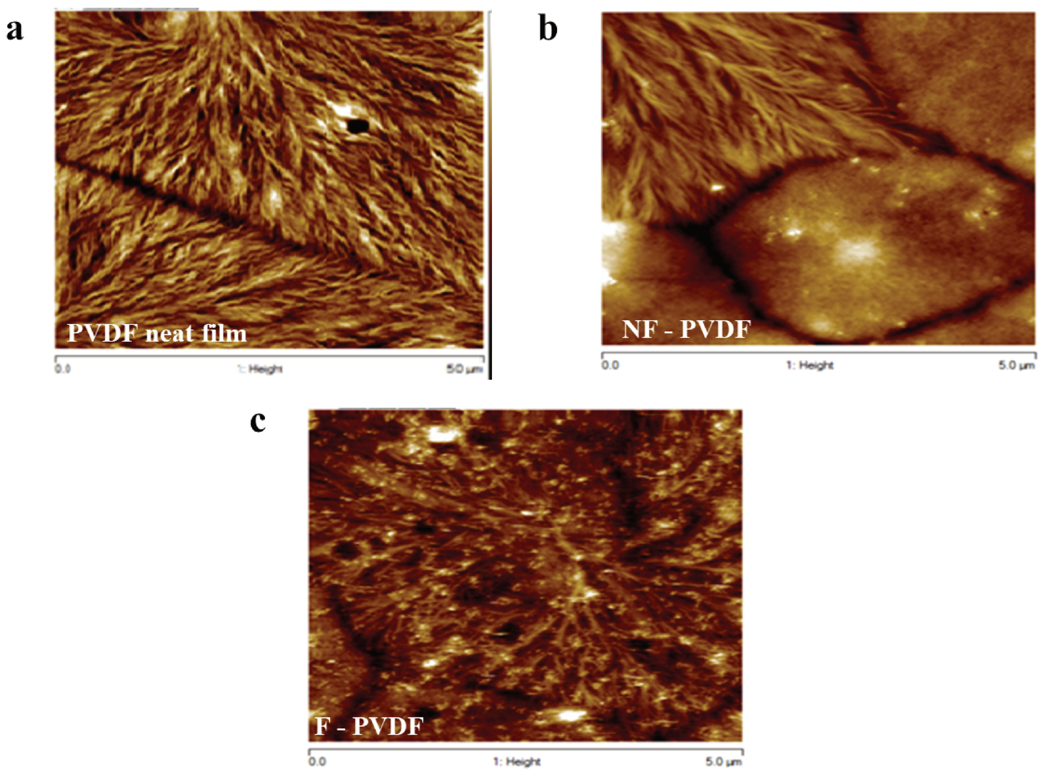

Figure 4.6: AFM images of: (a) PVDF neat film, (b) Non-functionalized NPs embedded in the PVDF film (NF-PVDF), (c) Functionalized NPs embedded in the PVDF film (F-PVDF).

Previous work has already demonstrated that the interaction between the negatively charged surface of the $NiFe_2O_4$ -NPs and the positively charged polymer CH_2 groups, promotes nucleation of the β-phase in the PVDF [102] [110] (see chapter 1, section 1.3.2, Figure 1.15). In order not to destroy the mechanical properties of the PVDF, we work at very low loading mass percentage (0.5 % wt) [140]. It is worth noticing here that ferrimagnetic nanoparticles behaves like strong nano-magnets, thus as soon as they are sufficiently nearby (closer than 10 nm) they attract each other. Once they agglomerate, it is very difficult to separate them. In this case, we studied two different hybrid structures: PVDF hybrid film with 0.5 % wt of functionalized nanoparticles (named from now on

F-PVDF) where nanoparticles were functionalized by organic molecules before including them into the PVDF solution, and PVDF hybrid one with 0.5 % wt of non-functionalized nanoparticles (named from now on NF-PVDF). Their electroactive local properties were then compared to the one of the PVDF neat film elaborated in similar conditions.

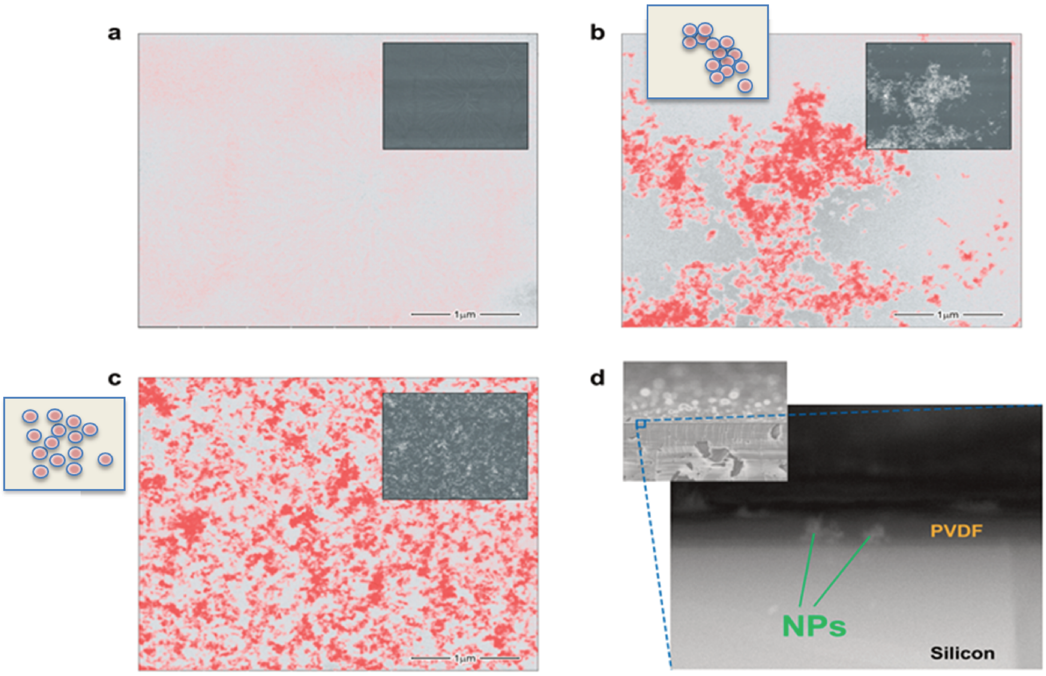

Figure 4.7: SEM images of: (a) a neat PVDF film, (b) Non-functionalized NPs embedded in the PVDF film (NF-PVDF), (c) Functionalized NPs embedded in the PVDF film (F-PVDF) and (d) cross section image of the NF-PVDF sample.

The microstructures at the surface of the different films were studied by SEM and AFM analysis as presented in Figure 4.6 and Figure 4.7 respectively. As shown in Figure 4.6, the characteristics micro-metric spherulitic structures with additional sub-micron fiber structures are clearly visible by the AFM images and they are in agreement with the previous reported morphology studies of the β-phase [16] [55] [101] [102] [133]. For each studied sample, five different zones (in the top, bottom and center) of the surface were imaged in order to study the surface roughness of the whole film. The overall topography roughness was statistically determined by calculating the mean value of the roughness's obtained by dividing each micrometric imaged area into 25 regions. Here above we reported the mean values and the standard deviation obtained from the 3 samples discussed in this section. The whole set of films present a mean thickness in the range of 75 to 85 nm and a mean roughness in the range of 3 to 6.5 nm (See Table 4.2).

Samples were also studied using SEM technique with both back-scattered (BSE) and secondary electrons (SE) standard mode. This latter provides information on the surface topography, size, and distribution of NPs while the BSE mode has been used to distinguish the components of sample with different chemical composition by detecting their atomic number, Z. The results show an homogeneous morphology of the large surfaces observed

Samples	PVDF neat film	NF-PVDF	F-PVDF
Thickness (nm)	83.3 ± 1.5	75.5 ± 3.7	80 ± 4
Mean roughness (nm)	3.5 ± 0.1	5.5 ± 0.1	6.3 ±0.1

Table 4.2: The thickness and mean roughness value of our samples.

by SEM technique. Figure 4.7(a) is the SEM image obtained for the bare PVDF in which no contrast can be seen for both BSE and SE images (inset). In Figure 4.7(b) and 4.7(c) we compare non-functionalized NPs embedded in the PVDF film (NF-PVDF), with their Functionalized NPs (F-PVDF) counterparts. BSE images provides a cleaner view of the dispersion of the nanoparticles, as they are related to the Z number of the material imaged. We found that functionalization is a key parameter into dispersing the magnetic nanoparticles inside the film, which indeed, can be applied for other types of NPs. The cross-section of the film shown in Figure 4.7(d) allows to state that the NPs are homogeneously embedded through the polymeric film thickness, and not dispersed only on its surface and forming aggregates in-depth.

To study the effect of the nanoparticle interface organization on the PVDF β - phase nucleation, FTIR [3] has been used, as this method is proven to be as suitable as X-Ray [4] diffraction for the determination of the different phases of PVDF. In fact, specific bands in the wavelength range between 500 and 1500 cm^{-1} have been previously identified to be characteristic of the different phases content [2] [73] [77]. We thus recorded the FTIR spectra of the three films at room temperature in the 600-2000 cm^{-1} wavenumber range, see Figure 4.8.

In this measurement, we also recorded the Si substrate transmittance (Figure 4.8 black line) in order to use it as a background for the PVDF film IR-measurements. The Si transmittance measurement let us put in evidence the existence of an unusual intensity decrease of the observed transmittance for wavelength lower than 850 cm^{-1} and a noise structure around 1380 cm^{-1}.

As can be seen, the FTIR spectrum of three samples exhibit both typical α and β peak. In order to be more clear, the FTIR absorption bands characteristic of the α (1212 cm^{-1}) and β (840 cm^{-1} and 1275 cm^{-1}) phases for the three films are zoom-in in Figure 4.9. Two crystalline bands located at 840 and 1275 cm^{-1} are identified and characterize the β-phase conformation (see Figure 4.9 (a) and (b)). These bands are related to the sequences of more than three and/or four trans conformations [2] [73] [77] of the ferroelectric (FE) polymer phase.

In Figure 4.9 (a) the characteristic absorption peak at 840 cm^{-1} shows an important increase in presence of the nanoparticles compared to the neat PVDF films. The same trend, even if less evident, is presented on the 1275 cm^{-1} peak (see Figure 4.9 (b)). Only one band identifying the non-polar α-phase is visible in our IR spectra and located at 1212 cm^{-1}(see Figure 4.9(c)). The intensities of this band, although very weak even for the neat PVDF films, slightly decreases with the increasing incorporation of the nanoparticles

---

[3] FTIR has been performed on a standard spectrometer, Thermo Nicolet, AVATAR 370 FTIR

[4] XRD analysis and measurements are still a ongoing work. We will not present it here.

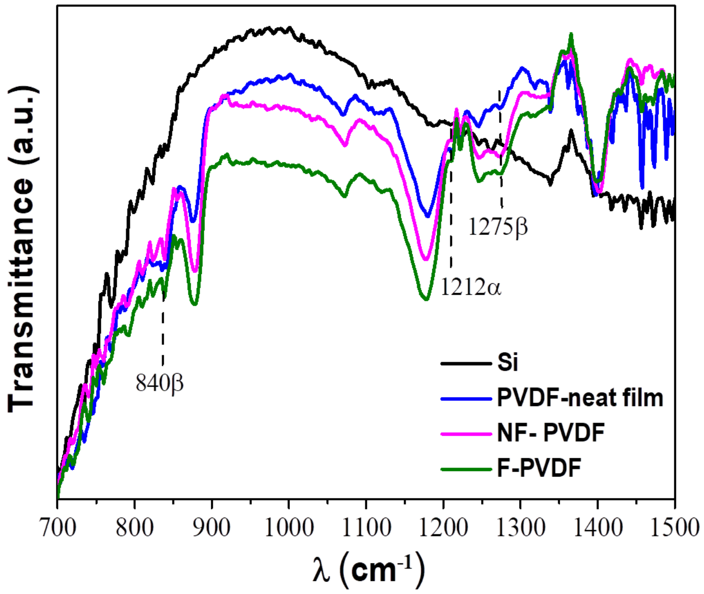

Figure 4.8: Infrared Transmittance (arbitrary units) of the whole set of samples. A baseline recorded at room temperature was subtracted from the corresponding spectrum using the spectrometer software.

along the polymer chains. This qualitative observations confirm optimization of the β-phase content in all our samples and is in agreement with the previous observations reported into literature concerning the effect of the nano-inclusions on the polymer phase [102] [110]. Besides, these results put in evidence that the NF-PVDF and the F-PVDF samples are comparable between them and optimized in term of β-phase content compared to the neat PVDF films.

The FTIR spectra recorded on the three samples, show also the presence of severals absorption bands at 875, 1070 and 1175 cm^{-1}. These latter bands are characteristic of the vibrations of the carbon-carbon skeleton in the polymer [14] [15] [110] [181] [232]. Due to their good resolution, we could study their evolution by analyzing the absorption intensity (i.e. area). The peak intensity evolution is reported here above and have been obtained by a standard ORIGIN polygon area analysis method. This study allows observing that in presence of both NF- and F nanoparticles, the intensities of these bands increase (especially 1175 cm^{-1}) emphasizing a better organization of the polymer structure in the case of the hybrid samples (see Table 4.3) [136] [5].

All these IR observations allow us to conclude that both neat PVDF films and hybrid ones present a majority of electro-active phase content with a slight increase of it (as

---

[5] H T T Nong, N A Nguyen, J Solard, C B O, M Simon-Sorbed, A E Carrillo, A Gomez, S Mercone, ”Local electromechanical control in PVDF–based thin films by the hybrid interphase optimization”, invited paper, submitted.

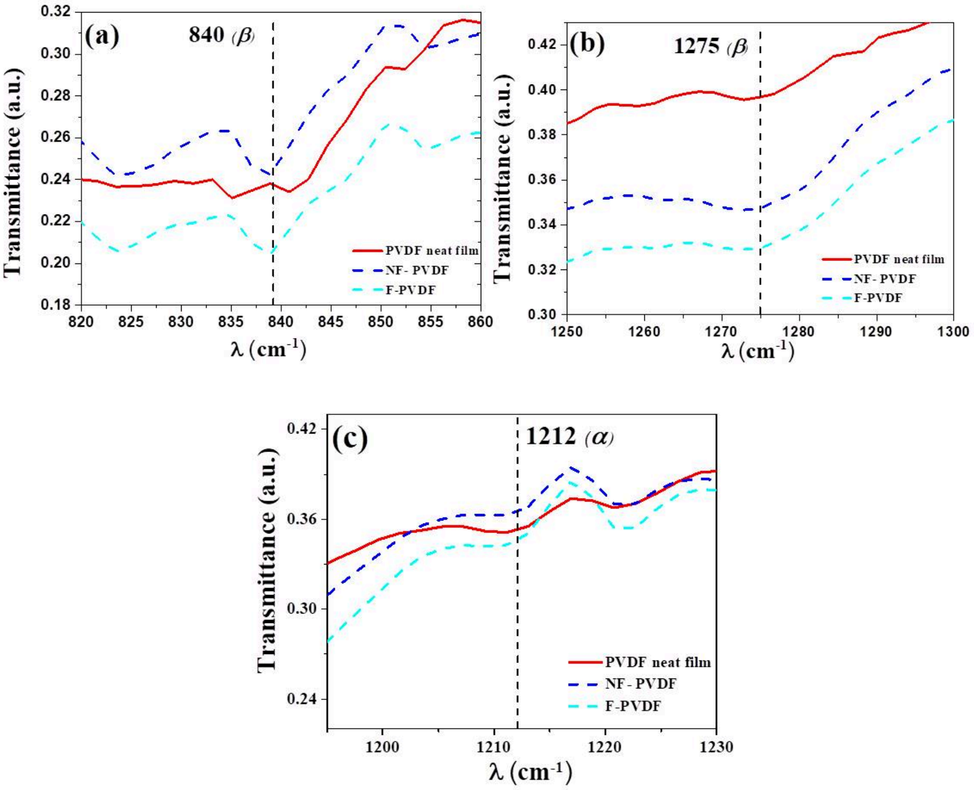

Figure 4.9: Specific infrared absorption bands typical of the β and α-phase have been identified and presented separately for neat PVDF films and hybrid ones respectively with non-functionalized nanoparticles (NF-PVDF) and functionalized nanoparticles (F-PVDF).

expected) in presence of the nano-inclusions.

4.3.2 Influence of the hybrid interface on the electromechanical response of PVDF/NZFO hybrid thin film

Comparison between the functionalized and non-functionalized hybrid films, allows us to study the effect of the dispersion of the nanoparticles inside the matrix not only over the optimization of the interface between the two phases but also over the local piezoelectric properties of the polymer. As we reported before, to efficiently stress the magnetostrictive phase of the NPs and thus to control their moment orientation by applying an electric field on the piezoelectric polymer, is a major key parameter for using these hybrid thin films in new magnetic sensor applications. In this content, the study of the local electromechanical response of the polymer by piezoelectric force microscopy is of primary importance.

In Figure 4.10 we show the piezoelectric response measured by applying an alternative electric bias field through the use of a nanometric-probing tip (PFM). This latter is in contact with the surface of the polymer and apply the field through the thickness of the film

λ	$875\ cm^{-1}$	$1070\ cm^{-1}$	$1175\ cm^{-1}$
PVDF neat film	3.2917	0.8833	6.7052
NF-PVDF	6.9503	1.2936	9.9480
F-PVDF	5.9804	1.1254	11.5359

Table 4.3: The peak absorptions characteristic of the carbon-carbon skeleton, have been analyzed in term of peak-area/intensities (arbitrary units) after the normalization of the spectra to the silicon transmittance.

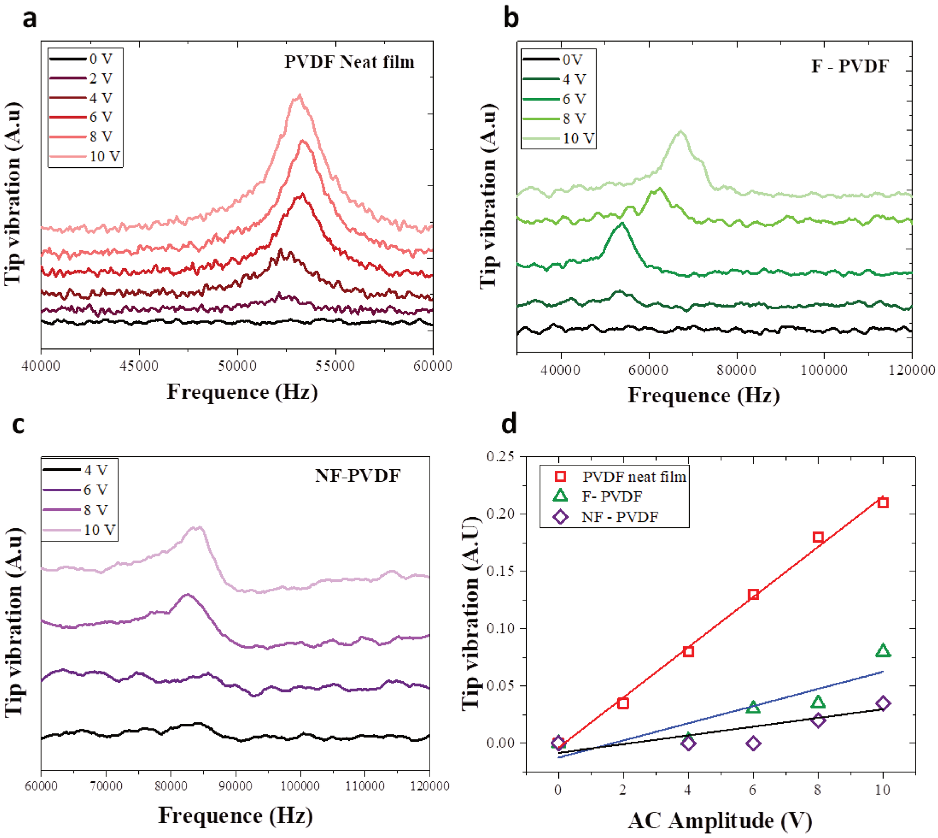

Figure 4.10: Electro-active response of: (a) neat PVDF film, (b) Functionalized NPs embedded in the PVDF film (F-PVDF), (c) Non-Functionalized NPs embedded in the PVDF film (NF-PVDF) and (d) Comparison of the piezoelectric behavior of all the samples.

(i.e. the conductive substrate is maintained at 0V). This electric bias results to a sample oscillation due to the converse piezoelectric effect. The piezoelectric surface displacement is detected by the reflection of a laser beam on the photodiode of the microscope that records the cantilever vibration/position (for more details, see section 2.1.2 in chapter 2). The out-of-plane electromechanical response is thus obtained by varying the AC electric bias from 0V to 10V by step of 2V. Figure 4.10(a), (b) and (c) shows the out-of-plane electromechanical response signal of the whole set of samples. As expected for piezoelectric material, the vibration amplitude of our films gradually increases with the increasing drive amplitude. These results confirm a linear piezoelectric effect in our neat PVDF films as well as the hybrid ones. This is in agreement with the presence of a majority of β-phase in all our films and with a measurable electro-active response at a local scale. However, in the case of hybrid-PVDF films (NF-PVDF and F-PVDF), the vibration amplitude is very small, showing a huge loss of the electromechanical response compared to the neat PVDF films. The comparison of the piezoresponse in all our samples is reported in Figure 4.10(d) where tip vibration pick is reported as function of the applied AC voltage. It is very interesting to notice that the F-PVDF film has a better local electro-active response than the NF-PVDF as well as the frequency range of resonance close to the one of the neat PVDf sample. All these observation underline the influence of the hybrid interface quality upon the piezoelectric response of the particulate 0-3 nanocomposite.

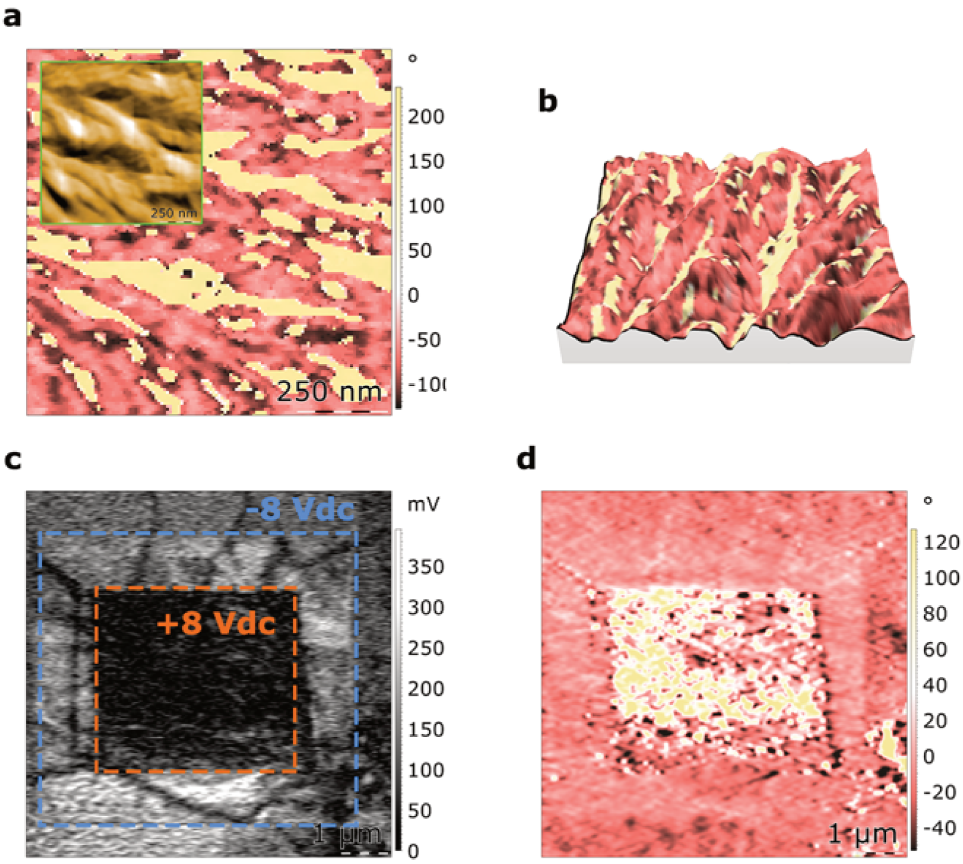

Figure 4.11: PFM images of PVDF neat film. (a) PFM phase image of the intrinsic ferroelectric domains. The insert image is the corresponding topography information; (b) 3D compositional image in which the colors represent PFM phase, while the roughness is the topography of the film; (c) PFM amplitude image of poled PVDF film with the voltage bias of ± 8 V represented by the blue and orange borders; (d) PFM phase image of the poled area.

We also succeed in recording the ferroelectric domains and locally polarized the PVDF neat film by applying a bias of ± 8 V (see Figure 4.11). It is worth mentioning that to record the PFM images of the ferroelectric domains of the hybrid films was very hard since their response is very weak or the relaxation time is very fast. Our best result of PFM images are shown in Figure 4.11. Note that the PVDF films are thin (< 100 nm) and soft (polymer surface), thus it is very easy to scratch them by the PFM tip during the scan. Therefore, we chose a soft PFM tip (with spring constant of 0.8 N/m). We also worked in an ambient of low humidity condition (lower than 10 %) in order to avoid artifacts. The ferroelectric intrinsic domains are shown in Figure 4.11(a) and (b) to ghether with the topography roughness. The contrast of colors in Figure 4.11(d) represents the opposite polarization direction of the ferroelectric domain which are switched by ± 8 V.

Our results clearly point out the increasing of the percentage of the electro-active β-phase as well as the carbon chains organization by including isotropic nano-fillers (see IR analysis) while on the other hand an unexpected huge decrease of the local piezoresponse is observed. Also, this seems to be in contrast with the previous literature presenting the optimization of macroscopic ferroelectric/piezoelectric properties of PVDF hybrid thin films as function of the β-phase content optimization. At this point, it is important to remind that our samples have not been poled (as it is usually done into literature) in order to study the intrinsic response of the as-grown PVDF films. The poling process, in fact, is well known to induce significant changes in the dipoles organization inside the polymer [133] and to eliminate the center of symmetry of the typical spherical structure. This means that our unpoled samples are probably affected by a slight disorder of the electric dipole moments of the molecular chains [94]. Thus, the unpoled thin films clearly show that the presence of nano-fillers locally decreases the polarization ordering and the FE domain structure of the PVDF. Optimizing the hybrid interface by well-dispersing the NPs, succeed in recovering part of the electro-active properties of the polymer.

It is reasonable to think that using the spin coating technique, and thus miming the drawing effect during the elaboration process, helped us to optimize the β-phase in the case of neat PVDF films. In fact, the polymer is free to stretch under the spinning effect of the rotating plate of the spin coating system. The polymer chain can organize in the fibers-structures observed in Figure 4.6 which are characteristic of the β-phase. Unfortunately this seems not to be homogeneously obtained through the sample. When NPs are included into the solution which is dropped on the spin coating plate, the polymer matrix stretching effect impressed by the speed of the rotation is likely disturbed by the presence of the nano-fillers inside the solution. Thus if a macroscopic drawing is still applied, and a majority of β-phase is still observed for the hybrid films, locally the nano-fillers destroys the charges/dipoles organization. These results are reported in Figure 4.10 and Figure 4.11. It is important to notice that the dispersion of the NPs inside the polymer matrix put in evidence a better-defined piezoelectric response (see Figure 4.10(b) and (c)). Figure 4.10(b) clearly show that the vibration presents a better define resonance in the case of F-PVDF films compared to the NF-PVDF one although the electromechanical responses of these two samples lays low compared to the neat-PVDF samples. The optimization of the interphase between the organic and inorganic phase by a good dispersion of the nanoparticles inside the polymer matrix, allows a better definition of the piezoelectric resonance associated with a better electromechanical response. This promotes the local dispersion of the nanoparticles as a possible way to reduce the observed electro-active losses due to the nano-inclusions presence and to enhance coupling performances for the next generation of magnetoelectric nanostructures.

4.3.3 Conclusion

In conclusion, we have shown that the 0-3 particulate nanocomposite thin films based on PVDF polymer can be elaborated by using a simple and low cost technique. High resolution AFM and SEM images together with profilometer measurements confirm that the whole set of samples discussed here are very flat, thin and homogeneous thin films with low roughnesses and mean thicknesses around 80 nm. Improvement of the electro-active has been obtained by embedding 0.5% wt of inorganic isotropic magnetostrictive nanoparticles inside the PVDF matrix. This improvement is confirmed by the intrinsic electromechanical local response given by a linear piezoelectric effect for the whole set of samples. Surprisingly enough, the hybrid sample does not show a better electromechanical resonances putting in evidence a local polarization disorder promoted by the nanoparticles. This effect is visible even thought the amount of nanoparticles is extremely low ($< 1\%$ wt). Last but not least, a uniform dispersion of the nanoparticles allows to recover part of the local electromechanical response. The hybrid interphase optimization obtained by the functionalization of the nanoparticles before their dispersion in the PVDF solution, opens a possible way towards the decrease of the electromechanical losses in the hybrid systems in view of the magnetoelectric applications.

4.4 Influences of the hybrid interface on the magnetic properties of the NPs

As discussed in the previous paragraphs, the nano-inclusions have an important effect on the piezoelectric properties of the polymer. Their size, their organization/dispersion inside the matrix induce considerable changes in the electro-active response of the polymer as well as of the mechanical [140] and chemical ones [102]. It is thus natural to think that also the converse influence is expected. One of the question that can be asked is linked to the elastic properties of the PVDF and the mechanical transfer of them at the interface between the polymer and the magnetostrictive NPs. PVDF is flexible and considered to be in a "rubbery" state at room temperature. However, as temperature decreases, PVDF begin to stiffen up and it goes through a transition phase that is called "glass transition" becoming effectively a glassy solid. Thus it becomes hard and also brittle. The temperature of the glass transition is called glass temperature, T_G. T_G of PVDF is -42 °C $\sim$ 231 K [22].

The elastic property of PVDF upon and below T_G is shown in Figure 4.12 (black line). As can be seen in the figure, the storage modulus (E' defined by the ratio between the

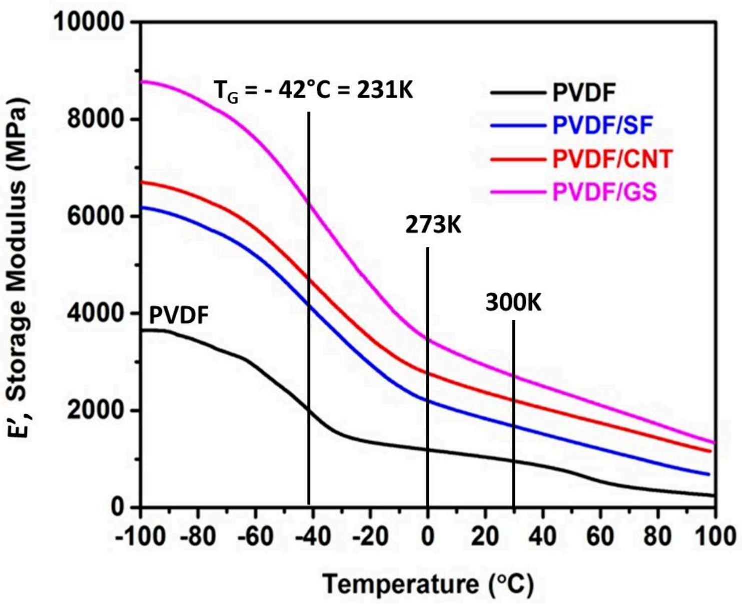

Figure 4.12: Elastic property of pure PVDF (black line) and PVDF nano-carbon composite as a function of temperature. The glass temperature of pure PVDF is -42 °C ∼ 231K. SF: Superfullerene, CNT: Carbon nanotubes, GS: Graphene sheets. [Figure is reported from the supplementary information of ref [22]].

stress and the strain under vibratory conditions) increase rapidly when temperature goes down to T_G. The storage modulus is measured by using a dynamic mechanical analysis where an oscillatory force (stress) is applied to a material and the resulting displacement (strain) is measured. Therefore, the higher storage modulus the stiffer is the material. In Figure 4.12 is also possible to notice that when stiffer materials are included and/or artificially melted together with the polymer, the storage modulus of the composite is higher than that of the neat-PVDF for all the range of temperature. The glass transition becomes smoother and smoother although the variation of the storage modulus between room and low temperature (T $<$ T_G) is high.

Looking at this property of the PVDF, it becomes questionable if the elastic properties changes between room and low temperature, can be transmitted to the inclusions at the hybrid interface and thus influence the magnetic properties of the NPs. The NPs (NZFO and CFO) included in the PVDF matrix are in our case, well know to be magnetostrictive (see section 1.1.4 in chapter 1). The storage modulus variation of the PVDF at low temperature and thus the change in the elastic properties of the NPs environment, may have a possibility to modify the magnetic properties of these latters by the inverse magnetostrictive effect. In order to answer the question above, we decided to study the magnetic properties of NPs (NZFO and CFO) included in a PVDF matrix as function of the temperature from 300K down to 5K by using a MPMS 3 SQUID VSM technique. These results have been compared to the results obtained for the sole NPs (i.e. dried nano-powders) shown in section 4.2.2 of this chapter.

4.4.1 Effect of the elastic properties of the PVDF matrix on the magnetic properties of $Ni_{0.5}Zn_{0.5}Fe_2O_4$ NPs

We measured here the magnetic hysteresis behavior of hybrid PVDF/NZFO (0.5% wt) thin film. As already studied before we get interested to understand if the transmission at the interface of the elastic strain, could be influenced by the organization/dispersion of the nanoparticles inside the PVDF. Thus we measured here the static magnetic properties of the non-functionalized (NF) and functionalized (F) NPs included in the PVDF nanometric film deposited on a silicon substrate (i.e. NF-PVDF and F-PVDF samples). Those measurements are presented in Figure 4.13.

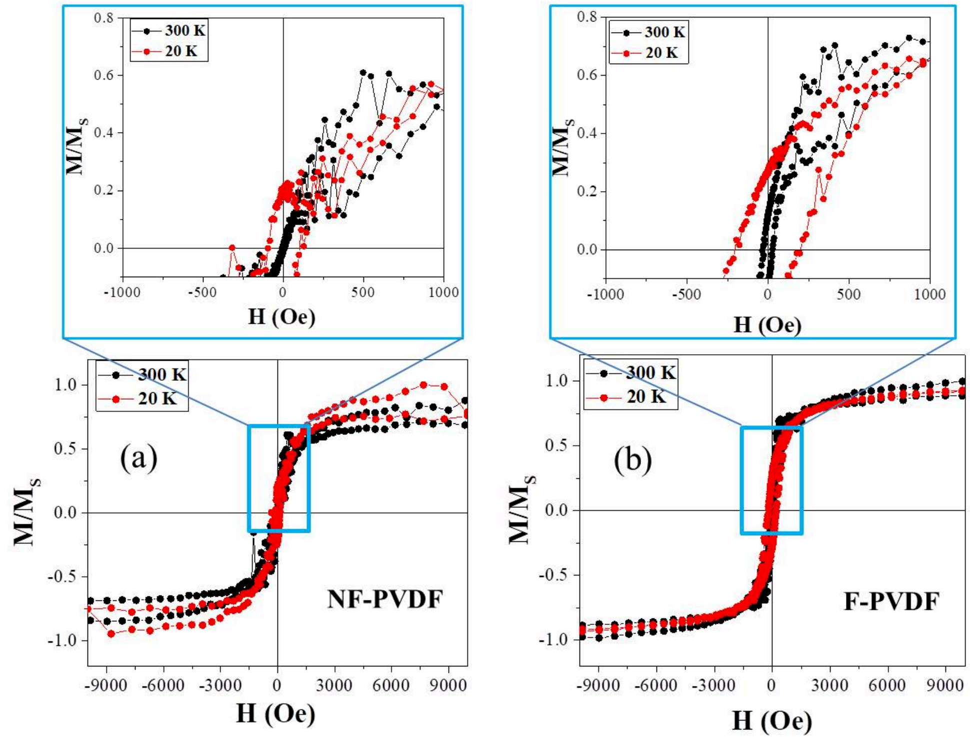

Figure 4.13: Magnetization curves of hybrid PVDF/NZFO (0.5% wt) thin films at room temperature (300 K) and low temperature (20 K): (a) NF-PVDF; (b) F-PVDF. The zoom-in of M-H loops at low field are showed on top of each graph.

As shown in Figure 4.13, the hysteresis loops of both two samples are typical loops of superparamagnetic NPs at room temperature ($H_C \approx 0$ for both cases and $M_r/M_S = 0$ for NF-PVDF, $M_r/M_S = 0.1$ for F-PVDF). It is interesting to notice that the magnetization behaves similarly to the case of the NZFO powder presented in section 4.2. In this configuration we could not deduced the exact weight of the nanoparticles. Therefore, the magnetic moment is kept normalized. It is important to realize that at a low field (see the insets in Figure 4.13), the hysteresis loops for both NF and F samples, show a lot of noise, especially in the curve at 20 K. We repeated the measurements several times to be sure that the noise was not coming from technical problem. However, the hysteresis loop of both samples is always the one observed in Figure 4.13. The hysteresis curves show a peculiar behavior before the saturation state, for both samples which is easy recognizable despite the noise. This feature was not observed for the sole NPs (see section 4.2) and could thus represent an effect of the PVDF on the magnetization of NZFO NPs. This peculiar feature of the hysteresis loop has already been reported for complex magnetic state [34] [152] in circular nanomagnets arrays of permalloy where the distance between the NPs is controlled and well dispersed. Note that, in these two samples, the amount of NPs is very small (0.5% wt) which means that the NPs are, at least for the functionalized sample, well dispersed inside the matrix. Therefore, the interface interaction between the PVDF matrix and the NPs is better than in the case of the higher percentage. In order to confirm this assumption, we decided to measure the magnetic properties of hybrid thin films of PVDF/NZFO (1% wt) elaborated and fabricated by using the same conditions as the previous one. The results are reported in Figure 4.14.

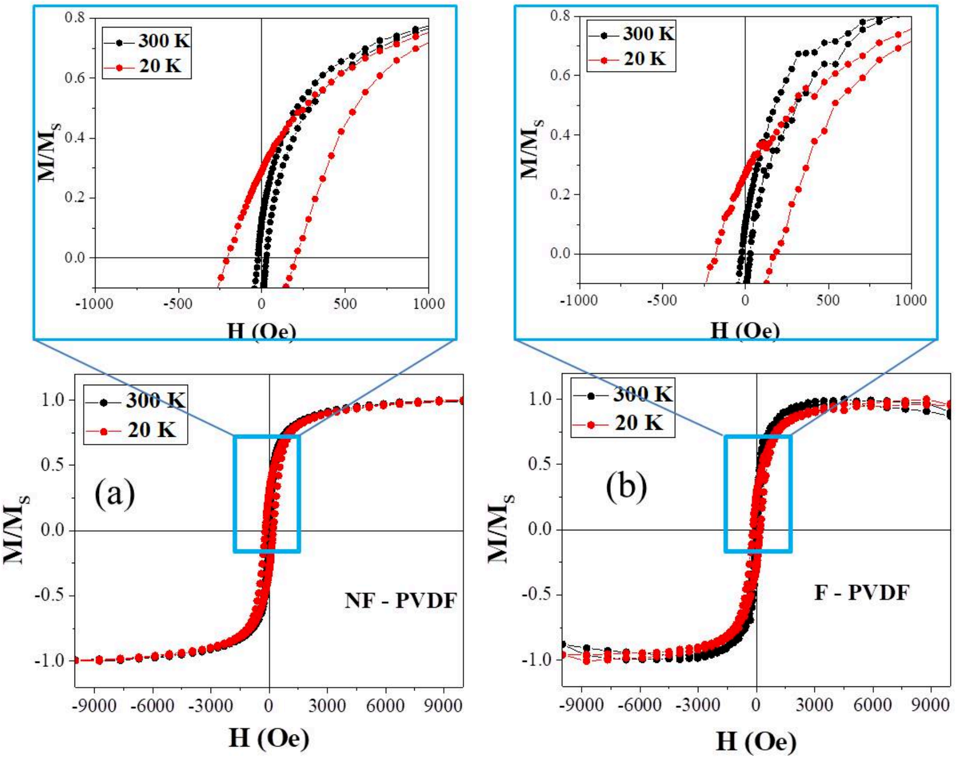

Figure 4.14: Magnetization curves of hybrid PVDF/NZFO (1% wt) thin film at different temperatures: (a) NF-PVDF; (b) F-PVDF. The zoom-in of M-H loops at low field are showed in the top of each graph.

Interestingly, the noise at low field has disappeared. Thus the noise at low field in the hysteresis loop seems to depend on the amount of NPs included inside the PVDF matrix. Moreover, the functionalized NPs still show the butterfly feature already observed. Again, this comparison between the NF and F behavior, seems to suggest that the effect of the PVDF matrix depends on the hybrid interface of the samples.

One important point concerning the studied samples is that the PVDF matrix is deposited on a Si substrate. This configuration can clamp the elastic properties of the composite film onto the substrate, then the deformation (linked to the elastic properties changing as function of temperature) may be less than the expected one and thus present only small changing on the magnetic properties of the nanoparticles. Due to this reason, we decided to go further on this study by measuring hybrid self-standing films. In the hybrid self-standing films, the clamping effect does not exist, as there is no substrate. Therefore, we do expect to observe stronger effects on the magnetic properties of the magnetostrictive NPs. Thanks to our collaboration with researchers at ITODYS team (C. Ben Osman, F. Mammeri, S. Ammar-Merah, Universite Paris Diderot). The magnetic studies on these samples are presented in the following section.

4.4.2 Effect of the elastic properties of the PVDF matrix on the magnetic properties of $CoFe_2O_4$ NPs

We studied here the hybrid self-standing film of PVDF/CFO with different percentage of CFO NPs (i.e. 5% wt, 1% wt and 0.5% wt, both functionalized and non-functionalized). To compare the results obtained for all the different percentage studied, we normalized all the magnetization curves again. The magnetic hysteresis loop at room temperature and low temperature (5K) are presented in Figure 4.15 in the case of hybrid sample with non-functionalized NPs, and in Figure 4.16 in the case of hybrid sample with functionalized nano-inclusions.

As shown in Figure 4.15, the hybrid self-standing film presenting 5% wt and 1% wt of NF-CFO inclusions exhibit the expected behavior observed on the sole NPs, whereas in the case of 0.5% wt an uncommon behavior at very low magnetic field appears. The zoom-in of Figure 4.15 (c) shows this latter and put in evidence a weird reversal mechanism of the magnetization for both room and low temperature.

In Figure 4.16, this uncommon reversal behavior is observed for all the different percentage of functionalized NPs included in the hybrid films. In particular, the samples of 5% wt and 1% wt clearly exhibit this peculiar mechanism at low temperature (5 K) while the 0.5% wt film shows it starting from room temperature. In order to study into details this uncommon behavior measured, we decided to focus our studies on the hybrid film containing the functionalized NPs as they are the one in which the effect is emphasized. We studied the magnetic hysteresis behavior for different temperatures in order to understand the specific effect of the PVDF elastic properties. The M-H curves have been thus measured for T > T_G as well as for T < T_G. Two opposite concentrations have been considered (the highest concentration of the NPs and the lowest one). The zoom-in of the magnetization at low field for the PVDF/CFO 5% wt and 0.5% wt F-NPs, measured at 300K, 200K, 100K and 5K are reported in Figure 4.17.

As can be clearly seen in Figure 4.17(a), the hybrid film with 5% wt of F-CFO NPs shows an important uncommon reversal mechanism for T < 200K. On the other hand, in the case of the hybrid sample with 0.5% wt of F-CFO nanoparticles, the same feature is already observed at room temperature.

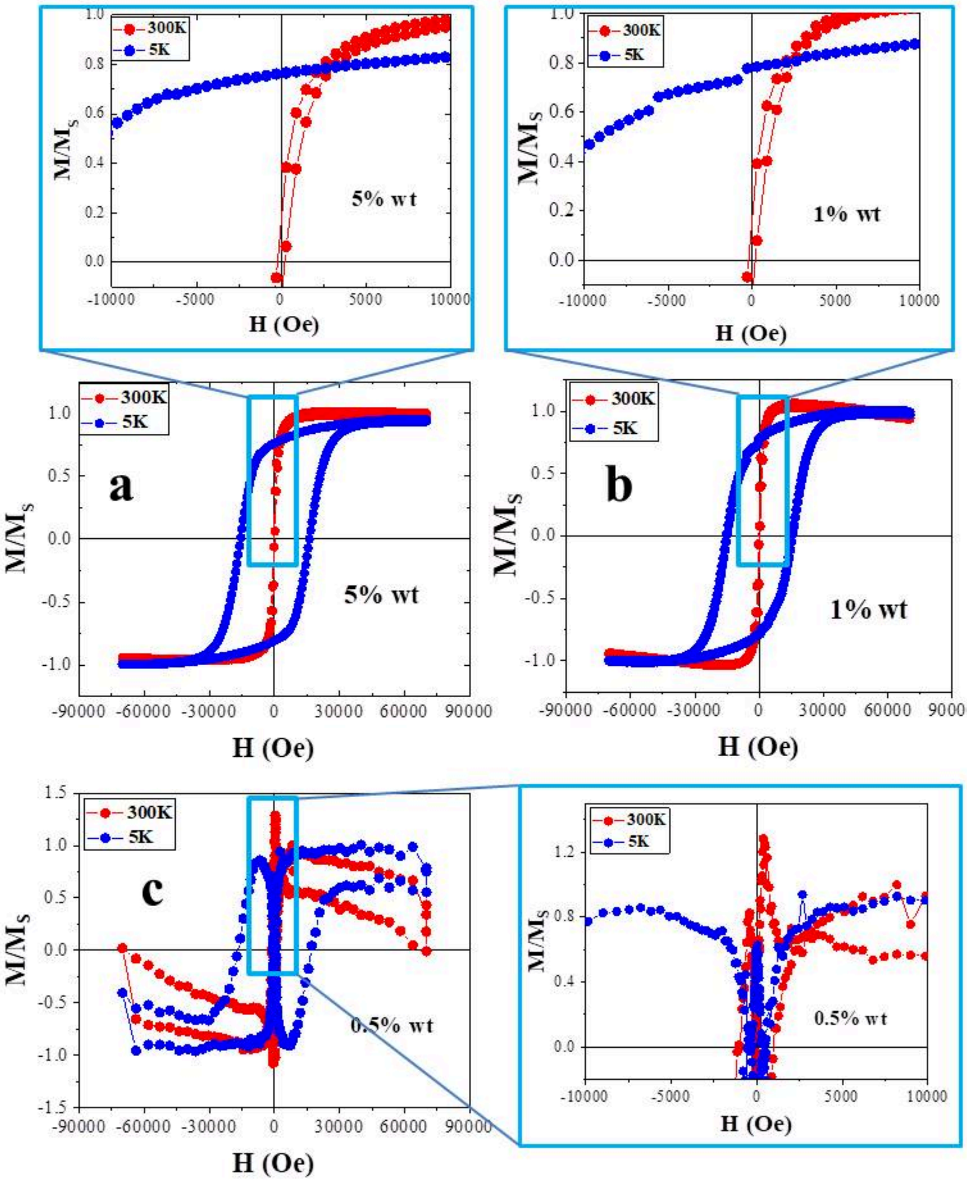

Figure 4.15: Magnetization curves of PVDF/CFO hybrid self-standing films with CFO NPs non-functionalized: (a) CFO 5% wt; (b) CFO 1% wt; (c) CFO 0.5% wt. The zoom-in of magnetization curves at low field are reported in the blue square.

From the results presented in Figure 4.15 and 4.16 as well as 4.17 in comparison with the Figure 4.1, it is logical to deduce that the quality of the hybrid interface (i.e. different amount and dispersion of the NPs) between the inorganic NPs and the organic polymer, have an influence on the uncommon reversal mechanism observed in the hysteresis loops reported. It is worth underlining here that the quality of this interface depends mainly from two factors: (i) the amount of nano-inclusions and (ii) the functionalization/dispersion of the NPs inside the polymer matrix. The higher is the amount of NPs, the

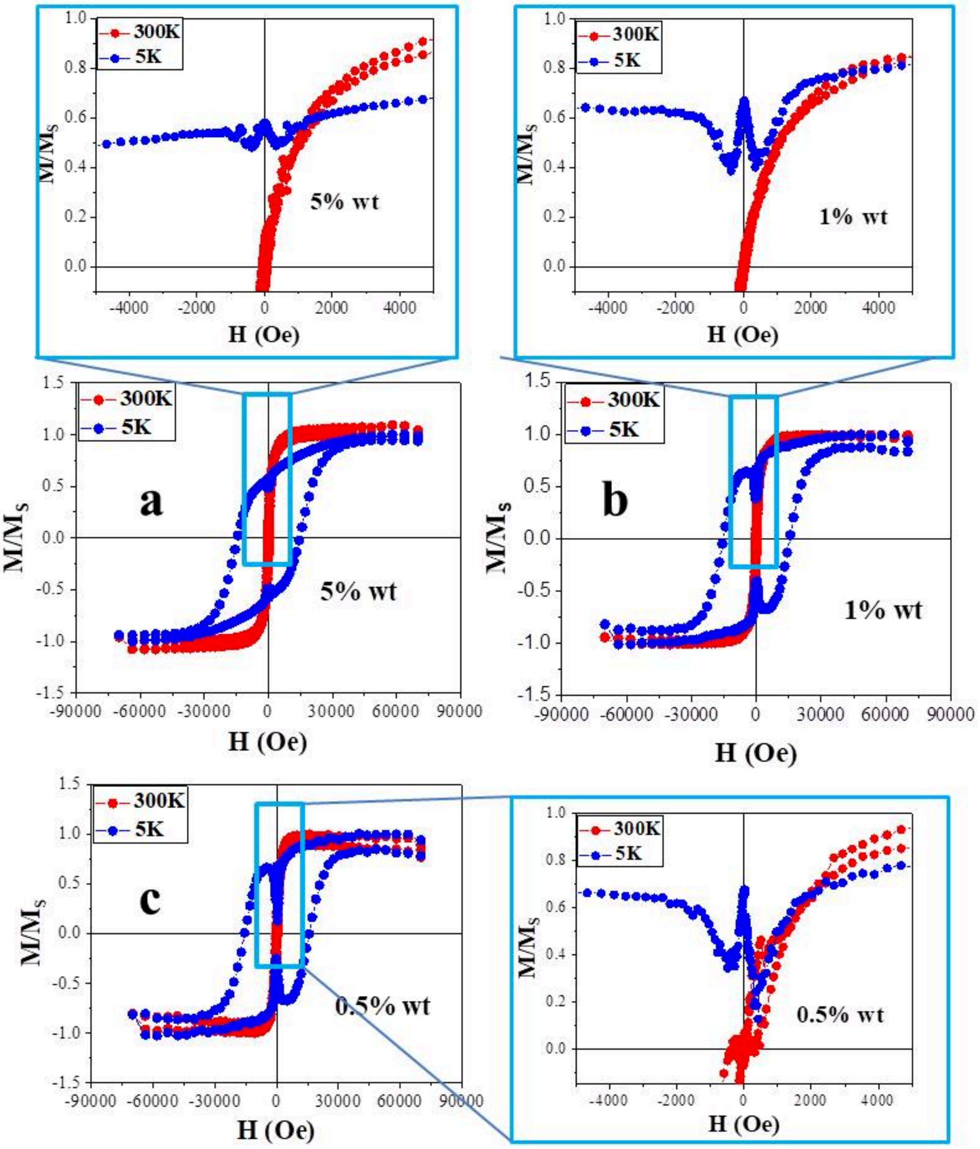

Figure 4.16: Magnetization curves of PVDF/CFO hybrid self-standing films with CFO functionalized nanoparticles: (a) CFO 5% wt; (b) CFO 1% wt; (c) CFO 0.5% wt. The zoom in of M-H curves at low field are presented in the blue square.

higher is the possibility of agglomeration of the nanopowder and thus the lower is the quality of the hybrid interface. Also, the functionalization helps the dispersion of the NPs by grafting molecular brushes on the NPs surface and thus preventing their agglomeration before their inclusion inside the polymer. These considerations together with the results reported before, allow speculating on the fact that the higher is the quality of the interface, the more important is the effect observed. Also, looking at Figure 4.17, the reversal mechanism seems to be dependent of the temperature and to enhance at low temperature. As the sole NPs do not present this uncommon behavior (see Figure 4.4),

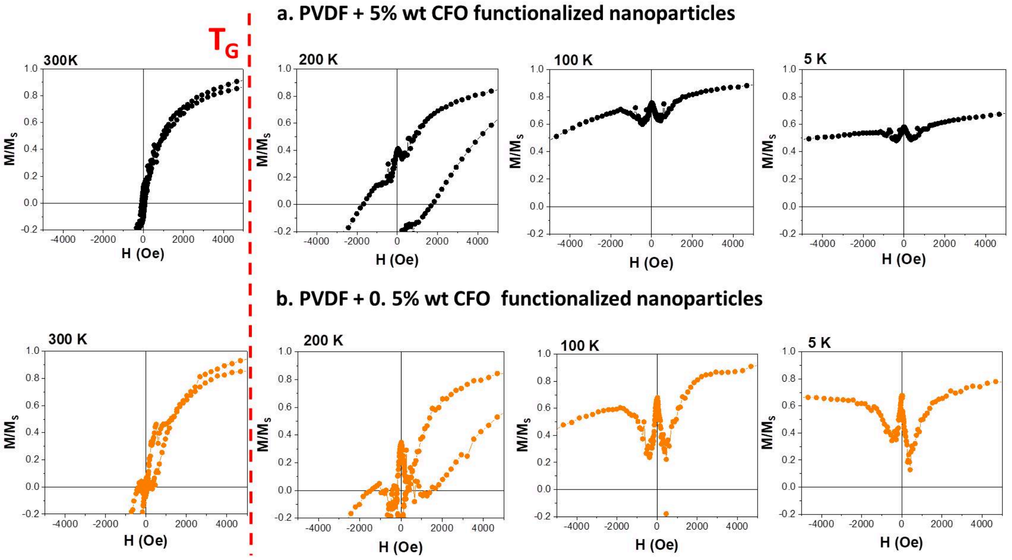

Figure 4.17: The zoom-in of the magnetization curves at low field for the PVDF/CFO functionalized nanoparticles. (a) PVDF/CFO 5% wt; (b) PVDF/CFO 0.5% wt.

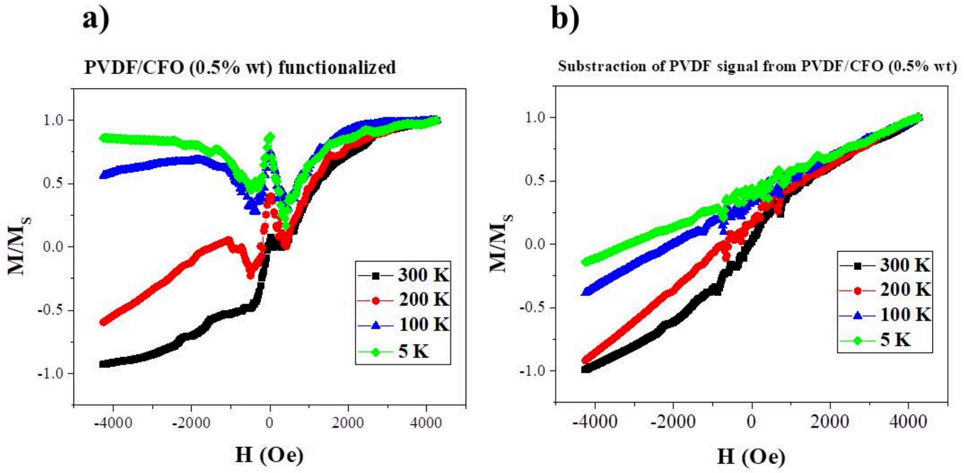

Figure 4.18: Zoom-in of the magnetization observed at low magnetic field. (a) Hybrid self-standing film of PVDF/CFO (0.5% wt) functionalized NPs at different temperature; (b) Corrected corresponding curves (see text for more detail).

this latter may be linked only to two different reasons: (a) the elastic properties of the polymer are changing as function of temperature (see Figure 4.12) and thus transferred a deformation to the magnetostrictive NPs; this behavior together with the fact that the magnetic properties of the NPs evolves as function of temperature becoming more and more ferromagnetic (higher M_r and H_C) can lead to higher interface effect while the temperature is lowering; (b) the polymer presents unforeseen magnetic properties at low field contributing to the final magnetization observed. While the first option is obviously linked to the very interesting question wondering either if it is possible to manipulate the magnetic properties of the NPs by using hybrid 0-3 type connectivity, the last one is not suitable in this purpose. In order to understand it, we firstly wanted to exclude this last hypothesis. We thus measured the hysteresis loop of the PVDF self-standing film without any inclusions, elaborated in the same condition of the functionalized hybrid films. We subtracted the magnetization obtained for the PVDF to the one obtained for the hybrid one with 0,5% wt of F-CFO NPs in the same temperature and magnetic field conditions. The results are presented in Figure 4.18 (a) and (b) respectively before and after the subtraction. As we can see in this figure, the correction is able to correct only the reversal behavior close to the zero magnetic field. Thus, even if the effect is small, it is still detected by the SQUID-VSM sensitivity at some symmetrical critical field. This latter depends on the T_G. It is smaller for T > T_G (i.e. $H_{critical}$ around 330 Oe) and constant but higher for T < T_G (i.e. $H_{critical}$ around 550 Oe).

4.4.3 Conclusion

To be honest, we were not completely satisfied by this analysis, as we are aware of the fact that this correction is not as accurate as the correction we could do by using what the magnetometer system call the raw data. In fact, subtracting the polymer magnetization from the hybrid one that we did, is a rough method assuming that both contribution simply add to each other. Obviously, the reality can be much more intertwined. Thus, a more precise analysis should be done by treating point-by-point the raw signal detected by the SQUID. This analysis is very time consuming, both for the measurements and for the treatment of the data. This is still an ongoing research, which a part is presented in the Appendix B. Also, it is important to underline here that, if the observed magnetic change are connected to a magnetoeleastic change, we should be able to detect it by measuring a different anisotropic constant of the sole NPs compared to the NPs inside the matrix. This is possible to do by performing AC measurement (i.e. low frequency susceptibility). We started to work on this, but unfortunately some technical at impediments low temperature came on the way. We are thus currently developing this point in collaboration with DR. S. Hebert (CRISMAT, ENSICAEN), it will be hopefully part of my oral presentation.

Chapter 5

Optimizing ferromagnetic properties of anisotropic nanoparticles toward 1-3 particulate ME nanocomposite

In this chapter, we discuss the optimization of the magnetic properties of cobalt-based anisotropic nanoparticles (nanowires, NWs) devote to be included into 1-3 nanocomposite ME materials. In the 1-3 nanocomposite structure, the magnetic Co-based NWs are dispersed in a piezoelectric polymer matrix. From the magnetic point of view, dispersing NWs in a matrix will rise some challenges since their magnetic properties depend on the organization inside the matrix and the interaction that may exist between them. Moreover, the magnetic properties of Co-based NWs are fully dependent on their morphology and crystal structure. Thanks to our collaboration with several colleagues in LSPM we had the opportunity to work on the magnetic optimization of these NWs as function of the morphology, crystal structure as well as their organization and interaction. We could perform this study by firstly dispersing and organizing the NWs inside their synthesis solution. This allows us to understand the ferromagnetic dependence of an *ensemble* of NWs in low density and weak interaction configuration. Afterward, the effects of higher density and strong interaction configuration have been studied in the case of disordered nanopowders and within nanostructured material obtained by sintering these latters. This study allowed to understand the magnetic properties of these NWs *ensemble* as function of their organization and thus interactions. We performed this study by both an experimentally point of view and by using simulations techniques.

The step forward this studies would have been to investigate the magnetic properties of these NWs while they are included in a polymer ferroelectric matrix (i.e. 1-3 particulate nanocomposite). The control of these inclusions is still an ongoing active research inside the chemistry groups not only in our laboratory but also in the frame of the Labex SEAM consortium of which our laboratory is partner. The biggest issue is to obtain a good control of the organization of the NWs inside the matrix, after their extraction from the synthesis solution. Due to their strong mutual magnetic attraction, they tend to agglomerate during this extraction thus a step of functionalization is needed. This should prevent the NWs to agglomerate together and thus allow us to organize them inside the polymer matrix. The chemical optimization of this step is still an ongoing research as I said before because of the higher surface/volume of the NWs compare to the NPs, thus the magnetic study of this 1-3 composite lays as a perspective of my work.

Albeit this inconvenience, I could study, as explained before, the effect of the interaction and organization of the NWs using alternative comparable configurations. One of these latter is the high density nanostructured sintered material obtained from the compaction of the nano-powders. This high density and strongly interacting NWs configuration is widely explored into literature in the scope of creating a new generation of permanent magnet. As required by this application, the materials have to show a high energy product (so called magnetic energy), BH_{max}, which expresses the performance of a permanent magnet. This BH_{max} value depends on the coercivity and the magnetization of the material (i.e. the hysteresis loop). The calculation of this parameter is presented in section 5.2.1. Therefore, an optimized magnetic properties with a high coercivity and high magnetization is desired to get a high BH_{max}.

Cobalt NWs are good candidates for the design of free rare-earth permanent magnets since they show high saturation magnetization ($M_S = 160$ emu/g $= 1424 \times 10^3$ A/m) and high Curie temperature ($T_c \approx 1400K$), without mentioning a high magnetocrystalline, ($K_1 = 450kJ/m^3$ for a hexagonal-close-packed, *hcp*, bulk crystal structure) and shape anisotropy (K_U depending on the size of NWs, as reported in section 1.1.3 of chapter 1). All these properties help stabilizing (thermally and spatially) the ferromagnetic (intrinsic) properties of the nano-magnet.

In order to use cobalt NWs for nanostructured permanent magnet, the fundamental requirement is optimizing their magnetic properties in order to reach a magnetic energy as high as possible. As a starting point, the magnetic properties of individual cobalt NW have been well optimized in literatures not only by micromagnetic simulation but also experimentally by an accurate control of their elaboration [182]. From the micromagnetic simulation point of view, the shape of single cobalt NW is optimized by several conditions [118] [141] [154] [233]: (i) the diameter of the NW should be as small as possible; (ii) the aspect ratio (i.e. the ratio of the length over the diameter) should be of 10; (iii) the morphology of the NW has to be as closer as possible to the nano-cylinder shape.

Due to the highly effective magnetic anisotropy of Co (*hcp*) NWs, these properties are strongly dependent on the orientation of the NWs compared to the direction of the magnetic field applied. Thus, one of the key-issues in the permanent magnet field is to preserve the good magnetic properties of the single NW inside the nanostructured permanent magnet based on the NWs assembly. This is rigorously connected with the perfect alignment of the NW *ensemble* inside the bulk structure. Several processes have been developed mainly under the application of a magnetic field, in order to optimize the nano-structuration of the NWs based bulk magnet [6] [64] [142] [143]. Two well-aligned NWs systems with a high magnetic energy ($350kJ/m^3$ [51] and $165kJ/m^3$ [6]) have been reported. However, the mechanical properties of these assemblies are unfortunately not well suited for bulk applications since in these systems, the NWs are aligned inside an epoxy matrix [51] or simply dried on a wafer. In order to improve the mechanical properties for bulk application, several compaction processes have been performed using Spark Plasma Sintering method. N. Ouar et al. [64] [142] [143] reported that the magnetic properties of nanostructured compacted samples obtained by the nanopowder compaction, are strongly affected by their mechanical properties. By increasing the hardness of nanostructured samples and so their density, they observed a decreasing of the coercive field, leading consequently to a loss of the magnetic energy. Nevertheless, the simulation results have shown the opposite behavior. Micromagnetic simulation shows that, the magnetic energy of Co NWs assembly, increases linearly with the density of the dense nanostructured materials [137] [150].

These studies show how delicate is the question of the optimization of the magnetic energy of the NWs assembly as this depends on the tight balance between the magnetic properties of each NW (i.e. intrinsic magnetic properties of nano-magnet) as well as of their organization and density inside the assembly (i.e. macroscopic arrangements/properties). In this chapter we will show our contribution to this experimental challenge. We will show how the structural control of the NWs, can be critical for their magnetic properties/energy. Also, we present here our experimental observations and analysis of the magnetic static properties of nanostructured magnet obtained by the compaction of the nano-powders. We discuss their magnetic behavior as function of the nanotructuration and we analyze our results by micromagnetic simulation of the magnetic properties of the dense NWs *ensemble*.

5.1 Magnetism of the nano-magnet: the Stoner - Wolfarth model

In order to study the magnetic behaviors of cobalt NWs, we used a standard model which is called Stoner-Wolfarth model. This model developed in 1948, allow easily to describe the magnetism of small particles [191]. We summarize here below the important features of this model which is going to be used as a term of comparison for the optimization of the magnetic properties of the nano-magnets/NWs.

Stoner-Wolfarth (SW) model considers a ferromagnetic material bringing a single magnetic moment (i.e. macrospin model). The material is therefore considered as a single magnetic domain, thus all multi-domain related effects, non-uniformities or inhomogeneities are not considered. A single domain occurs when the size of the grain is smaller than some critical length and thickness (length of few 100 nm and 10 nm diameter are the critical sizes for Fe, Ni and Co). At T = 0K, a grain with a single magnetic moment $\mathbf{M}$ is an ellipsoid-shaped object (see Fig. 5.1) since a material with uniform magnetization ought to have an ellipsoid form [81]. This ellipsoid-like shape nanoparticle owns an uniaxial anisotropy axis (also called easy axis - EA) which is an axis along which the magnetization prefers to lie in order to minimize the total energy of the nanoparticle (see section 1.1.3). When an external magnetic field is applied, the magnetic behavior of the nanoparticle is described by the magnetization, $\mathbf{M}$, and the angle φ that $\mathbf{M}$ forms with the EA, as well as by θ which is the angle that the external applied magnetic field

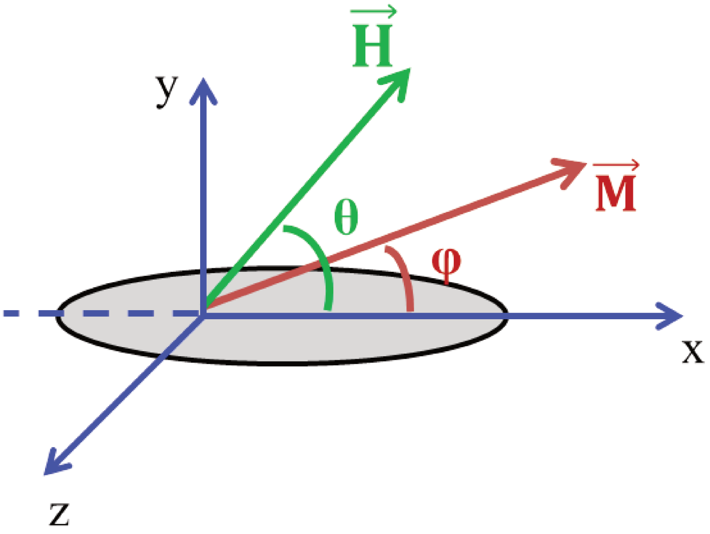

Figure 5.1: An ellipsoidal grain with the easy axis (EA) along x-axis, the angle φ and θ are the angle that the magnetic field applied H and the magnetic moment M form respect to the EA.

forms with the EA (see Figure 5.1).

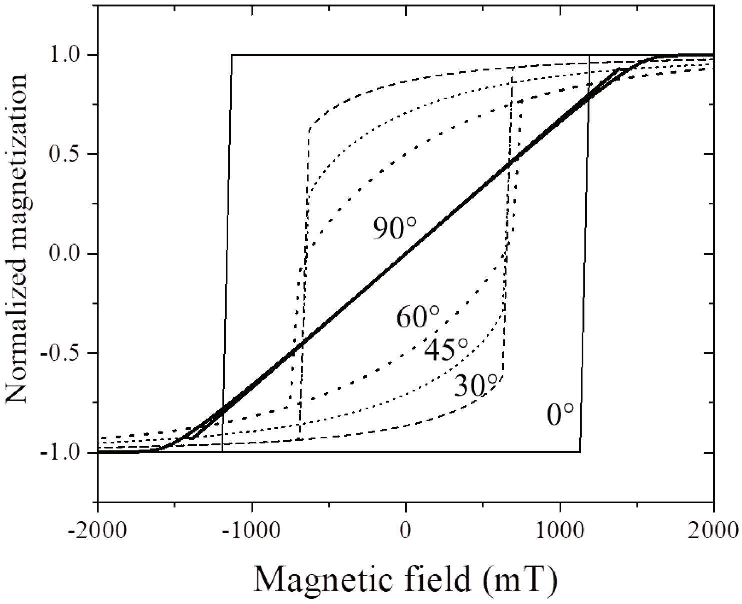

Figure 5.2: An example of hysteresis loop obtained by the SW model. The θ angle between **H** and EA, varies from 0° to 90°.

Thus, the magnetic moment **M** is driven by a competition of two forces: one is due to the uniaxial anisotropy and tends to align **M** along the anisotropy axis and the other is due to the external magnetic field **H**, forcing **M** to align along the field. The total free energy density of the nanoparticle is thus:

$$E = E_A + E_Z = K \sin^2 \varphi - HM_S \cos(\varphi - \theta) \tag{5.1}$$

Where: $E_A = K \sin^2 \varphi$ is the anisotropy energy which is characterized by the anisotropy constant K_U, $E_Z = -HM_S \cos(\varphi - \theta)$ is the Zeeman energy and M_S is the magnetization at saturation. It is important to verify that E_A is minimum when $\varphi = 0$ for $\mathbf{K} > 0$. The magnetic moment will choose the direction that minimizes the total energy.

In the case of a finite nanoparticle, in the previous free energy density we have to add the demagnetizing term (E_D) which is linked to the shape of the particle (see chapter 1, section 1.1.3). The total free energy is then given by:

$$E = E_A + E_Z + E_D \tag{5.2}$$

Where the third term is defined by $E_D = K_d \sin^2(\varphi)'$, in which φ' is the angle between **M** and longer axis of the grain. The K_d, is the shape anisotropy constant which depends on the shape of the ferromagnetic nanoparticle, and it is defined by $K_d = 2\pi N_{ij} M_i M_j$ where N_{ij} is determined by $N_{xx} + N_{yy} + N_{zz} = 1$. These geometric coefficient can be calculated for different shapes (see chapter 1, table 1.1). For an infinite cylindrical wire with longer axis in the x-direction, $N_{xx} = 0, N_{yy} = \frac{1}{2}$ and $N_{zz} = \frac{1}{2}$ [27].

The typical hysteresis loops, obtained with this model by the minimization of the magnetic energy, are presented in Figure 5.2. The coercivity, H_C, is determined by both the anisotropy and demagnetizing field contribution ($H_C = H_A + H_d$).

It is easy to see that, the squareness (M_r/M_S) of the hysteresis cycle is close to 1 when the external field is parallel to the EA ($\theta = 0°$). In this case, the hysteresis loop is closest to the perfect square shape. When the angle θ increases, the coercivity (H_C) decreases.

As described by the SW model, an ellipsoid-shape nanoparticle is desired to optimize the magnetic anisotropy and thus the magnetic coercive field of the nano-magnet. However, this shape seems to be complicate to be obtained in the experiment since very different size, shape (i.e. dumbbell, diabolo and cylinder) and morphology are observed in literature depending on the elaboration process [93] [198] [199]. The simulation study shows that the cylinder-like shape presents a better coercivity comparing to the dumbbell- and diabolo-like shape obtained experimentally, (see Figure 5.3) [154] [233]. The morphological relevant parameters are then: the diameter (D), the length (L), the aspect ratio (L/D), the thickness of the head (T) and the width of the head (W) (see the sketch in Figure 5.5(b)). They have to be controlled in order to magnetically optimize the NWs performances. Indeed, cylindrical shaped Co NWs with a high aspect ratio and without irregularities at the edge are expected to be the better option (see Figure 5.3). The polyol process have been developed and showed a well control of the size, the shape and the morphology of Co NWs [24] [182] [198]. In our case, our colleagues in LSPM used this process to elaborate our samples. The experimental study on the static magnetic properties of Co NWs *ensemble* synthesized by polyol process is presented in the following section. Three

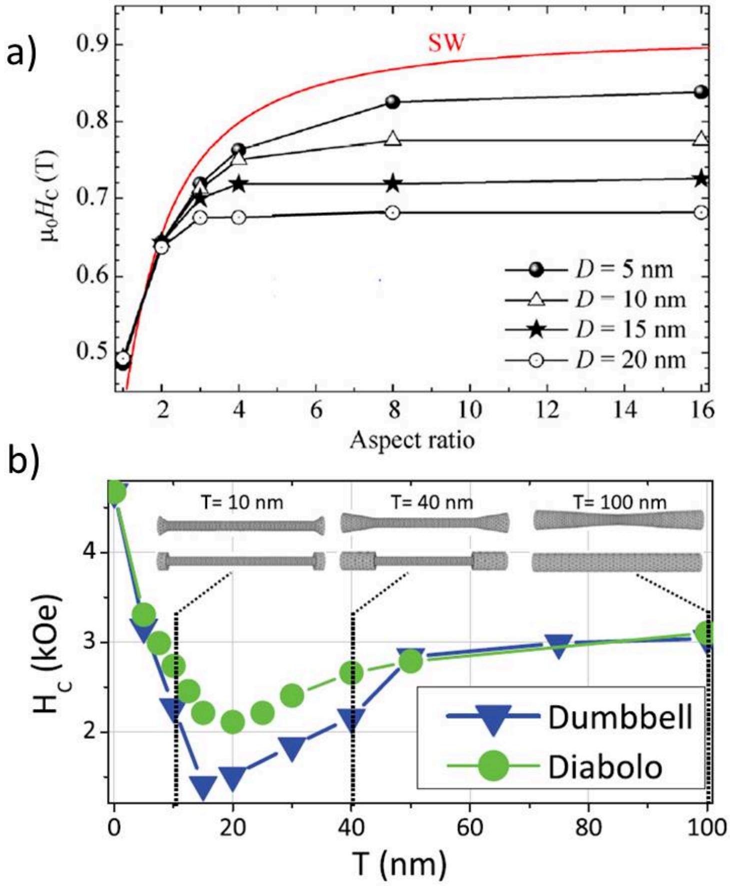

Figure 5.3: (a) Coercivity values of Co cylinders with different diameters D as a function of their aspect ratio (L/D). The prediction of the SW model is plotted as a continuous red line [154]. (b) Coercive field values for dumbbell and diabolo nanowires with an aspect ratio L/D = 20 (i.e., Length L = 200 nm, diameter D = 10 nm, and the width of the head W = 20 nm) as function of the thickness T of the head; meshes of the nanowires for three different thickness are shown in the upper part of the figure [233].

effects will be considered: the morphology, the growing fault in the Co crystal structure and the interaction depending on the density of the NWs *ensemble*.

5.2 Optimizing the ferromagnetic properties of a nanowires *ensemble*: The experimental study

As discussed in the previous paragraph, the magnetic properties of anisotropic nanoparticles depend strongly on their magnetic anisotropy. In addition to the shape anisotropy, the magnetocrystalline anisotropy is an important term contributing to the magnetic anisotropy of nanoparticles. In general, Co NWs may be grown with two types of crystalline structures, either face-centered cubic (*fcc*) or hexagonal close packed (*hcp*) crystal structure [44] [46] [153] [164] [165] [206] [212]. In the case of *fcc*-Co NWs, the shape anisotropy dominates over the crystal anisotropy, while for *hcp*-Co NWs, the crystal anisotropy energy density is of the same order of magnitude of the shape anisotropy energy density [20] [145]. Thus, the crystallographic orientation of the *hcp* structure is expected to optimize the magnetic anisotropy, and thus their magnetic properties. Unfortunately, experimental studies has been shown that the hexagonal cobalt structure is known to easily present regular occurrence of stacking faults [121] [180]. A stacking fault in this case creates layers of atoms presenting a *fcc* symmetry. This *fcc* layer is magnetically more isotropic (i.e. a smaller anisotropic constant, $K_1 = 63kJ/m^3$).

Moreover, the obtained Co NWs are not isolated (i.e. assembly of NWs within their polyol solution) and thus it may exist important interactions among them. Simulation studies have been shown that Co NWs interact by dipolar interaction depending on their mutual distance. This interaction reduces linearly the magnetic properties of the assembly toward the decreasing of the distance between NWs [111] [235]. In addition, since Co NWs own a high magnetic anisotropy, their magnetic properties depend strongly on their organization inside the *ensemble* and also on the direction of applied the magnetic field. Thus, the magnetic optimization of Co NWs *ensemble* is a tight balance between the magnetic properties of each NWs (i.e. the shape and the crystal structure), their organization and their density inside the *ensemble* (i.e. distance between NWs).

The final goal is to optimize the magnetic energy, BH_{max} value. The calculation of this parameter is presented in the following section.

5.2.1 The magnetic energy

In order to detect the relevant parameter driving the magnetic behavior of NWs, we decided to calculate the magnetic energy product (BH_{max}) from the measured hysteresis loops. In this purpose, we used the following standard equations reported in literature [6]:

$$BH_{max} = \begin{cases} \frac{B_r^2}{4\mu_0(1+\alpha)}, & \text{if } \mu_0 H_c \geq \frac{B_r}{2(1+\alpha)}; \\ H_c(B_r - \mu_0(1+\alpha)H_c), & \text{if } \mu_0 H_c \leq \frac{B_r}{2(1+\alpha)}; \end{cases} \tag{5.3}$$

Where $B_r = 4\pi M_r D$ (Gauss) is the magnetic flux density through the structure at the remanent state, $D = 8.92g.cm^{-3}$ is the cobalt bulk density, μ_0 is the magnetic permeability of the vacuum, H_c (Oe) the measured coercive field and $\alpha = \frac{2M_r(1-SQ)}{H_c}$ a dimensionless parameter taking into account the squareness of the measured hysteresis loop. This latter coefficient shows how the magnetic energy product BH_{max} strongly depends on the squareness (SQ) of the hysteresis behavior. In this standard model, the SQ is defined as $A/(H_c M_s)$, where A is the area under the second quadrant of the loop (see figure 5.4), H_C (Oe) and M_S (emu/g) are respectively the coercive field and the magnetization at saturation. The final BH_{max} product has been converted from MGOe in the CGS system to kJm^{-3} in the international system of units.

In this calculation, the unity of the remanent magnetization (M_r) and the saturation one (M_S) is in emu/g. This is necessary to calculate the magnetic flux density at rema-

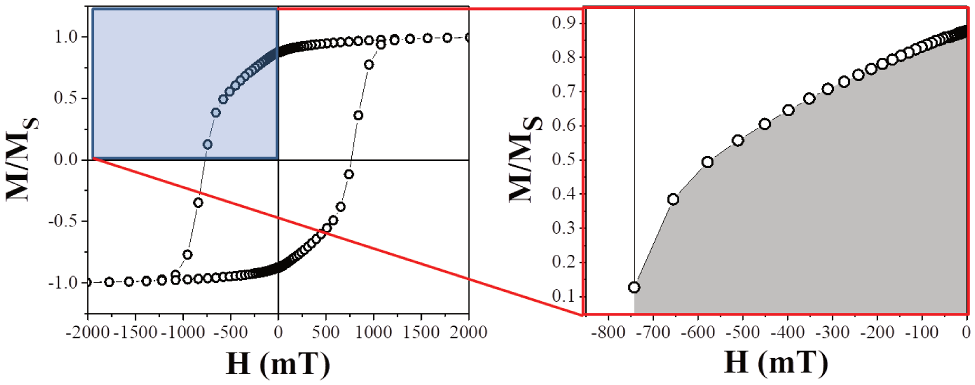

Figure 5.4: (left side) Hysteresis loop in which the second quadrant is evidenced by a blue color; (right side) Zoom-in of the area under the second quadrant (grey color) of the hysteresis loop.

nent (B_r) and the squareness (SQ) value. Obviously, the calculation of the magnetization at saturation was possible only in the case of the powder and bulk samples which we could weight before measuring them. In the case of the NWs in their elaboration solution we could not do this. Also, depending on the elaboration conditions, it is difficult to estimate the density of magnetic mass/volume inside the synthesis solution. Thus to give a first estimation of the magnetic energy product also in this latter case, we decided to calculate the BH_{max} by using simple considerations on the measured hysteresis loops. For all our samples the condition $\mu_0 H_c \geq \frac{B_r}{2(1+\alpha)}$ is verified. It can be deduced from equation 5.3 that the ratio between the magnetic energy product of the batch of NWs inside their synthesis solution to the one of their corresponding dried powder (i.e.$BH_{max}(polyol)/BH_{max}(powder)$) is proportional to the ratio between the corresponding areas under the hysteresis loop in the second quadrant (grey area in figure 5.4). So after normalizing the hysteresis curves in order to make them comparable, we deduced the ratio of those areas:

$$\frac{S_{polyol}}{S_{powder}} = a \approx \frac{BH_{max}(polyol)}{BH_{max}(powder)} \tag{5.4}$$

where S_{polyol}, S_{powder} are the area under the second quadrant of the hysteresis curve respectively of NWs in polyol and their corresponding powder samples.

In experimental studies, the magnetic energy of the Co NWs has been calculated from the standard hysteresis loop. For this purpose we recorded the magnetic hysteresis cycles by field cooling (FC) the samples under the application of H = 7T at different temperatures. For each batch (i.e. each morphology), we measured the magnetic properties of the nanowires inside their synthesis solution (polyol) and their corresponding dried powder. Thanks to our collaboration with the chemistry group in LSPM, we could work on cobalt NWs synthesized by the polyol process [128] [182] [198] and then compacted by Spark Plasma Sintering (SPS) method [142] assisted by an external magnetic field at a high temperature and a high pressure. This allows us to work on well-controlled samples and to study the effect of morphology, shape and interaction on the magnetic properties of Co NWs. Our collaborators concerning the synthesis are: K. Mrad (PhD at LSPM), F. Schoenstein (Maître de Conférence, LSPM), N. Jouini (Professor, LSPM) and J.Y. Piquemal (Professor, ITODYS).

5.2.2 Magnetic properties: results and discussion

Experimental proof of the morphology effect

Figure 5.5(a) presents the typical morphology of Co NWs observed in our systems by TEM image. All the samples we studied here, are constituted of NWs having a mean diameter (D) in the range of 17–26 nm and a mean length (L) of 89 nm up to 276 nm (see Figure 5.5 (b)). They present an elongated morphology with a mean thickness (T) of the head ranging between 11.2 to 52.3 nm and with a mean width (W) of 24 to 33 nm (see table 5.1). Obviously, in order to put in evidence the effect of the edge irregularities in the cobalt NWs, we had to be sure that our samples were perfectly homogeneous and thus well controlled. The hysteresis loops of two samples in their polyol solution and their corresponding powders are presented in Figure 5.6. Sample 1 presents a low L/D ratio and sample 7 a high one.

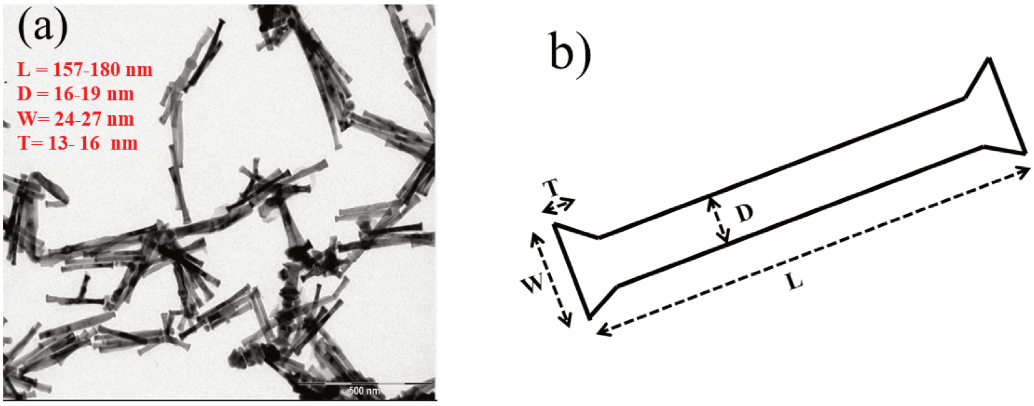

Figure 5.5: (a) TEM image of Co nanowires having morphological parameters: $L = 157 - 180nm$, $D = 16 - 19nm$, $W = 24 - 27nm$ and $T = 13 - 16nm$; (b) sketch of morphological relevant parameters for Co nanowires.

The coercivity, H_C, and magnetic energy product, BH_{max}, as function of the relevant morphological parameter (i.e.$\frac{L}{D}$, $\frac{D}{W}$, T) are presented in Figure 5.7 and Figure 5.8. As expected, higher coercive field and better performances of the magnetic energy product are obtained at low temperature for each morphology. This behavior cannot be attributed to the shape contribution to the reversal mechanism of the nanowires (i.e. H_d) as this does not change in function of temperature. Considering a simple model in which the shape anisotropy contribution to the coercive field of the nanowires is added to the magnetocrystalline contribution ((i.e. $H_C = H_d + H_{MC}$, being $H_{MC} = 2K_1/M_s$ [84] [118], then a higher value of the magnetocrystalline anisotropy constant (K_1) expected at low

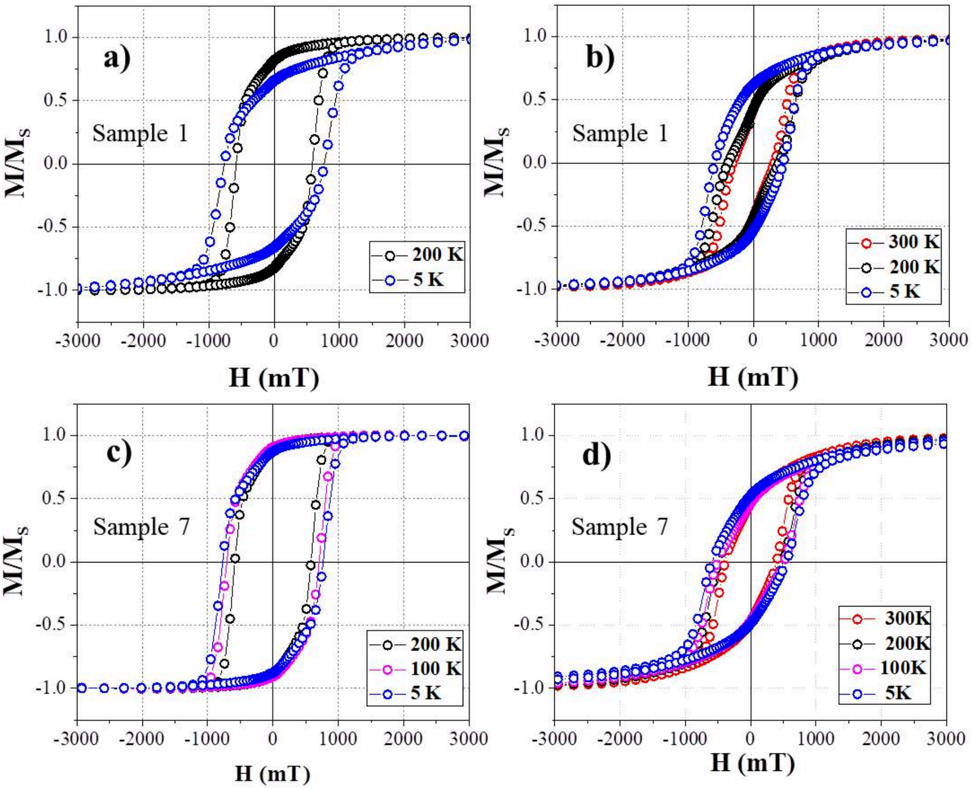

Figure 5.6: The hysteresis loops of sample 1 and sample 7 with NWs dispersed within their polyol solution (a, c) and NWs as-dried nanopowder (b, d).

Sample	L/D	D/W	T	α	M_S	δ	M_r/M_S		H_C (Oe)	
			(nm)	powder	(emu/g)	(%)	polyol	powder	polyol	powder
1	4.29	0.77	12.86	2.39	157	-	0.65	0.621	7659	5231
2	6.38	0.69	11.84	2.21	136	0.082	0.53	0.455	6779	4954
3	7.34	0.75	14.17	1.05	133	0.063	0.64	0.48	6382	5790
4	9.16	0.88	11.20	2.73	149	0.074	-	0.44	6456	4120
5	10.26	0.65	19.73	2.43	169	0.050	0.87	0.53	7674	5640
6	10.7 0	0.78	52.36	1.27	143	0.056	-	0.48	7130	5240
7	12.23	0.74	18.86	1.90	141	0.054	0.76	0.48	7275	5769

Table 5.1: Morphology details (L/D, D/W and T) of several studied samples, magnetic parameters at low temperature (5 K) for both nanowires in their polyol solution and as dried powder.

temperature will lead to a higher value of the coercive field. As a result, a higher magnetic energy product is observed at low temperature. The striking feature of the graphs in figure 5.7 and 5.8 is the absence of any clear dependence of the coercive field and magnetic energy product to the morphology variations.

This observations are suggesting that these are not the relevant parameters which drive the magnetic energy of the Co NWs. Moreover, comparing our results with the literature

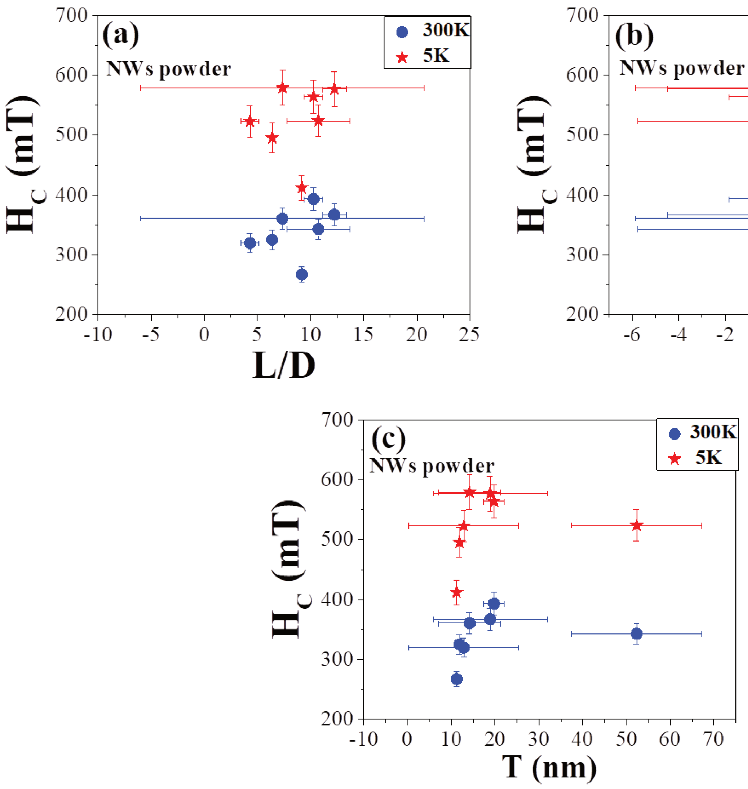

Figure 5.7: Coecivity as a function of (a) $\frac{L}{D}$, (b) $\frac{D}{W}$ and (c) T. The non-homogeneity of the nanowires was a reason for reducing the coecivity.

we cannot again see any coherence between the magnetic energy product value and the NWs morphological characteristics [51]. Also, the observed polydispersion of the NWs (see big error bars in figure 5.7 and 5.8) cannot explain the magnetic energy behavior observed. In fact the biggest polydispersed samples do not present the lowest magnetic energy value as expected. It is worth noting that our higher magnetic energy product at room temperature is significantly lower (i.e. $35kJ/m^3$) than the highest values achieved in [51] (i.e. $350kJ/m^3$ for monodispersed cobalt nano-powders and $278.5kJ/m^3$ for the polydispersed one). It is important to underline that we show here the morphology results for nano-powder samples where an important effect of the strong interactions between NWs is expected to happen. This point will be discussed later in this chapter but we can already stress out that we found exactly the same trend for the corresponding NWs inside the synthesis solution. At this point, we can conclude that the effect of morphology in these case is not changed when the density of the NWs increases. At this point, we can conclude that the effect of morphology in these case does not significantly change the magnetic features in our system. This must be related to the fact that all NWs are strongly coupled together and do not behave independently. This collective behavior smoothies the effect of the individual morphology.

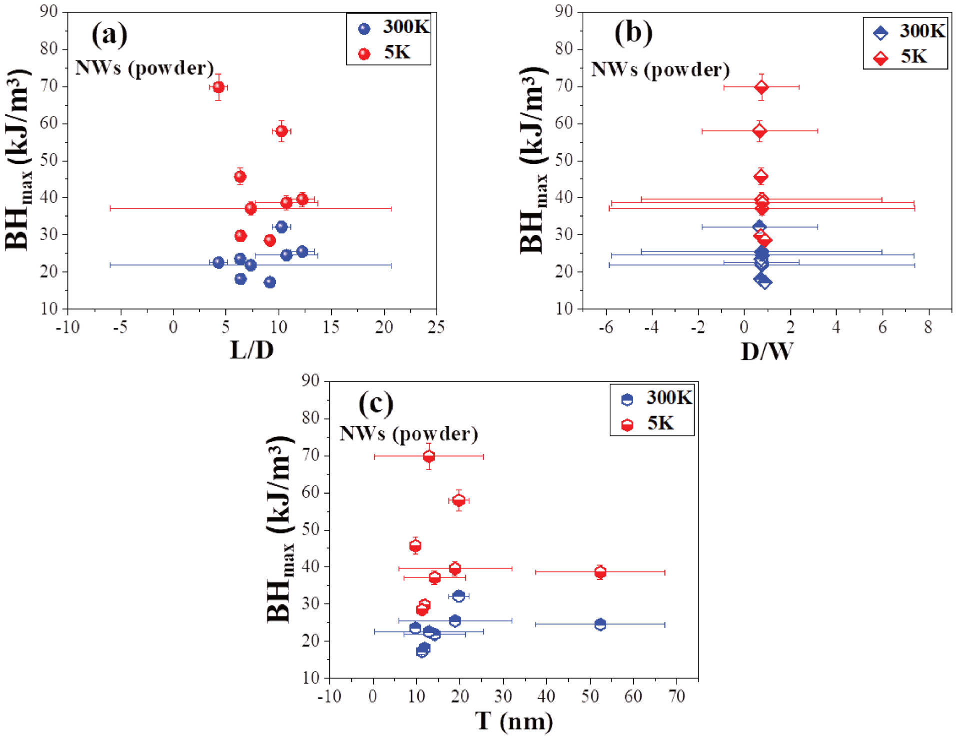

Figure 5.8: Magnetic energy product as a function of (a) $\frac{L}{D}$, (b) $\frac{D}{W}$ and (c) T. All these parameter define the morphology of the NWs.

Experimental proof of the stacking fault density effect

In order to go further and to understand the relevant parameter driving the magnetic energy behavior observed previously, we decided to take into account the effect of the crystalline structure. The stacking fault density (δ) was determined by using the X-ray diffraction and the TEM technique. In the XRD measurement method, the stacking fault density is analyzed by the X-Ray line broadening of *hcp* phase (i.e. detail of calculation procedure is presented in [24]). By using the TEM technique, δ is determined by counting the white line over a uniform grey contrast of NWs in the HR-TEM image (i.e. detailed in [127], [128]).

Figure 5.9 presents the BH_{max} as function of the stacking fault density (δ) obtained for our samples. The magnetic energy behavior for both NWs inside their polyol solutions (figure 5.9(a)) and the corresponding powder (figure 5.9(b)) are reported at room temperature and low temperature. As stated previously [1] [117] [175] [178] [192] [209], the stacking fault density, δ, strongly affects the magnetocrystalline anisotropy of Co *hcp* nanowires. Sokalski et al [178], reported an important decrease (exponential-like decay) of the magnetocrystalline anisotropy constant with the increasing of stacking fault density in cobalt thin films. Looking into our results in figures 5.9(a) and (b), we found the exponential decay being coherent also in the case of nano-objects (green and red lines).

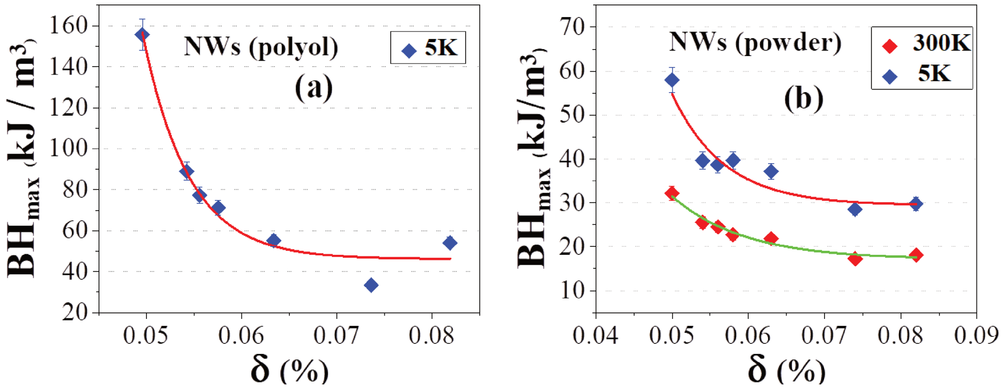

Figure 5.9: BH_{max} of Co nanowires as a function of stacking fault density, (a) polyol sample, (b) powder sample. The lines (green and red for 300 K and 5 K, respectively) are exponential fits showing the rapid decrease of BH_{max} with the increasing of stacking fault density.

The striking feature in figure 5.9 is that, no matter what the dispersion and morphology of the NWs, the stacking fault density drives exponentially the collapse of the magnetic energy product. The exponential decay factor **c** ($BH_{max} = Ae^{-x/\mathbf{c}}$ where x is the stacking fault density) is expected to be affected by the dipolar interactions between NWs. We could observe a different value for the exponential decay (i.e. different c factor) for low and high interaction (respectively dispersed in polyol and powders sample).

Effect of the nanostructuration in NWs assembly

As required from practical applications, the permanent magnet have to present a good mechanical properties. This obviously means that applications are not going to be done by using the nanopowders but they need bulk nanostructured material obtained by using the cobalt NWs as building blocks. Due to the high effective magnetic anisotropy, the perfect alignment of Co NWs *ensemble* within their bulk structured is a key-issues to preserve the good magnetic properties of the single NW (see Figure 5.2 in the S-W model). Thus, the compaction processes that has been choosen by our collaborators is the Spark Plasma Sintering (SPS) method. The reason is linked to the uniqueness properties of this technique. Thanks to the rapid time and the soft conditions of the SPS sintering, NWs inside the bulk structure may keep their morphology and nanometric size. This increases the chances to keep the good magnetic properties of the single nano-magnet inside the bulk nanostructured material.

Following this idea, our colleagues chose, in order to perform the SPS compaction, batches of synthesized NWs showing the lowest stacking fault density and polydispertion of the morphological parameters . This choice of sample batches allows us to neglect the effect of morphology and stacking fault which was studied in previous paragraph. The NWs have been thus compacted by SPS and become a bulk pellet sample (see the TEM images of samples in Figure 5.10(d)). This allows the study of the nanostructuration

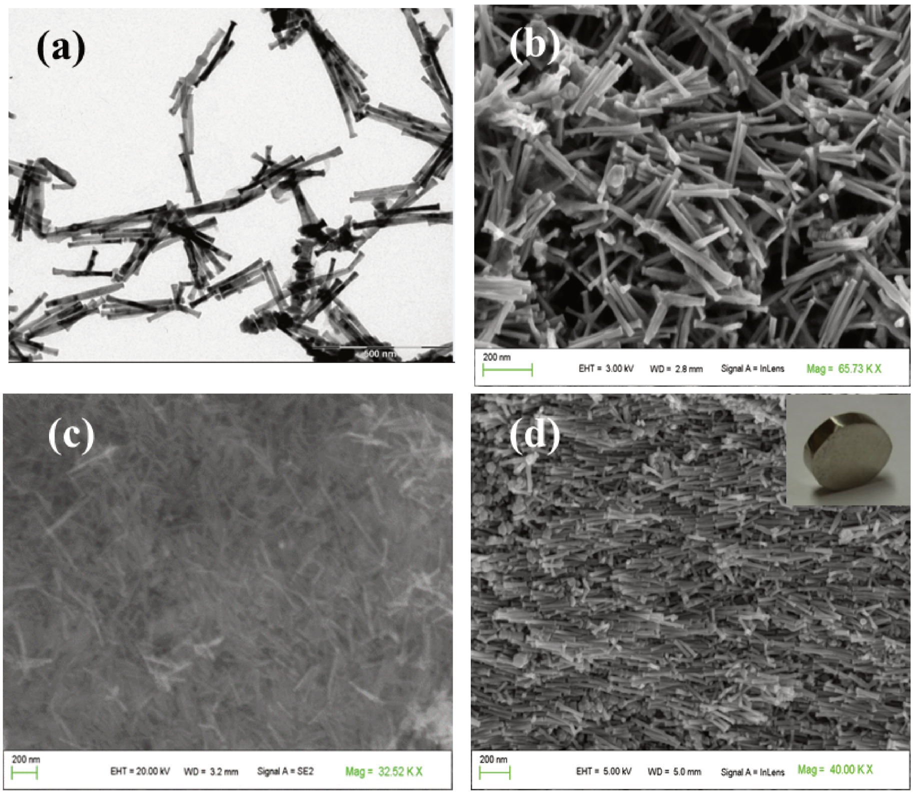

Figure 5.10: TEM images of studied samples: (a) NWs in polyol; (b) NWs powder; (c) NWs compacted under zero field (H = 0) and (d) NWs compacted under H = 1 T.

effect and thus the effect on the magnetic properties of the NWs assembly in the case of strong interacting NWs and high density configuration. In principle, NWs have to be well aligned parallel to each other inside their bulk-nanostructured assembly in order to optimize the magnetic anisotropy. The SPS method allows to do this by using an external magnetic field (H = 1 T) during the SPS process. The ordered assembly of NWs for different conditions of elaboration is shown in Figure 5.10(d).

In Figure 5.10(a), the TEM image shows the monodispersion of NWs inside their polyol solution at room temperature. The Figure 5.10(b) and (c) depict the disorder of NWs respectively in powder (low density) configuration and in compacted (high density) one. This last TEM image concerns the sintered assembly without any external magnetic field applied. In contrast, Figure 5.10(d) shows a TEM image of the NWs assembly obtained by SPS assisted by an external field of 1 T. It is clear, in this last image, that the organization of the high density assembly of NWs is less random and better aligned along a preferential axis. This latter is strictly defined by the external magnetic field applied during the SPS sintering. We do expect that the alignment of the assembly will play an important role on the coercivity as well as the magnetic energy BH_{max} of the NWs assembly. This alignment effect should be, at its turn, affected by the strongness of the interactions between the NWs inside the assembly. Thus, this effect is expected to be dependent of the density of NWs inside the different *ensembles* (NWs in polyol,

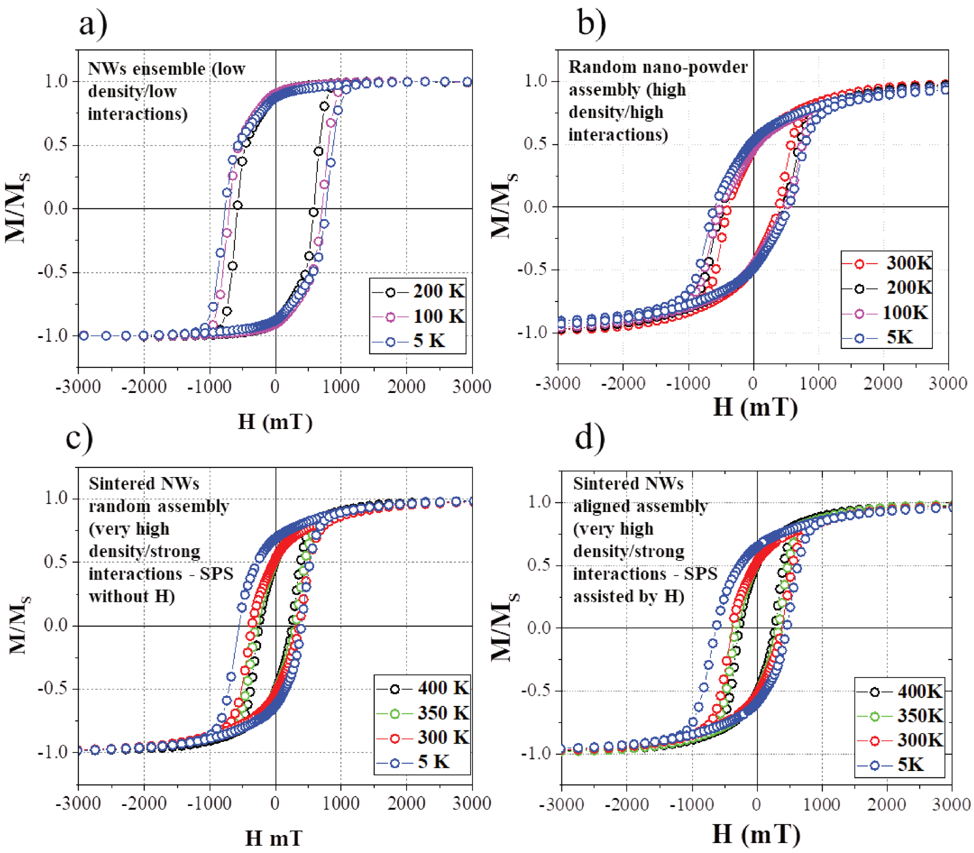

Figure 5.11: Magnetic hysteresis loop at different temperature for: (a) NWs in polyol; (b) NWs powder, (c) NWs compacted under H = 0 and (d) NWs compacted under H = 1 T. Hysteresis loop at 5K shows the typical exchange bias shift causes by the Co NWs surface oxidation (for more details see the main text).

nanopowders and nanostructured assembly). On the contrary, in literature is reported that simulation results of NWs assembly having higher packing density [1] should show better BH_{max}. These studies obtained linear increase of H_C values toward the increasing of the packing density of the NWs *ensembles* [137] [150]. Therefore, in this case, the compacted samples are expected to present a better magnetic properties compare to the disordered nanopowder samples.

The magnetic hysteresis loops of four samples presenting different interactions/densities are shown in Figure 5.11. The hysteresis loops are normalized to compare the squareness of the hysteresis cycle as this represents clearly the order/disorder of the NWs (Stoner-Wolfarth model). As can be seen in Figure 5.11(a), in the case of low density NWs assembly (NWs diluted in their synthesis solution) aligned by the application of a magnetic field, the assembly has the highest M_r/M_S (≈ 0.9) squareness while the random

---

[1] Packing density (also called packing fraction) is the density of NWs inside the compacted sample. The equation for calculating the packing density is presented in reference [142] [150]

nanopowder assembly (Figure 5.11(b) has a M_r/M_S of 0.5. The high density and thus compacted samples display a better M_r/M_S compared to the powder, both in the cases for with and without the magnetic field during the elaboration.

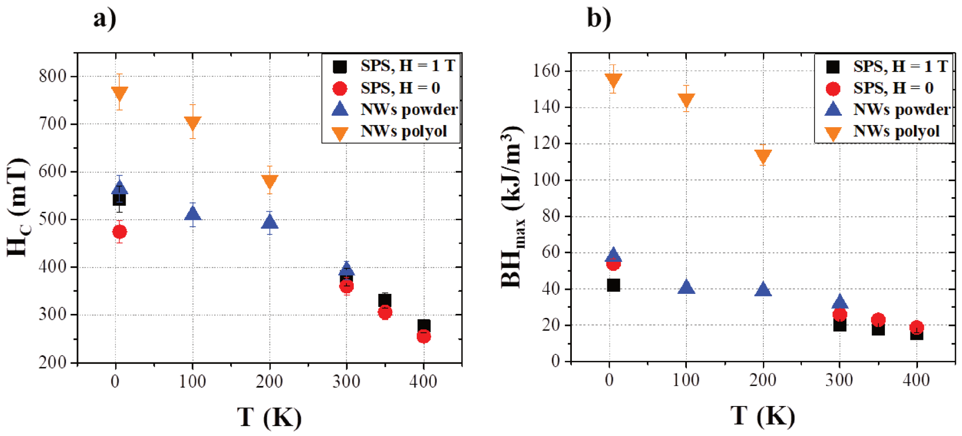

Figure 5.12: Comparing magnetic properties of different samples: (a) Magnetic coercive field (H_C), and (b) Magnetic energy product (BH_{max}).

Samples	SQ	M_r (emu/g)	M_S (emu/g)	M_r/M_S	H_C (mT)	BH_{max} (kJ/m^3)
NWs in polyol	0.6	-	-	0.88	767.4	155.7
Powder	0.31	89.5	169	0.53	564	58
SPS under 1 T	0.48	63	97.7	0.65	543.1	42.2
SPS under 0 T	0.52	77.3	120	0.64	474.6	54

Table 5.2: Magnetic properties of samples at 5 K

The magnetic properties (H_C and BH_{max}) of these four samples at different temperatures are presented in Figure 5.12. Obviously, the polyol sample (see orange symbol) exhibits a highest coercive field and energy product (BH_{max}) since NWs are well aligned within their low density solution (low interactions). In principle, a better alignment lead to reach a higher magnetic anisotropy then improving the coercive field and magnetic energy. Surprisingly enough, the compacted samples (see black and red symbols), especially the compacted sample under a magnetic field (H = 1 T), do not show a higher coercivity neither a higher BH_{max} compared to the nanopowder as expected by simulation (see Figure 5.12 and Table 5.2). This result becomes questionable since the compacted samples presents a higher packing density and better NWs alignment compare to the powder. In this case, a factor that can explain this loss of the coercive field is the strong dipolar interaction between the NWs inside their bulk assembly. It is well known that the dipolar interaction becomes stronger when the NWs are closer to each other (higher packing density) [111] [235]. However, as we already stressed before, Panagiotopoulos et al. reported that the effect of dipolar interaction should not be predominant for Co high density assembly. The intrinsic magnetocrystalline anisotropy of Co should have much higher impact on the magnetic properties of NWs assembly [149] [150]. Therefore, it should exist another factor that drives the observed magnetic coercive field loss. This latter leads to reduce the magnetic energy product of compacted materials. We can note that, the energy product of materials depend also on the magnetization (M_r and M_S). In the case of our SPS samples, the remanent magnetization (M_r) and magnetization at saturation is also reduced after the SPS process, see table 5.2. These reduction may derive from the oxidation of NWs surface. A thin layer of CoO can easily growth on the surface of the Co NWs when it enters in contact with air. This thin layer has been already reported to be able to reduce the magnetization of the cobalt NWs but cannot explain quantitatively the loss we observed here [142]. The effect and the presence of this thin layer of CoO can be also observed in Fig. 5.11 where a shift of the hysteresis loop is observed at low temperature (5K).

All our results on several NWs assembly, going from low density and low interaction up to strong interactions and high density assembly, put in evidence few discrepancies. From one side the simulations indicate that increasing the packing fraction in high density assembly should keep good magnetic properties (H_C and BH_{max}). From the other side if we take into account our results as well as the experimental results observed in literature [6] [51], increasing the NWs density brings to the decreasing of the magnetic properties of the NWs assembly. Also, if the loose in magnetization can be explained by the oxidation of the NWs, the decreasing of the coercive field, in well organized high dense assembly, still remain challenging to explain. Answering to this question is only a possibility to achieve an optimized coercive field and reach a high energy product in the bulk-assembly. In order to explain our experimental observations, we decided to performed micromagnetic simulations using an open source package (NMAG). The detail of this study is presented in the section below.

5.3 Magnetic properties of nanowires assembly: Micromagnetic simulation study

5.3.1 Introduction

In the previous paragraph, our magnetic measurements of cobalt NWs shows that the coercivity of the Co nanocrystals as well as the magnetic energy do not increase with the increase in aspect ratio monotonously suggesting that the tip shape and the microstructure also play an important role in the magnetization reversal process of the Co nanocrystals. We thus could demonstrate that the morphology (i.e. aspect ratio and tip shape) plays a much less crucial role than the crystal defaults and NWs interactions/organization. To further understand the effect of the alignment and thus of the interactions on the magnetic properties in the Co NWs assembly, micromagnetic simulations are performed here.

It is worth mentioning that the effect of the dipole interaction was recently studied by micromagnetic simulation. F. Zighem et al. [235] depicted the effect of the dipolar interactions upon the magnetic behavior of finite/infinite rows and hexagonal arrays of perfect ordered NWs. They demonstrated that the dipolar interactions are more and more effective when the inter-nanowires distance decreases. In other words, the impact of dipolar interaction becomes important when the packing fraction density is larger than a critical value. In the case of a packing fraction density (**P**) value (**P**=0.4) (equivalent to a inter-nanowires distance of 5 nm), the infinite hexagonal arrays of nanowires lose 30% of both coercivity and remanence magnetization. This loss finally reduced the magnetic energy of the nanostructure assembly and confirms the previous C. Kittel theory [76] on the decreasing of the coercivity behavior with the increasing packing density of the particles. Even if we could not calculate the magnetic energy loss in the

finite/infinite rows and hexagonal arrays case because of the normalized magnetic properties presented [235], this study allows understanding how the magnetic interactions between NWs may be very destructive even in a perfect (not really realistic) hexagonal arrangements of NWs.

Focusing on the same issues, L. Panagiotopoulos et al. [149] reported that the dipolar interactions are not a predominant factor in the case of large bundles of aligned cobalt NWs. They claim that, due to the intrinsic high magnetocrystalline anisotropy of the Co, the bundles of NWs with a large packing fraction density $\mathbf{P} = 0.7$, should be able to reach the maximum magnetic energy expected for an isolated Co nanowire (i.e. 630.65 kJ/m^3). In the frame of these conflicting results, D. Niarchos et al. [137] confirmed that by increasing the packing fraction density of Co NWs assembly having high magnetocrystalline anisotropy, a high magnetic energy is reached. These latter results pointed out the important role of the magnetocrystalline anisotropy not taken into account in the case of the infinite hexagonal NWs arrays of the previous cited reference [235]. Also, these studies show how delicate is the question of the optimization of the magnetic energy of NWs assembly as this depends on the tight balance between the magnetic properties of each nanowire (i.e. intrinsic magnetic properties of nano-magnet) as well as of their organization and density inside the assembly (i.e. macroscopic arrangements/properties).

As a matter of fact, from the simulation point of view, a dense packed structure of Co NWs with high magnetocrystalline anisotropy and perfect alignment is the best solution to obtain a high magnetic energy and thus a good permanent nanostructured magnet [149]. However, our experiments have been showing that this is not a trivial task and to reach this optimized structure is still a challenge since the misalignment of nanowires inexorably occurs and likely reduces the magnetic properties of the final nanostructured assembly. Besides, the comparison between several experiments performed on NWs assembly also suggests that when good bulk mechanical properties are reached, an important loss of the magnetic properties is observed, followed by an inescapable misalignment/disorder of the nanostructured bulk system (see Figure 5.13). As shown in Figure 5.13(a), our experiments have depicted a significant reduction of the BH_{max} when the packing fraction density increases. A similar behavior is observed in literatures (Figure 5.13(b)). In the experiments of Gandha's group, the Co NWs assembly are dispersed and aligned in an epoxy matrix under an external applied magnetic field [51]. This structure has a low packing fraction density and shows a high BH_{max} value (i.e.

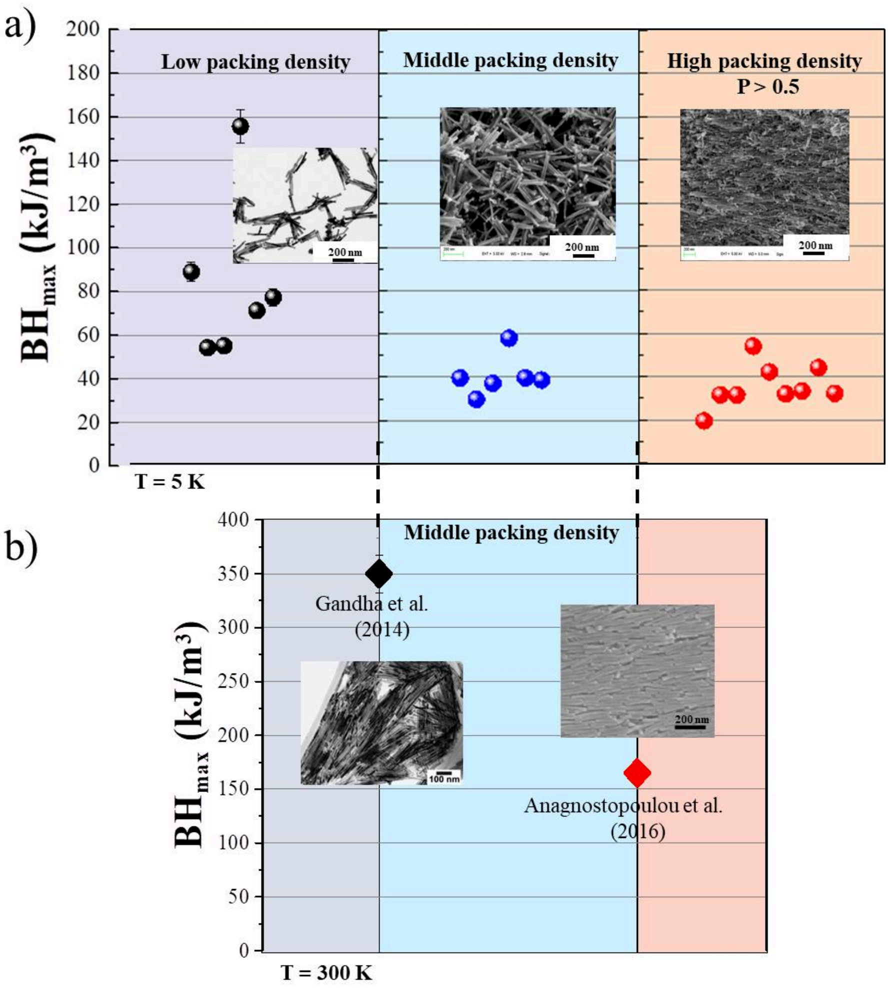

Figure 5.13: Magnetic energy, BH_{max}, of Co NWs assembly in different range of their packing fraction density (described by the background color). (a) Our experimental results; (b) Experimental results from literatures (Anagnostopoulou et al. [6] and Gandha et al. [51]).

350 kJ/m^3). However, when the packing fraction density is increased as described in the experiment of Anagnostopoulou et al. (i.e. Co NWs powders, are aligned under an applied magnetic field on a wafer), the BH_{max} value decreases sharply (i.e. 165 kJ/m^3). These complex scenario points out the ”tricky” problem of the magnetic and mechanical properties optimization and of their reconciliation with the theoretical expectations.

In this section, I am going to present micromagnetic simulation study. We decided to perform this study in order to understand the discrepancy between the previous studies on dipolar interactions effects and the experimental results reported into literatures. I will thus report in the following paragraphs the magnetic behaviors of Co NWs organized in a realistic compacted assembly where an unavoidable percentage of NWs are misaligned. I took here into account various misalignment angles, α (from 0°to 90°) compared to both a specific easy direction of the assembly and the magnetic field applied and we vary the percentage of misaligned NWs inside the bulk structure (from 0 to 75% of misalignment). The magnetic anisotropy of the final macroscopic assembly is finally discussed as a function of different geometrical arrangements.

5.3.2 Effect of the macroscopic shape of the Nanowires assembly

In this paragraph, we raise the question of understanding if the magnetic behavior of nanowires (NWs) organized in a well-defined macroscopic assembly, may be affected by the macroscopic shape of this latter. In order to answer this question, we propose to simulate a bi-dimensional finite arrangement of NWs with two different macroscopic shapes (see Figure 5.14).

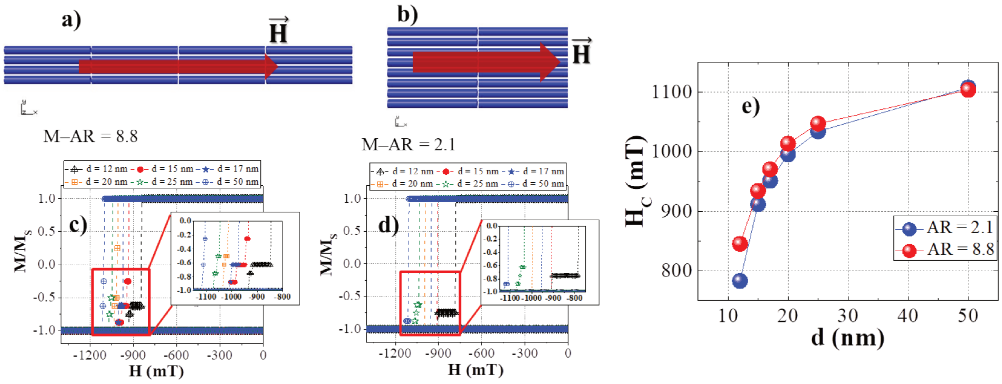

Figure 5.14: The hysteresis loops of 2D NWs arrangements with: (a, c) M-AR = 8.8 and (b, d) M-AR = 2.1. The distance between the centers of NWs varied from d = 12 nm to 50 nm in order to study the effect of the dipolar interactions. The field is applied parallel to the length of the NWs as shown by the red arrows in the top sketches of the 2D arrangements. (e) The coercivity values obtained in c and d are shown as function of d for both the 2D arrangements presented in a and b and having different M-AR.

As already discussed before, the magnetic properties of a finite row of nanowires were reported by F. Zighem et al. [235]. In this case the regular finite arrangement of nanowires has put in evidence the important role of the dipolar interactions upon the static magnetic properties of the nanowires ensemble. T. Maurer et al. [111] had also previously shown that the dipolar field distribution is localized mainly around the tip of the nanowire and decreased rapidly toward the long axis and the radial direction outside the NWs. Since it has previously been demonstrated that the magnetic behavior of rows of infinite nanowires is equivalent to the row of a sufficient ($N > 13$) amount of finite [235] NWs, we decided to simulate 16 nanowires ordered in a matrix of [4x4] cylinders lying in the Oxz plane (see Figure 5.14). The Macroscopic Aspect Ratio (i.e. the aspect ratio of the bi-dimensional assembly of NWs), M-AR from now on, is the ratio between the two macroscopic lengths of the matrix taking into account the side dimension of the NWs and their separation. It is important to underline here, that in order to take into account the effect of the dipolar interactions/field on the magnetic properties ensemble, the distance between the NWs in the macroscopic assembly is kept in the nanometric scale.

The matrix [4x4] in Figure 5.14 (a) presents a M-AR = 8.8. From this M-AR value (see Figure 5.14), it becomes questionable if the macroscopic shape anisotropy can have an impact on the magnetic reversal mechanism of the global arrangement. As a matter of fact the arrangements of NWs in Figure 5.14(a) with a M-AR=8.8 is macroscopically shaped as a unidimensional structure more than a bi-dimensional one. Thus, in order to understand the effect of the bi-dimensional arrangement on the same total number of NWs, we also simulated a matrix of [8x2] with a M-AR = 2.1. In both these 2D arrangements, the distance between the centers of the long axis of closest nanowires (called *d*) is varied from 12 nm to 50 nm (diameter of nanowire is kept at 10nm - see paragraph 2.2). This means that the distance between the lateral surface of the nanowires changes from 2 nm to 40 nm. This minimum value of 2 nm takes into account the fact that in the experimental cases reported into literature, it seems to be unavoidable the presence of a very thin oxide layer (CoO). In fact, the oxidation of the cobalt NWs surface is usually experimentally observed [112]. The typical magnetization curves obtained by simulating these two bi-dimensional arrangements are shown in Figure 5.14.

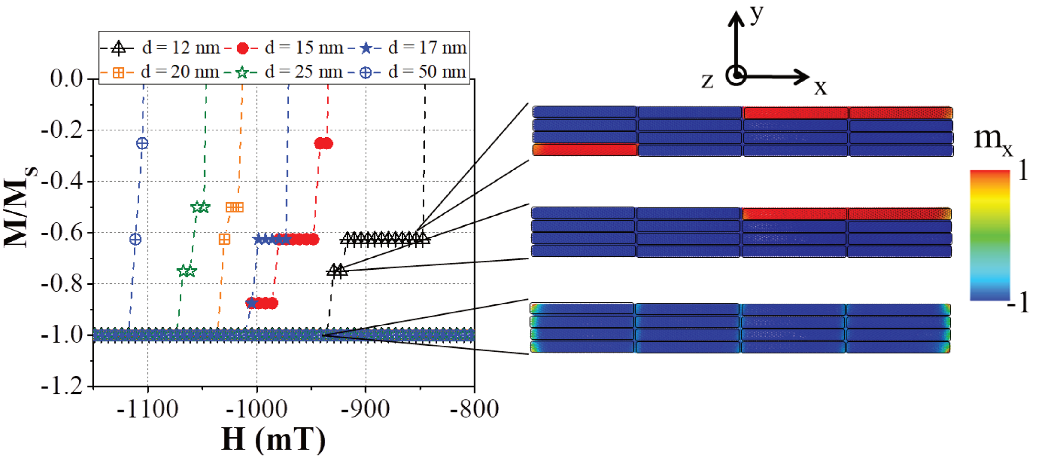

Figure 5.15: Sketch of the reversal mechanism of nanowires at the plateau-like behavior observed in the third quadrant of the magnetic hysteresis loop.

The simulated magnetization curves are shown in Figure 5.14 only for the second and third quadrant of the magnetic hysteresis loop, as the first and the forth are completely symmetrical and thus redundant. They show a similar behavior in both cases: the reversal mechanism depends on the distance *d* as the coercivity increases with the increasing distance between the NWs and several magnetization steps appears mainly at small distance *d* ($d < 20$nm). It is worth explaining here that the reversal mechanism is mainly given by the incoherent reversal of the spins inside the NWs. We could not identify clear domain wall at the reversal field by NMAG results. Nevertheless, a starting point for the reversal mechanism is nucleated at the edge of the NWs where the demagnetizing field is high. We report in Figure 5.14(e) the obtained coercivity as a function of d for both the studied arrangements.

The difference between the coercivity of the two cases becomes more and more negligible as the distance between the NWs increases. This is coherent with the previous study [235] showing the decreasing effect of the dipolar interaction with the increasing of the distance between the NWs. Our results put in evidence though, that even if the dipolar field is less important on the lateral radial direction of the NWs [111] the effect is clearly important for distances $d < 25$nm. At $d = 12$ nm, the difference between the coercive field of the two structures is of 62 mT which is not negligible for the applications. This result also points out an important effect linked to the global shape of the assembled structure. When nanowires are close to each other ($d < 25$ nm), they behave collectively even if not necessarily simultaneously. Thus, the demagnetizing field of the thin film (or 2D NWs arrangement) is predominant, so that a lower external field is needed to demagnetize the magnetic ensemble (also called the coercive field). In this frame the film of NWs having the higher M-AR (i.e. M-AR = 8.8), presents the lower demagnetizing field and thus the higher coercivity. Indeed, the calculated demagnetizing field is 430.4 mT for M-AR = 8.8 and 726.5 mT for M-AR = 2.1 when magnetization is at the saturation value. By increasing d, the demagnetizing field of the ensemble of NWs decreases rapidly both for the high and for the low M-AR as reported before [235]. Therefore, the coercivity increases for both cases (see Figure 5.14 (e)) and approaches rapidly the maximum value of the single isolated nanowire as a function of the NWs distance d. In the case of the maximum distance experimented, a simultaneous reversal mechanism of the ensemble of NWs is in fact observed within the arrangements (see Figure 5.14, the absence of steps in the hysteresis loops is observable).

In order to better explain the magnetization steps that appears mainly at small distance d (see Figure 5.14) we report in Figure 5.15 a zoom of the third quadrant of the simulated magnetic cycles in the case of the 2D arrangement with a M-AR=8.8 (see Figure 5.14 (c)). The plateau-like or step behavior in these curves is connected to the non-reversal mechanism of the magnetization of few nanowires. As reported in Figure 5.15 for the 2D structure composed by 16 NWs with a separation $d = 12$nm and a shape defined by a M-AR = 8.8, the magnetization of 13 NWs reversed simultaneously under the application of -850 mT (blue cylinders in Figure 5.15) while 3 of them (randomly distributed on the border of the 2D structure) stayed non-reversed (red cylinders in Figure 5.15). One of these 3 NWs reverses when the magnetic field has reached a higher value of 922 mT and the other two reverse at 936 mT. At each reversal mechanism, the magnetization approaches more and more the saturation value and the mechanism is not continuous but by steps. When the distance d increases, the plateau/step becomes smaller and smaller then disappears for $d > 20$nm, giving rise to a concomitant reversal mechanism of the NWs ensemble. This happens earlier ($d = 15$ nm) in the case of the 2D arrangement with a shape of M-AR = 2.1 (see Figure 5.14.b).

This behavior is likely linked to the effect of the dipolar field distribution. As mentioned before, the dipolar fields values are higher around the nanowire tips where the existence of a nucleation point promoting the reversal of the neighboring NWs has been already demonstrated [111] [235]. The strength of dipolar field drops quickly toward to the long axis and the radial direction outside the NWs [111]. Thus the number of nucleation points in the 2D arrangements, is driven by the predominant dipolar field at the NWs tips. In Figure 5.14, it is easy to note that the number of NWs interacting by the tip-side (and thus the possible nucleation points) is higher in the 2D structure with a M-AR = 8.8. This can explain the reason why the plateau-like behavior is stable on a higher range of distances d in the case of this latter shaped 2D arrangement.

5.3.3 Competition between the lateral dipolar field interactions and the axial ones

After having studied the effect of the dipolar interaction and the macroscopic shape in the bi-dimensional NWs arrangements and before going towards the study of the 3D bulk nanostructured assembly, we here analyze into details the effect of the NWs misalignment on the reversal magnetic mechanism of an assembly. As reported before [111], the dipolar interactions on the coercivity are very sensitive to the geometrical arrangement of the NWs. Thus here, we decided to use a simple model counting from 4 to 6 NWs arranged in different geometries. Two main cases have been considered (see Figure 5.16(a)): the misaligned NWs are at the tip-tip interaction (B – in Figure 5.16(a)); the misaligned NWs are out of tip-tip interaction (C – in Figure 5.16(a)). The case of the perfect alignment has been taken into account as a reference (A – in Figure 5.16(a)). As already reported [111], the dipolar field at the tips is strongly dependent from the distance between the tips as well as the lateral dipolar field of the wire. Therefore, we set the lateral surface distance between the NWs equal 2 nm (corresponding to the smallest possible distance between the NWs due to the usual oxide layer observed experimentally). This allowed a lateral proximity of the tips strongly enough to study the effect of the stray field upon the variation of the parameters a and b reported in Figure 5.16(a). These parameters are respectively the inter-distance between the tips (a) and the lateral surface distance between the misaligned NWs (b) (see for clarity Figure 5.16(a)). We thus performed the hysteresis loops in the 3 cases (A, B and C) by varying a and b. The analysis of these simulations (H_C mainly) is reported as a function of the varied geometrical parameters (Figure 5.16(c) and 5.16(d)). The hysteresis loops of the 3 systems (A, B and C) having a and b equal 2 nm, are presented in Figure 5.16(b) in order to compare the reversal process in the 3 different arrangements.

Case A: this case considers 4 NWs ordered parallel to each other in the Oxy plane with parameter a changing from 2 nm to 50 nm. Considering a = 2 nm, NWs reverse homogeneously when the reversal field is applied (see black line in Figure 5.16(b)). This behavior is similar to the one of an isolate NW. However, the coercive field is lower of about 18 % than the isolate case due to the dipolar interaction. When a increases up to 10 nm, the system starts to reverse randomly and about 3 NWs reverse at 954 mT, while the last one reverses at 985mT (the hysteresis loop is not shown here). This observation confirms previous discussed results [111] and it depends on the balance between the behavior of the stray field outside the tip, along the length axis of the NW, compared to the decreasing

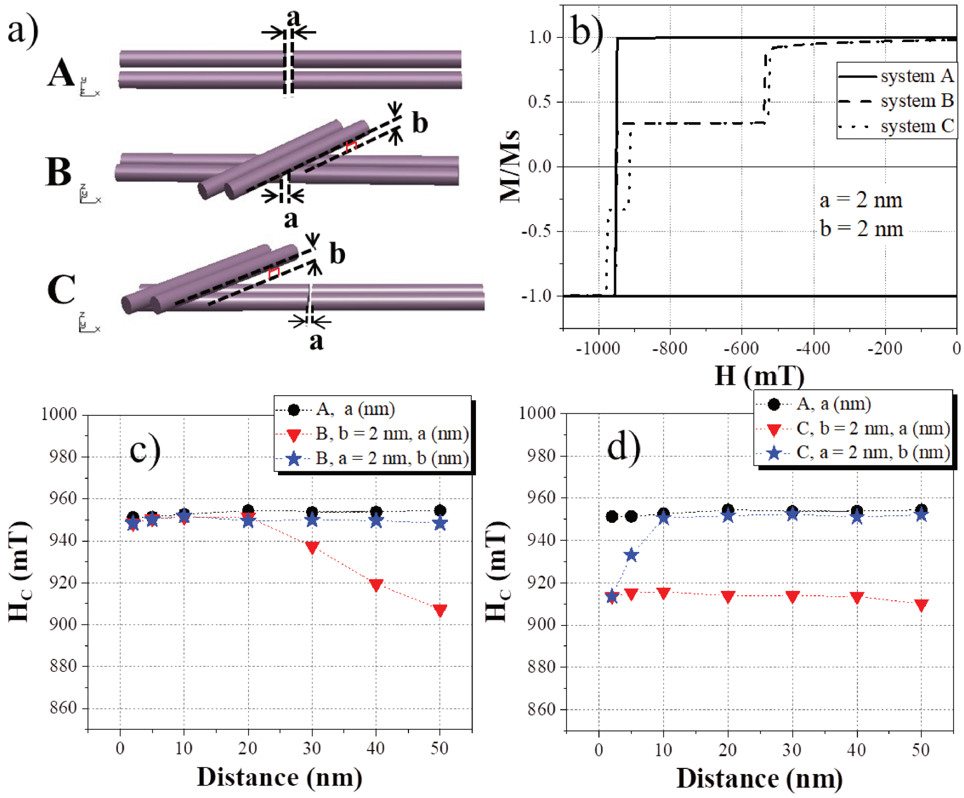

Figure 5.16: Effect of misaligned NWs: (a) NWs configuration used in the calculation for the case A, B and C. a is the tips-tips distance and b is the distance between the lateral surface of the misaligned NWs on the top and the lateral surface of the aligned NWs on the bottom; (b) Hysteresis loops in both 3 cases (A, B and C) when a and b are fixed at 2 nm. Coercivity as a function of parameters a and b are reported for: (c) case B and(d) case C. (see text for better explanation)

along the radial direction. The decreasing of interaction at the tip-tip (i.e. increasing a) leads to the insignificantly increase (3 mT) of the overall coercivity of the 4 NWs. Therefore the coercive field seems to be constant as a function of a (see black circle symbol in Figure 4(c) or (d)).

Case B: in this case we considered the effect of two misaligned NWs on the top of the four nanowires tips aligned as in the case A. Two misaligned NWs are thus placed near the tip-tip interaction, as this is the area where the stronger dipolar field should be experienced [111]. In this case, we varied alternately a and b from 2 nm up to 50 nm (see Figure 5.16(c) and (d) for the case B). The aim was to investigate the role of the misalignment/disorder on the reverse magnetic process of the whole assembly (i.e. 6 NWs) and thus on the coercivity values. As can be seen in Figure 5.16.b (dash line), when the misaligned NWs are placed close to the tips where the stray field is strong (a and b fixed at 2 nm) the appearance of a step-like reversal behavior is observed as function of the magnetic field applied. Nevertheless, the coercivity of the overall system is not affected. By fixing a and changing b, the coercive field remains constant (see blue symbol in Figure 5.16(c)). Thus, the presence of the misaligned NWs has no effect on the coercive field of the system when the tip-tip interaction is strong. It is important to notice that this configuration is slightly different from the ones studied in [111]. Here the lateral dipolar field of the misaligned NWs is acting at the same time of the dipolar field at the tip-tip position (depending on the distance b). Also the NWs ensemble here is tri-dimensional and not bi-dimensional arranged as in the case of the [111]. The configuration used here is much relevant for the further studies on the 3D assembly. To verify the relation between these two contributions, we set b at its smallest value (2 nm) and we varied a. In this case, the tip-tip interaction becomes less and less important when the distance a increases. The coercive field as a function of a in this case, is shown in Figure 5.16(c) (red symbol). We can notice that, starting from $a = 20$ nm, the coercive field starts to decrease. This behavior clearly indicates that the presence of the misaligned NWs have the ability to promote the switching of the closest NWs when the tip-tip interaction becomes weak, leading to the loss of the overall coercivity of the NWs *ensemble*. In conclusion the case B taught us that although the misaligned NWs has no effect on the coercivity in the case of strong dipolar interaction at the tip-tip spot, their lateral dipolar field becomes more and more effective once the tip-tip interaction start to be negligible compared to the lateral dipolar field of the misaligned NWs. We remind here that the final goal of an assembly is to keep the coercivity at the maximum value in order not to destroy the cobalt nano-magnet properties inside the 3D assembly.

Case C: in this case we considered the effect of the misaligned NWs placed far from the tip-tip interaction (see Figure 5.16(a) – C). Similarly as studied in the previous case, we varied a and b respectively from 2 nm up to 50 nm. These results are presented in Figure 5.16(d). When b is fixed by 2 nm then a is increased (see red symbol), the coercivity drops down to 913 mT compare to 951 mT of the case A. This loss is clearly linked to the non-concomitant reversal switching of the NWs and thus to the “plateau-like” behavior observed in Figure 5.16(b). (see dashed line). The first large “plateau” comes from the early switching of the misaligned NWs at - 526 mT applied magnetic field. The second one is linked to the consecutive random switching of the aligned NWs. This latter non-concomitant reversal behavior leads to the loss of the coercivity observed in Figure 5.16(d). Increasing a and thus decreasing the dipolar interaction at the tip-tip spot does not change the coercivity as the lateral dipolar field of the misaligned NWs is still strong and thus predominant. By increasing b and keeping $a = 2$ nm, the role of the misaligned NWs is obviously reduced and the system recovers its coercivity rapidly (at b = 10 nm).

In conclusion, this 3 cases bring us to learn that in a tri-dimensional arrangement of misaligned NWs, the lateral dipolar interactions are predominant compared to the tip-tip ones. Thus, contrary to the bi-dimensional case studied before [111]) and ([235], the reciprocal arrangement between the NWs plays an important role due to the delicate balance between the axial and radial interactions. This point will be crucial for the bulk nanostructured assembly.

In the frame of this simple model, we can thus conclude that the effect of misaligned NWs on the reversal and coercive field of the tri-dimensional ensemble are extremely sensitive to the geometrical arrangement of the aligned NWs compared to the misaligned ones. Indeed, when the assembly is highly packed ($a = 2$ nm; $b = 2$ nm in our case), misaligned NWs located at the tip-tip interaction have no effect on the coercivity of the ensemble while out of tip-tip interaction the loss of coercivity is significant. In terms of dipolar field, this lets us understand that the competition between the lateral dipolar field and the axial field of the NWs is mostly won by the first one in the geometrical arrangement of the case C in a packed nanostructured ensemble and by the second one for the case B. Also, we understand that the destructive influence of the first one is of higher impact than the second on the coercive field of the packed ensemble.

5.3.4 Effect of the misalignment inside the packed nanostructure Permanent Magnet

Based on the background described above, we investigated the effect of the misaligned NWs on different geometry arrangements in both 2D and 3D structures for a higher number of NWs (sufficiently enough to reproduce the bulk nanostructured pellet properties, experimentally obtained by SPS sintering [64], [142], [143]. We thus considered here a 2D arrangement of 16 NWs (see Figure 5.17) and a 3D arrangement of 27 NWs (see Figure 5.18) reproducing the observed misalignment in the nanostructured cobalt based ceramics [64], [142], [143]. It is worth noticing here, that misalignment concerns have been already addressed in micromagnetic modeling [137] for bundles of NWs. In this case while the misalignment degree of the NWs inside the bundle increases (i.e. the inclination angle of the NWs increases), the packing density of the bundle decreases. We did address here the misalignment issue while the high packing density is kept constant in order to simulate the realistic structure obtained in the experimental results of [6] [143].

In order to provide a comparison between the magnetic properties of two different macroscopic shaped arrangements, we considered 2D and 3D NWs organization. In both cases we considered various NWs misalignment: 25%, 50% and 75% (see Figure 5.17 and 5.18). These percentages were calculated by considering the number of misaligned NWs divided by the total number of NWs constituting the ensemble. Also, we considered various degrees of misalignment by varying the angle α between 0 °and 90 °(see the sketches on top of figure 5.17 and 5.18). This allows us to study the effect of the disorder for each degree of misalignment (see graphs in Figure 5.17.a, 5.17.b and 5.17.c). For each percentage of misalignment and for each degree of disorder for the misaligned NWs (i.e. for each α value), we studied the reversal mechanism of the magnetization as a function of the direction of the applied external field. We could thus analyze the behavior of the coercive field of the NWs ensemble as function of θ (see Figure 5.17). In these simulations the lateral surface distance between wires has been set at the minimum (i.e. 2 nm) in order to consider a high packing density of the final ensemble. In fact, in our case of the 3D structure, the packing fraction $\mathbf{P}$ is obtained by: $\mathbf{P} = N.V_{cyl}/V_{total}$, where N is the number of NWs; V_{cyl} is the volume of one cylinder with the length of 100 nm and the

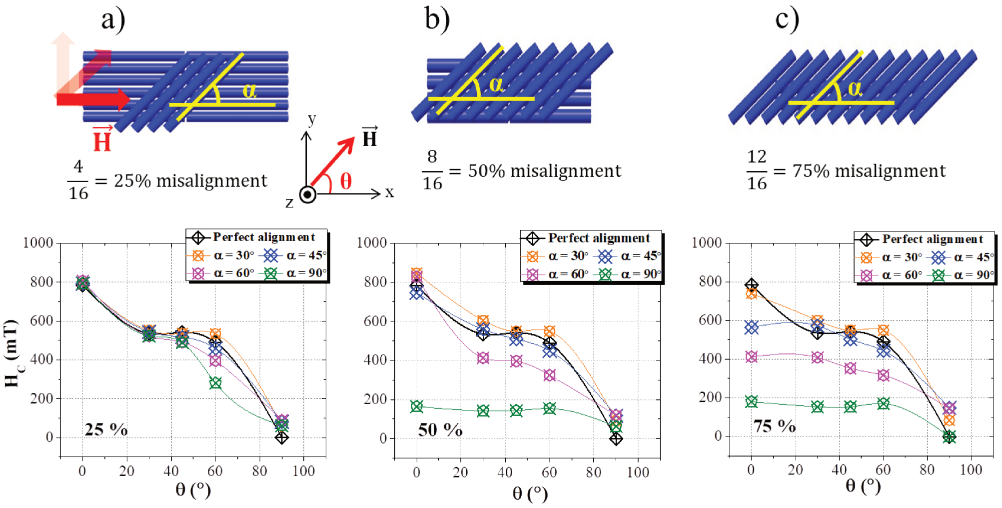

Figure 5.17: (bottom) Coercivity behavior of various two-dimensional geometry arrangements of NWs with different percentages of misaligned NWs: (a) 25 % (i.e. 4 NWs are misaligned over a total of 16); (b) 50 %; (c) 75 %. Typical sketches are presented on top. The considered misaligned angles (α) varies from 0 °to 90 °compared to the x direction of the aligned NWs (see the sketches). The direction of the applied magnetic field is considered in the plane of the two-dimensional structure (xOy) and it increases from Ox by an angle θ (θ = 0 °, 30 °, 45 °, 60 °and 90 °) in the anti-clockwise rotation.

radius of 5 nm; V_{total} is total volume of the system which depends on the distance between NWs. The highest packing fraction in our 3D structure (with a distance of 2 nm between NWs) is $\mathbf{P}$ = 0.603 (which is close to the experimental values obtained in literature for nanostructured bulk materials based on NWs [142] [143]. To take into account all the dipolar interactions (radial and axial field) already discussed in the previous section, the misaligned NWs were placed both on the tip and on the lateral surface of the aligned NWs. In all the studied configurations, the perfect aligned structure is reported in sake of comparison (i.e. the total number of NWs is aligned along the Ox axis).

In the case of the two-dimensional arrangement, it is interesting to notice that in the case of the 25 % of misaligned NWs, the coercivity behavior does not deviate from the one of the perfect structure even when the degree of disorder is maximum (α = 90 °) (see Figure 5.17.a). As in the case of perfect aligned structure, the coercivity goes to zero when the applied magnetic field is perpendicular to the aligned axis of the NWs. These results demonstrate that a nanostructured ensemble with 25 % of misaligned NWs has a strong easy axis along Ox (axis of the aligned NWs) whatever is the angle of misalignment of the NWs (i.e. the degree of disorder). Surprisingly enough this is also true for the higher percentage of misalignment (i.e. 50 %) (see Figure 5.17.b) where only in the case of the highest disorder (i.e. α =90 °) a big loss of coercivity is observed. In this latter case, the system losses 80 % of the coercive field compared to the perfect aligned case and show almost no easy macroscopic axis (see the green symbols in Figure 5.17.b). Finally for the case of 75 % of misalignment (Figure 5.17.c), the coercivity drops down quickly

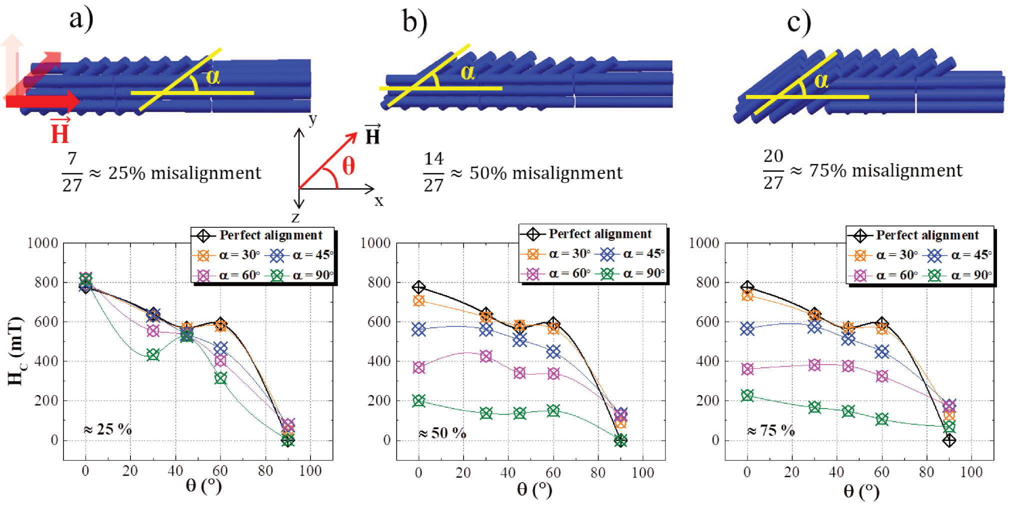

Figure 5.18: (bottom) Coercivity behavior of various two-dimensional geometry arrangements of NWs with different percentages of misaligned NWs: a) 25 % (i.e. 7 NWs are misaligned over a total of 27); b) 50 % ; c) 75 %. Typical sketches are presented on top. The considered misaligned angles (α) varies from 0°to 90 °compared to the x direction of the aligned NWs (see the sketches). The direction of the applied magnetic field is considered in the plane of the two-dimensional structure (xOy) and it increases from Ox by an angle θ (θ = 0°, 30°, 45°, 60°and 90°) in the anti-clockwise rotation.

toward the increasing of α (i.e. of the disorder). However, a small disorder ($\alpha = 30$ °) still keeps the coercivity value as high as the perfect aligned case (see orange symbol in Figure 5.17.c). The Ox axis is less and less easy for the magnetization of the ensemble as a function of the increasing α, except for the $\alpha = 90$ °.

Figure 5.18 shows the coercive field behavior of different bundles of 27 NWs arranged in three-dimensional structure. Again, several percentages of misalignment are considered (i.e. 25%, 50% and 75%). Similarly to the previous bidimentional case, the 25% of misalignment does not affect the coercivity behavior of ensemble (see Figure 5.18.a). Also in this case, the easy axis is clearly along the length of the aligned NWs (Ox axis). Thus the mean behavior of the 2D and 3D arrangement behaves qualitatively in the same way for the smallest percentage of misalignment considered. In fact, for 50% of misalignment (see Figure 5.18.b) the coercive field of the system decreases rapidly with the increasing degree of disorder (α). Only for $\alpha \leq 30$ °, the coercivity loss is smaller than 10% compared to the one of the perfect aligned case. The highest percentage of misalignment (i.e. 75%) shows the same behavior than the previous one (see Figure 5.18.c).

To summarize these results we can say that the misalignment effect leads, as expected, to a loss of the coercivity for a finite number of NWs arranged in both two and three-dimensional. However, the misalignment is acceptable (i.e. no loss of coercivity is observed compared to the perfect aligned structure) when one of the two following conditions is satisfied: i) the percentage of misaligned NWs is smaller than 50%; ii) the degree of disorder, (i.e. value of α), is not higher than 30 °. It is also remarkable that the bidimentional ensemble is more stable in term of coercivity than the tridimensional one (higher degree of disorder and/or misalignment are possible). Both 2D and 3D arrangement presents the easy axis along the length of the aligned NWs opening an interesting way to obtain macroscopic material with a strong uniaxial magnetic anisotropy (comparable to the one of the cobalt nano-object).

5.3.5 Macroscopic Uniaxial stability in nanostructured assembly

In order to study the uniaxial anisotropy in all the previously discussed arrangements, we calculated the anisotropy field ΔH_C and thus the uniaxial anisotropy constant K_U from the observed behavior of Figure 5.17 and 5.18. The ΔH_C and K_U are presented in Figure 5.19 as a function of the disorder degree for the 3 different percentages of misalignments and for both 2D and 3D structures. The anisotropy field in the plane of the 2D and 3D arrangement (xOy) was calculated by the following simple formula: $\Delta H_C = H_C(\theta = 0°) - H_C(\theta = 90°)$. As can be seen in figure 5.19.a and 5.19.b, in the case of the 25% of misaligned NWs (see blue symbol) the anisotropy field is pretty much constant as a function of the increasing degree of disorder α. Moreover, in 2D structure, the ΔH remains stable even when the percentage of misalignment increases up to 50%, with $\alpha \leq 60\ °$.

The magnetic anisotropy can be transformed into a uniaxial (K_U) anisotropy constant by considering a simple model with a free energy density described by (see section 1.1.3 in chapter 1):

$$E = K_U(\sin^2\theta) - M_S H \cos(\varphi - \theta) \tag{5.5}$$

Where φ and θ are respectively the angles direction of the magnetization $\mathbf{M}$ and external field $\mathbf{H}$ from the uniaxial easy axis. The uniaxial anisotropy constant, K_U, is extracted by deriving the energy ($\partial E/\partial\theta = 0$), and taking $\varphi = 0$. In our case, the uniaxial easy axis is in the Ox axis, which is parallel to the aligned NWs. The effective uniaxial anisotropy constant of the NWs assembly as a function of the misalignment angles is reported in Figure 5.19.c for the 2D ensemble and in figure 5.19.d for the 3D one.

This allows concluding on the fact that, nanostructured magnetic materials present high uniaxial anisotropy constant (comparable to the one of the cobalt nano-object). The K_U is tuned by the disorder for misalignments higher than 50% and quite stable in the lower case and/or lower disorder (i.e. α). This studies shade light on the fact that, if misalignment and disorder are experimental inescapable as seen in the first part of this chapter, their effect can be kept negligible under some critical conditions.

5.4 Conclusion

After investigated the magnetic behavior of NWs by both experimental and simulation analysis, we conclude that it is mandatory to optimize the single NW magnetic anisotropy and to align the easy axis of the each NW inside the compacted assembly (or

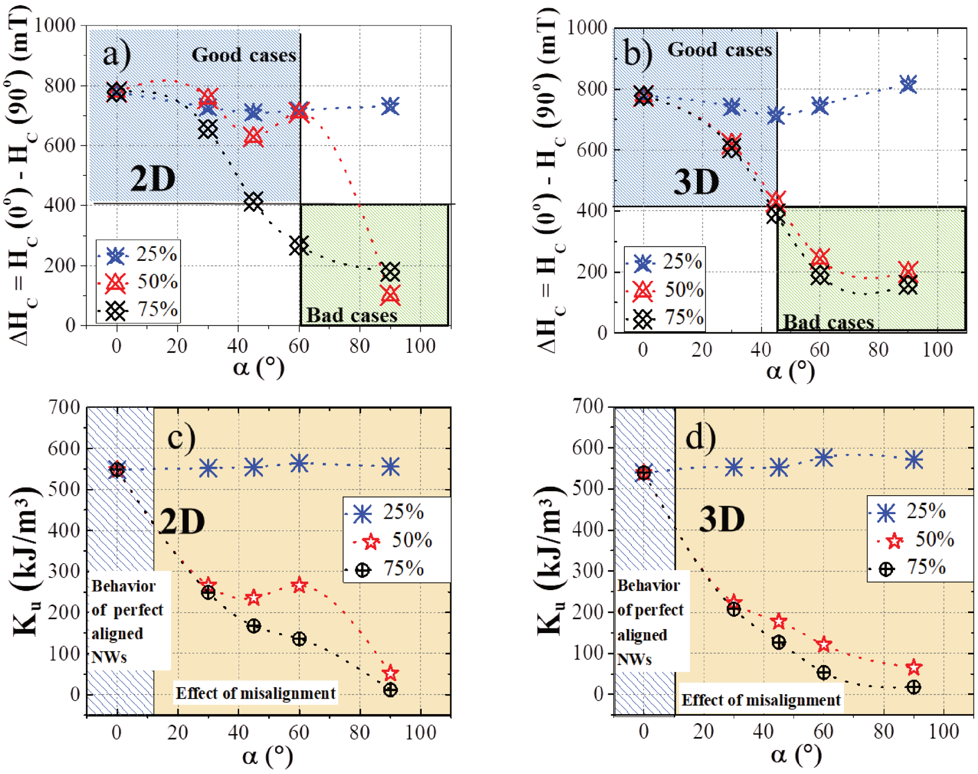

Figure 5.19: Anisotropy field ΔH_C of the nanowires ensemble in: (a) 2D arrangements, (b) 3D arrangement; the correspondent calculated uniaxial constant in: (c) for the 2D arrangement, (d) for the 3D arrangement.

bulk nanostructured material) in order to obtain high magnetic energy for this latter. In the first case, two effects have to be take into account: the shape and the purity of the hexagonal crystalline structure along the NWs length (stacking fault density). Our experimental observations have been showing a clear dependence of the H_C and BH_{max} upon the stacking fault density, no matter is the dispersion and the morphology of the NWs.

In the NWs assembly, the magnetic behavior of NWs depends on their organization. These latter systems can present high uniaxial anisotropy constant (comparable to the one of the cobalt nano-object). The misalignment of NWs inside the assembly leads to a huge loss of the magnetic coercive field, and reduces at its turn their magnetic energy. However, the misalignment is acceptable if one of the following condition is satisfied: (i) the percentage of misaligned NWs is smaller than 50 %; (ii) the degree of disorder (α) is not higher that 30°.

The optimization of cobalt-based bulk-nanostructured from an experimental point of view is still in progress. The perspectives for the next study is to develop the compacted process to improve the magnetic properties of the *ensembles*. One of the proposed method is to use an organic/inorganic environment to disperse and well align the NWs and thus obtaining at the same time a new multiferroic materials and a good rare-earth free permanent magnet.

Chapter 6

General conclusion and perspective

Multiferroic composite materials artificially combining together more than one ferroic phase are extremely attractive not only for their potential applications in multifunctional devices but also because they offer a rich playground for fundamental studies. For instance, a composite nanostructure based on the combination of a ferromagnetic phase with a piezoelectric one, opens fascinating studies thanks to the richness of the physical mechanisms allowing a strong coupling between the two phases. This latter, also called magnetoelectric (ME) coupling, allows controlling the ferromagnetic properties by the application of an electric field and vice versa the ferroelectric ones by a magnetic stimulus. Depending on the nature and the dimension of the connectivity between the two phases, this ME coupling can derive from different mechanisms (exchange coupling, charge carrier, strain mediated effect) and it strongly depends on the interface between the two-ferroic phases. The objective of this Ph.D thesis has been to focus on the strain-mediated ME effect in different artificial composites based on the combination of an inorganic (I) ferromagnetic/magnetostrictive phase and an organic (O) ferroelectric/piezoelectric one. We studied the effect of the connectivity dimension on the magnetic properties of the magnetostrictive phase by local and macroscopic magnetic techniques as well as the dependence of the piezoelectric local behavior upon the hybrid (I/O) interface quality. The dispersion, organization and dipolar interactions of the ferromagnetic phase into a non-magnetic media have also been deeply analyzed both by experimental and simulation studies.

In these purposes, we firstly reported the electric (E)/strain (σ) control of the magnetic stripe nano-domain pattern in a soft ferromagnetic/magnetostrictive finemet alloy thin film deposited on a polymer (kapton) substrate (2-2 connectivity). We compared these results with the magnetic nano-domain pattern behavior under an in-plane magnetic field. In both cases, the external stimulus has been applied *in situ* during local Magnetic Force Microscopy measurements. Our results show that both the E/σ and H external fields allow the destabilization of the magnetic nano-pattern in favor of an homogeneous magnetic configuration and let us deducing that both the external stimulus are able to twist the domain magnetization from the out-of-plane direction to the in-plane one of the film. Relatively low fields are needed to do this. In this contest, we did a statistical analysis of the angle θ between the magnetic nano-domain orientations and the surface of the film (in-plane direction). Our results clearly state that the strain-induced/E control is more efficient and reversible compare to the H-control method. These studies reinforce the idea that the ME hybrid heterostructures can open the way for the electric control of the magnetic information (state) at a nanoscale level via the strain-mediated local mechanism.

Subsequently, we focused on hybrid (I/O) composite thin films based on an electro-active polymer (PVDF) embedding magnetostrictive spherical nanoparticles (NPs). In this case, the connectivity between the two phases is 0-3 although the final ME materials is bidimentional (thin film). In order to study the effect of the hybrid interface quality and the coupling between the two ferroic phases, we considered here two different hybrid films: (a) (PVDF+NPs) nanometric-thin films deposited on a metallic substrate (silicon) and (b) self-standing micrometer-thick films. In both cases we compare the hybrid films response, to the external stimulus (E/σ/H), with the one of the pure phase (ferroelectric and/or ferromagnetic). Different amounts of NPs as well as different degree of dispersion inside the polymer matrix have been considered for our purpose. In the case (a) of very thin films we could observe a piezoelectric local response for either pure PVDF and hybrid samples. Surprisingly enough, the composite film did not show a better electromechanical resonance than the pure PVDF one, putting in evidence a local polarization disorder promoted by the nanoparticles. Although the nano-inclusions are demonstrated to improve the macroscopic polarization properties of the hybrid films, our results point out the important effect of the hybrid interface at a local scale level. A uniform dispersion of the nanoparticles, obtained by functionalization of these latters, allowed improving the local electromechanical response, and slightly re-enhances the local piezoelectric response observed by piezo-response microscopy (PFM). Thus the hybrid interface optimization obtained by the functionalization of the nanoparticles, opens a possible way towards the drop of the electromechanical response in the hybrid systems. Simultaneously to this study, we also could observe an uncommon magnetic behavior at low field (few hundreds of Oe) of the nano-inclusions while increasing the elastic Young modulus of the polymer matrix by decreasing the temperature (the Young modulus was not measured during this work but we referred to its the temperature behavior observed in literature [140] [22]). This behavior has been studied on the 0-3 hybrid self-standing film and it has been observed by performing static magnetic measurements as function of temperature and under a magnetic field applied. These observations confirm again the strong coupling between the two ferroic phases as well as the importance of the hybrid interface quality. In fact, the hysteresis loops measured have shown a strong dependence on the quality of the hybrid interface (i.e. strong dependence on the functionalization and the amount of NPs included in the PVDF film). In order to confirm the magneto-elastic origin of this uncommon behavior and thus the strain-mediated effect on the magnetic properties of these 0-3 composites, more analysis and measurements are needed. This opens several perspectives to this Ph.D. work for the ongoing researches on these hybrid films.

Finally, we investigated the magnetic response of anisotropic nanoparticles (nanowires, NWs) by both experimental and simulation analysis. This ferromagnetic phase is willing to be included into a ferroelectric polymer matrix and to give rise to a (1-3) hybrid composite. Previous studies, on both 2-2- and 0-3 connectivity, have confirmed the crucial importance of the quality of the hybrid interface on the strain-mediated ME coupling between the two ferroic phases. Hence here, in the 1-3 type of composite, we firstly got interested on the optimization of the single ferromagnetic phase as function of its organization in a non-magnetic media. Important incoherencies between the experimental results and the expected theoretical behavior on the magnetic properties of an *ensemble* of NWs reported into literature are discussed here and motivate us to firstly focus on this issue. Thanks to a tight collaboration with a group of elaborators in our laboratory, we could study the static magnetic properties of very well controlled NWs *ensembles*. Our experimental observations have been showing a *dramatic* dependence of the magnetic properties of the NWs not only on their dispersion and organization but also on their crystal structure. If on one hand our experimental results integrate quite well the experimental scenario reported in literature, all these magnetic properties seem not to be in agreement with what is expected by the reported simulation studies. Huge losses of the magnetic energy are observed by increasing the mechanical properties of the *ensemble* of NWs, while micromagnetic simulation of dense bundles of NWs suggest that we should obtain the opposite result. By performing micromagnetic simulations, we could conclude on the relevant parameter driving the misalignment and disorder effect upon the magnetic properties of the *ensemble*. These results together with our experimental observations, suggest that an organic/inorganic environment for controlling the dispersion and the alignment of the NWs will help improving considerably the magnetic properties of the *ensemble*.

Although several improvements on the understanding of the hybrid nano-composites materials have been done during my three years Ph.D. work, I am conscious that many others should be done for fully understand the complex mechanisms in play in these complex artificial materials. Several perspectives of this work have been discussed along the manuscript as they appear so far, the logical follow up of the research we have developed during this work.

- One of them concerns the analysis of the magnetic NPs behavior in 0-3-hybrid structure under the influence of the elastic properties variation of the PVDF. In order to fully corroborate our interpretations of the magnetic observations, a refinement of the analysis by using the magnetic raw data is mandatory. This analysis is very time consuming, both for the measurements and for the treatment of the data and it is still an ongoing research (see Appendix B).

- AC measurements aiming to study the anisotropic constant of the NPs inside the PVDF matrix are also an interesting perspective. By simply analyzing the blocking temperature behavior of the NPs versus the relaxation time for different Young Modulus range of the PVDF (T$<T_G$ and T$>T_G$), may be a way to demonstrate the strain-mediated ME effect observed here on the magnetic moment of the NPs at low magnetic field. This study is now in collaboration with DR. S. Hebert (CRISMAT-ENSICAEN) du to some technical problems we have been experiencing lately on our MPMS system.

- Our studies on the anisotropic magnetic nanoparticles are a fertile background opening a number of studies on their integration inside a piezoelectric polymer matrix. In the case of the strain-mediated ME coupling between the two ferroic phases, increasing the surface/volume ratio of the hybrid interface may enhance the ME coupling in the 1-3 composite [3]. Several challenges have to be overcome for the elaboration of these 1-3 hybrid systems, but they certainly open the promising field of tuning the magnetic properties of the nano-magnets inside the flexible/polymer matrix by the application of an electric (E)/strain (σ) external stimulus. From a fundamental point of view, it will allow our researches to go ahead the comprehension of the delicate balance between the quality of the hybrid interface and the dipolar interaction.

- Last but not least, it would be very interesting from a fundamental point of view, to work on the spatial confinement of the interfaces explored here. The collaboration started during this work with the Clean Room of our University ("Centrale de proximité de Paris Centre" – LPL (UP13)) via the work I had the opportunity to supervise during my Ph.D, of Anh Ngoc Nguyen (Master 2 USTH – Labex SEAM Fellowship at LSPM in 2017), it will allow to perform a specific nano-lithography of the hybrid films by a lithography process developed previously on organic optical devices [12]. This will open a reach scenario of fundamental studies willing to optimize the ME coupling at a nano-scale level towards the new ME nanotechnology.

References

[1] C J Aas et al. “Effect of stacking faults on the magnetocrystalline anisotropy of hcp Co: a first-principles study”. In: *Journal of Physics: Condensed Matter* 25.29 (2013), p. 296006.

[2] I Y Abdullah et al. “Influence of the substrate on the crystalline phase and morphology of poly (vinylidene fluoride)(PVDF) thin film”. In: *Surface Review and Letters* 23.03 (2016), p. 1650005.

[3] M Alnassar et al. “Magnetoelectric polymer nanocomposite for flexible electronics”. In: *Journal of Applied Physics* 117.17 (2015), p. 17D711.

[4] S Ammar et al. “Magnetic properties of ultrafine cobalt ferrite particles synthesized by hydrolysis in a polyol mediumBasis of a presentation given at Materials Discussion No. 3, 26–29 September, 2000, University of Cambridge, UK.” In: *Journal of Materials Chemistry* 11.1 (2001), pp. 186–192.

[5] S Ammar et al. “Magnetic properties of zinc ferrite nanoparticles synthesized by hydrolysis in a polyol medium”. In: *Journal of Physics: Condensed Matter* 18.39 (2006), p. 9055.

[6] E Anagnostopoulou et al. “Dense arrays of cobalt nanorods as rare-earth free permanent magnets”. In: *Nanoscale* 8.7 (2016), pp. 4020–4029.

[7] J S Andrew and D R Clarke. “Enhanced ferroelectric phase content of polyvinylidene difluoride fibers with the addition of magnetic nanoparticles”. In: *Langmuir* 24.16 (2008), pp. 8435–8438.

[8] A Arnau and D Soares. “Fundamentals of piezoelectricity”. In: *Piezoelectric transducers and applications*. Springer, 2009, pp. 1–38.

[9] M Artus et al. “Size-dependent magnetic properties of CoFe2O4 nanoparticles prepared in polyol”. In: *Journal of Physics: Condensed Matter* 23.50 (2011), p. 506001.

[10] E Ascher et al. “Some Properties of Ferromagnetoelectric Nickel-Iodine Boracite, Ni3B7O13I”. In: *Journal of Applied Physics* 37.3 (1966), pp. 1404–1405.

[11] D N Astrov. “The magnetoelectric effect in antiferromagnetics”. In: *Sov. Phys. JETP* 11.3 (1960), pp. 708–709.

[12] G T Ayenew et al. “Self-organized nanoparticle photolithography for two-dimensional patterning of organic light emitting diodes”. In: *Optics express* 22.106 (2014), A1619–A1633.

[13] K Ban et al. “Giant ME effect of multiferroic BaTiO/sub 3/–LaMnO/sub 3/ceramic composites”. In: *IEEE transactions on magnetics* 41.10 (2005), pp. 2793–2795.

[14] F Bargain et al. “From solvent-cast to annealed and poled poly (VDF-co-TrFE) films: New insights on the defective ferroelectric phase”. In: *Polymer* 105 (2016), pp. 144–156.

[15] F Bargain et al. “Semicrystalline organization of VDF- and TrFE-based electroactive terpolymers: Impact of the trans-1, 3, 3, 3-tetrafluoropropene termonomer”. In: *Macromolecules* 50.8 (2017), pp. 3313–3322.

[16] M Benz and W B Euler. “Determination of the crystalline phases of poly (vinylidene fluoride) under different preparation conditions using differential scanning calorimetry and infrared spectroscopy”. In: *Journal of applied polymer science* 89.4 (2003), pp. 1093–1100.

[17] M Bibes and A Barthélémy. “Multiferroics: Towards a magnetoelectric memory”. In: *Nature materials* 7.6 (2008), p. 425.

[18] M I Bichurin et al. “Investigation of magnetoelectric interaction in composite”. In: *Ferroelectrics* 204.1 (1997), pp. 289–297.

[19] A S Borowiak et al. “Electromechanical response of amorphous LaAlO3 thin film probed by scanning probe microscopies”. In: *Applied Physics Letters* 105.1 (2014), p. 012906.

[20] R M Bozorth. “Ferromagnetism”. In: *Van Nostrand Company, New York* 849 (1951).

[21] A Brandlmaier et al. “In situ manipulation of magnetic anisotropy in magnetite thin films”. In: *Physical Review B* 77.10 (2008), p. 104445.

[22] Y Cao et al. “Enhanced thermal conductivity for poly (vinylidene fluoride) composites with nano-carbon fillers”. In: *Rsc Advances* 6.72 (2016), pp. 68357–68362.

[23] C Cavaco, M Van Kampen, and G Lagae Land Borghs. “A room-temperature electrical field–controlled magnetic memory cell”. In: *Journal of materials research* 22.8 (2007), pp. 2111–2115.

[24] N Chakroune et al. “Cobalt-based anisotropic particles prepared by the polyol process”. In: *Journal of materials chemistry* 13.2 (2003), pp. 312–318.

[25] S Chen et al. “Ferroelectric poly (vinylidene fluoride) thin films on Si substrate with the β phase promoted by hydrated magnesium nitrate”. In: *Journal of Applied Physics* 102.10 (2007), p. 104108.

[26] R O Cherifi et al. “Electric-field control of magnetic order above room temperature”. In: *Nature materials* 13.4 (2014), p. 345.

[27] S Chikazumi. *Physics of ferromagnetism, 2nd edn. Clarendon.* 1997.

[28] R V Chopdekar and Y Suzuki. “Magnetoelectric coupling in epitaxial CoFe2O4 on BaTiO3”. In: *Applied physics letters* 89.18 (2006), p. 182506.

[29] B Chu et al. “Large enhancement in polarization response and energy density of poly (vinylidene fluoride-trifluoroethylene-chlorofluoroethylene) by interface effect in nanocomposites”. In: *Applied Physics Letters* 91.12 (2007), p. 122909.

[30] T K Chung, G P Carman, and K P Mohanchandra. “Reversible magnetic domain - wall motion under an electric field in a magnetoelectric thin film”. In: *Applied Physics Letters* 92.11 (2008), p. 112509.

[31] M Coisson et al. “Magnetic properties of FeSiB thin films displaying stripe domains”. In: *Journal of Magnetism and Magnetic Materials* 321.7 (2009), pp. 806–809.

[32] V Corral-Flores et al. “Magnetic properties of nickel–zinc ferrite nanoparticles synthesized by coprecipitation”. In: *physica status solidi (a)* 204.6 (2007), pp. 1742–1745.

[33] V Corral-Flores et al. “Magnetic Properties of Spinel Cobalt–Manganese Ferrites”. In: *IEEE Transactions on Magnetics* 51.4 (2015), pp. 1–4.

[34] RP Cowburn. “Property variation with shape in magnetic nanoelements”. In: *Journal of Physics D: Applied Physics* 33.1 (2000), R1.

[35] O De Abril, M C Sánchez, and C Aroca. “The effect of the in-plane demagnetizing field on films with weak perpendicular magnetic anisotropy”. In: *Journal of applied physics* 100.6 (2006), p. 063904.

[36] P Debye. “Bemerkung zu einigen neuen Versuchen uber einen magneto-elektrischen Richteffekt”. In: *Zeitschrift fur Physik* 36.4 (1926), pp. 300–301.

[37] P Dineva et al. *Dynamic fracture of piezoelectric materials: solution of time-harmonic problems via BIEM.* Vol. 212. Springer Science & Business Media, 2014.

[38] A M Dos Santos et al. “Evidence for the likely occurrence of magnetoferroelectricity in the simple perovskite, BiMnO 3”. In: *Solid State Communications* 122.1 (2002), pp. 49–52.

[39] I E Dzyaloshinskii. “K voprosu o magnitno-elektricheskom effekte v antiferromagnetikakh”. In: *Sov. Phys. JETP* 10.3 (1960), p. 628.

[40] W Eerenstein et al. “Giant sharp and persistent converse magnetoelectric effects in multiferroic epitaxial heterostructures”. In: *Nature materials* 6.5 (2007), p. 348.

[41] S W Fackler et al. “Local control of magnetic anisotropy in transcritical permalloy thin films using ferroelectric BaTiO3 domains”. In: *Applied Physics Letters* 105.21 (2014), p. 212905.

[42] W Fang et al. “Optimization of the magnetic properties of aligned Co nanowires/polymer composites for the fabrication of permanent magnets”. In: *Journal of nanoparticle research* 16.2 (2014), p. 2265.

[43] Z Feng et al. “Effect of uniaxial stress on the electromechanical response of¡ 001¿-oriented Pb (Mg 1/ 3 Nb 2/ 3) O 3–Pb Ti O 3 crystals”. In: *Journal of applied physics* 97.2 (2005), p. 024103.

[44] R Ferré et al. “Magnetization processes in nickel and cobalt electrodeposited nanowires”. In: *Physical Review B* 56.21 (1997), p. 14066.

[45] F A Ferri, M A Pereira-da-Silva, and E Marega. “Magnetic force microscopy: Basic principles and applications”. In: *Atomic Force Microscopy Imaging, Measuring and Manipulating Surfaces at the Atomic Scale.*

[46] A Fert and L Piraux. “Magnetic nanowires”. In: *Journal of Magnetism and Magnetic Materials* 200.1-3 (1999), pp. 338–358.

[47] M Fiebig. “Revival of the magnetoelectric effect”. In: *Journal of Physics D: Applied Physics* 38.8 (2005), R123.

[48] T Fischbacher et al. “A systematic approach to multiphysics extensions of finite-element-based micromagnetic simulations: Nmag”. In: *IEEE Transactions on Magnetics* 43.6 (2007), pp. 2896–2898.

[49] A Franco Jr and F C Silva. “High temperature magnetic properties of cobalt ferrite nanoparticles”. In: *Applied Physics Letters* 96.17 (2010), p. 172505.

[50] M Gajek et al. “Tunnel junctions with multiferroic barriers”. In: *Nature materials* 6.4 (2007), p. 296.

[51] K Gandha et al. “High energy product developed from cobalt nanowires”. In: *Scientific reports* 4 (2014), p. 5345.

[52] S Geprägs et al. “Electric field controlled manipulation of the magnetization in Ni/BaTiO3 hybrid structures”. In: *Applied Physics Letters* 96.14 (2010), p. 142509.

[53] T Gioutsos. *Vehicle passenger weight sensor.* US Patent 5,739,757. Apr. 1998.

[54] R Gonçalves et al. “Nucleation of the electroactive β-phase, dielectric and magnetic response of poly (vinylidene fluoride) composites with Fe2O3 nanoparticles”. In: *Journal of Non-Crystalline Solids* 361 (2013), pp. 93–99.

[55] R Gregorio. “Determination of the α, β, and γ crystalline phases of poly (vinylidene fluoride) films prepared at different conditions”. In: *Journal of Applied Polymer Science* 100.4 (2006), pp. 3272–3279.

[56] H Haddadi and S Belhabib. “Improving the characterization of a hardening law using digital image correlation over an enhanced heterogeneous tensile test”. In: *International Journal of Mechanical Sciences* 62.1 (2012), pp. 47–56.

[57] S Hameed et al. “Analysis of disordered stripe magnetic domains in strained epitaxial Ni (001) films”. In: *Physical Review B* 64.18 (2001), p. 184406.

[58] J S Harrison and Z Ounaies. “Piezoelectric Polymers; NASA/Cr 2001-21142. ICASE, 2001”. In: *Report N 2001* 43 ().

[59] G Harshe, J P Dougherty, and R E Newnham. “Theoretical modelling of multilayer magnetoelectric composites”. In: *International Journal of Applied Electromagnetics in Materials* 4.2 (1993), pp. 145–145.

[60] H-c He et al. “Orientation-dependent multiferroic properties in Pb(Zr 0.52 Ti 0.48) O3–Co Fe2O4 nanocomposite thin films derived by a sol-gel processing”. In: *Journal of Applied Physics* 103.3 (2008), p. 034103.

[61] J T Heron et al. “Electric-field-induced magnetization reversal in a ferromagnet-multiferroic heterostructure”. In: *Physical review letters* 107.21 (2011), p. 217202.

[62] J Holterman and P Groen. *An introduction to piezoelectric materials and applications*. Stichting Applied Piezo, 2013.

[63] C J Hsu, J L Hockel, and G P Carman. “Magnetoelectric manipulation of domain wall configuration in thin film Ni/Pb[(Mn1/3 Nb2/3)O3] 0.68 - [PbTiO3] 0.32 (001) heterostructure”. In: *Applied Physics Letters* 100.9 (2012), p. 092902.

[64] S Imine et al. “Bottom-up and new compaction processes: a way to tunable properties of nanostructured cobalt ferrite ceramics”. In: *Journal of the European Ceramic Society* 31.15 (2011), pp. 2943–2955.

[65] NT-MDT Spectrum Instrument. *Application note*. URL: `http://www.ntmdt.com`.

[66] NT-MDT Spectrum Instrument. *Piezoresponse Force Microscopy (PFM) - Introduction, Principles and Instrumental Aspects of Piezoresponse Force Microscopy by NT-MDT*. URL: `http://www.ntmdt.com`.

[67] Q H Jiang et al. “Magnetoelectric composites of nickel ferrite and lead zirconnate titanate prepared by spark plasma sintering”. In: *Journal of the European Ceramic Society* 27.1 (2007), pp. 279–284.

[68] J Jin et al. “Multiferroic polymer composites with greatly enhanced magnetoelectric effect under a low magnetic bias”. In: *Advanced Materials* 23.33 (2011), pp. 3853–3858.

[69] F Jona and G Shirane. *Ferroelectric crystals*. Vol. 1. Pergamon, 1962.

[70] R Kalvig et al. “Ferromagnetic resonance in Mn5Ge3 epitaxial films with weak stripe domain structure”. In: *Journal of Physics D: Applied Physics* 50.12 (2017), p. 125001.

[71] C-C Kim et al. “Highly stretchable, transparent ionic touch panel”. In: *Science* 353.6300 (2016), pp. 682–687.

[72] H K D Kim et al. “Magnetoelectric control of superparamagnetism”. In: *Nano letters* 13.3 (2013), pp. 884–888.

[73] K J Kim, N M Reynolds, and S L Hsu. “Spectroscopic analysis of the crystalline and amorphous phases in a vinylidene fluoride/trifluoroethylene copolymer”. In: *Macromolecules* 22.12 (1989), pp. 4395–4401.

[74] S-K Kim et al. “Voltage control of a magnetization easy axis in piezoelectric/ferromagnetic hybrid films”. In: *Journal of magnetism and magnetic materials* 267.1 (2003), pp. 127–132.

[75] T Kimura et al. “Magnetic control of ferroelectric polarization”. In: *nature* 426.6962 (2003), pp. 55–58.

[76] C Kittel. “Physical theory of ferromagnetic domains”. In: *Reviews of modern Physics* 21.4 (1949), p. 541.

[77] M Kobayashi, K Tashiro, and H Tadokoro. “Molecular vibrations of three crystal forms of poly (vinylidene fluoride)”. In: *Macromolecules* 8.2 (1975), pp. 158–171.

[78] K M Krishnan. *Fundamentals and applications of magnetic materials.* Oxford University Press, 2016.

[79] D Y Kusuma, C A Nguyen, and P S Lee. “Enhanced ferroelectric switching characteristics of P(VDF-TrFE) for organic memory devices”. In: *The Journal of Physical Chemistry B* 114.42 (2010), pp. 13289–13293.

[80] N T Lan et al. “Magnetic domain-wall motion study under an electric field in a Finemet® thin film on flexible substrate”. In: *Journal of Magnetism and Magnetic Materials* 373 (2015), pp. 259–262.

[81] L D Landau et al. *Electrodynamics of continuous media.* Vol. 8. elsevier, 2013.

[82] J-W Lee, S-C Shin, and S-K Kim. “Spin engineering of CoPd alloy films via the inverse piezoelectric effect”. In: *Applied physics letters* 82.15 (2003), pp. 2458–2460.

[83] N Lei et al. “Magnetization reversal assisted by the inverse piezoelectric effect in Co-Fe-B/ferroelectric multilayers”. In: *Physical Review B* 84.1 (2011), p. 012404.

[84] D L Leslie-Pelecky and R L Schalek. “Effect of disorder on the magnetic properties of SmCo5”. In: *Physical Review B* 59.1 (1999), p. 457.

[85] J Li et al. “Dramatically enhanced polarization in (001),(101), and (111) BiFeO3 thin films due to epitiaxial-induced transitions”. In: *Applied physics letters* 84.25 (2004), pp. 5261–5263.

[86] J Li et al. “Self-assembled multiferroic nanostructures in the CoFe2O4-PbTiO3 system”. In: *Applied Physics Letters* 87.7 (2005), p. 072909.

[87] M Li et al. “Controlling the microstructure of poly (vinylidene-fluoride)(PVDF) thin films for microelectronics”. In: *Journal of Materials Chemistry C* 1.46 (2013), pp. 7695–7702.

[88] Z Li et al. “A magnetoelectric memory cell with coercivity state as writing data bit”. In: *Applied physics letters* 96.16 (2010), p. 162505.

[89] J Liu et al. “Magnetoelectric coupling in BaTiO3/(NiFe2O4/BaTiO 3) n (n= 1, 2, 3, 4) multilayered thin films”. In: *Journal of Applied Physics* 105.8 (2009), p. 083915.

[90] M Liu et al. “E-Field Control of Exchange Bias and Deterministic Magnetization Switching in AFM/FM/FE Multiferroic Heterostructures”. In: *Advanced Functional Materials* 21.13 (2011), pp. 2593–2598.

[91] M Liu et al. “Giant electric field tuning of magnetic properties in multiferroic ferrite/ferroelectric heterostructures”. In: *Advanced Functional Materials* 19.11 (2009), pp. 1826–1831.

[92] M Liu et al. “Strong magnetoelectric coupling in ferrite/ferroelectric multiferroic heterostructures derived by low temperature spin-spray deposition”. In: *Journal of Physics D: Applied Physics* 42.4 (2009), p. 045007.

[93] Q Liu et al. “Cobalt nanowires prepared by heterogeneous nucleation in propanediol and their catalytic properties”. In: *Nanotechnology* 19.36 (2008), p. 365608.

[94] Y Liu et al. “Facile surface functionalization of hydrophobic magnetic nanoparticles”. In: *Journal of the American Chemical Society* 136.36 (2014), pp. 12552–12555.

[95] I Lopatin Seand Lopatina and I Lisnevskaya. “Magnetoelectric PZT/ferrite composite material”. In: *Ferroelectrics* 162.1 (1994), pp. 63–68.

[96] B Lorenz et al. “Large magnetodielectric effects in orthorhombic HoMnO3 and YMnO3”. In: *Physical Review B* 70.21 (2004), p. 212412.

[97] A J Lovinger. “Annealing of poly (vinylidene fluoride) and formation of a fifth phase”. In: *Macromolecules* 15.1 (1982), pp. 40–44.

[98] T G Lupeiko et al. “Laminated magnetoelectric composites based on nickel ferrite and PZT materials”. In: *Inorganic materials* 31.9 (1995), pp. 1139–1142.

[99] J Ma et al. “Recent progress in multiferroic magnetoelectric composites: from bulk to thin films”. In: *Advanced Materials* 23.9 (2011), pp. 1062–1087.

[100] K Maaz et al. “Synthesis and magnetic properties of cobalt ferrite (CoFe2O4) nanoparticles prepared by wet chemical route”. In: *Journal of Magnetism and Magnetic Materials* 308.2 (2007), pp. 289–295.

[101] SK Mahadeva et al. “Effect of poling time and grid voltage on phase transition and piezoelectricity of poly (vinyledene fluoride) thin films using corona poling”. In: *Journal of Physics D: Applied Physics* 46.28 (2013), p. 285305.

[102] P Martins, C M Costa, and S Lanceros-Mendez. “Nucleation of electroactive β-phase poly (vinilidene fluoride) with CoFe2O4 and NiFe2O4 nanofillers: a new method for the preparation of multiferroic nanocomposites”. In: *Applied Physics A* 103.1 (2011), pp. 233–237.

[103] P Martins and S Lanceros-Méndez. “Polymer-based magnetoelectric materials”. In: *Advanced Functional Materials* 23.27 (2013), pp. 3371–3385.

[104] P Martins, A C Lopes, and S Lanceros-Mendez. “Electroactive phases of poly (vinylidene fluoride): determination, processing and applications”. In: *Progress in polymer science* 39.4 (2014), pp. 683–706.

[105] P Martins et al. “Dielectric and magnetic properties of ferrite/poly (vinylidene fluoride) nanocomposites”. In: *Materials Chemistry and Physics* 131.3 (2012), pp. 698–705.

[106] P Martins et al. “Interface characterization and thermal degradation of ferrite/poly (vinylidene fluoride) multiferroic nanocomposites”. In: *Journal of Materials Science* 48.6 (2013), pp. 2681–2689.

[107] P Martins et al. “Large linear anhysteretic magnetoelectric voltage coefficients in CoFe2O 4/polyvinylidene fluoride 0–3 nanocomposites”. In: *Journal of nanoparticle research* 15.8 (2013), p. 1825.

[108] P Martins et al. “Novel anisotropic magnetoelectric effect on δ-FeO (OH)/P (VDF-TrFE) multiferroic composites”. In: *ACS applied materials & interfaces* 7.21 (2015), pp. 11224–11229.

[109] P Martins et al. “Optimizing piezoelectric and magnetoelectric responses on CoFe2O4 / P (VDF-TrFE) nanocomposites”. In: *Journal of Physics D: Applied Physics* 44.49 (2011), p. 495303.

[110] P Martins et al. “Role of nanoparticle surface charge on the nucleation of the electroactive β-poly (vinylidene fluoride) nanocomposites for sensor and actuator applications”. In: *The Journal of Physical Chemistry C* 116.29 (2012), pp. 15790–15794.

[111] T Maurer et al. “Dipolar interactions in magnetic nanowire aggregates”. In: *Journal of Applied Physics* 110.12 (2011), p. 123924.

[112] T Maurer et al. “Exchange bias in Co/CoO core-shell nanowires: Role of antiferromagnetic superparamagnetic fluctuations”. In: *Physical Review B* 80.6 (2009), p. 064427.

[113] T Maurer et al. “Magnetic nanowires as permanent magnet materials”. In: *Applied Physics Letters* 91.17 (2007), p. 172501.

[114] I D Mayergoyz. *Handbook of giant magnetostrictive materials.* Elsevier, 1999.

[115] A McDannald et al. “Magnetoelectric coupling in solution derived 3-0 type Pb Zr0.52 Ti0.48 O3: xCo Fe2O4 nanocomposite films”. In: *Applied Physics Letters* 102.12 (2013), p. 122905.

[116] M Mehrmohammadi et al. “Enhanced pulsed magneto-motive ultrasound imaging using superparamagnetic nanoclusters”. In: *Nanotechnology* 22.4 (2010), p. 045502.

[117] J Meier, B Doudin, and J-Ph Ansermet. “Magnetic properties of nanosized wires”. In: *Journal of applied physics* 79.8 (1996), pp. 6010–6012.

[118] S Mercone et al. “Morphology control of the magnetization reversal mechanism in Co80Ni20 nanomagnets”. In: *Journal of Applied Physics* 117.20 (2015), p. 203905.

[119] CSInstruments Atomic Force Microscopes. *Magnetic Force Microscopy Mode.* URL: `https://www.csinstruments.eu/afm-modes/magnetic-force-microscopy-mode/`.

[120] L Mitoseriu and V Buscaglia. “Intrinsic/extrinsic interplay contributions to the functional properties of ferroelectric-magnetic composites”. In: *Phase Transitions* 79.12 (2006), pp. 1095–1121.

[121] G B Mitra and N C Hadler. “Stacking fault probabilities in hexagonal cobalt”. In: *Acta Crystallographica* 17.7 (1964), pp. 817–822.

[122] SO R Moheimani and A J Fleming. “Fundamentals of piezoelectricity”. In: *Piezoelectric transducers for vibration control and damping* (2006), pp. 9–35.

[123] A H Morrish. “The Physical Principles of Magnetism, John Wiley& Sons”. In: *New York* (1965).

[124] S A Morrison et al. “Magnetic and structural properties of nickel zinc ferrite nanoparticles synthesized at room temperature”. In: *Journal of Applied Physics* 95.11 (2004), pp. 6392–6395.

[125] J Moulin et al. “Internal stress influence on the coercivity of FeCuNbSiB thin films”. In: *Journal of Magnetism and Magnetic Materials* 322.9-12 (2010), pp. 1275–1278.

[126] N Moutis, D Suarez-Sandoval, and D Niarchos. “Voltage-induced modification in magnetic coercivity of patterned Co50Fe50 thin film on piezoelectric substrate”. In: *Journal of Magnetism and Magnetic Materials* 320.6 (2008), pp. 1050–1055.

[127] Khouloud Mrad. “Elaboration et étude de matériaux magnétiques nanostructurés”. PhD thesis. Paris 13 university, 2019.

[128] K Mrad et al. “Control of the crystal habit and magnetic properties of Co nanoparticles through the stirring rate”. In: *CrystEngComm* 19.25 (2017), pp. 3476–3484.

[129] SR Murthy and TS Rao. “Magnetostriction of Ni-Zn and Co-Zn ferrites”. In: *physica status solidi (a)* 90.2 (1985), pp. 631–635.

[130] C-W Nan, G Liu, and Y Lin. “Influence of interfacial bonding on giant magnetoelectric response of multiferroic laminated composites of Tb 1- x Dy x Fe 2 and PbZr x Ti 1- x O 3”. In: *Applied Physics Letters* 83.21 (2003), pp. 4366–4368.

[131] C-W Nan et al. “Multiferroic magnetoelectric composites: historical perspective, status, and future directions”. In: *Journal of Applied Physics* 103.3 (2008), p. 1.

[132] T Nan et al. “Quantification of strain and charge co-mediated magnetoelectric coupling on ultra-thin Permalloy/PMN-PT interface”. In: *Scientific reports* 4 (2014), p. 3688.

[133] M Nasir et al. “Formation of β-phase crystalline structure of PVDF nanofiber by electrospray deposition: Additive effect of ionic fluorinated surfactant”. In: *Polymer journal* 39.7 (2007), p. 670.

[134] A Neuweiler and H Kronmüller. “Magnetization processes in amorphous and nanocrystalline FeCuNbSiB thin films”. In: *Journal of magnetism and magnetic materials* 177 (1998), pp. 1269–1270.

[135] R E Newnham, D P Skinner, and L E Cross. “Connectivity and piezoelectric-pyroelectric composites”. In: *Materials Research Bulletin* 13.5 (1978), pp. 525–536.

[136] Ngoc-Anh Nguyen. *Spin-Coating optimization for very-thin hybrid films based on PVDF and Co-based nano-objects: the effect of inclusions on the electro-mechanical properties.* 2017.

[137] D Niarchos et al. “Toward Rare-Earth-Free Permanent Magnets: A Combinatorial Approach Exploiting the Possibilities of Modeling, Shape Anisotropy in Elongated Nanoparticles, and Combinatorial Thin-Film Approach”. In: *JOM* 67.6 (2015), pp. 1318–1328.

[138] I C Nlebedim and David C Jiles. “Dependence of the magnetostrictive properties of cobalt ferrite on the initial powder particle size distribution”. In: *Journal of Applied Physics* 115.17 (2014), 17A928.

[139] J A Osborn. “Demagnetizing factors of the general ellipsoid”. In: *Physical review* 67.11-12 (1945), p. 351.

[140] C B Osman et al. “In situ monitored stretching induced α to β allotropic transformation of flexible poly (vinylidene fluoride)-CoFe2O4 hybrid films: The role of nanoparticles inclusion”. In: *European Polymer Journal* 84 (2016), pp. 602–611.

[141] F Ott et al. “Effects of the shape of elongated magnetic particles on the coercive field”. In: *Journal of Applied Physics* 105.1 (2009), p. 013915.

[142] N Ouar et al. “Spark Plasma Sintering of Co80Ni20 nanopowders synthesized by polyol process and their magnetic and mechanical properties”. In: *Journal of Alloys and Compounds* 615 (2014), S269–S275.

[143] N Ouar et al. “Spark-plasma-sintering magnetic field assisted compaction of Co80 Ni 20 nanowires for anisotropic ferromagnetic bulk materials”. In: *Journal of Applied Physics* 114.16 (2013), p. 163907.

[144] L Ourry et al. “Influence of nanoparticle size and concentration on the electroactive phase content of PVDF in PVDF–CoFe2O4-based hybrid films”. In: *physica status solidi (a)* 212.2 (2015), pp. 252–258.

[145] D M Paige, B Szpunar, and B K Tanner. “The magnetocrystalline anisotropy of cobalt”. In: *Journal of magnetism and magnetic materials* 44.3 (1984), pp. 239–248.

[146] V R Palkar, J John, and R Pinto. “Observation of saturated polarization and dielectric anomaly in magnetoelectric BiFeO 3 thin films”. In: *Applied Physics Letters* 80.9 (2002), pp. 1628–1630.

[147] H Palneedi et al. “Status and perspectives of multiferroic magnetoelectric composite materials and applications”. In: *Actuators*. Vol. 5. 1. Multidisciplinary Digital Publishing Institute. 2016, p. 9.

[148] D A Pan et al. “Ni–PZT–Ni trilayered magnetoelectric composites synthesized by electro-deposition”. In: *Journal of Physics: Condensed Matter* 20.2 (2007), p. 025203.

[149] I Panagiotopoulos et al. “Low dipolar interactions in dense aggregates of aligned magnetic nanowires”. In: *Journal of Applied Physics* 114.23 (2013), p. 233909.

[150] I Panagiotopoulos et al. “Packing fraction dependence of the coercivity and the energy product in nanowire based permanent magnets”. In: *Journal of Applied Physics* 114.14 (2013), p. 143902.

[151] K K Patankar et al. “Role of sintering on magneto-electric effect in CuFe1.8Cr0.2O4–Ba0.8Pb0.2Ti0.8 Zr0.2O3 composite ceramics”. In: *Ceramics international* 27.8 (2001), pp. 853–858.

[152] M J Pechan et al. “Vortex magnetodynamics: Ferromagnetic resonance in permalloy dot arrays”. In: *Journal of applied physics* 99.8 (2006), p. 08C702.

[153] KR Pirota et al. “Magnetic and structural properties of fcc/hcp bi-crystalline multilayer Co nanowire arrays prepared by controlled electroplating”. In: *Journal of Applied Physics* 109.8 (2011), p. 083919.

[154] M Pousthomis et al. “Localized magnetization reversal processes in cobalt nanorods with different aspect ratios”. In: *Nano Research* 8.7 (2015), pp. 2231–2241.

[155] T Prabhakaran and J Hemalatha. “Ferroelectric and magnetic studies on unpoled Poly (vinylidine Fluoride)/Fe3O4 magnetoelectric nanocomposite structures”. In: *Materials Chemistry and Physics* 137.3 (2013), pp. 781–787.

[156] T Prabhakaran and J Hemalatha. “Ferroelectric Studies On Poly (Vinylidene Fluoride)/NiFe2O4 Polymer Nanocomposite Structures”. In: *AIP Conference Proceedings*. Vol. 1349. 1. AIP. 2011, pp. 343–344.

[157] T Prabhakaran and J Hemalatha. “Flexible Films of β-Phase Poly (vinylidene fluoride)/ZnFe2O4 Polymer Nanocomposite for Magnetoelectric Device Applications”. In: *Science of Advanced Materials* 6.7 (2014), pp. 1313–1321.

[158] T Prabhakaran and J Hemalatha. “Highly flexible poly (vinyldine fluoride)/bismuth iron oxide multiferroic polymer nanocomposites”. In: *AIP Conference Proceedings*. Vol. 1447. 1. AIP. 2012, pp. 1309–1310.

[159] T Prabhakaran and J Hemalatha. “Magnetoelectric investigations on poly (vinylidene fluoride)/NiFe2O4 flexible films fabricated through a solution casting method”. In: *RSC Advances* 6.90 (2016), pp. 86880–86888.

[160] T Prabhakaran and J Hemalatha. “Synthesis and characterization of magnetoelectric polymer nanocomposites”. In: *Journal of Polymer Science Part B: Polymer Physics* 46.22 (2008), pp. 2418–2422.

[161] S Priya et al. “Recent advancements in magnetoelectric particulate and laminate composites”. In: *Journal of Electroceramics* 19.1 (2007), pp. 149–166.

[162] A P Pyatakov and A K Zvezdin. “Magnetoelectric and multiferroic media”. In: *Physics-Uspekhi* 55.6 (2012), pp. 557–581.

[163] Wilhelm Conrad R. “Ueber die durch Bewegung eines im homogenen electrischen Felde befindlichen Dielectricums hervorgerufene electrodynamische Kraft”. In: *Annalen der Physik* 271.10 (1888), pp. 264–270.

[164] A Ramazani, M A Kashi, and G Seyedi. “Crystallinity and magnetic properties of electrodeposited Co nanowires in porous alumina”. In: *Journal of Magnetism and Magnetic Materials* 324.10 (2012), pp. 1826–1831.

[165] Y Ren et al. “Tailoring coercivity and magnetic anisotropy of Co nanowire arrays by microstructure”. In: *Journal of materials science* 46.23 (2011), p. 7545.

[166] J Ryu et al. “Magnetoelectric properties in piezoelectric and magnetostrictive laminate composites”. In: *Japanese Journal of Applied Physics* 40.8R (2001), p. 4948.

[167] S Ryu, Jung H Park, and Hyun M Jang. “Magnetoelectric coupling of [00 l]-oriented Pb (Zr0.4 Ti0.6) O3–Ni0.8 Zn0.2 Fe2O4 multilayered thin films”. In: *Applied Physics Letters* 91.14 (2007), p. 142910.

[168] S Sahoo et al. “Ferroelectric control of magnetism in BaTiO3/ Fe heterostructures via interface strain coupling”. In: *Physical Review B* 76.9 (2007), p. 092108.

[169] A Salimi and A A Yousefi. “Analysis method: FTIR studies of β-phase crystal formation in stretched PVDF films”. In: *Polymer Testing* 22.6 (2003), pp. 699–704.

[170] J Schöberl, H Gerstmayr, and R Gaisbauer. *NETGEN-automatic mesh generator.* 2012.

[171] W Scholz et al. “Scalable parallel micromagnetic solvers for magnetic nanostructures”. In: *Computational Materials Science* 28.2 (2003), pp. 366–383.

[172] D Seguin et al. “Growth and characterization of epitaxial Fe 0.8 Ga 0.2/0.69 PMN-0.31 PT heterostructures”. In: *Journal of Crystal Growth* 311.12 (2009), pp. 3235–3238.

[173] P Sharma and A Gupta. “Effect of preparation condition on the soft magnetic properties of FeCuNbSiB thin films”. In: *Journal of magnetism and magnetic materials* 288 (2005), pp. 347–353.

[174] P Sharma and A Gupta. “Ion beam sputtered thin films of finemet alloy for soft magnetic applications”. In: *Nuclear Instruments and Methods in Physics Research Section B: Beam Interactions with Materials and Atoms* 244.1 (2006), pp. 105–109.

[175] T Shimatsu et al. “Large uniaxial magnetic anisotropy by lattice deformation in CoPt/ Ru perpendicular films”. In: *Journal of applied physics* 99.8 (2006), 08G908.

[176] C H Sim, A Z Z Pan, and J Wang. “Thickness and coupling effects in bilayered multiferroic CoFe2O4/Pb (Zr 0.52 Ti 0.48)O3 thin films”. In: *Journal of Applied Physics* 103.12 (2008), p. 124109.

[177] G Singh et al. “Strain induced magnetic domain evolution and spin reorientation transition in epitaxial manganite films”. In: *Applied Physics Letters* 101.2 (2012), p. 022411.

[178] V Sokalski, D E Laughlin, and J-G Zhu. “Magnetic anisotropy and stacking faults in Co and Co84Pt16 epitaxially grown thin films”. In: *Journal of Applied Physics* 110.9 (2011), p. 093919.

[179] C Song et al. “Recent progress in voltage control of magnetism: Materials, mechanisms, and performance”. In: *Progress in Materials Science* 87 (2017), pp. 33–82.

[180] J Sort et al. “Role of stacking faults in the structural and magnetic properties of ball-milled cobalt”. In: *Physical Review B* 68.1 (2003), p. 014421.

[181] T Soulestin et al. “Vinylidene fluoride- and trifluoroethylene- containing fluorinated electroactive copolymers. How does chemistry impact properties”. In: *Progress in Polymer Science* 72 (2017), pp. 16–60.

[182] Y Soumare et al. “Kinetically Controlled Synthesis of Hexagonally Close-Packed Cobalt Nanorods with High Magnetic Coercivity”. In: *Advanced Functional Materials* 19.12 (2009), pp. 1971–1977.

[183] N A Spaldin. *Magnetic materials: fundamentals and applications*. Cambridge University Press, 2010.

[184] G Srinivasan, R Hayes, and M I Bichurin. “Low frequency and microwave magnetoelectric effects in thick film heterostructures of lithium zinc ferrite and lead zirconate titanate”. In: *Solid state communications* 128.6 (2003), pp. 261–266.

[185] G Srinivasan, E T Rasmussen, and R Hayes. “Magnetoelectric effects in ferrite-lead zirconate titanate layered composites: The influence of zinc substitution in ferrites”. In: *Physical Review B* 67.1 (2003), p. 014418.

[186] G Srinivasan et al. “Magnetoelectric bilayer and multilayer structures of magnetostrictive and piezoelectric oxides”. In: *Physical Review B* 64.21 (2001), p. 214408.

[187] G Srinivasan et al. “Magnetoelectric effects in bilayers and multilayers of magnetostrictive and piezoelectric perovskite oxides”. In: *Physical Review B* 65.13 (2002), p. 134402.

[188] G Srinivasan et al. “Magnetoelectric interactions in hot-pressed nickel zinc ferrite and lead zirconante titanate composites”. In: *Applied Physics Letters* 85.13 (2004), pp. 2550–2552.

[189] S Stein et al. “Magnetoelectric effect in sputtered composites”. In: *Journal of applied physics* 97.10 (2005), 10Q301.

[190] G E Sterbinsky et al. “Strain-driven spin reorientation in magnetite/barium titanate heterostructures”. In: *Applied Physics Letters* 96.9 (2010), p. 092510.

[191] E C Stoner and E P Wohlfarth. “A mechanism of magnetic hysteresis in heterogeneous alloys”. In: *IEEE Transactions on Magnetics* 27.4 (1991), pp. 3475–3518.

[192] L Sun et al. “Tuning the properties of magnetic nanowires”. In: *IBM Journal of Research and Development* 49.1 (2005), pp. 79–102.

[193] P E Tannenwald and R Weber. “Exchange integral in cobalt from spin-wave resonance”. In: *Physical Review* 121.3 (1961), p. 715.

[194] C Thiele et al. “Influence of strain on the magnetization and magnetoelectric effect in La 0.7 A 0.3 Mn O 3/ PMN- PT (001)(A= Sr, Ca)”. In: *Physical Review B* 75.5 (2007), p. 054408.

[195] B B Tian et al. “Tunnel electroresistance through organic ferroelectrics”. In: *Nature communications* 7 (2016), p. 11502.

[196] H F Tian et al. “Strain induced magnetoelectric coupling between magnetite and BaTiO3”. In: *Applied Physics Letters* 92.6 (2008), p. 063507.

[197] E Tuncer et al. “Enhancement of dielectric strength in nanocomposites”. In: *Nanotechnology* 18.32 (2007), p. 325704.

[198] D Ung et al. “Growth of magnetic nanowires and nanodumbbells in liquid polyol”. In: *Chemistry of materials* 19.8 (2007), pp. 2084–2094.

[199] D Ung et al. “Magnetic nanoparticles with hybrid shape”. In: *Progress in solid state chemistry* 33.2-4 (2005), pp. 137–145.

[200] J Van Den Boomgaard, A M J G Van Run, and J Van Suchtelen. “Magnetoelectricity in piezoelectric-magnetostrictive composites”. In: *Ferroelectrics* 10.1 (1976), pp. 295–298.

[201] J Van den Boomgaard et al. “An in situ grown eutectic magnetoelectric composite material”. In: *Journal of Materials Science* 9.10 (1974), pp. 1705–1709.

[202] A M J G Van Run, D R Terrell, and J H Scholing. “An in situ grown eutectic magnetoelectric composite material”. In: *Journal of Materials Science* 9.10 (1974), pp. 1710–1714.

[203] C A F Vaz et al. “Magnetic anisotropy modulation of magnetite in Fe3O4/BaTiO 3 (100) epitaxial structures”. In: *Applied Physics Letters* 94.2 (2009), p. 022504.

[204] C A F Vaz et al. “Magnetoelectric coupling effects in multiferroic complex oxide composite structures”. In: *Advanced Materials* 22.26-27 (2010), pp. 2900–2918.

[205] Carlos AF Vaz. “Electric field control of magnetism in multiferroic heterostructures”. In: *Journal of Physics: Condensed Matter* 24.33 (2012), p. 333201.

[206] L G Vivas et al. “Coercivity of ordered arrays of magnetic Co nanowires with controlled variable lengths”. In: *Applied Physics Letters* 98.23 (2011), p. 232507.

[207] M M Vopson. “Fundamentals of multiferroic materials and their possible applications”. In: *Critical Reviews in Solid State and Materials Sciences* 40.4 (2015), pp. 223–250.

[208] H B Wang and Z H Feng. “A highly sensitive magnetometer based on the Villari effect”. In: *IEEE Transactions on Magnetics* 49.4 (2013), pp. 1327–1333.

[209] J J Wang et al. “Magnetic anisotropy of epitaxially grown Co and its alloy thin films”. In: *Journal of Physics: Condensed Matter* 21.18 (2009), p. 185008.

[210] J Wang et al. “Epitaxial BiFeO3 thin films on Si”. In: *Applied Physics Letters* 85.13 (2004), pp. 2574–2576.

[211] J Wang et al. “Large electric-field modulation of magnetic properties in Fe films on BiScO3-PbTiO3 ceramics”. In: *Journal of Nanomaterials* 2010 (2010), p. 6.

[212] X W Wang, Z H Yuan, and H F Luo. “Interatomic force of hexagonal close packed and face centered cubic Co nanowires with different diameters”. In: *Solid State Sciences* 13.5 (2011), pp. 1211–1214.

[213] H A Wilson. "III. On the electric effect of rotating a dielectric in a magnetic field". In: *Phil. Trans. R. Soc. Lond. A* 204.372-386 (1905), pp. 121–137.

[214] D Wu et al. "Understanding the dense stripe domains in soft magnetic film". In: *Applied Surface Science* 346 (2015), pp. 567–573.

[215] B Xu and S Ren. "Integrated charge transfer in organic ferroelectrics for flexible multisensing materials". In: *Small* 12.33 (2016), pp. 4502–4507.

[216] Y Xu. *Ferroelectric materials and their applications.* Elsevier, 2013.

[217] X Xue et al. "Electric field induced reversible 180 magnetization switching through tuning of interfacial exchange bias along magnetic easy-axis in multiferroic laminates". In: *Scientific reports* 5 (2015), p. 16480.

[218] J J Yang et al. "Electric field manipulation of magnetization at room temperature in multiferroic CoFe2O4/ Pb(Mg 1/3 Nb 2/3)0.7 Ti0.3 O3 heterostructures". In: *Applied physics letters* 94.21 (2009), p. 212504.

[219] L Yao et al. "Synthesis of cobalt ferrite with enhanced magnetostriction properties by the sol- gel- hydrothermal route using spent Li-ion battery". In: *Journal of Alloys and Compounds* 680 (2016), pp. 73–79.

[220] F Zavaliche et al. "Electric field-induced magnetization switching in epitaxial columnar nanostructures". In: *Nano letters* 5.9 (2005), pp. 1793–1796.

[221] J Zhai et al. "Giant magnetoelectric effect in Metglas/polyvinylidene-fluoride laminates". In: *Applied Physics Letters* 89.8 (2006), p. 083507.

[222] Q Zhan et al. "Structure and interface chemistry of perovskite-spinel nanocomposite thin films". In: *Applied physics letters* 89.17 (2006), p. 172902.

[223] J X Zhang et al. "The effect of magnetic nanoparticles on the morphology, ferroelectric, and magnetoelectric behaviors of CFO/P (VDF-TrFE) 0–3 nanocomposites". In: *Journal of Applied Physics* 105.5 (2009), p. 054102.

[224] S Zhang et al. "Electric-field control of nonvolatile magnetization in Co40 Fe40 B20/ Pb(Mg 1/3 Nb 2/3)0.7 Ti0.3O3 structure at room temperature". In: *Physical review letters* 108.13 (2012), p. 137203.

[225] Y Zhang et al. "Large reversible electric-voltage manipulation of magnetism in NiFe/BaTiO3 heterostructures at room temperature". In: *Journal of Physics D: Applied Physics* 43.8 (2010), p. 082002.

[226] X Zhao and DG Lord. "Application of the Villari effect to electric power harvesting". In: *Journal of applied physics* 99.8 (2006), p. 08M703.

[227] H Zheng et al. "Controlling self-assembled perovskite- spinel nanostructures". In: *Nano letters* 6.7 (2006), pp. 1401–1407.

[228] H Zheng et al. "Multiferroic BaTiO3 - CoFe2O4 nanostructures". In: *Science* 303.5658 (2004), pp. 661–663.

[229] H Zheng et al. “Self-Assembled Growth of BiFeO3–CoFe2O4 Nanostructures”. In: *Advanced Materials* 18.20 (2006), pp. 2747–2752.

[230] H Zheng et al. “Three-dimensional heteroepitaxy in self-assembled BaTiO3 – Co Fe2 O4 nanostructures”. In: *Applied Physics Letters* 85.11 (2004), pp. 2035–2037.

[231] G Zhong et al. “Understanding polymorphism formation in electrospun fibers of immiscible poly (vinylidene fluoride) blends”. In: *Polymer* 52.10 (2011), pp. 2228–2237.

[232] L Zhu. “Exploring strategies for high dielectric constant and low loss polymer dielectrics”. In: *The journal of physical chemistry letters* 5.21 (2014), pp. 3677–3687.

[233] F Zighem and S Mercone. “Magnetization reversal behavior in complex shaped Co nanowires: A nanomagnet morphology optimization”. In: *Journal of Applied Physics* 116.19 (2014), p. 193904.

[234] Fatih Zighem et al. “Combining ferromagnetic resonator and digital image correlation to study the strain induced resonance tunability in magnetoelectric heterostructures”. In: *Review of Scientific Instruments* 85.10 (2014), p. 103905.

[235] F Zighem et al. “Dipolar interactions in arrays of ferromagnetic nanowires: A micromagnetic study”. In: *Journal of Applied Physics* 109.1 (2011), p. 013910.

[236] F Zighem et al. “Micro-strip ferromagnetic resonance study of strain-induced anisotropy in amorphous FeCuNbSiB film on flexible substrate”. In: *Journal of Applied Physics* 116.12 (2014), p. 123903.

[237] F Zighem et al. “Voltage-induced strain control of the magnetic anisotropy in a Ni thin film on flexible substrate”. In: *Journal of Applied Physics* 114.7 (2013), p. 073902.

Appendices

Appendix A: 2-2 type heterostructure of Finemet / Kapton / PE actuator: MFM images and corresponding angle images

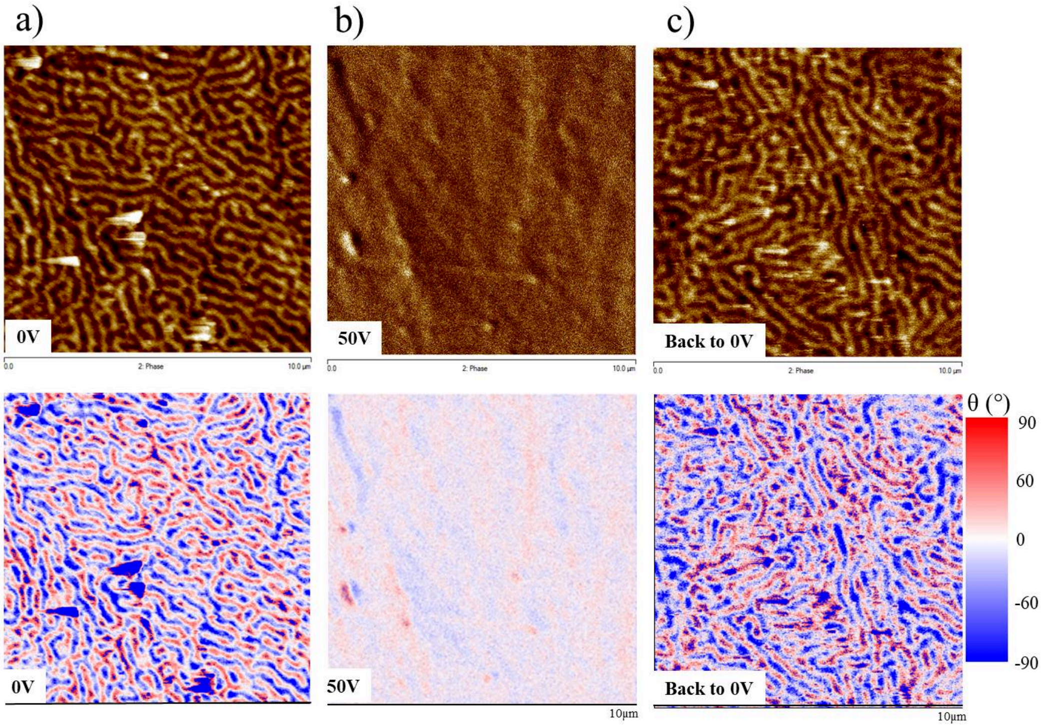

Figure 1: (top) MFM images at different applied positive E-field; (bottom) corresponding angle images. (a) E = 0V; (b) E = 50 V; (c) E back to 0V (after reach 50V). MFM image size: $10\mu m \times 10\mu m$.

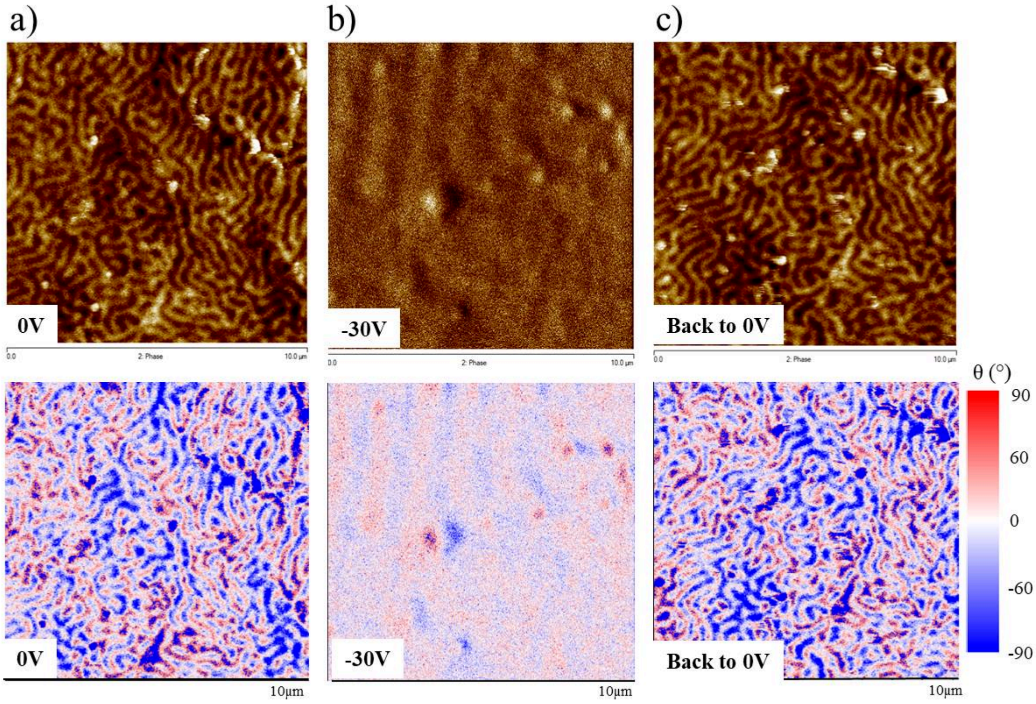

Figure 2: (top) MFM images at different applied negative E-field; (bottom) corresponding angle images. (a) E = 0V; (b) E = -30 V; (c) E back to 0V (after reach -50V). MFM image size: 10μm × 10μm

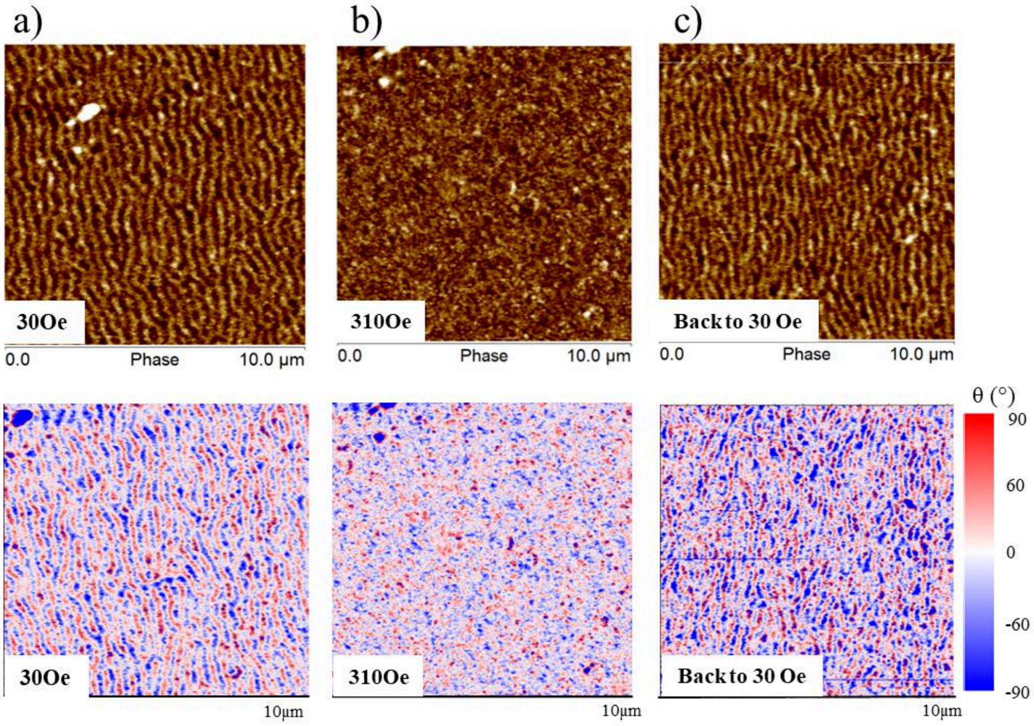

Figure 3: (top) MFM images at different applied positive H-field; (bottom) corresponding angle images. (a) H = 30 Oe; (b) H = 310 Oe; (c) H back to 30 Oe (after reach 400 Oe). MFM image size: 10μm × 10μm

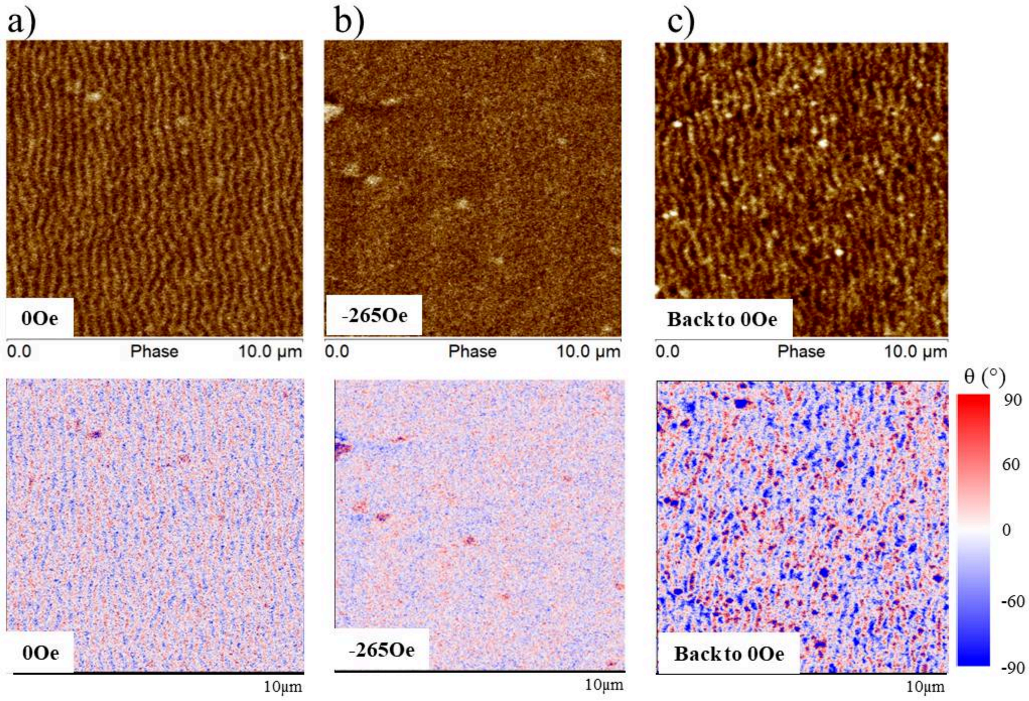

Figure 4: (top) MFM images at different applied negative H-field; (bottom) corresponding angle images. (a) H = 0 Oe; (b) H = -265 Oe; (c) H back to 0 Oe (after reach -400 Oe). MFM image size: 10μm × 10μm

Appendix B: Analysis of the raw signal of MPMS 3 VSM SQUID

In order to understand the magnetic behavior in Figure 4.12, 4.13, 4.14 and 4.15, I decided to record and analyze the raw data of these M-H curve. As described in chapter 2, section 2.1.1, the output of MPMS 3 DC measurement is the raw data which is the curve of the voltage signal as function of the sample position. From a raw curve, a magnetic moment value is calculated automatically by a MPMS MultiVu fit. Therefore, each point in the M-H loop corresponds to a raw V(z) curve. Note that the output file data of the raw signal is a big file which contains all the raw data of a M-H loop. To analyze each raw curve, they need to be separated from each others. One of the useful ways is using the "split" tool in the Ubuntu PC like we did here.

Since the PVDF/CFO 0.5% wt exhibits the highest uncommon behavior, I decided to analyze the raw signal of this sample at low field and low temperature. The raw signal of the PVDF/CFO 0.5% wt with functionalized NPs at different magnetic fields are shown in Figure 5.

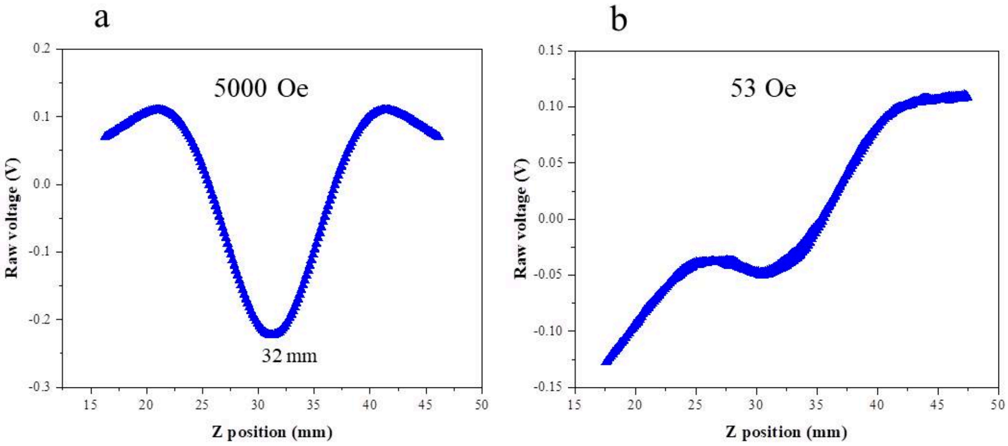

Figure 5: Raw signal of the PVDF/CFO 0.5% wt functionalized at different applied magnetic field. (a) 5000 Oe; (b) 53 Oe.

Figure 5(a) represents a typical raw signal which is a function of the position of the sample inside the pick-up coil. The peak indicates at the coil center (see Figure 2.1, chapter 2). This typical raw signal presenting a different form can lead to a bad systematic fit from the MPMS program and thus to an incorrect magnetic moment automatically calculated.

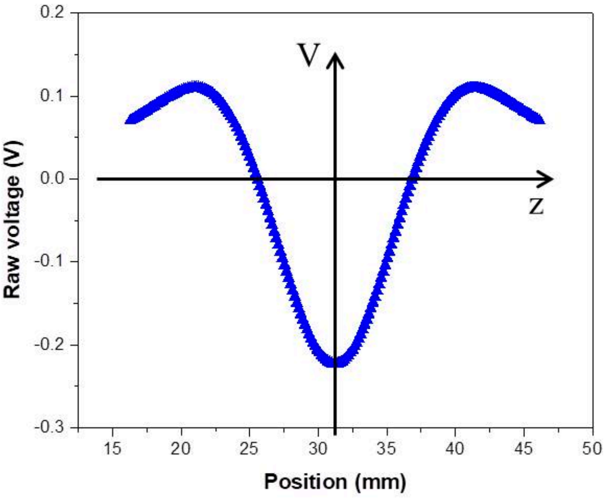

Figure 6: Raw signal V(z) where the center of the signal is marked by the V-axis and z represents the position of the sample inside the coils during the scan-measurements.

In order to confirm the magnetic moment values recorded in the M-H hysteresis loop, we need to verify the raw signal for each points of the loop by using the equations 1. Where V is the raw voltage and z is the position of the sample. The coordinate axis of V(z) is described in Figure 6. Several raw signals have been chosen at different applied magnetic field ranges from H = 375 Oe to H = -375 Oe.

$$\begin{aligned} \text{Even} &= \frac{V(z) - V(-z)}{2} \\ \text{Odd} &= \frac{V(z) + V(-z)}{2} \end{aligned} \tag{1}$$

The results are shown in Figure 7. As it can be seen in Figure 7(a), the even curve is zero as expected for a V(z) signal symmetric respect to the center of the pick-up coils. In this case, the magnetic moment recorded in the M-H loop is correct since their raw signal show a typical signal for the magnetic moment which the MPMS is able to correctly fit. However, in Figure 7(b), several odd curves are also zero. The odd curve should be the half V(z) signal (in the case of a symmetric raw data like in Figure 5(a)). This seems not to be the case here for several measurements although the correspondent even curve are zero. More measurement and analysis are needed to understand these complex results.

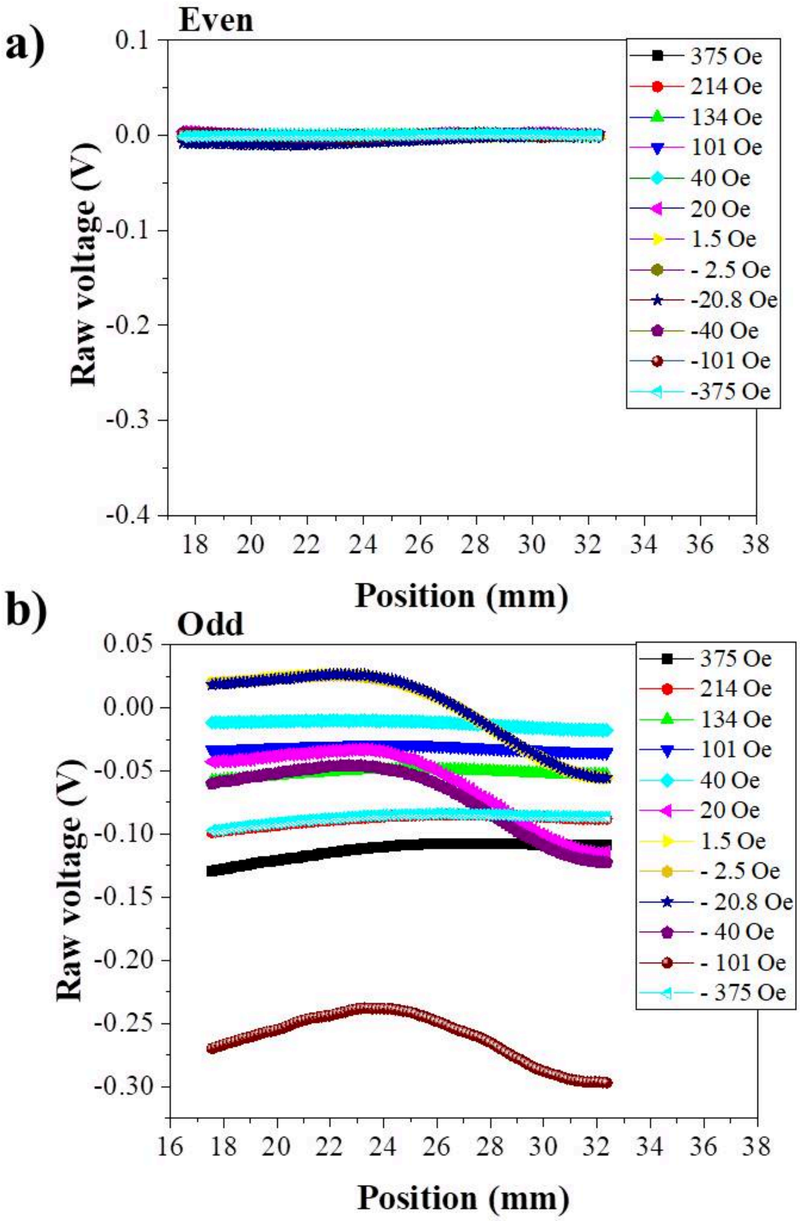

Figure 7: (a) Applying the even equation; (b) Applying the odd equation.

Appendix C: Optimizing ferromagnetic properties of anisotropic nanoparticles

I report here some complementary results from the micromagnetic simulation studies on the Co NWs *ensemble.*

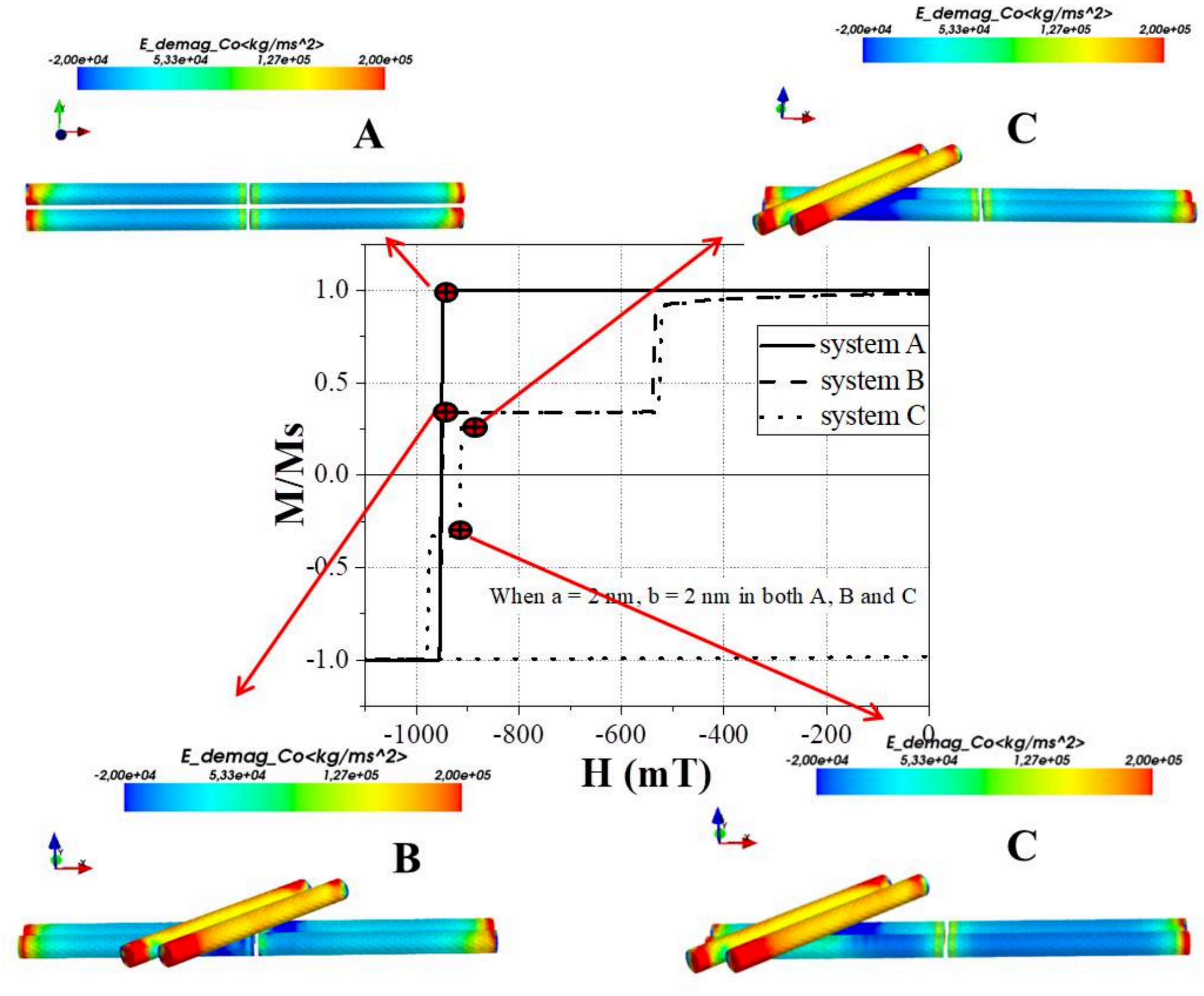

Figure 8: The demagnetizing field distribution inside each NW of the NWs assembly studied in the section 5.3.3. The configuration of A, B and C structures are reported at different point of the reversal mechanism of the ensemble. To visualize the A, B and C structures, please refer to Figure 5.16 of the section 5.3.3.

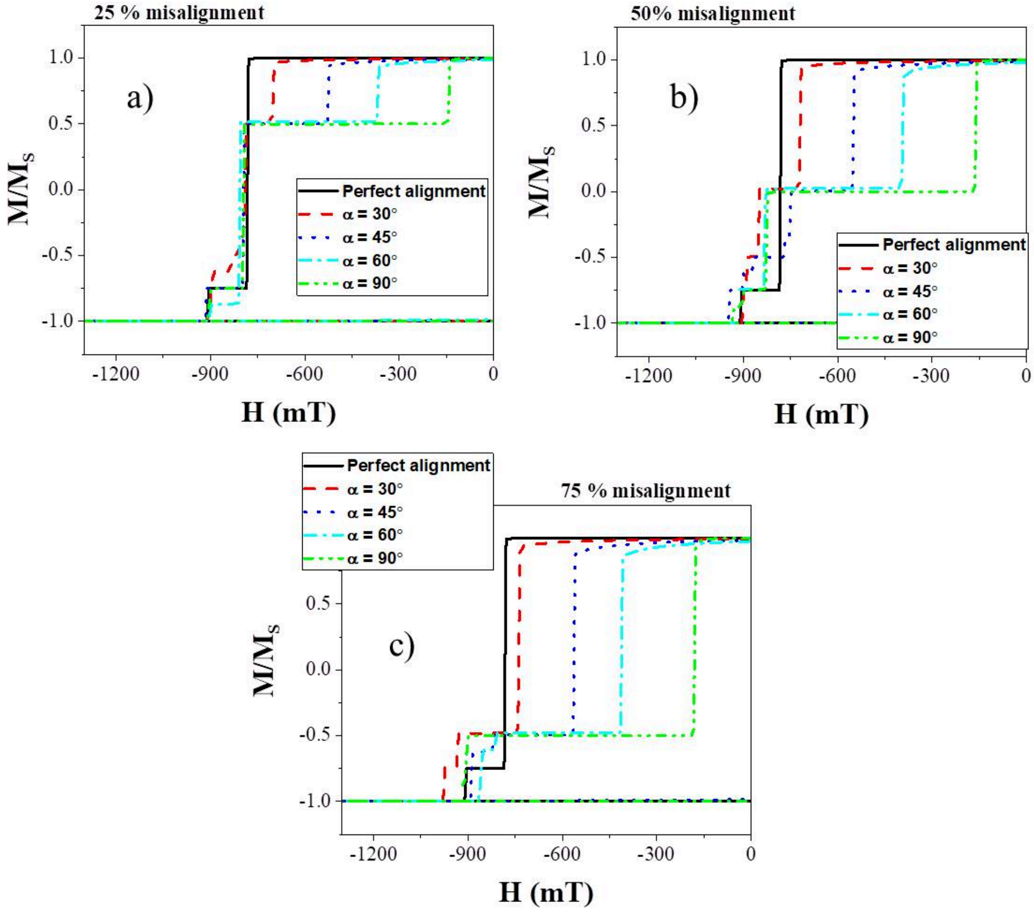

Figure 9: Hysteresis loops of various two-dimensional geometry arrangements of NWs with different percentages of misaligned NWs: (a) 25 % (i.e. 4 NWs are misaligned over a total of 16); (b) 50 %; (c) 75 %. The considered misaligned angles (α) varies from 0°to 90°compared to the x direction of the aligned NWs. The external applied magnetic field parallel to the x direction, $\theta = 0$. These hysteresis loops are taken by the second- and third-quadrant of the full hysteresis loops since the rest are symmetrical respect to H = 0 Oe. To visualize the two-dimensional arrangements, please refers to chapter 5, section 5.3.

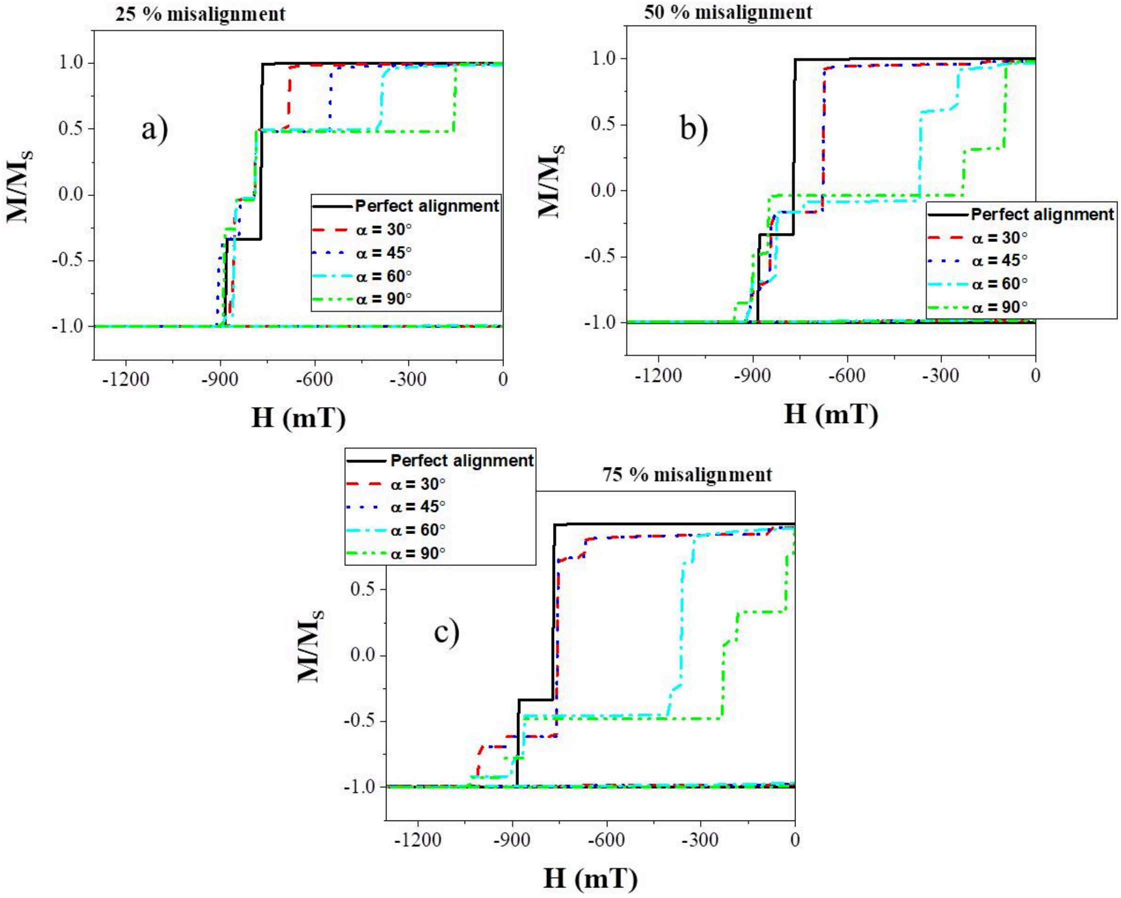

Figure 10: Hysteresis loops of various three-dimensional geometry arrangements of NWs with different percentages of misaligned NWs: (a) 25 % (i.e. 7 NWs are misaligned over a total of 27); (b) 50 %; (c) 75 %. The considered misaligned angles (α) varies from 0°to 90°compared to the x direction of the aligned NWs. The external applied magnetic field parallel to the x direction, $\theta = 0$. To visualize the three-dimensional arrangements, please refers to chapter 5, section 5.3

Appendix D: Disclosing real quantitative data in piezoelectric ceramic materials through Piezoresponse Force Microscopy

During my PhD, I had the opportunity to be part of a NFFA EUROPE project which provides the access to experimental European facilities and gives support for performing specific researches all around Europe (*https://www.nffa.eu/*). In this project, I worked on the ferroelectric properties and piezoresponse of PVDF film using the Piezoresponse Force Microscopy under the supervision of A. Gomez at Scanning Probe Microscopy Laboratory, ICMAB, at Barcelona Autonoma University UAB (Spain) (see chapter 4). In addition to the PVDF film, I have also contributed to the research on a real quantitative data measuring in piezoelectric ceramic materials by Piezoresponse Force Microscopy. In this research, I have measured the piezoresponse (d_{33}, d_{31}, g_{33} and g_{31}) of the PZT, PPLN, PMN-PT samples. These results are in the second step of reviewing of Nature Communications Physics. Here in the following the abstract of our work.

Disclosing real quantitative data in piezoelectric ceramic materials through Piezoresponse Force Microscopy

A. Gomez[1]*, H.T.T Nong[2], S. Mercone[2], T. Puig[1], X. Obradors[1]

[1]Instituto de Ciencia de Materiales de Barcelona (ICMAB-CSIC), Campus UAB, 08193, Bellaterra, España
[2]Laboratoire de Sciences des Procédés et des Matériaux (LSPM-CNRS UPR-3407), Université Paris 13, Sorbonne Paris Cité, 99, Av. J. Clément, 93430 Villetaneuse, France

*Corresponding author: agomez@icmab.es

ABSTRACT

Piezoelectric material characterization is a key part into the iterative process to develop materials or improve their properties. From the portofolio of characterization techniques, Piezoresponse Force Microscopy (PFM) arised as a possible quantitative characterization tool of the piezoelectric effect. In this manuscript we report a systematic study in which different Lead Zirconate Titanate (PZT) piezoelectric materials, with different piezoelectric coefficients, are measured following the standard procedure available for PFM. We demonstrate the method cannot be considered quantitative. The d_{33} values measured with PFM does not correlate with the reference values provided by the manufacturer. To turn things around, we propose a correction factor taking into consideration the piezoelectric stroke needed to move the tip. We calculate the maximum stroke, blocking force, that a piezoelectric material can exert and compare it with the force needed to move the AFM tip. We demonstrate that in most cases, such stroke is a strong limiting factor into the probe vibration amplitude. To correct this effect, we introduce a new factor, named Open Piezopotential Gauge, introducing the force as a limiting vibration factor. With the use of this factor, we are able to correct this effect and provide an accurately interpretation of PFM data. Further in this study we demonstrate, applying the exact same constant force to the material, but with different cantilever stiffness, the first measurements of the piezoelectric stiffness at the nanoscale.

Publications and presentations

Publications

1. **H. T. T. Nong** et al., "Electrical reversible control of the magnetic domain distribution in artificial planar multiferroic nanostructures" (under writing process).

2. **H. T. T. Nong**, A. Nguyen, J. Solard, C. Ben Osman, M. Simon, E. Carrillo, A. Gomez and S. Mercone, "Local electromechanical control in PVDF – based thin films by the hybrid inter-phase optimization", Nano-Structures and Nano-Objects (submitted).

3. A. Gomez, **H. T. T Nong**, S. Mercone, T. Puig, X. Obradors, "Disclosing real quantitative data in piezoelectric ceramic materials through Piezoresponse Force Microscopy", Nature communications Physics (submitted).

4. **H. T. T. Nong**, T. M. K. Kha, S. Mercone, Tunable magnetic anisotropy by bulk nanostructuration: a micromagnetic study. J. Magn. Magn. Mater. (accepted).

5. **H. T. T. Nong**, A. Garcia-Sanchez, C. Ibrahim, N. T. Lan and S. Mercone, "Electric Control of the Magnetic domains in artificial magnetoelectric composite heterostructure", IEEE Trans.Mag. 54, 1-6 (2018).

6. **H. T. T Nong**, K Mrad, F Schoenstein, JY Piquemal, N Jouini, B Leridon, S.Mercone, "Stacking faults density driven collapse of magnetic energy in hcp-cobalt nano-magnets", Adv. Nat. Sci.: Nanosci. Nanotechnol. 8, 025012 (2017).

7. K. Mrad, F. Schoenstein, **H. T. T. Nong**, E. Anagnostopoulou, A. Viola, L. Mouton, S. Mercone, C. Ricolleau, N. Jouini, M. Abderraba, L.-M. Lacroix, G. Viau and J.-Y. Piquemal, "Control of the crystal habit and magnetic properties of Co nanoparticles through the stirring rate", Cryst. Eng. Comm. 19, 3476-3484 (2017).

Presentations

1. International Conference on Magnetism, **ICM 2018**, 15th - 20th July 2018, San Francisco, USA. *Mapping of the magnetic anisotropy in nanostructured permanent magnet: a micromagnetic study.* **H. T. T. Nong**, T. Mai Kha, F. Schoenstein, N. Jouini and S. Mercone (Poster).

2. Young Physicist Meetings, 26th October 2017, Paris, France. *Electric control of magnetic behavior in artificial multiferroics.* **H.T.T. Nong**, S. Mercone (Poster).

3. Journées Nationales sur le frittage par courant pulse, **SPS 2017**, 5-6 Octobre 2017 – Villetaneuse (France). *Magnetic Properties of Nanostructured Permanent Magnet*, **H. T. T. Nong**, K. Mrad, F. Schoenstein, N. Jouini, B. Leridon and S. Mercone (Poster).

4. 18th Colloque Louis Néel, **CLN 2017**, 24th - 27th September 2017, Paris, France. *Optimization of nanowires dense assembly: the strategy for a nanostructured permanent magnet.* **H. T. T. Nong**, K. Mrad, F. Schoenstein, N. Jouini, B. Leridon and S. Mercone (Poster).

5. Nanotech France 2017, 28th -30th June 2017, Paris, France. *Controlling the energy product of hcp-Cobalt nano-magnets.* **H. T. T. Nong**, K. Mrad, F. Schoenstein, N. Jouini, B. Leridon, J-Y. Piquemal et S. Mercone (Oral).

6. Magnetic society IEEE summer school, 19th - 22th June 2017, Santander, Spain. *Mapping of the Magnetic properties in Co-based nano-magnets.* **H. T. T. Nong**, T. M. Kha, F. Schoenstein, N. Jouini, B. Leridon and S. Mercone (Poster).

7. Competition: presenting thesis in 180s, 2017, Doctoral school Galilee, Villetaneuse, France. *Electric control of magnetic behavior in artificial multiferroics* (Oral and Poster).

8. LSPM doctorate day, 24th April 2017, Villetaneuse, France. *Electric control of magnetic behavior in artificial multiferroics* (Oral).

9. 8th International Workshop on Advanced Materials Science and Nanotechnology, **IWAMSN 2016**, 8th - 12th November 2016, Ha Long, Vietnam. *Magnetic energy control of nanostructure Cobalt-based magnet.* **H. T. T. Nong**, K. Mrad, F. Schoenstein, N. Jouini, B. Leridon, J.-Y. Piquemal, C. Ricoleau et S. Mercone (Oral).

10. Marie Curie summer school, Domain Wall and Spintronics **ITN − WALL 2016**, 12th - 16th September 2016, Spetses, Greece. *Magnetic force microscopy study of magnetic domains wall motion in an artificial Multiferroic.* **H. T. T. Nong**, A. Garcia-Sanchez, C. Ibrahim, N. T. Lan et S. Mercone. (Oral and Poster).

Abstract

Contrôle électrique du comportement magnétique dans des multiferroïques artificiels

Résume

Les matériaux multiferroïques présentent plusieurs ordres ferroïques, i.e. ferromagnétiques, ferroélectriques et/ou ferroélastiques. Le couplage entre ses ordres ferroïques permet de contrôler les propriétés magnétiques en appliquant un champ électrique et vice versa. Afin d'utiliser leur multifonctionnalités dans des nouvelles applications, ce couplage doit être efficace à température ambiante. Cette thèse étudie les systèmes couplant artificiellement ensemble une phase ferromagnétique / magnétostrictive à une phase ferroélectrique / piézoélectrique. Le couplage entre ces deux phases est appelée magnétoélectrique (ME). Le premier chapitre décrit l'état de l'art de ce couplage ME dans différents structures composites multiferroïques. Tandis que les techniques de caractérisation et les outils de simulation micromagnétiques utilisés sont présentés dans le deuxième chapitre. Dans le troisième chapitre, une hétéro-structure type film magnétostrictif/substrat flexible/actuateur piézoélectrique (FeCuNbSiB/Kapton/PE) a été étudiée. Les domaines magnétiques du FeCuNbSiB ainsi que leur orientation sont contrôlés en appliquant un champ électrique et étudiés par microscopie locale (MFM). Le quatrième chapitre étudie un composite incluant des nanoparticules magnétostrictives dans une matrice piézoélectrique flexible (polymère PVDF). L'effet des inclusions (nanoparticules) sur la réponse piézoélectrique locale du PVDF est étudié par microscopie de piézoréponse (PFM). Symétriquement, l'influence de la matrice piézoélectrique sur les propriétés magnétiques des nanoparticules est analysée. Dans le dernier chapitre, l'optimisation des propriétés magnétiques statiques d'un ensemble de nanoparticules anisotropes (nanofils de cobalt) est étudiée sous l'influence de leur structure, de leur forme et de leurs interactions. Cette étude expérimentale est corroborée par les simulations et vise des nouveaux composites incluant ces nanoparticules anisotropes dans une matrice piézoélectrique flexible.

Mots-clés: Multiferroïques artificiels, nano-composites, couplage magnétoélectriques, énergie magnétique, nano-aimants, PVDF, piézoélectricité, MFM, PFM, VSM, simulation micromagnétiques.

Electric control of magnetic behavior in artificial multiferroic composites

Abstract:

Multiferroic materials present several ferroic orders, i.e. ferromagnetic, ferroelectric and/or ferroelastic. The coupling between these ferroic orders allow the control of the magnetic properties by applying an electric field and vice versa. In order to use their multifunctionality in new applications, this coupling must be efficient at room temperature. This thesis concentrates on materials artificially coupling together a ferromagnetic/ magnetostrictive phase with a ferroelectric/piezoelectric one. The coupling between these two phases is called magnetoelectric (ME). The first chapter describes the state of the art of this ME coupling for different multiferroic composite structures. Characterization techniques and micromagnetic simulation tools are presented in the second chapter. In the third chapter, a hetero-structure given by a magnetostrictive film/flexible substrate/piezoelectric actuator (FeCuNbSiB/Kapton/PE) is studied. The magnetic domains of FeCuNbSiB as well as their orientation are controlled by applying an electric field and studied by local microscopy (MFM). The fourth chapter focuses on a nanocomposite material including magnetostrictive nanoparticles in a flexible piezoelectric matrix (PVDF polymer). The effect of these inclusions (nanoparticles) on the local piezoelectric response of the PVDF is studied by piezoeponse microscopy (PFM). Symmetrically, the influence of the piezoelectric matrix on the static magnetic properties of the nanoparticles is analyzed. In the last chapter, the optimization of the magnetic properties of a set of anisotropic nanoparticles (cobalt nanowires) is studied as fonction of their structure, shape and mutual interactions. This experimental study is corroborated by simulations and targets new composites ME materials including the anisotropic nanoparticles in a flexible piezoelectric matrix.

Key words: Artificial multiferroics, nanocomposite materials, magnetoelectric coupling, magnetic energy, nano-magnets, PVDF, piezoelectricity, MFM, PFM, VSM, micromagnetic simulation.